

Various Test Specimens on Emissivity Assessment Apparatus: An Experimental Approach

Dr. K. Srividya¹, Dr. Sd. Abdul Kalam², Ch. Mohan Sumanth³, K. Sai dikshit⁴, Md. Sameer⁵, B. Tarun kumar⁶

¹Associate Professor, Mechanical Engineering Department, P V P Siddhartha Institute of Technology, Vijayawada

^{2,3}Assistant Professor, Mechanical Engineering Department, P V P Siddhartha Institute of Technology, Vijayawada

^{4,5,6}III B.Tech student, Mechanical Engineering Department, P V P Siddhartha Institute of Technology, Vijayawada

srividya@pvpsiddhartha.ac.in

Abstract. In the current examination, to discover the emissivity of a test example by contrasting and the reference example of known emissivity. The essential target of the paper is to decide the complete emissivity of the offered test to high precision utilizing a straightforward and practical trial arrangement. In this examination utilized in a dark body at a predetermined temperature and frequency, no surface can radiate more energy than a dark body. It retains all episode radiation, paying little heed to frequency and course, and the dark body utilized it utilizes every one of the genuine surfaces are approximated as dim surfaces. The warmth produced from the surface goes through the warmth transition sensor, the hemispherical all out emissivity of the surface can be determined utilizing the Stephen-Boltzmann law of radiation. Emissivity's of metals at high temperatures impact the energy balance in a wide scope of assembling measures just as innovative work exercises and accordingly decide execution even financial practicality. Exact and far reaching estimations of metal's warm emissivity have consistently been a test because of various powerful factors. A trial arrangement for emittance estimation noticeable all around at high temperature was created during the course study. Indoor regulators and temperature sensors can be mounted straightforwardly on the warmers for direct temperature control. Substances retain various frequencies and transmit out lower frequencies because of impact utilization. Emissivity is likewise reliant on the temperature of the article and the occurrence frequency of light on the material. The all out emissivity estimating contraption is planned and dissected dependent on mathematical and warm imperatives. Appropriate materials were chosen dependent on their mechanical properties, cost, and accessibility on the lookout. The effectiveness of the hardware increments with an increment in working temperature. The aligned effectiveness is discovered to be higher than the past equipment's.

Keywords: Emissivity, black body, gray body, incident radiation

INTRODUCTION

The overall capacity of its surface to produce energy by radiation is the emissivity of material (generally composed ϵ or e). Emissivity is the proportion of at similar temperatures, the energy emanated by a specific material to the energy transmitted by a dark body. A genuine dark body has an emissivity(ϵ) = 1 while any genuine item has emissivity(ϵ) < 1. Emissivity is a dimensionless amount. Emissivity relies upon factors like temperature, frequency, and discharge point. That a surface phantom emissivity and absorptive don't rely upon frequency is an average designing presumption, so the emissivity is consistent. This is known as the "gray body presumption".

$$\varepsilon = \frac{\text{Emissive Power Of Body}}{\text{Emissive Power Of Blackbody}} = \frac{E}{E_b}$$

LITERATURE REVIEW

Giovanni Tanda [1] examined the estimation of absolute hemispherical emittance and explicit warmth of aluminium and Inconel 718 by a calorimetric method. S Moghaddam [2] examined the Heat Flux-Based Emissivity Measurement. Zhang R-H [3] concentrated on emissivity scaling and relativity of homogeneity of surface temperature. RuiPitarma [4] assessed wood emissivity by a methodology technique. Petra Honnerova Jiri [5] examined the emissivity estimation strategy for cloudy coatings at encompassing temperature. Seban R.A. [6] introduced the emissivity of progress metals in the infrared. Yunus A Cengel [7] printed a book on warmth and mass exchange. Naga Swapna M [8] contemplated the Radiation Effect of MHD Casson liquid stream straightly permeable extending sheet in the presence of substance response

DESIGN

Design considerations

1. Area of the specimen $\leq (1/1000) \times$ Total Surface area of the enclosure
 - Enclosure is cuboidal in shape
where Length (l) = 1m or 1000mm,
Breadth (b) = 0.75m or 750mm,
Height (h) = 1m or 1000mm.
 - Total surface area of enclosure = $2(lb+bh+hl)$
 $= 2(1 \times 0.75 + 1 \times 0.75 + 1 \times 1)$
 $= 5 \text{ m}^2$ or $5 \times 10^6 \text{ mm}^2$
 - $(1/1000) \times$ Total Surface area of the enclosure = $5/1000 = 0.005 \text{ m}^2$ or 5000 mm^2
 - Area of the square shaped specimen = $0.028 \times 0.028 = 0.000784 \text{ m}^2$ or 784 mm^2
2. The temperature difference between specimen and surrounding is maintained as high as possible.
 - Temperature at the specimen surface, $T_s \geq 100^\circ\text{C}$
 - Temperature in the surrounding, T_a or $T_\infty = 27^\circ\text{C}$

Design parameters

✚ Power parameters

- Power rating of heater: 3.3W to 11.36W
- Input Voltage range: 10V to 18V AC
- Resistance of heater: 28.5Ω
- Current carrying capability of heater: 0.35 to 0.63A

✚ Geometric parameters

- Geometric Shape of specimen: Square
- Side length: 28mm or 0.028m
- Area of cross section of specimen: 784 mm^2 or 0.000784 m^2
- Thickness of specimen: 1mm or 0.001m
- Size of enclosure: Length (l) = 1m or 1000mm,

Breadth (b) = 0.75m or 750mm,

Height (h) = 1m or 1000mm.

- Total surface area of enclosure: $5 \times 10^6 \text{ mm}^2$ or 5 m^2

Thermal parameters

- Maximum operating temperature of heater: 120°C
- Maximum value of Syndanio insulation temperature: 350°C
- Maximum value of ceramic fiber blanket insulation temperature: 983°C
- Maximum temperature which alumina plate can withstand: 1750°C
- Temperature measuring range of FeK thermocouple: -50 to 900°C

Specimen holder

The example holder is made of syndanio cover block. Two square scores of 28 mm^2 are sliced up to a profundity of 9mm is cut. For this reason, 2 syndanio sheets 9mm and 12mm are utilized independently. Absolutely 6 subset screws alongside nuts are utilized to hold it. The earthenware fiber up to a thickness of 2mm is set inside the sections to give protection just as padding impacts the base size of the heater. The warmer is put on it. The alumina plate of 1mm thick is set on the heater to forestall direct contact between the heating component (silver palladium) and aluminium plate else it will prompt short out. On the highest point of a warmer sandwich aluminium plate of 4mm thick plate is set which gives a stage to put test and reference examples. This aluminium plate is put in the furrows. The two thermocouples are utilized to decide the temperature of the test and reference examples. Third thermocouple is utilized for estimating encompassing temperature inside the container.

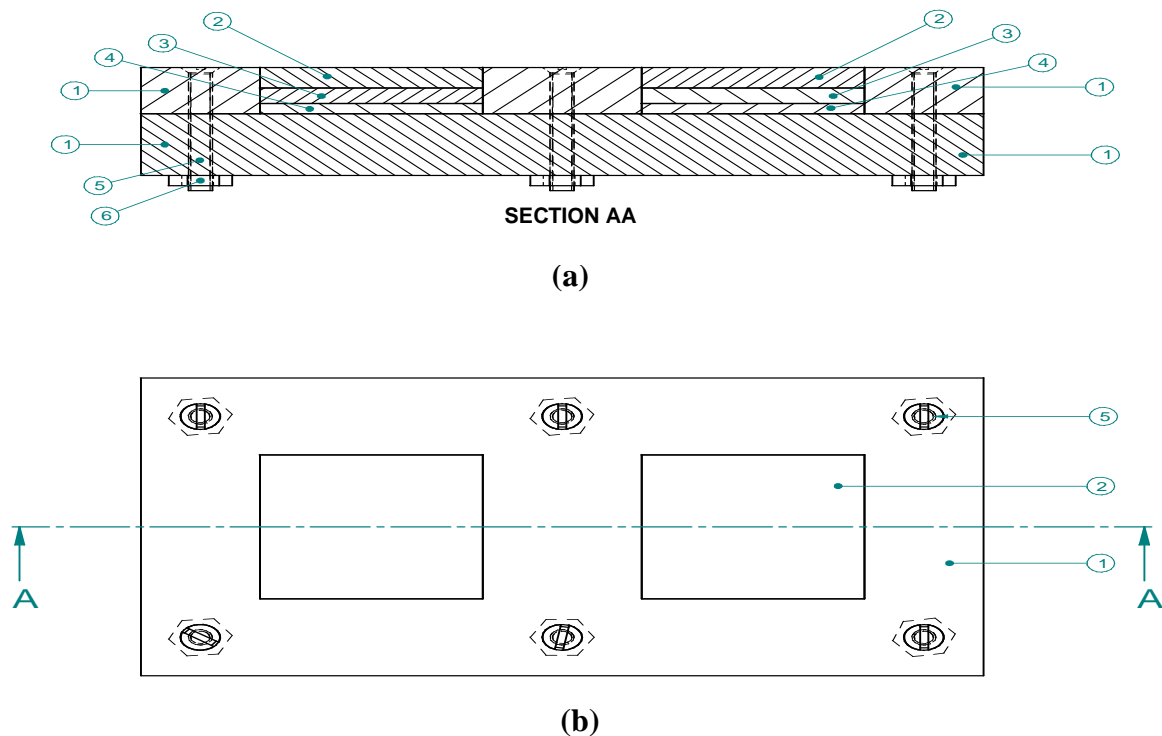


Figure1. Specimen holder (a) Sectional view (b) Top view

Table 1. Part Labeling Table

Component Number	Name	Qty	Breadth (in mm)	Length (in mm)	Thickness (in mm)	Other Specifications
1	Syndanio	1	58	106	21	
2	Aluminium	2	28	28	4	
3	Heater + Alumina plate	2	28	28	3	
4	Ceramic Fiber Blanket	2	28	28	2	
5	Counter sink screws	6	-	-	-	8mm diameter 390mm length Counter sink angle $\alpha = 120^\circ$
6	Nuts	6	-	-	-	5mm hole

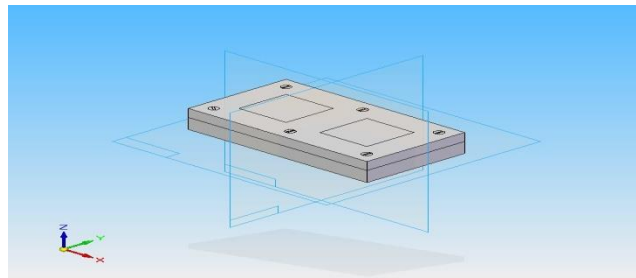


Figure2. Specimen holder 3-dimensional view

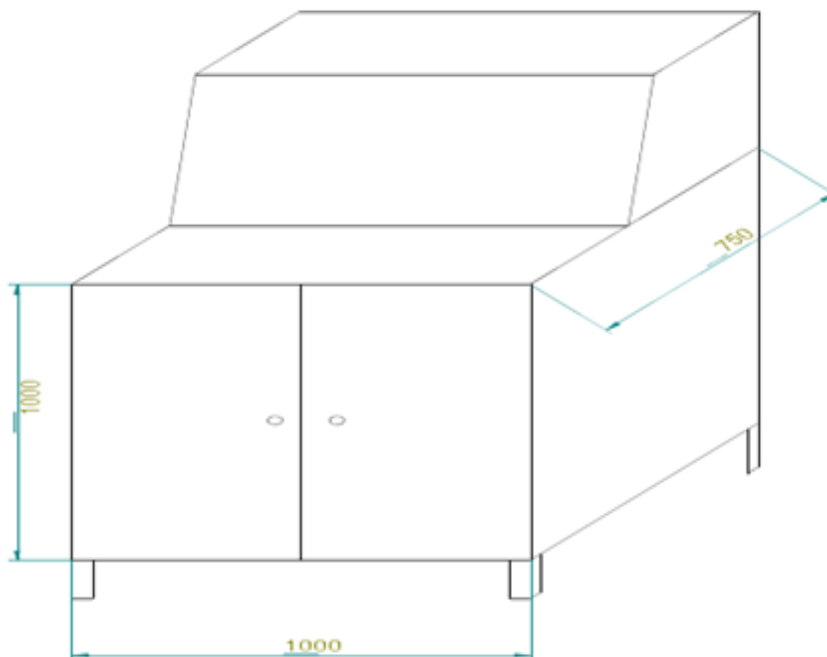


Figure3. Test cabinet

Overall view

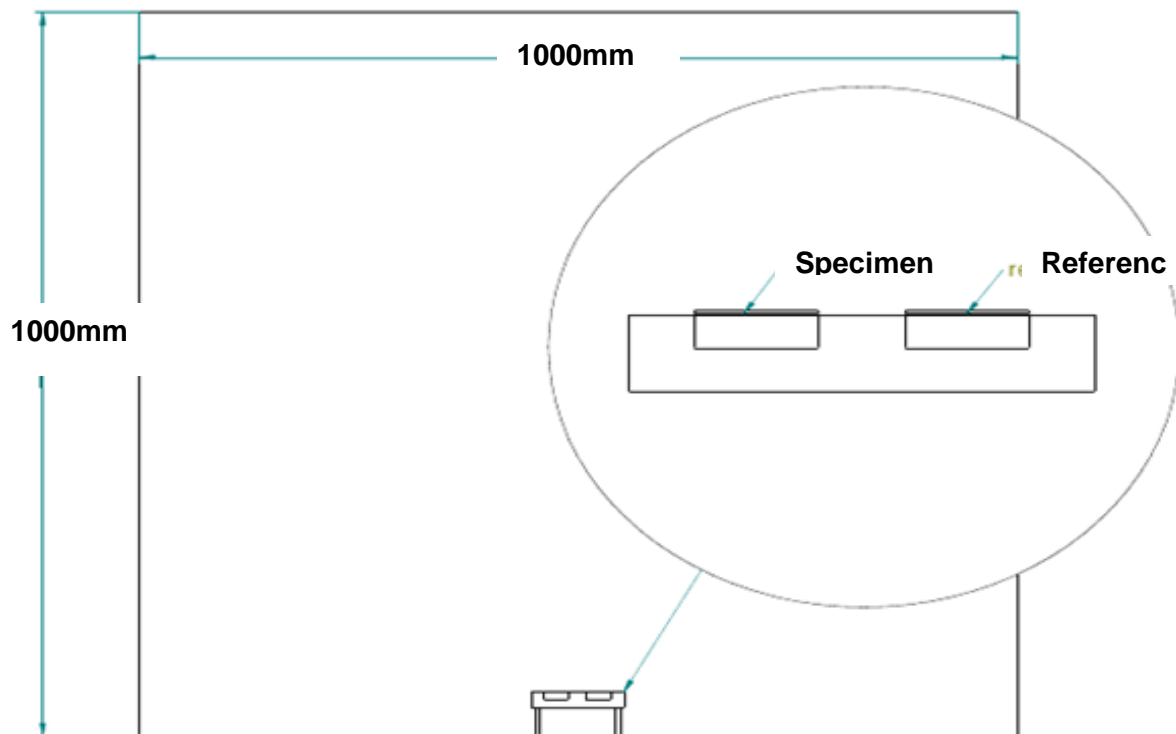


Figure4. Cross sectional view of test cabinet Inset: enlarged view of specimen setup

Test cabinet

The test bureau comprises of fenced-in area and control board. The whole bureau is made of gentle steel CR. To forestall rusting of gentle steel it is painted. Within dividers of the nook is painted with a dark matte paint to assimilate heat. To keep the warmed surface from seeing its appearance on the lower part of the chamber, within dividers of the nook are covered with 2 layers of steel wire network. The nook is furnished with 2 ways to approach the examples which are put on the example holder.

OVERALL DIMENSIONS OF ENCLOSURE: -

Length = 1m or 1000mm

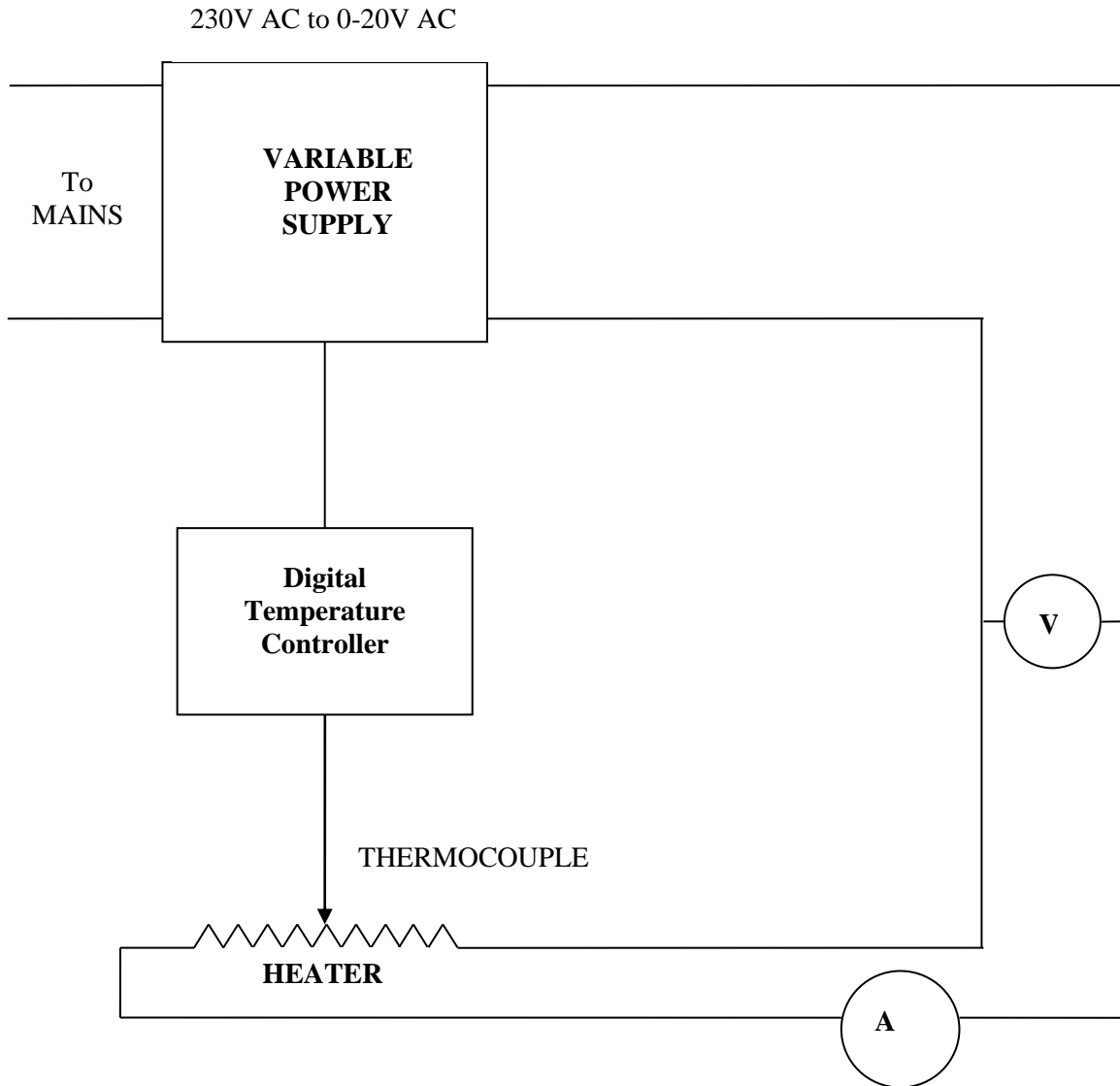
Breadth = 0.75 or 750mm

Height = 1m or 1000mm

Total surface area = 5 m² or 5 × 10⁶ mm²

Table2. List of electric components used

SERIAL NO.	COMPONENT NAME	QUANTITY (in no's)
1	POWER SUPPLY	2
2	AMMETER	2
3	VOLTMETER	2
4	DIGITAL TEMPERATURE CONTROLLER	2
5	THERMOCOUPLES	3



Photographs of the apparatus



Figure5.View of finished apparatus

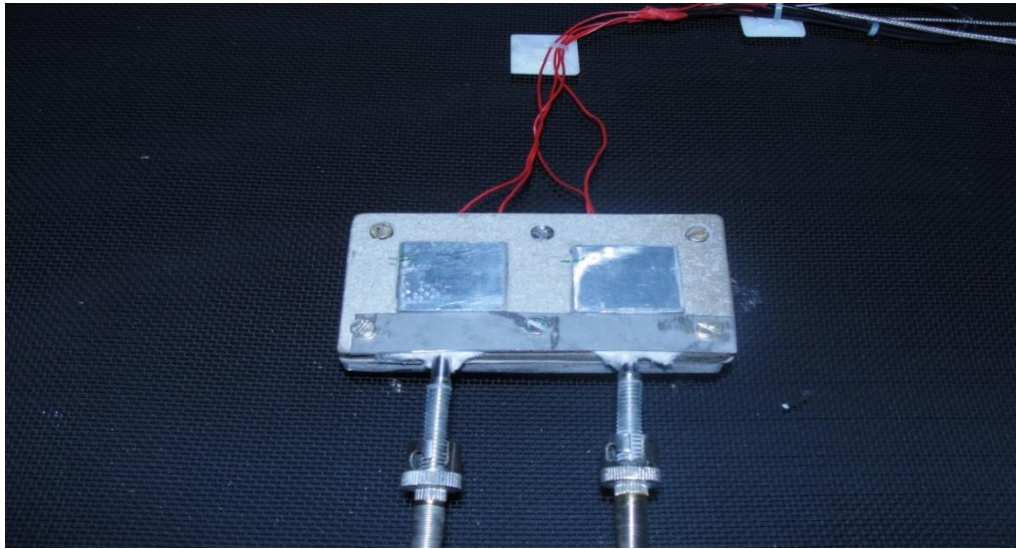


Figure 6. View of Specimen Holder

CALCULATIONS & INFERENCE

Sample

Test plate: Alumina

Reference plate: Anodized aluminium

OBSERVATIONS: -

PARTICULARS		
V_t in Volts		12
TEST PLATE	I_t in Amps	0.36
Temperature on test plate °C		88
V_r in Volts		13
REFERENCE PLATE	I_r in Amps	0.36
Temperature on reference plate in °C		87
Ambient temperature T_a in °C		27
Emissivity of test plate ϵ		0.62

TOTAL EMISSIVITY OF VARIOUS MATERIAL SURFACES

MATERIAL	TEMPERATURE Deg.C	EMISSIVITY
STAINLESS STEEL	216	0.44
STEEL	500	0.35
SILVER	200	0.02

BRASS	200	0.03
ASBESTOS	200	0.96
CERAMIC	93	0.90
COPPER	20	0.07
GRAPHITE	3600	0.80
GLASS	200	0.95

CALCULATIONS: -

Rate of heat transfer from the test plate, $Q_t = V_t I_t = \epsilon_t \sigma A_t (T_t^4 - T_a^4)$ Eq (1)

Rate of heat transfer from the reference plate, $Q_r = V_r I_r = \epsilon_r \sigma A_r (T_r^4 - T_a^4)$...Eq (2)

Dividing Eq(1) by Eq(2) we get

$$\frac{V_t I_t}{V_r I_r} = \frac{\epsilon_t \sigma A_t (T_t^4 - T_a^4)}{\epsilon_r \sigma A_r (T_r^4 - T_a^4)}$$

But Area of test specimen = Area of reference specimen

$$A_t = A_r$$

Therefore

$$\epsilon_t = \frac{\epsilon_r V_r I_r (T_r^4 - T_a^4)}{V_t I_t (T_t^4 - T_a^4)} = \frac{0.84 \times 12 \times 0.36 \times (351^4 - 300^4)}{13 \times 0.36 \times (361^4 - 300^4)} = 0.62$$

$$\boxed{\epsilon_t = 0.62}$$

ACCURACY OF MEASUREMENT: -

Actual value of emissivity of alumina $\epsilon_a = 0.65^*$

Experimental value of emissivity of alumina $\epsilon_e = 0.62$

% of accuracy of measurement = (Experimental value / Actual value) \times 100

$$\begin{aligned} &= (\epsilon_e / \epsilon_a) \times 100 \\ &= (0.62/0.65) \times 100 \\ &= 95.38\% \end{aligned}$$

Improvements achieved over the previous equipment

- The heat misfortune through the radiators is limited toward all paths aside from one, along these lines making unidirectional warmth stream.
- This strategy gives exact outcomes than the prior one because of a decrease in heat misfortunes because of convection by utilizing the example of more modest measurements.
- Efficient and uniform warming of screen printed ceramic radiators when contrasted with mica warmers.
- In the prior technique the reference and test example were fixed. In this technique, various examples can be utilized.
- Power utilization is 6W, which is low contrasted with the past one, which is 120W.

CONCLUSION

The absolute emissivity estimating contraption is planned and broke down dependent on mathematical and warm limitations. Appropriate materials were chosen dependent on their mechanical properties, cost, and accessibility on the lookout. The plan is finished utilizing SOLID EDGE v18. The manufacture was done dependent on the plan boundaries. Protection for the whole contraption is never really a heat misfortune. To accomplish a serious level of precision touchy thermocouples are utilized. The effectiveness of the hardware increments with expansion in working temperature. The adjusted effectiveness is discovered to be higher than the past hardware.

Following steps can be implemented in future to improve the accuracy of the apparatus:

- Better and exact, electronic and electrical estimating instruments can be utilized
- Vacuum siphon can be utilized to empty the air from the fenced in area where the example is kept. With this the impacts of the convection can be diminished.
- Heater with better plan can be utilized.

REFERENCES

- [1] Giovanni Tanda & Mario Misale. (2006). Measurement of Total Hemispherical Emittance and Specific Heat of Aluminium and Inconel 718 by a Calorimetric Technique, *J. Heat Transfer*, 128(3), 302-306.
- [2] Saeed Moghaddam, John Lawler, Collin McCaffery & Jungho Kim. (2005). Heat Flux-Based Emissivity Measurement, *AIP Conference Proceedings*. 746, 32.
- [3] Zhang. R.-H., Zhao-Liang Li, Tang.X.-Z., & Xiaomin Sun. (2010). Study of Emissivity Scaling and Relativity of Homogeneity of Surface Temperature, *International Journal of Remote Sensing*. 25, 249-259.
- [4] Rui Pitarma & João Crisóstomo. (2019). An Approach Method to Evaluate Wood Emissivity, *Journal of Engineering*. Article ID 4925056, 2019.
- [5] Petra Honnerová, Jiří Martan, Zdeněk Veselý, & Milan Honner. (2017). Method for emissivity measurement of semitransparent coatings at ambient temperature, *Scientific reports*. Article number 1386.
- [6] Seban, R. A., (1965). The Emissivity of Transition Metals in the Infrared, *J. Heat Transfer*. 87(2), 173-176.
- [7] Yunus A Cengel, & Afshin J. Ghajar. (2017). Heat and Mass Transfer: Fundamentals and Applications. *Book*.
- [8] Naga Swapna, M., Anusha, P., Chittaranjandas, V., Srividya, K. (2021). Radiation Effect of MHD Casson fluid flow linearly porous stretching sheet in the presence chemical reaction, *Annals of R.S.C.B.*, 25(3), 1858-1869.

Computation Fluid Dynamics Analysis of Flow over a Flat Plate for Different Fluids

¹Dr.P.Anusha, ²Dr.M.Naga Swapna Sri, ³ E.Kavitha

^{1,2}Assistant Professor, Mechanical Engineering Dept, PVP Siddhartha Institute of
Technology, Kanuru, Vijayawada, Andhra Pradesh, India.

ABSTRACT: As a part of this project, CFD analysis is performed on pipe with fins for various header sections. Heat exchangers are used in a number of sectors, and one such heat exchanger (a pipe with fins) is considered in this paper. It is created to meet the industry's business requirements. The condenser is designed using the CREO parameters programme. The design procedure resulted in a condenser with 22 tubes, 20mm outer diameter, 18mm inner diameter, and a length of 90mm. Because the design technique does not specify the type of to be utilized header, investigated 3 different headers that provide equal velocity in the tube's entrance. Various geometries were used in multiple points of header's input nozzle. Optimal location of the, which might be used for equal liquid and velocity distribution across each and every tube, is done using CFD models. The major goal of this project is to employ commercial Computational Fluid Dynamics [CFD] software to verify the planned condenser. CREO parameters 3.0 software is used to create a symmetric representation of the simplified geometry of a condenser [Pipe with Fins] for simulation purposes. The velocity, pressure, and temperature characteristics are calculated using the fin as a rectangular plate and air and water as fluids. The procedure is then repeated for the plate with a hole.

IndexTerms – CFD, Pipe with Fins, Condenser, Velocity, Pressure, Temperature.

I. Introduction

Computational Fluid Dynamics [CFD] is a wonderful concept which uses problematic analysis to solve fluid flow problems. Softwares will perform the necessary calculations to model liquids and gases interactions with surfaces specified by boundary equations. Due to latest advancements, software's are now handling complex applications like steady/unsteady, laminar/turbulent fluid flow applications. In the early days, these software's are used for flight tests and also for multiple applications in various sectors. The best alternatives for planning and determining the efficiency level of HVAC systems are often derived using this simulation. To guarantee that the design criteria are met, data from CFD analyses can be utilized to validate a variety of design elements. CFD modeling also helps with the design verification for variety of systems. The CFD model can also be used to spot weaknesses in HVAC design or product failures.

By modifying the exterior material, Praveen Kumar Kanti et al [01] investigated work related to counter flow heat exchangers without baffle plates. According to Amol S. Niphade et al. [02] Heat exchangers are so important in practise, especially those that involve chemical reactions and phase changes, to develop cost effective tools. Ankit Uppal and colleagues [03] determined ideal configuration of baffle shape by seven types of baffle layouts for enhancing HT. This analysis was carried out using ANSYS 14.5 Fluent, a three-dimensional finite volume based CFD tool. A heat exchanger tube composed of Al and Cu with a length of 0.1m

and a diameter of 0.01m was considered. All computations were done with a Reynolds number of 10,000. Greatest heat transfer is possible for rectangular and triangular shaped baffle surfaces. The reason for the highest heat transfer rate was that baffles increased turbulence by allowing more mixing of fluid layers, which boosted heat transmission through the heat exchanger tube.

A twin pipe heat exchanger's performance rate is shown. by Sk.M.Z.M.Saqheb et al[04]. By altering the materials that use the heat input from the refinery's waste steam recovery process. CATIA and GAMBIT are used to design double pipe heat exchangers. ANSYS is used to perform CFD analysis. The final results were achieved using three different materials: steel, aluminium, and copper. The project of Kranthi Kumar Mamidala et al [05] intends the % inaccuracy in experimental and analytical data by analysing the heat flow pattern of a heat exchanger using Fluent Software.

In industrial processes, exchangers of heat are used for heat recovery fluids, according to Jibin Johnson et al [6]. Heat exchangers are designed to play a certain purpose in any application. Even though the multiple equations are available, validating the design with these equations takes time. The analytical design of the exchanger was done in this work depending on CFD simulation results. Traditional k-modeling was used in this paper's CFD research.

The work of Swapnaneel Sarma et al [7] was done with the goal of predicting the efficiency of a waste heat recovery heat exchanger with fluent CFD , and the findings were compared to existing experimental values. The performance of the heat exchanger was determined for triangular and the results were compared with traditional rectangular fins.

II. CFD Analysis Process

The standard approach for performing a CFD study is outlined here to help you understand the many components of a CFD simulation. The technique includes the following steps:

1. Create a diagram of flow for the problem
2. Geometry and Flow Domain Modeling
3. Set the Boundary and the Starting constraint values
4. Grid generation
5. SimulationStrategy
6. Parameters/ Files for Input
7. Execute the Simulation
8. Monitoring
9. post-process the simulation results.
10. Make observations between the outcomes

III. Condenser Design:

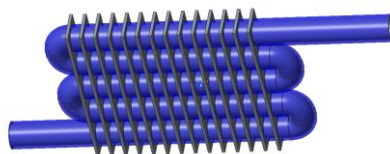


Fig 1. Condenser Design

Parameters:

- The pipe's outside diameter: 20mm
- Pipe inner diameter : 18mm
- Length of the fin : 12mm
- Width of the fin : 16mm
- Thickness : 1mm

IV. RESULTS AND DISCUSSION:

The CREO parameter 3.0 programme is used to create a symmetric image of the simplified geometry of a condenser [Pipe with Fins] for simulation purposes.

Initially, by considering fin as a rectangular plate and air as fluid analyzed the variation of parameters either by keeping velocity as constant or temperature as constant.

FLUID AS AIR

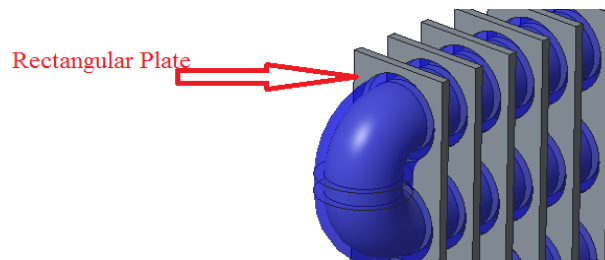
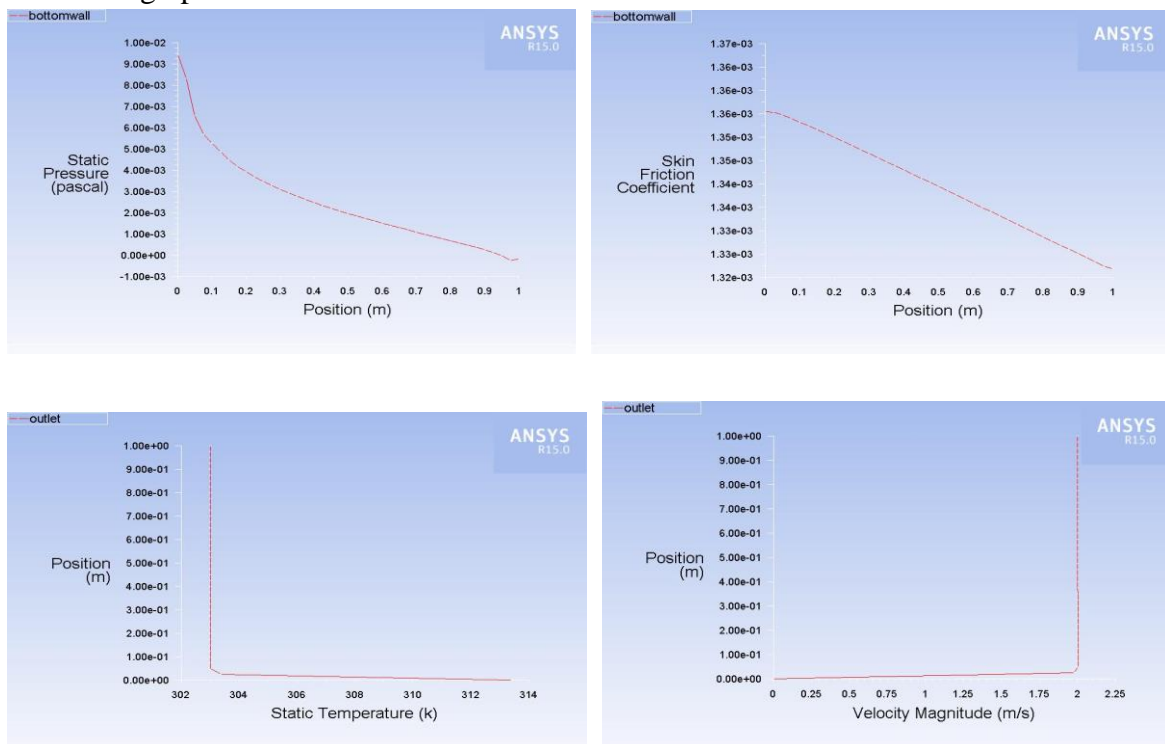


Fig 2. Laminar Flow over a Rectangular Plate considering Fluid as Air

Analysis 1: CFD ANALYSIS OVER A PLATE, Fluid as AIR

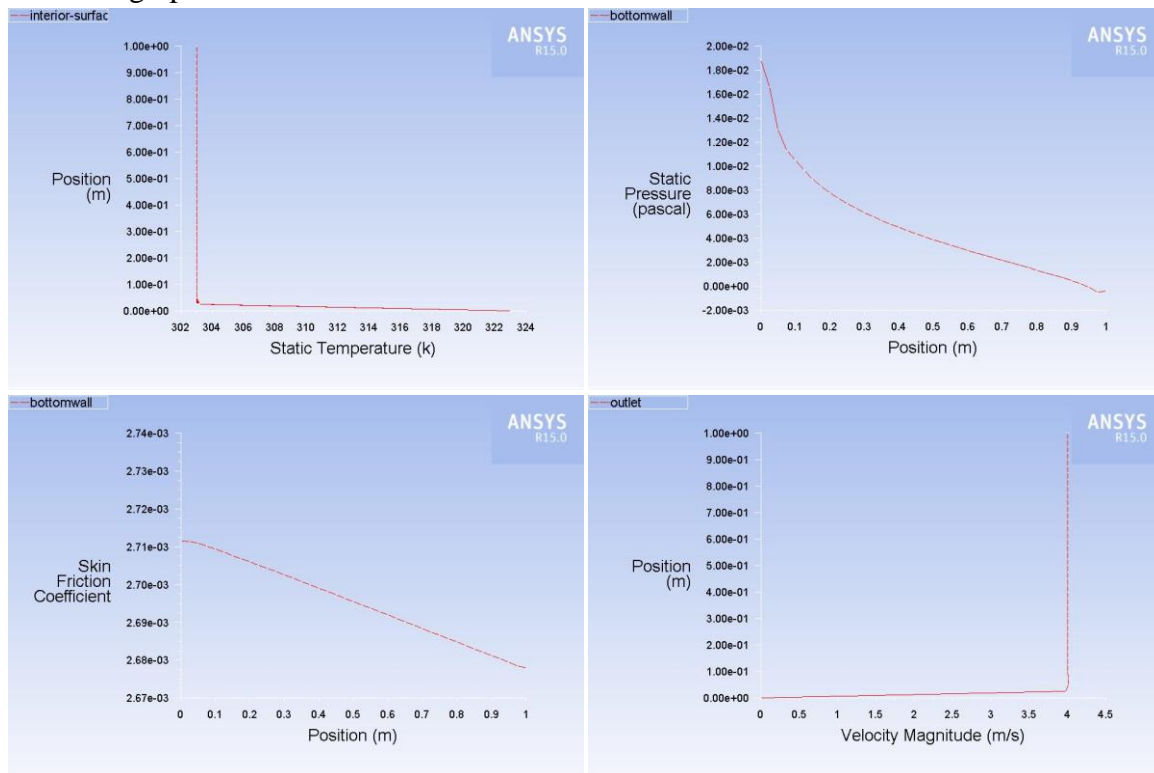
CASE 1: FLUID AS AIR BY KEEPING TEMPERATURE AT 323K & VARYING VELOCITY 2m/s:

Obtained graphs:



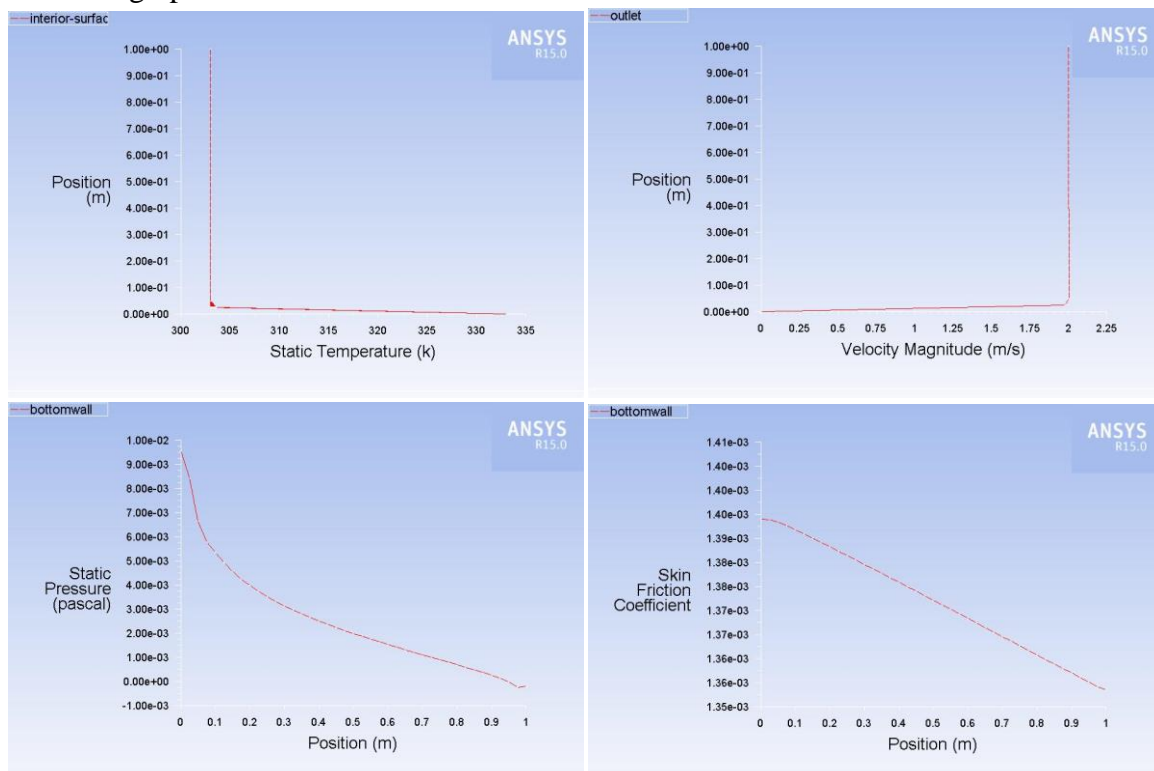
CASE 2: FLUID AS AIR BY KEEPING TEMPERATURE AT 323K & VARYING VELOCITY 4m/s:

Obtained graphs:



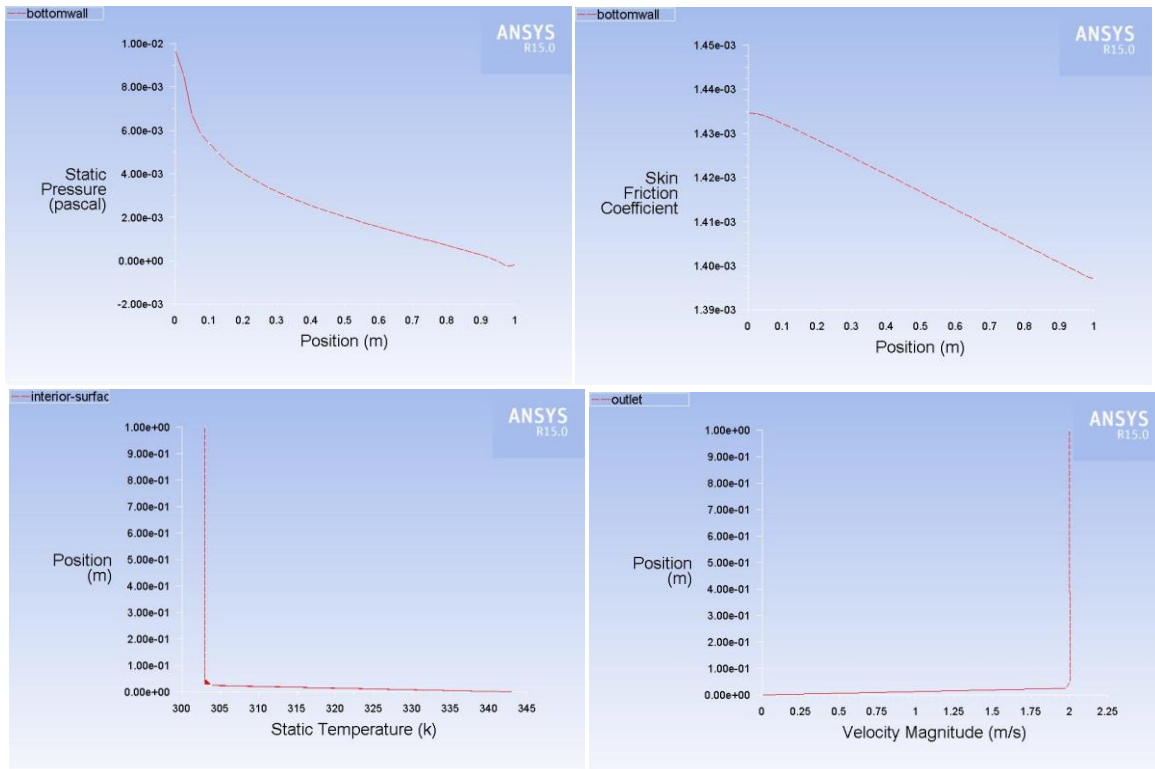
CASE 3: FLUID AS AIR BY KEEPING VELOCITY 2m/s & VARYING TEMPERATURE 333K

Obtained graphs:



**CASE 4: FLUID AS AIR BY KEEPING VELOCITY 2m/s & VARYING TEMPERATURE
AT 343K.**

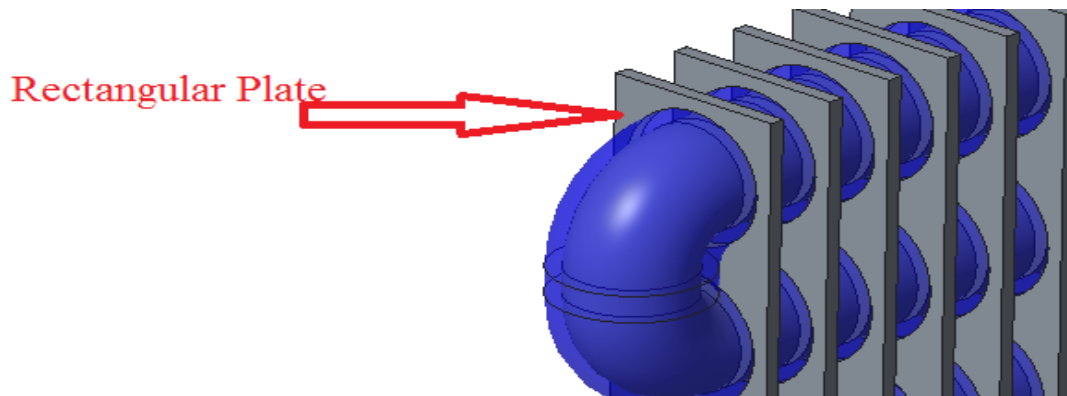
Obtained graphs:



Analysis 2: CFD ANALYSIS OVER A PLATE, Fluid as WATER

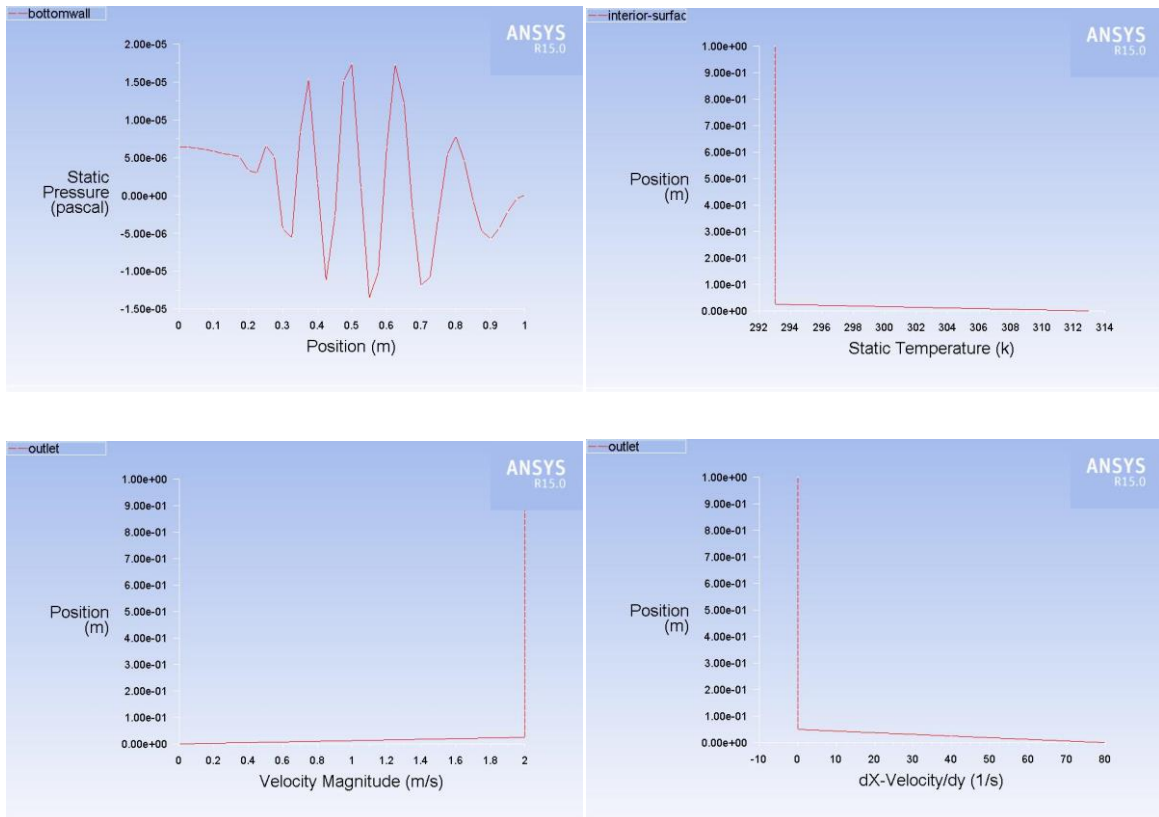
By considering fin as a rectangular plate and water as fluid analyzed the variation of parameters either by keeping velocity as constant or temperature as constant.

FLUID AS WATER



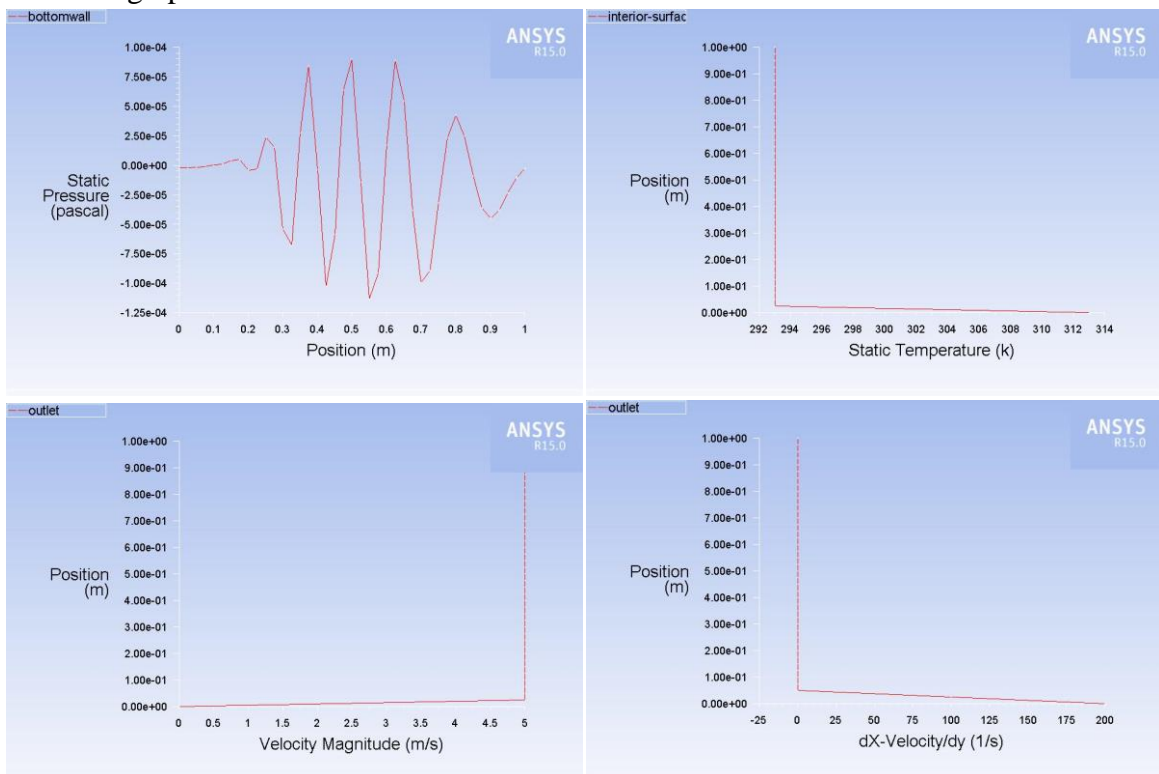
CASE 5: FLUID AS WATER BY KEEPING TEMPERATURE CONSTANT & VARYING VELOCITIES 2m/s

Obtained graphs:



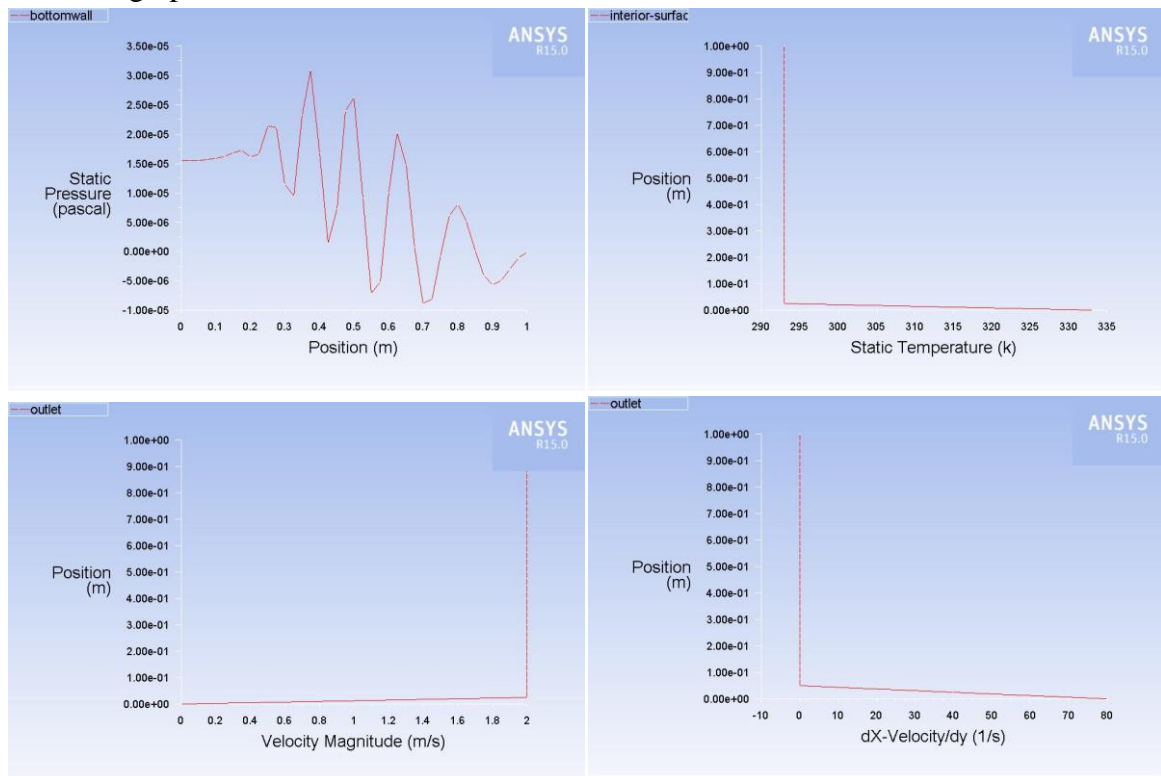
CASE 6 : FLUID AS WATER BY KEEPING TEMPERATURE CONSTANT & VARYING VELOCITIES 4 m/s

Obtained graphs:



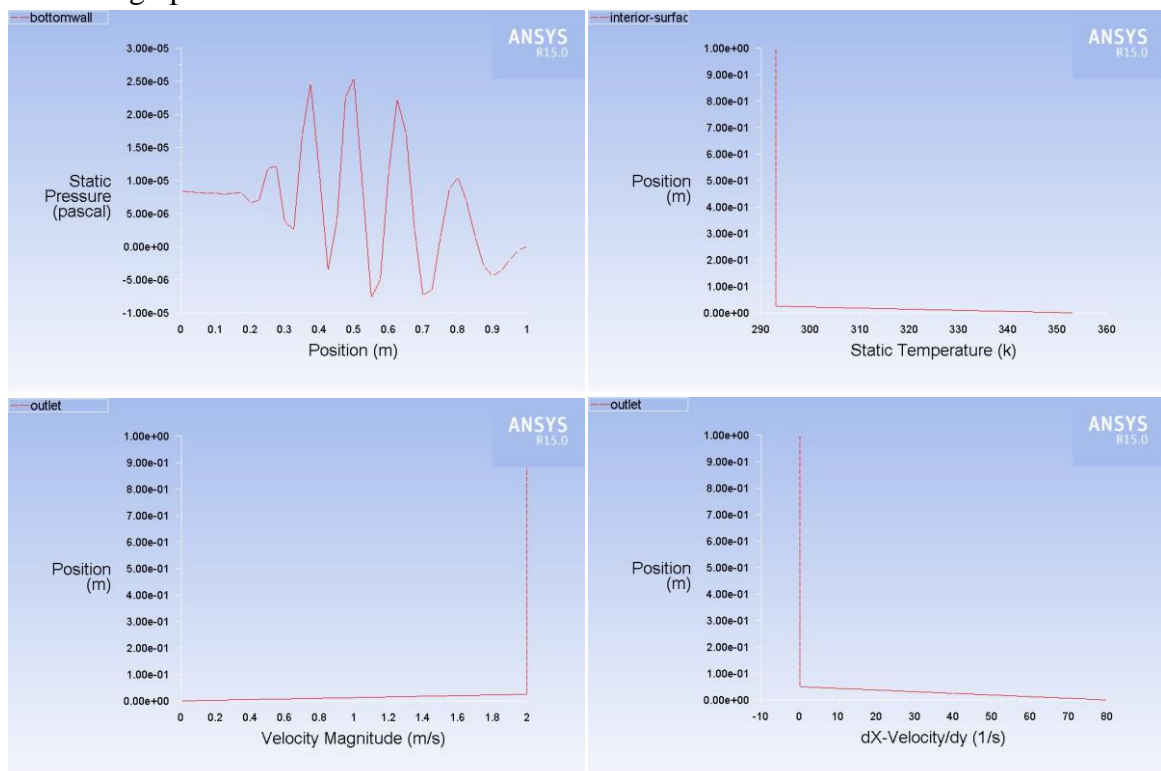
CASE 7 : FLUID AS WATER BY KEEPING VELOCITY CONSTANT & VARYING TEMPARATURES 323k :

Obtained graphs:



CASE 8: FLUID AS WATER BY KEEPING VELOCITY CONSTANT & VARYING TEMPARATURES 343k :

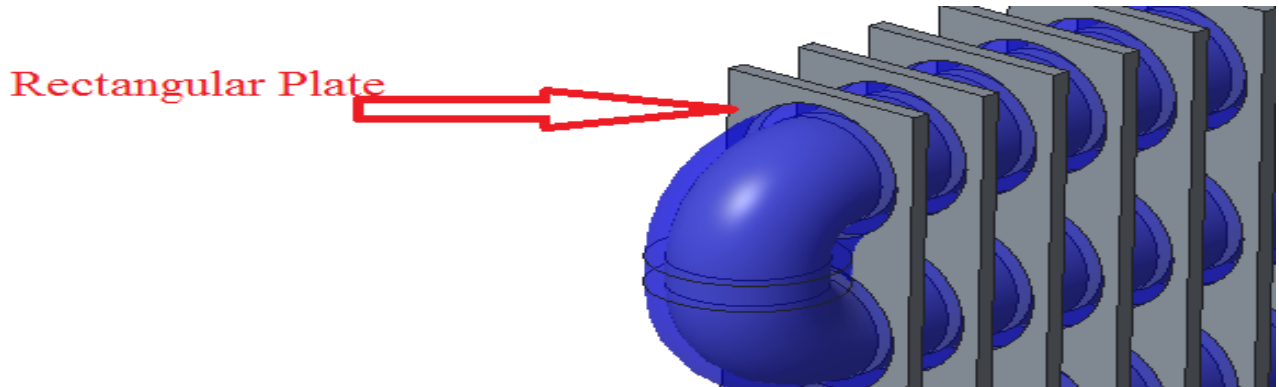
Obtained graphs:



Analysis 3: CFD ANALYSIS OVER A PLATE, Fluid as ENGINE OIL

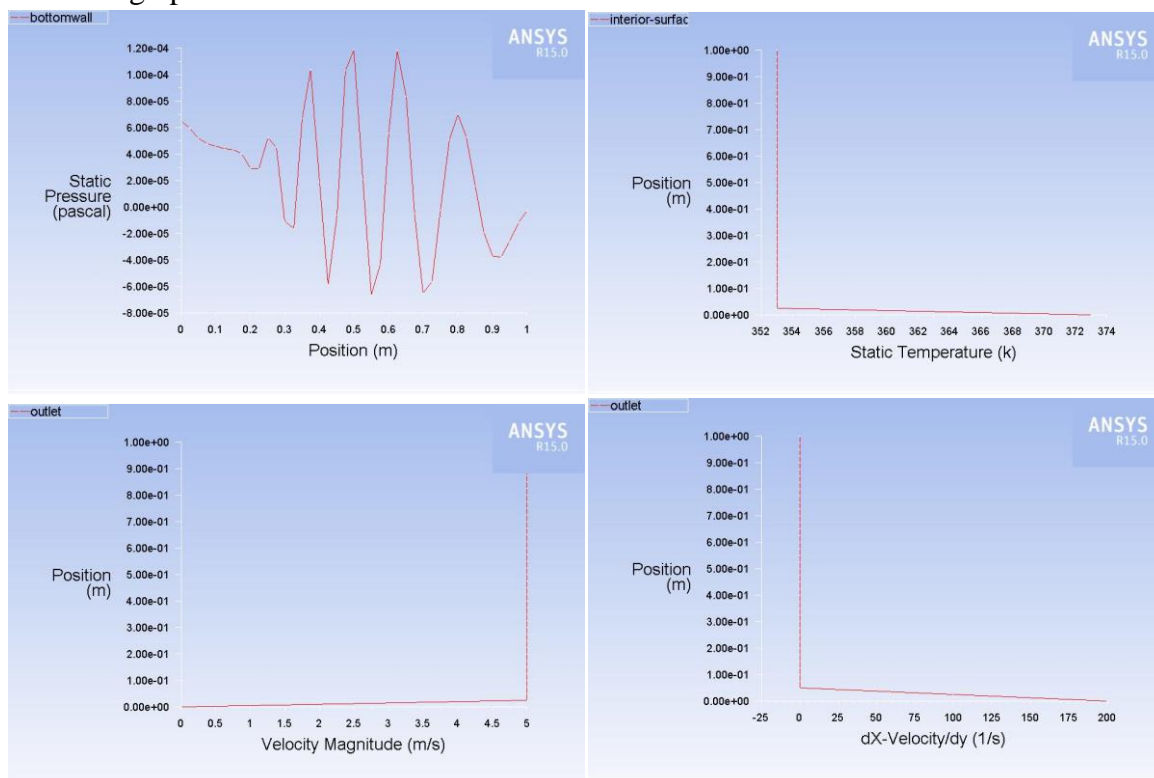
By considering fin as a rectangular plate and Engine Oil as fluid analyzed the variation of parameters either by keeping velocity as constant or temperature as constant.

FLUID AS ENGINE OIL



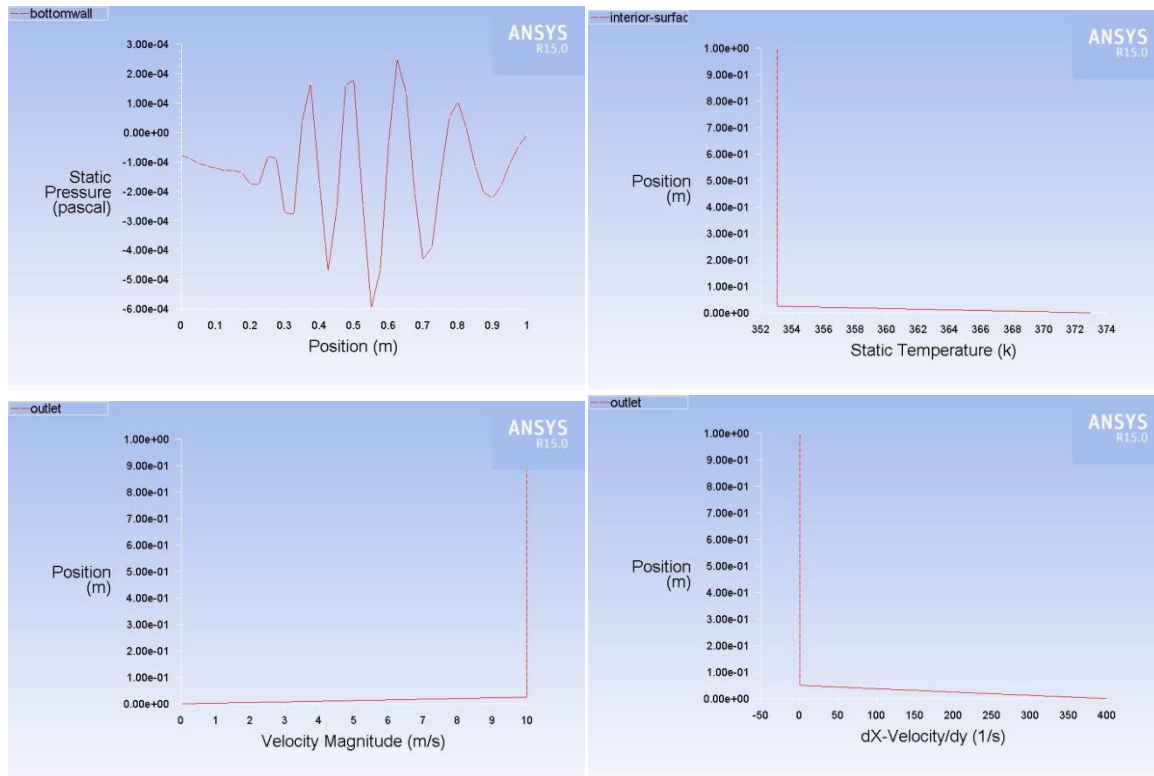
CASE 9: FLUID AS ENGINE OIL BY KEEPING TEMPERATURE CONSTANT & VARYING VELOCITY 5m/s:

Obtained graphs:



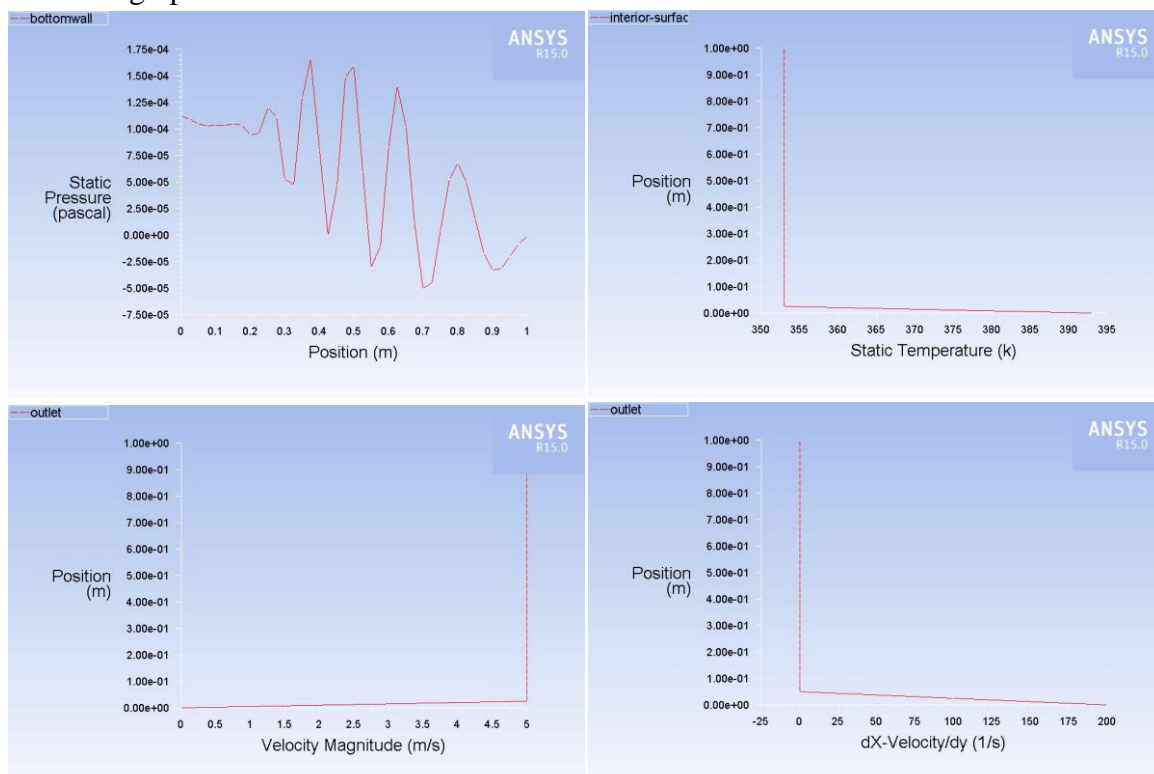
CASE 10: FLUID AS ENGINE OIL BY KEEPING TEMPERATURE CONSTANT & VARYING VELOCITY 10m/s:

Obtained graphs:



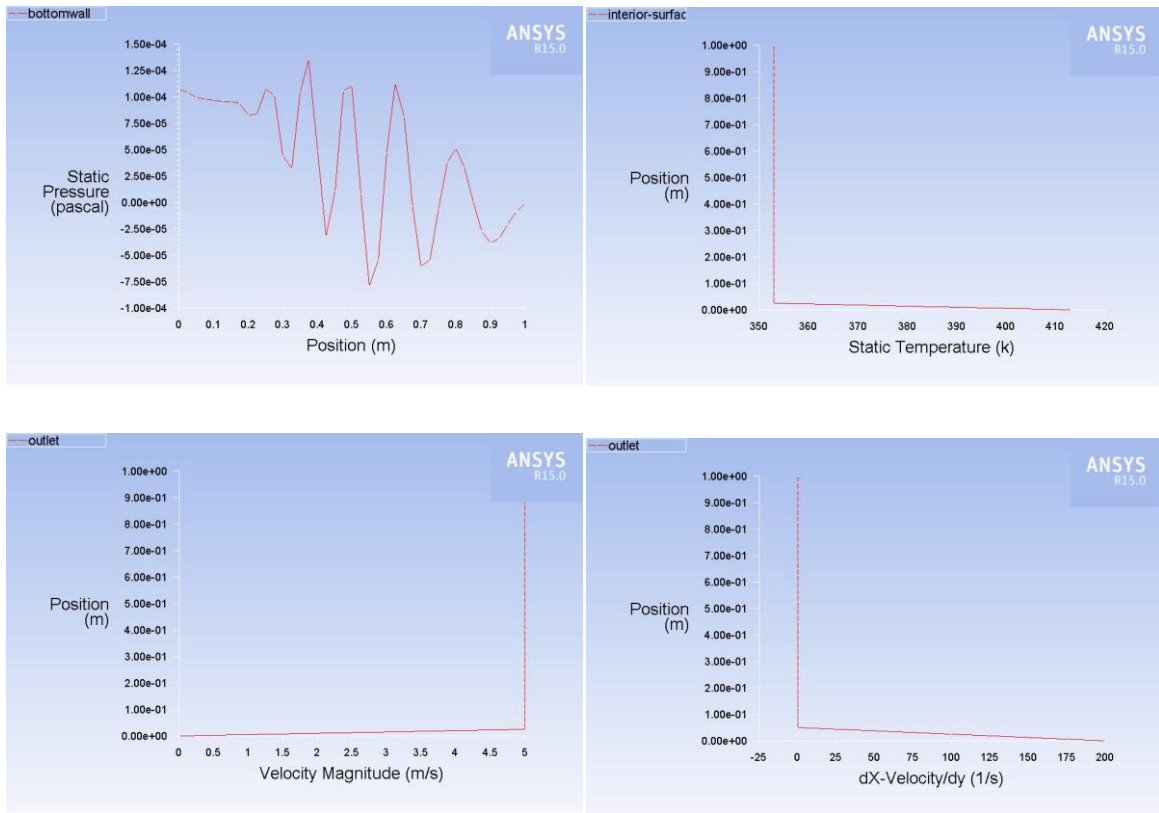
CASE 11: FLUID AS ENGINE OIL BY KEEPING VELOCITY AS CONSTANT & VARYING TEMPARATURE 393 k :

Obtained graphs:



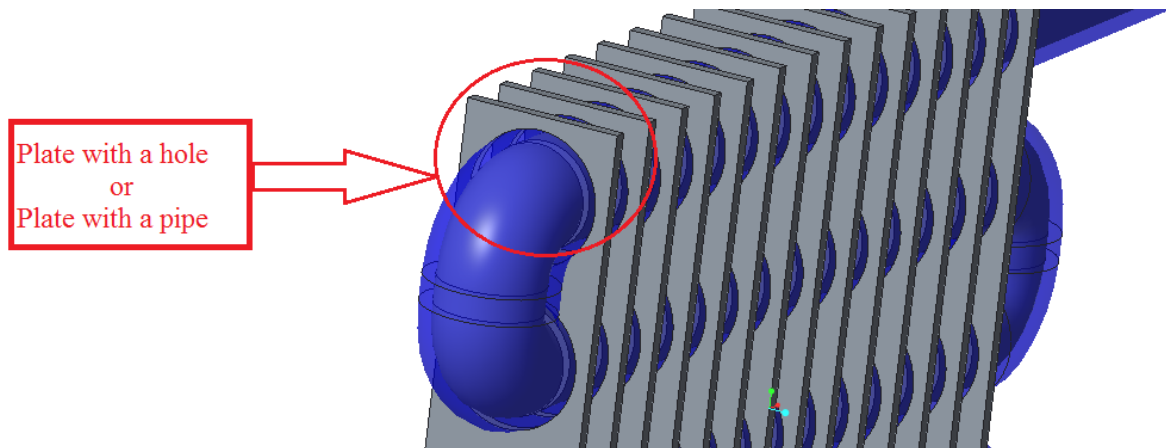
**CASE 12: FLUID AS ENGINE OIL BY KEEPING VELOCITY AS CONSTANT &
VARYING TEMPERATURE 413 k :**

Obtained graphs:



CFD ANALYSIS ON LAMINAR FLOW OVER A PIPE WITH FIN

Geometry:



MESHING :

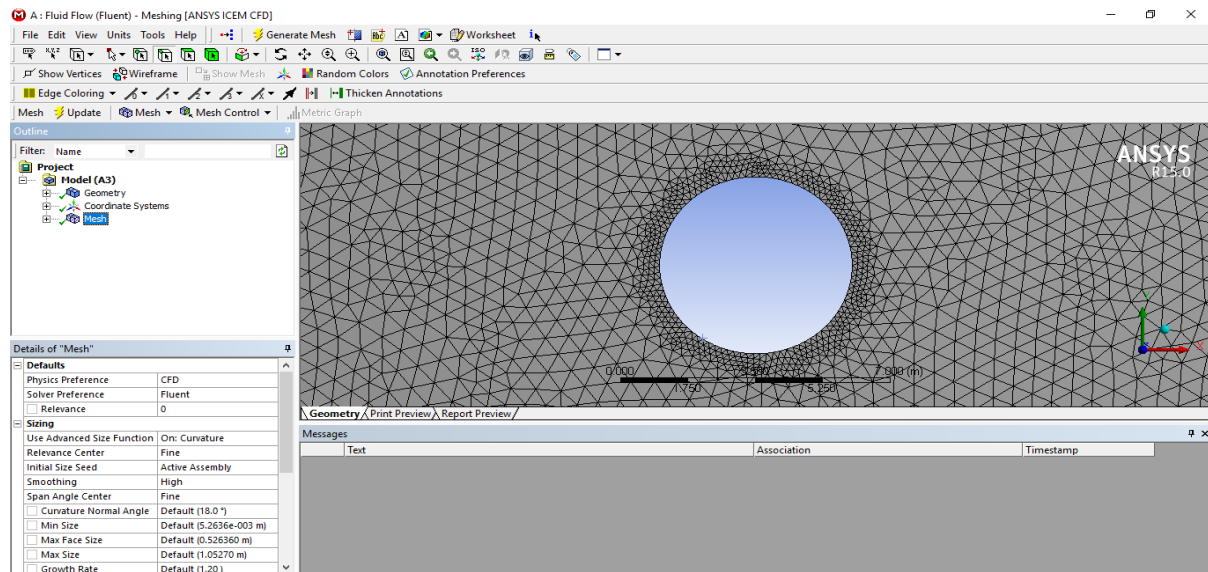
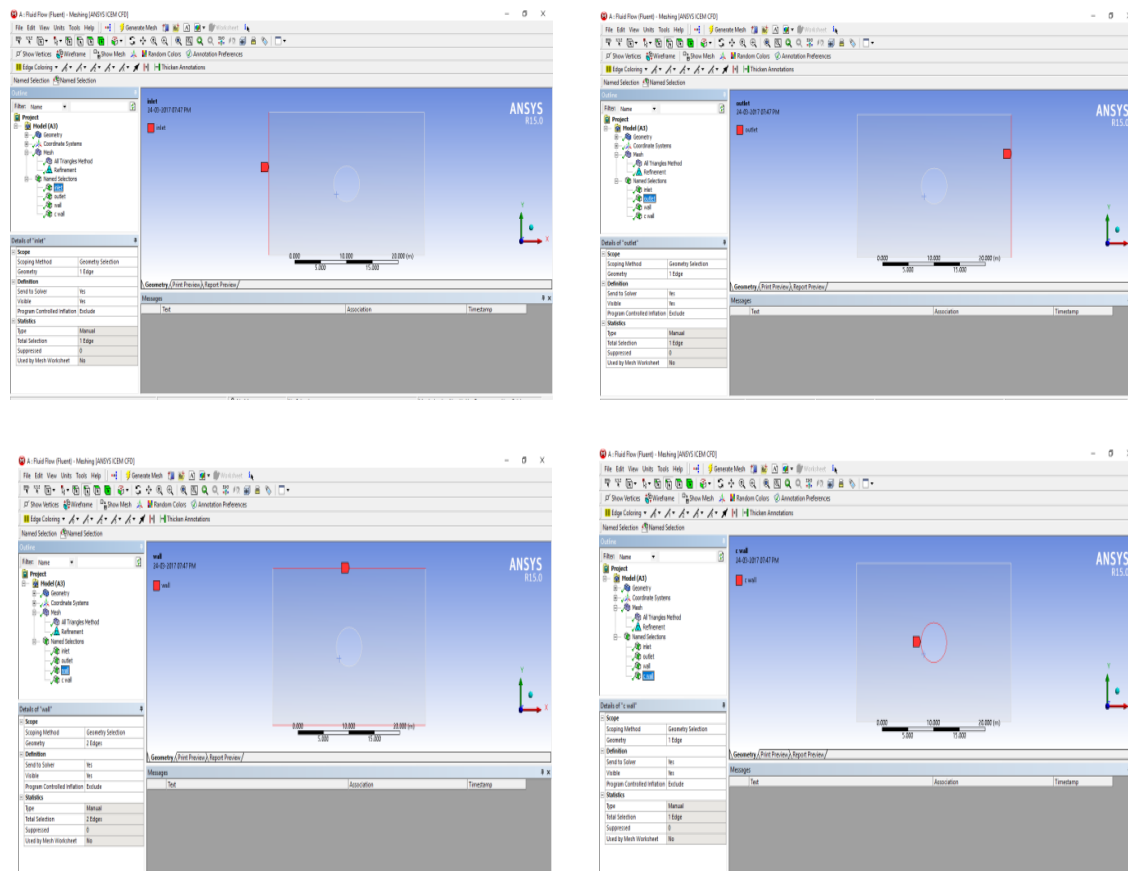


Fig:-Meshing of Plate with a Hole.

Strategy:

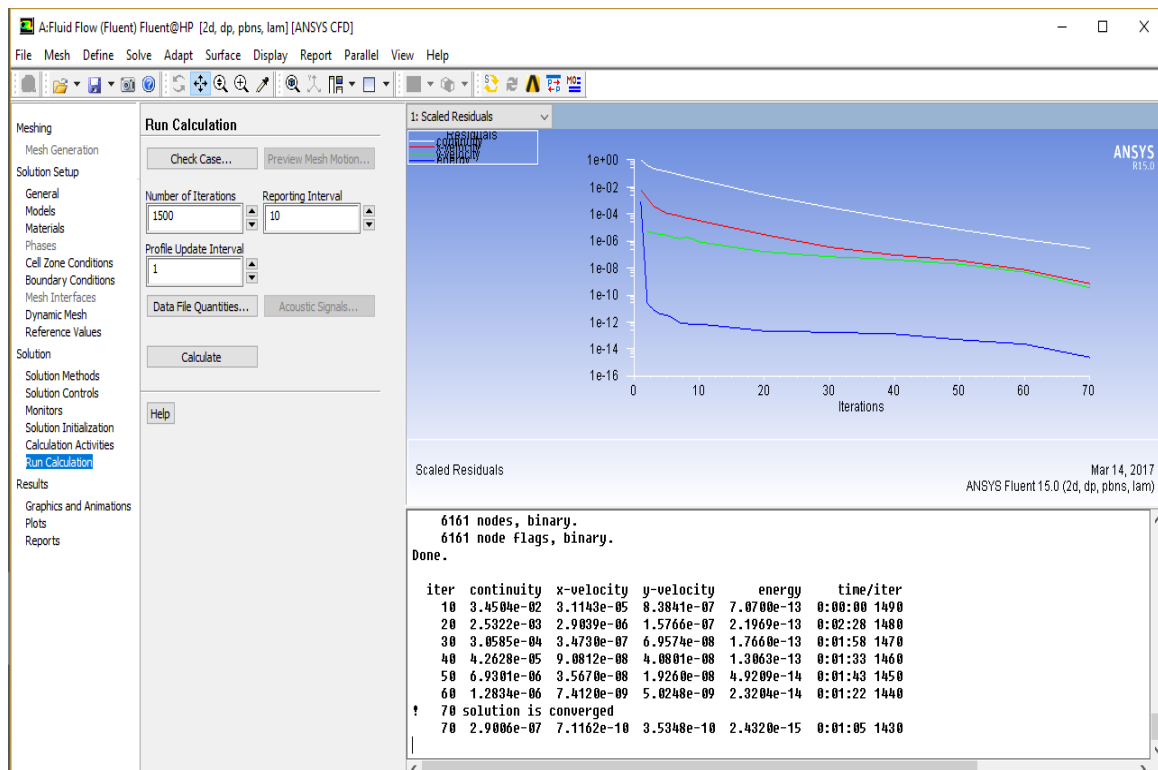
Firstly we determine the flow in and flow out of the fluent.

Later, the wall and centre wall are determined. They are shown in the fig.



Performing and Monitoring :

By performing and monitoring the simulation process, the solution is calculated by the simulation and the graph is obtained.



V. CONCLUSIONS

In the present work, by considering fin as a rectangular plate and air, water and Engine oil as fluids velocity, pressure and temperature variations were analyzed. Similarly, the simulations are repeated for the plate with a hole. The condenser was created using CREO parameters software, and the designed condenser was confirmed using commercial Computational Fluid Dynamics software. CREO parameters 3.0 software is used to create a symmetric representation of the simplified geometry of a condenser [Pipe with Fins] for simulation purposes. CFD models or packages give outlines and data that may be used to forecast Heat exchanger designs which function well and are extensively used because of their ability to discover the optimum solutions.

VI. FUTURE SCOPE

The current computational fluid dynamic analysis can be used for complex geometries that necessitate a thorough understanding of boundary conditions. Using 3D geometry, this work can be extended to a complete tube with fin condenser. Modern turbulence simulation methods, can also be added to the analysis. Working in CFD necessitates a strong foundation in both fluid mechanics and numerical analysis.

REFERENCES

- [1] Praveen Kumar Kanti, Karthika.U.P, Sabeer Ali, Sanath Kumar.N, Shyam Chandran C,

- “CFD analysis of shell and tube heat exchanger”, International Journal of Engineering Research ISSN:2319-6890(online),2347- 5013(print) Volume No.5 Issue: Special 6, pp: 1129 -1254 20 May 2016.
- [2]Amol S. Niphade, Prof. H. A. Chavan, “Design, CFD Analysis of Shell & Tube Heat Exchanger CFD Analysis for Dairy Application”, International Journal of Advance Foundation And Research In Science & Engineering (IJAFRSE) Volume 2, Issue 9, March 2016.
- [3] Ankit Uppal, Dr.Vinod Kumar, Dr. Chanpreet Singh, “Analysis of Heat Transfer Enhancement in a Heat Exchanger Using Various Baffle Arrangements” , IJRMET Vol. 4, Issue 2, May - October 2014
- [4]sk.M.Z.M.Saqheeb Ali, k.Mohan Krishna, et al “Thermal Analysis of Double Pipe Heat Exchanger by Changing the Materials Using CFD” International Journal of Engineering Trends and Technology 26(2):95-102.
- [5]Kranthi Kumar Mamidala,Srikesh “Computational Fluid Dynamics of Parallel Flow Heat Exchanger” International Journal of Sciences: Basic and Applied Research (IJSBAR) (2015) Volume 24, No 5, pp 111-120.
- [6] Jibin Johnson, Abdul Anzar V M, Abith Shani, Harif Rahiman P, Hashmi Hameed T S, Nithin V S, “CFD Analysis of Double Pipe Heat Exchanger”, International Journal of Science, Engineering and Technology Research (IJSETR), Volume 4, Issue 5, May 2015
- [7] Swapnaneel Sarma, D.H.Das, “CFD Analysis of Shell and Tube Heat Exchanger using triangular fins for waste heat recovery processes” , IRACST – Engineering Science and Technology: An International Journal (ESTIJ), ISSN: 2250-3498, Vol.2, No.6, December 2012

Contemporary Progress on Mechanical and Wear of Aluminium Alloys Stir Casting Composites: A Review

Dheya Mohammed¹, Md Tanwir Alam^{2*}

¹Research Scholar, Department of Mechanical Engineering, Glocal University, Saharanpur, 247121, India.

^{2*}Assistant Professor, Department of Mechanical Engineering, Maulana Mukhtar Ahmad Nadvi Technical Campus, Malegaon, 423203, India.

^{2*}Corresponding author: tanwir@mmantc.edu.in

ABSTRACT: Light weight materials having a wide scope of properties which makes specialist centre around them to additional applications and are broadly used in the different sectors like automobile, airspace, sports, etc. Aluminium matrix based composites (AMMCs) of Al 7075 and Al 6061 alloys are very common in structural applications. The stir casting technique is overwhelming as a result of its minimal effort and adaptability. In view of this, reasonable composites are chosen as alluring materials which are produced by various strategies with chosen quality of composites. A review on mechanical characteristics like hardness and strength and tribological performance such as wear resistance, friction, etc. of AMMCs with Al 6061 and Al 7075 alloy matrix reinforced with different micro/nano particles is presented in this paper which provides how the process variables affect the mechanical performance and wear behavioural characteristics of Al 6061 and Al 7075 composites. Further, the factors affecting on the various mechanical properties and tribological performance with stir casting process variables are also discussed in this review. This recent assessment of aluminium alloy based AMMCs would guide to the contemporary researchers to choose the right reinforcement for Al 6061 and Al 7075 matrix and will also monitor for the selection of the optimum process variables.

Keywords: Aluminium Composites, Stir Casting, Mechanical Behaviour, Wear Characteristics

1. INTRODUCTION

In materials studies, the scientist and researchers are developing new engineering materials with improved performance one such model is a composite material. Likely alloys, composites are also made of two or more materials, the main difference between them is in composite two materials are insoluble in each other. Material continuous in nature is termed as matrix and material which is having discontinuous phase are termed as reinforcement. Further, matrix and reinforcement individually retain their properties. Matrix is either organic matrix or metal matrix, reinforcement is existed in the form of flakes, fibres and particles and made of ceramic, organic compounds or metal alloys. Reinforcement always does not influence structural properties, but it also affects physical properties like the coefficient of friction, wear resistance, thermal conductivity, etc [1-3]. Based on the uniformity of the properties, reinforcements are either discontinuous or continuous. Continuous reinforcement has anisotropic properties due to its directional nature whereas discontinuous has opposite nature. Generally, the anisotropic properties of metallic matrix composites (MMCs) are because of discontinuous reinforcement. Different

types of reinforcements used are ceramic, metals, organic compounds. Reinforcements are selected based on the desirable properties for the composites [4, 5]. In MMCs, a matrix is generally lighter materials like titanium, aluminium and magnesium gives support to reinforcement. AMMCs are the most well-known type of MMCs due to the wide range of properties of aluminium. AMMCs are used in the aerospace, automobile industry and it is gaining its application even in sports, for example, bicycle frames are made of aluminium. MMCs manufacturing is categorised into two groups i.e solidus-state and liquidus-state process, liquid state method is further categorised into infiltration method and casting method [6]. The type of manufacturing method influences the properties and quality of composites [7, 8]. Traditionally, stir casting use is very common due to its flexibility in production and cost. AMMCs produced from stir casting is influenced by process parameters like stirrer speed, stir time, stirrer design, pouring temperature [9].

2. STIR CASTING

A largely recognised and efficient method used to manufacture MMCs is the stir casting route. In this mode, a matrix is in molten form and reinforcement is in the form of flakes or particle. To avoid the accumulation of reinforcement in the metallic matrix and to get proper spreading throughout the mixture a mechanical mixture is used called a stirrer. Due to the stirring molten base metal vigorously mixed the reinforcement particles along with impurities. Other than reinforcement some extra agent like Mg is also added to improve wettability, bonding and other properties based on the requirement [10]. Uniformity in the distribution of reinforcement depends on the stirrer's geometry and process conditions like stirring speed, stirring time, temperature, etc. To enhance the stirring process different techniques are used like heating matrix material in two steps or creating the vortex of molten metal in which reinforcement particles are added to enhance uniformity in the composites. The properties of the composites are very sensitive which not only depends on process variables but also on the method of the process selected. Studies shown that AMMCs produced from powder metallurgy has higher mechanical characteristics than composites produced from stir casting but there is the size limitation of the components to be produced. AMMCs is unique because of its ability to manufacture with different manufacturing processes. AMMCs also has good machinability as different types of machining can be done on it. Further, these composites with particle reinforced are light in weight but high hardness due to the hard particles of reinforcement, this property causes a decrease in machinability of a material to perform machining operation special tools made of carbides and diamonds are used [12]. Figure 1 shows the basic set-up of a stir casting route. The various affecting parameters of stir casting composites are illustrated in Figure 2. The stir casting is the simplest and economical method of liquidus state production of MMCs [13-15]. Also, it is flexible and applicable to a mass production. Moreover, the nano-composite products of the said process are more capable of more load capacity with cheaper than the products manufactured by other approaches [16-18]. Table 1 shows a comparative study of different processes to fabricate MMCs. Further, manufacturing methods of the composites are associated with economy and methodology used [13]. Generally, AMMCs are manufacturing through stirring technique and powder metallurgical technique. But, second one is limited to size of the product. Also, stirring technique enables to solve the problems

of economy and difficulties of manufacturing to develop composites of required properties.

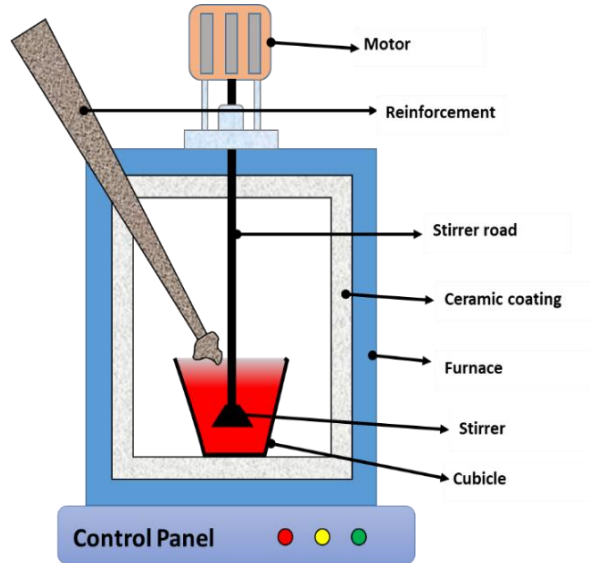


Figure 1: Schematic diagram of stir casting

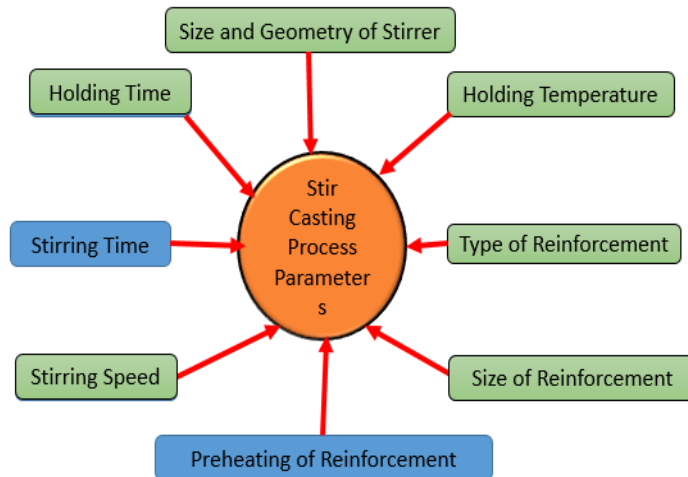


Figure 2: Parameters affecting stir casting process

Table 1. Comparative study of different processes to fabricate AMMCs [19, 20]

S.No.	Process	Shape	Size	Volume Fraction	Reinforcement Condition	Cost
1	Stir casting	wide range of shape	larger size up to 500 kg	up to 0.3	no damage	least expensive
2	Squeeze casting	limited shape	up to 2cm height	up to 0.5	severe damage	moderate expensive
3	Spray casting	limited shape	large size	0.3-0.7	reinforcement damage	expensive
4	Powder metallurgy	wide range	restricted size		reinforcement fracture	expensive

3. LITERATURE REVIEW

In AMMCs, the matrix of different aluminium alloys are used from series 1XXX to 8XXX, each series has its advantages and these are due to the alloying elements. Aluminium alloy 2024 is from the 2XXX series containing Copper as a main alloying element which has poor resistance towards corrosion and also poor wettability [21]. Al 6061 and Al 7075 are

conventionally used aluminium alloys in industries for automobile and aerospace components. Al 6061 is having silicon and magnesium as chief alloying elements that give high strength to composite. Similarly, Al 7075 has zinc as the main alloying elements along with a minor amount of magnesium providing a high strength along with corrosion resistance. The chemical compositions and properties of Al 6061 and Al 7075 are mentioned in the Table 2 and 3 respectively. Both Al 6061 and Al 7075 can undergo a heat treatment process which furthermore enhances the mechanical characteristics of the composites and make them more feasible in the aerospace and automobile industry [22].

Table 2: Chemical Composition of Al 6061 and Al 7075 [21]

Element	Si	Fe	Mg	Zn	Cr	Cu	Mn	Ti	Al
Al 6061	0.62	0.23	0.84	0.10	0.22	0.22	0.03	0.1	Bal
Al 7075	0.4	0.5	2.5	5.5	0.15	1.6	0.3	0.2	Bal

Table 3: Properties of Al 7075 and Al 6061 [21]

Properties	Al 6061	Al 7075
Elastic Modulus (GPa)	70-80	70-80
Density (g/cc)	2.7	2.81
Poisson's Ratio	0.33	0.33
Hardness (HB500)	30	60
Tensile Strength (T) Compressive Strength (C) (MPa)	115(T)	220(T)

3.1 Composites based on Al 6061

A number of research works are available on Al 6061 alloy-based composites. An analysis of the influence of quenching agent on the hardness of Al₂O₃ reinforced composite of A6061 [23]. Composite samples consist of 0 and 10 wt.% of Al₂O₃ with or without particle treatment of reinforced particle and it subjected to quenching with three quenching agent water, oil, brine solution. Specimens were produced through stir casting at 830 °C for 10 min at 550 rpm. Wettability of reinforcement increased if reinforcement coated with electroless. Quenching with brine solution had higher hardness and distortion compare to oil and water. The cooling rate also effects on hardness as the cooling rate affects the formation of Mg₂Si phase in the grain boundary which affects hardness [23]. A study has done on tribological and mechanical behaviour of silicon carbide and porcelain hybrid composite fabricated through stir casting [24]. A6061 and reinforcements were preheated at 200 °C later molten metal maintained at 900 °C and stirred at 350 rpm for 10 min. samples were made into 5 categories based on compositions of SiC and porcelain. The hardness of material increases with an increase in porcelain content with 107 HV of highest hardness at 6 wt.% porcelain though density decreases with increase in porcelain content till 4.5 wt.%. At this content of porcelain, the specimen had the highest wear resistance [24]. Annigeri *et al.* inspected the influence of B₄C reinforcement on fatigue life, shock wave and damping fabricated through solid-state stir casting and turning operation on CNC [25]. Percentage of B₄C had a significant effect on surface roughness as B₄C has

low plastic flow with the increase in content surface roughness increased but fatigue life was increased. Interference damping affected by finishing due to machining and it was found that composite with 4 wt.% B₄C had better damping. Even shock wave treatment is better for 4 wt.% B₄C. Chak *et al.* [26] evaluated the mechanical behaviour of aluminium and copper composite with SiC as reinforcement. Samples were produced via stir casting and it is forged later. Different techniques were used to analyse the cast and forged samples. Results revealed that microhardness increased by 17.58 and 28.39% compare to metal matrix element. Samples with 3 wt.% SiC had the highest UTS whereas 7 wt.% SiC had the highest hardness of 179 HV.

Tribological and mechanical properties of the hybrid composite containing agricultural and industrial waste were studied [27]. Hybrid composites were produced via stir casting where molten metal, fly ash and coconut shell ash were mixed for 9 minutes at 600 rpm to get the homogeneity dispersion of reinforcement in Al6061 metal matrix. Reinforcements were preheated at a different temperature to remove moisture. Outcomes have shown that samples with 20% fly ash, 10% SiC and 10% of coconut shell ash had 589.61 BHN. Further, the sample had 213 MPa of tensile strength which had 10% of coconut shell ash [27]. Mohamed *et al.*, 2020, deliberated the characteristics of tribology of a hybrid composite of an aluminium metal matrix with zirconia and fly ash as reinforcement [28]. The vortex method was applied to fabricate specimen where liquified metal and reinforcement particles were mixed for 10 minutes at 380 rpm. Results revealed that zirconia with 2% content has a minimum wear rate at 400 m sliding distance, 1 m/s sliding speed, 30 N load and the same parameters for minimum friction coefficient 4% zirconia. Moreover, an analysis on casting characteristics of stir casted composites affected by boron carbide and silicon carbide as reinforcement were examined. Reinforcements were preheated for 2 hrs between 250-800 °C. These preheated reinforcements were stirred at 150-200 rpm for 10 min. UTS and hardness of specimen with 3% B₄C and 3% SiC were highest and B₄C content proportionally increased hardness whereas SiC content had the opposite effect [29]. The numerous reports are available on AMMCs reinforced with various micro-nano reinforcements fabricated by liquid phase process of stir casting [30-41]. They have studied the various input parameters like pouring temperature (600-900°C), stirring duration (5-30 minutes), stirring speed (100-800 rpm), etc and investigated several output parameters such as mechanical, wear, physical, morphological characterisation, etc. Overall, their results were shown that there are the enhancement in mechanical and wear properties. Further, an exploration on mechanical performance of an aluminium matrix with reinforcement of granite powder (5 wt%) and SiC (10 wt%) fabricated using stir casting was studied and found UTS 221 MPa and hardness 74.2 HV [42]. Wear and mechanical characteristics of TiC/Al6061 composite with different wt % of reinforcement fabricated through stir casting were evaluated [43]. They depicted that UTS and hardness increased by 43.9% and 9.74% respectively with the increase in 12% of TiC. However, the Wear rate was minimum at 9% of TiC and reduced with rise in TiC. Singh and Bhowmick, stir casted the hybrid composite of aluminium Al6061, granite and SiC and performed reohological and wear testing [44]. Surfactant-multi wall carbon nanotube in oil thickness ratio increased by 47% and surfactant and MWCNT in oil decreased friction coefficient of composite about 1.5-2 times. The researchers [45-49] reported that the wettability of the Al 6061 based stir casting composites improved by adding Mg and K₂TiF₆

and hence improving the mechanical properties significantly. A wear experiment of Al alloy/SiC composite made-up via vortex was conducted at several wear parameters [50]. Results have shown that an increase in both particle and mesh size decreased wear rate whereas applied load and sliding distance rise in wear. Further, the optimum friction coefficient and wear were found to be for 600 mesh size and 35% SiC. A stir cast Al based composites studies showed the uniform dispersion of fly-ash particles improve wear resistance and ductility [51]. UTS and hardness of 6061Al/ZrO₂/graphite hybrid composite produced through stir casting were evaluated that composite with 6% ZrO₂ and 2% graphite had a maximum UTS and hardness [52]. It is revealed that graphite content decreased the hardness because of poor wettability whereas SiC content increased hardness and wear resistance [53]. The several works on Al6061 based MMCs fabricated through the stir casting process have been presented during last few decades [54-56]. Auradi *et al.* [57] also studied behaviour of AMMCs and concluded a decrease in ductility because of strain hardening but 42.6% UTS is increased. Bhandare and Sonawane [58] and Adeosun *et al.* [59], observed mechanical features of the Al 6061/SiC composite with NH₄CL, NaCl, PbCl₂, SnCl₂ agents used to enhance interfacial bonding between the reinforcement and alloy. Bharath *et al.* [12], and Kandpal *et al.* [60] prepared composites of Al-Al₂O₃ via stir casting. They showed that composite brittleness increases with the increase in Al₂O₃ particles. Sonawane and Karnik [61] fabricated composites by stir casting with different compositions out of which 4% Al₂O₃, 7% SiC and 4% Gr composition had a minimum coefficient of friction as well as low wear using a three-level L9 orthogonal array while Umanath *et al.* [54] made-up a composite with Al₂O₃ and SiC by stir casting with particle size 25 mm and 45 mm respectively and results concluded that the porosity of the particle, surface roughness and reinforcement particle size proportionally augmented. Suresh *et al.* [62] observed aluminium hybrid composite hardness as 91.4 HV fabricated through stir casting with 20 % TiB₂ and 2% Gr at 450 rpm and 20 min stirring rate. James *et al.* [63] compared the wear rate and microstructure of composites fabricated via stir casting and strengthened by TiB₂ and SiC particles with a speed of 350 rpm and 150 minutes. Raviraj *et al.* [64], Krishna and Murugan, [65], Moses and Sekhar [66], Pandey *et al.* [67] prepared AMMCs with TiC as reinforcement through stir casting and evaluated mechanical characteristics. With the augmentation of TiC composition, the strength was enhanced however decreased the friction coefficient and wear rate. Results have also shown that the in-suit process has low wear loss when compared to stir casting. Ilandjezian and Gopalankanan [68] conducted experiments on AMMCs prepared with a cenosphere of particle size 50-150 mm. The outcome of the experiment depicted that the cenosphere composite had higher mechanical characteristics like tensile and compressive strength, and hardness. Fracture strength of AMMCs with Si₃N₄ as reinforcement is evaluated by Ramesh *et al.* [69] and concluded the strong bonding between Si₃N₄ with base metal Al6061 and the results also revealed strength of 306 MPa hardness 94.6 VHN. Jin *et al.* [10] prepared Al 6061 based composites by stir casting with reinforcement CuO-ZnO coated with Mg₂B₂O₅. Sharma *et al.* [70] examined the wear behaviour, flexural, UTS, hardness of AMMCs with graphite as reinforcement made-up via vortex. Kumar *et al.* [71] estimated sliding action of AMMCs with AlN as reinforcement produced from stir casting. Results of the experiment were shown that the wear rate and the AlN percentage by weight were inversely proportional and depend on velocity, normal load and sliding distance. Further,

wear and various mechanical performance of Al 6061 stir casting composites reinforced with several reinforcements (TiB_2 , B_4C , SiC , Al_2O_3 , Gr, etc.) have been evaluated [71-76]. Their results showed the similar trend for mechanical and wear characterisation. From the above literature it is depicted that few reinforcements were persistently used for Al 6061 alloy-based metal matrix composites.

Shiri *et al.* [77] explored the aging temperature effect on impact strength of Al6061 composite with 7.5% and 15% SiC particles as reinforcement. Impact strength was measured with Charpy Impact testing machine and found aging parameter like temperature has significant effect on impact strength while type of solution and aging time didn't have significant effect. Panwar *et al.* [78] studied reinforcement impact Al 6061 composite on the impact strength. Results revealed that impact strength rises with rise in size of particle with reinforcement content for low aging time. Maximum impact strength was 10.5 J for 8 % by wt., 250 μm and 6 hr of aging time. Abdul kader *et al.* [79] deliberated Al6061 composite with SiC nano particles. Impact charpy test result revealed enhancement in impact strength by increasing SiC and maximum strength was 80 J noted at 12% of SiC. Mummoorthi *et al.* [80] fabricated Fe_2O_3 and Al6061 hybrid composite through stir casting with different compositions of B_4C . The outcomes declared an increase in hardness, compressive strength while decreasing impact strength with the addition of B_4C and Fe_2O_3 to minimum value of 11 J on Charpy impact testing machine. Prakash *et al.* [81] deliberated mechanical performance of Al6061 and SiC nanoparticle composite with different compositions and were enhanced with the addition of SiC with impact strength 13 J at 7% of SiC. Murugandam *et al.* [82] investigated mechanical performance of Al6061 composite by changing SiC from 3 to 12% in the steps of 3 and fabricated using vortex mixing. Outcomes shown enhancement in mechanical performance with increase in SiC content while impact strength was 25 J at 12% SiC. Yashpal *et al.* [45] declared the bagasse ash effect on mechanical performance of hybrid aluminium composite. Samples consist of three different particle sizes of ash and fabricated via vortex at a stirring speed of 400-500 rpm for 10 minutes at 700 °C and the wettability of the composite improved by adding magnesium. Samples with the least particle size (37 μm) were having the highest strength (180 MPa) and micro-hardness (30.5 VHN). Maximum impact strength of 180 J was depicted with 5% Al_2O_3 on Charpy impact testing machine. Sarkar *et al.* [83] illustrated mechanical characteristics of Al6061 alloy composite using reinforcement of SiC and Rice husk ash (RHA). Specimens were fabricated through stir casting at 400 rpm and 800°C for 10 minutes of stirring. Results shown the reduction in mechanical performance with addition of RHA. Sample of 32% RHA and 48% SiC had 40.2 BHN hardness, 108.6 MPa of tensile strength and 2.5 J of impact strength. Anwesh *et al.* [84] assessed wear features of Al6061 based composites with rice husk ash as reinforcement fabricated through stir casting at 400 rpm of stirring speed. The results of wear test presented that minimum wear rate was at 29.43 load and 2 m/s speed. Chinnamahammad *et al.* [85] estimated the mechanical behaviour of Al6061 hybrid composites of 3 wt.% RHC and different composition of TiC as reinforcement. Results illustrated that specimen with 3% RHA and 6% TiC has highest ultimate and flexural strengths of 20 MPa and 219 MPa while impact strength was 11.1 J at 3% RHA and 3% TiC. Hammar *et al.* [86] assessed mechanical performance of Al6061 composite with sea sand as reinforcement. They

described that composite with 2% of electroless coating had maximum hardness and ultimate tensile strength.

3.2 Composites based on Al 7075

Al 7075 alloy matrix based composites made-up via vortex technique have also been deliberated by the several researchers [87- 92]. During these research, the reinforcements used were SiC, B₄C, BN, TiO₂, Gr, TiB₂, etc. Further, they have taken the process parameters as: pouring temperature (600-900 °C), reinforcement (2-30 wt %), stirring speed (200-800 rpm), stirring duration (5-20 minutes), etc. The published results showed the various outcomes as: hardness (30-162 HV), strength (129-297 MPa), and an improvement in wear resistance and microstructure. Sethi *et al.* [93] fabricated Aluminium metal matrix K₂TiF₆ and KBF₄ salt in-situ reaction through stir casting having TiB₂ as reinforcement and concluded that the addition of TiB₂ increases hardness and tensile strength as 141 HV and 287.95 MPa respectively at 12 wt.% TiB₂. Gudipudi *et al.* [94] improved mechanical characteristics of B₄C reinforced composite in Al 7075 made-up through two-step vortex assisted with ultrasonic to get uniform microstructure. The impact of porosity on Si₃N₄ reinforced composite in Al 7075 fabricated through stir casting and heat-treated under various conditions investigated by Kumar *et al.* [95]. In addition, Hemalatha *et al.* [96] fabricated Graphene with SiC reinforced composite through stir casting having Al7075 as a base metal. They found maximum hardness as 94.8 HV, maximum tensile strength of 266.62 MPa and wear resistance also enhanced. The impact of black carbon on Al₂O₃ and B₄C hybrid composite of Al 7075 produced through stir casting [97]. Preheated carbon black at 300 °C was stirred for 5 min at 800 °C along with Al₂O₃ and B₄C. They depicted that 5 wt.% carbon black along with 4 wt.% B₄C enhances tensile strength, flexural strength and hardness as 282 MPa, 343 MPa and 149 BHN respectively.

Optimization of turning operation parameters for Al7075 with graphite and SiC hybrid composite conducted by Kannan *et al.* [98] made-up through vortex mode at 650 rpm and 720 °C temperature in a nitrogen gas environment. Rajasekaran and Pugazhenti [99] rolled the stir cast SiC reinforced Al7075 composite to enhance the mechanical properties. Results have shown rolled composites were having higher tensile strength and hardness than the unrolled composite. Sahu and Sahu [100] fabricated Al 7075 metal matrix composite with fly-ash and B₄C as reinforcement through the stir casting method. Kumar *et al.* [101] estimated the impact of heat treatment on strength of Al₂O₃ and SiC as reinforcement Al 7075 composite manufactured through stir casting. Stir cast specimens were heat-treated at 140 °C, 160 °C and 180 °C for 4 hours. Tensile strength of samples increased with an increase in temperature and having a maximum value of 271 MPa at 180 °C. Devaganesh *et al.* [102] assessed wear and mechanical characteristics of Al7075 hybrid composite with 5 wt.% of different reinforcements. Using MoS₂, Gr and hexagonal boron nitride (hBN) different specimens were invented through stir casting with preheating of reinforcements at 400 °C before adding molten metal. Strength of graphite reinforced composite was highest followed by hBN and MoS₂. However, hBN had the highest wear rate.

Wear resistance with mechanical performance of Al 7075- Al₂O₃/Mg nanoparticles composites produced through vortex technique were discussed [72]. Results showed maximum hardness and tensile strength at 4 wt.% Al₂O₃. However, specific wear rate decreased with an increase in nano Al₂O₃. Mechanical performance of Al 7075 composites

with SiC reinforcement via stir casting also demonstrated by the various researchers [14, 72-75, 103-105]. Magnesium was applied to prevent the formation of Al_4C_3 . Researcher found that the porosity of the composite with 10% SiC with a particle size of 20-40 μm decreased with increased stirring time, holding time and holding temperature [105]. The porosity was in the range of 4.31-5.13%. Research revealed hardness as 200 BHN, compressive as 310 MPa and tensile as 290 MPa [22]. Further, outcomes of wear study indicate that wear resistance improved with an increase in the percentage of B_4C composition by volume [22]. The several studies on wear with mechanical performance of Al 7075/ Al_2O_3 composites [106], Al 7075/TiC composites with T6 heat treatment [107], Al 7075/ Al_4C_3 composites [108], and Al 7075/Graphite and bagasse-ash reinforced composites [109] processed through stir casting conserving various process parameters were investigated. The important factors affecting the properties of composites are deliberated in Figure 3 whereas Table 4 presents the mechanical testing of the composites. The Table 5 and Table 6 illustrate the summary of the numerous studies on behaviour of Al6061 and Al 7075 vortex composites.



Figure 3: Fishbone diagram of factors affecting mechanical and wear properties

Table 4: Mechanical testing of the composite

Mechanical Testing of the Composite			
Properties	Tests	Standard used for Test	Description
Hardness	Rockwell, Brinell, Vickers	ASTM E18-79, ASTM E-384, ASTM E384, EN ISO 6507, ASTM E-92	Force Applied, Indentation Area and Depth of Penetration
Tension or compression	Universal Testing Machine	ASTM E8, ASTM E8-95, E9-95, ASTM B557 M94, ASTM E8M-15a	Tensile or Compressive Strength, Stress & Strain
Impact	Charpy, Izod	STM G195-13a, ASTM G99	Fracture Toughness
Wear Behaviour	Dry Sliding/ Pin-on-disk	ASTM E32-20, ASTM E32-02A	Wear Rate or Sliding Distance / Velocity

Table 5: Summary of Mechanical properties of Al6061 and Al 7075 based stir casting composite

S.No	Reinforcement	Particle size	Stirring Speed	Stirring time	Temperature	Hardness	Tensile Strength	Refer ence
1.	3% Al ₂ O ₃	125 μm	550	10	-	72	-	[23]
2.	5% SiC, 6% Porcelian	34 μm	350	10	900	107	-	[24]
3.	4.5% Cu/SiC _p		350	-	700	170	-	[26]
4.	20% Fly-ash, 10% SiC	45-50 μm	600	9	700	589.6 BHN	213	[27]
5.	3% B ₄ C, 3% SiC	35-40 μm	150-200	10	750	87 BHN	197	[29]
6.	0.8% GO	0.35-3.2 mm	400	10	580	-	-	[30]
7.	11% B ₄ C	33 μm	350	5	750	152.04 VHN	-	[31]
8.	5% SiC	32 μm	500	12	350	45.5 HRB	288	[32]
9.	10% Si ₃ N ₄	20 μm	-	-	847	54.4 BHN	169.5	[38]
10.	10% SiC, 5% Gr	40-60 μm	-	-	680	74.42 HV	221	[42]
11.	10% TiC _p	18 μm	400	12	750	64-45 BHN	124-126	[43]
12.	5% Al ₂ O ₃ , 8% BA	37-75 μm	400-500	10	700	30.5 VHN	180	[45]
13.	1.5% Al ₂ O ₃		450	10-3	700	150-160 BHN	300-350	[46]
14.	11% B ₄ C	10 μm	300	5	920	80.8 HV	215	[47]
15.	6% ZrO ₂ , Gr 2% Gr		450	10	1000	43 HRC	175 MPa	[52]
16.	12% SiC	125 μm	400	10	730	145-150	185-195	[53]
17.	10% Fly-ash, 15% SiC	5-20 μm		15	400	84.9 BHN	535	[54]
18.	11% B ₄ C	88	250	5-8	750	157.3 VHN	195	[57]
19.	10% B ₄ C	25	400	10-15	800	68 HV	145 MPa	[55]
20.	2% Gr/20% TiB ₂ /2%	200-250 graphite	450	20	700	91.4 HV	90	[62]
21.	10% TiB ₂	10 μm	350	15	750	59 HV	195	[63]
22.	10% SiC	25 μm	350	15	750	80 HV	150.1	[63]
23.	12% Al ₂ O ₃	125 μm	200	10	750	180 VHN	195	[12]
24.	20% Al ₂ O ₃	-	-	-	-	88.91	310	[60]
25.	7% TiC	2 μm	700	-	900-950	66 HV	55.2	[64]
26.	2% Cenosphear	50-100	-		900	57	65	[68]
27.	10% SiC	0.3 μm	-	120	750	77 BHN	-	[110]
28.	10% Si ₃ N ₄	5-30 μm	400		720	94.6	201	[69]
29.	2.5% Al ₂ O ₃ /3% SiC/4% Gr	-	300	8	630	95.47	140.35	[72]
30.	B ₄ C	25 μm	550	15	750	-	340	[73]

31.	6%SiC	20 μm	400	10	720	97 VHN	150	[74]
32.	6%Al ₂ O ₃	20 μm	400	10	720	109 VHN	270	[75]
33.	9%TiB ₂	2-10 μm	350	15	700	150 HV	257	[48]
34.	3%SiC	30-80 nm	600	10	750	162	391	[87]
35.	3%BN	10 μm	500	15	850	-	-	[88]
36.	7.5%SiC	50 μm	200-250	-	850	124 VHN	-	[90]
37.	15%SiC	-	200	10	-	94.8	266.62	[96]
38.	10%SiC	30\ μm	125	-	800	56 HV	146 MPa	[99]

Table-6: Summary of Tribological properties of Al6061 and Al 7075 Based stir casting Composites

S.No.	Reinforcement	Test	Load	Sliding Velocity	Wear Rate	References
1.	12% Al ₂ O ₃	pin-on-disc	19.62 N	1.256	0.02 mg	[12]
2.	10% B ₄ C	pin-on-disc	30 N	0.6	0.012	[22]
3.	Al6061 + 5 % Fe ₂ O ₃ +6%B ₄ C	pin-on-disc	40 N	-	0.244 mg	[80]
4.	12% Rice Husk	pin-on-disc	29.43 N	2	16.56 μm	[84]
5.	SiC	pin-on-disc	40 N	2 m/s	0.3041 mm ³ /s	[37]
6.	9%TiCp	pin-on-disc	10 N	2	41.2 mm ³ /m	[43]
7.	6% Fly Ash	pin-on-disc	2 Kg	3	0.085 mm ³ /m	[51]
8.	12%Gr	pin-on-disc	30 N	1.6	0.375 mm ³ /N-m	[53]
9.	7%SiC, 6%Gr.	pin-on-disc	--	-	32.5mg	[61]
10.	7 % TiC	-	29.4 N	3	9 X 10 ⁻⁶ mm ³ /s	[65]
11.	AlN	pin-on-disc	25 N	2	0.0061	[71]
12.	TiB ₂	pin-on-disc	40 N	300 rpm	0.0035 mm ³ /m	[92]
13.	4% Al ₂ O ₃	pin-on-disc	30 N	4	0.015 gm/s	[72]
14.	8% TiC	pin-on-disc	20 N	2	1.2 mm ³ /Km	[107]
15.	10% SiC,10%Al ₂ O ₃ ,Fly Ash	pin-on-disc	3.5 Kg	3.5	198.81 mm ³ /m	[111]
16.	3% Al ₂ O ₃	pin-on-disc	2.5 Kg	1.758	0.484mm ³ /m	[112]
17.	5% SiC,5% MoS ₂	pin-on-disc	5.093 N	-	3.15 X 10 ⁻¹² m ³ /N-m	[113]

4. CONCLUSION

The review reports suggest that reinforcement particles with different sizes and types change the mechanical performance of fabricated 6061 and 7075 alloys based aluminium composites. The distribution of reinforced particles in a metal matrix influences by the stirrer configuration. To obtain the desired performance characteristics of the composites, agitating speed, agitating time, reinforcement size and quantity are different

for different alloys. Recent studies have shown that high wear resistance is developed in hybrid composites. Carbide reinforcement such as B₄C, TiC, SiC can work at high holding temperature and reduces the percentage of elongation which makes composite more brittle. Mechanical performance of the produced composites could be strengthened by way of preheating reinforcement particles. Heat treated composite decreases machinability and elevate wear resistance, hardness, and tensile strength. Agro and industrial wastes such as cenosphere and bagasse-ash, when used with sufficient alloys of the metal matrix, may also have satisfying hardness like traditional metals. On thorough scrutiny of the published works, author found that the researchers and scientists have been repeatedly used few reinforcements like SiC, TiC, B₄C, TiB₂, TiO₂, ZrO₂, Al₂O₃, AlN, BN, Graphite, Fly-Ash, etc. There are numerous others reinforcements are available such CNT, Graphene, Si₃N₄, etc. on which the limited literature are available. Further, only few research work have been done by the researchers on nano-reinforcements. These lacunae can be filled by the new and hybrid composite fabrication processes.

Conflict of Interest: None declared

Funding: There is no funding for this work

REFERENCES

1. R. Ashok Kumar & A. Devaraju, Modeling of Mechanical Properties and High Temperature Wear Behavior of Al7075/SiC/CRS Composite Using RSM, *Silicon*, 13, pp. 3499–3519, (2021), <https://doi.org/10.1007/s12633-020-00801-x>
2. Balasubramani Subramaniam, Balaji Natarajan, Balasubramanian Kaliyaperumal, and Samson Jerold Samuel Chelladurai, Investigation on mechanical properties of aluminium 7075 - boron carbide - coconut shell fly ash reinforced hybrid metal matrix composites, *China Foundry*, Vol.15 No.6 (2018), pp. 449-456. <https://doi.org/10.1007/s41230-018-8105-3>
3. M. Shettar, P. Hiremath, G. Shankar, A. Kini and S. Sharma, Tribolayer Behaviour and Wear of Artificially Aged Al6061 Hybrid Composites, *International Journal of Automotive and Mechanical Engineering*, Vol. 18, Issue 2, pp. 8668 – 8676. <https://doi.org/10.15282/ijame.18.2.2021.04.0660>
4. Mohammad Azad Alam, H.H. Ya, Akhlaq Ahmad, Mohammad Yusuf, Mohammad Azeem, Faisal Masood, Influence of aluminum addition on the mechanical properties of brass/Al composites fabricated by stir casting, *Materials Today: Proceedings xxx (xxxx) xxx*, 2021, <https://doi.org/10.1016/j.matpr.2021.02.321>
5. Md Tanwir Alam, Physical, Corrosion and Microstructural Analysis of A356/SiC Nanocomposites Fabricated through Stir Casting Process, *Materials Science Forum*, Vol. 1034, pp 73-86, 2021, [doi:10.4028/www.scientific.net/MSF.1034.73](https://doi.org/10.4028/www.scientific.net/MSF.1034.73)
6. Zheng, K.L., Wei, X.S., Yan, B., and Yan, P.F. 2020. Ceramic waste SiC particle-reinforced Al matrix composite brake materials with a high friction coefficient. *Wear*, 458-459: 203424. <https://doi.org/10.1016/j.wear.2020.203424>
7. Alam, M.T., Ansari, A.H., Arif, S., and Alam, M.N. 2017. Mechanical properties and morphology of aluminium metal matrix nanocomposites-stir cast products. *Advances in Materials and Processing Technologies*, 3(4), 600-615. <https://doi.org/10.1080/2374068X.2017.1350543>
8. Samal, P., Vundavilli, P.R., Meher, A., and Mahapatra, M.M. 2020. Recent progress in aluminum metal matrix composites: A review on processing, mechanical and wear properties. *Journal of Manufacturing Process*. 59, 131–152. [doi: 10.1016/j.jmapro.2020.09.010](https://doi.org/10.1016/j.jmapro.2020.09.010).
9. Alam, M.T., Arif, S., Ansari, A.H., and Alam, M.N. 2019. Optimization of wear behaviour using Taguchi and ANN of fabricated aluminium matrix nanocomposites by two-step stir casting. *Materials Research Express*, 6(3): 065002. <https://doi.org/10.1088/2053-1591/ab0871>
10. Jin, P.P., Chen, G., Han, L., and Wang, J.H. 2014. Dry sliding friction and wear behaviors of Mg₂B₂O₅ whisker reinforced 6061Al matrix composites. *Transactions Nonferrous Metals Society of China (English Ed.)*, 24(1), 49–57. [doi: 10.1016/S1003-6326\(14\)63027-2](https://doi.org/10.1016/S1003-6326(14)63027-2).
12. Bharath, V., Nagaral, M., Auradi, V., and Kori, S.A., 2014. Preparation of 6061Al-Al₂O₃ MMC's by Stir Casting and Evaluation of Mechanical and Wear Properties. *Procedia Material Science*. 6, 1658–1667. [doi: 10.1016/j.mspro.2014.07.151](https://doi.org/10.1016/j.mspro.2014.07.151).

13. Naher S, Brabazon D and Looney L, (2005), "Development and assessment of a new quick quench stir caster design for the production of metal matrix composites", *Journal of Material Process Technology*, Vol. 1669(3), 430-439.
14. Wu Y, Gap-Yong Kim, Anderson I E and Lograsso T A, (2010), "Experimental Study on Viscosity and Phase Segregation of Al--Si Powders in Microsemisolid Powder Forming", *Journal of Manufacturing Science and Engineering, Transactions of the ASME*, Vol. 132, Issue 1, pp. 011003-011007.
15. Vogel A, Doherty R D and Canto B, (1978), "Solidification and Casting of Metals", *Metals Society, London*.
16. Amir Khanlou S and Niroumand B, (2010), "Synthesis and characterization of A356-SiCp composites by stir casting and compocasting methods", *Transactions of Nonferrous Metals Society of China*, Vol. 20, pp. s788-s793.
17. Yigezu B S, Jha P K and Mahapatra M M, (2013), "The Key Attributes of Synthesizing Ceramic Particulate Reinforced Al-Based Matrix Composites through Stir Casting Process: A Review", *Materials and Manufacturing Processes*, Vol. 28, Issue 9, pp. 969-979.
18. Balasubramanian I and Maheswaran R, (2015), "Effect of inclusion of SiC particulates on the mechanical resistance behaviour of stir-cast AA6063/SiC composites", *Materials & Design*, Vol. 65, pp. 511-520.
19. Mavhungu S T, Akinlabi E T, Onitiri M A and Varachia F M, (2017), "Aluminum Matrix Composites for Industrial Use: Advances and Trends", *Procedia Manufacturing*, Vol. 7, pp. 178-182.
20. Bhandare R K G and Sonawane P M, (2014), "Preparation of Aluminium Matrix Composite by using Stir Casting Method & its Characterization", *International Journal of Current Engineering and Technology*, Vol. 4, Special Issue 3, pp. 114-155.
21. Kumar, G.B.V., Rao, C. S. P., Selvaraj, N., and Bhagyashekar, M. S. 2010. Studies on Al6061-SiC and Al7075-Al2O3 Metal Matrix Composites. *Journal of Minerals Material Characterisation. Engineern.* 09(01), 43-55.
[doi: 10.4236/jmmce.2010.91004](https://doi.org/10.4236/jmmce.2010.91004).
22. Baradeswaran, A., and Perumal, A.E. 2013. Influence of B4C on the tribological and mechanical properties of Al 7075-B4C composites. *Composite Part B Engineering*. 54(1),146-152.
[doi: 10.1016/j.compositesb.2013.05.012](https://doi.org/10.1016/j.compositesb.2013.05.012).
23. Akbar, H.I., Surojo, E., Ariawan, D., and Prabowo, A. R. 2020. Experimental study of quenching agents on Al6061-Al2O3 composite: Effects of quenching treatment to microstructure and hardness characteristics. *Results in Engineering*. 6, 100105.
[doi: 10.1016/j.rineng.2020.100105](https://doi.org/10.1016/j.rineng.2020.100105).
24. Anand, V. K., Aherwar, A., Mia, M., Elfakir, O., and Wang, L., 2020. Influence of silicon carbide and porcelain on tribological performance of Al6061 based hybrid composites. *Tribology International*. 151, 106514.
[doi: 10.1016/j.triboint.2020.106514](https://doi.org/10.1016/j.triboint.2020.106514).
25. Annigeri, U. K., Rao, S.T., and Kumar, G. B. 2020. Sequel of B4C reinforcement treatment in Al6061 on fatigue, damping, chip formation behaviour and shock wave interaction – A proposition. *Materials Today: Proceedings*, (xxxx).
[doi: 10.1016/j.matpr.2020.10.415](https://doi.org/10.1016/j.matpr.2020.10.415).
26. Chak, V., Chattopadhyay, H., and Kumar, A. 2019. Synthesis, characterization and deformation of Al-4.5Cu/SiCp composites. *Materials Today: Proceedings*. 26, 2833-2838.
[doi: 10.1016/j.matpr.2020.02.590](https://doi.org/10.1016/j.matpr.2020.02.590).
27. Devanathan, R., Ravikumar, J., Boopathi, S., Selvam, D.C., and Anicia, S.A. 2019. Influence in Mechanical Properties of Stir Cast Aluminium (AA6061) Hybrid Metal matrix Composite (HMMC) with Silicon Carbide, Fly Ash and Coconut coir Ash Reinforcement. *Materials Today: Proceedings*. 22, 3136-3144.
[doi: 10.1016/j.matpr.2020.03.450](https://doi.org/10.1016/j.matpr.2020.03.450).
28. Mohamed, M.F., Yaknesh, S., Radhakrishnan, G., and Mohankumar, P. 2020. Optimization of dry sliding wear behavior of flyash & zirconia reinforced Al-Mg-1Si-Cu HMMC using Taguchi technique. *Materials Today: Proceedings*. 22, 1203-1208.
[doi: 10.1016/j.matpr.2019.12.122](https://doi.org/10.1016/j.matpr.2019.12.122).
29. Gowrishankar, M.C., Hiremath, P., Shettar, M., Sharma, S., and Rao, U.S. 2020. Experimental validity on the casting characteristics of stir cast aluminium composites. *Journal of Material Research Technology*. 9(3), 3340-3347.
[doi: 10.1016/j.jmrt.2020.01.028](https://doi.org/10.1016/j.jmrt.2020.01.028).
30. Hedayatian, M., Momeni, A., Nezamabadi, A., and Vahedi, K. 2020. Effect of graphene oxide nanoplates on the microstructure, quasi-static and dynamic penetration behavior of Al6061 nanocomposites. *Composite: Part B Enginerring*. 182, 107652.
[doi: 10.1016/j.compositesb.2019.107652](https://doi.org/10.1016/j.compositesb.2019.107652).
31. Lakshmikantha, R.G., and Auradi, V. 2019. Processing and evaluation of Al/B4C particulate MMC's:

- Tensile strength and wear properties under different elevated temperature test condition. *Materials Today: Proceedings*. 28, 504–509.
[doi: 10.1016/j.matpr.2019.12.209](https://doi.org/10.1016/j.matpr.2019.12.209).
32. Maurya, N.K., Maurya, M., Srivastava, A.K., Dwivedi, S.P., Kumar, A., and Chauhan, S. 2019. Investigation of mechanical properties of Al 6061/SiC composite prepared through stir casting technique. *Materials Today: Proceedings*. 25, 755–758.
[doi: 10.1016/j.matpr.2019.09.003](https://doi.org/10.1016/j.matpr.2019.09.003).
33. Mohanasundaram, S., Vijay, S.J., Vasanth, X.A., Rai, R.S., and Kantharaj, I. 2020. Optimization of coating thickness and coating width for friction surfaced Al6061-B4C over Al6061. *Materials Today: Proceedings*. 33, 939–945.
[doi: 10.1016/j.matpr.2020.06.492](https://doi.org/10.1016/j.matpr.2020.06.492).
34. Meraj, M., Khan, M., and Azhar, M. (July 1, 2020). "Performance Analyses of Photovoltaic Thermal Integrated Concentrator Collector Combined With Single Effect Absorption Cooling Cycle: Constant Flow Rate Mode." *ASME. J. Energy Resour. Technol.* 2020; 142(12): 121305.
<https://doi.org/10.1115/1.4047407>
35. Md Meraj, S.M. Mahmood, M.E. Khan, Md Azhar, G.N. Tiwari, Effect of N-Photovoltaic thermal integrated parabolic concentrator on milk temperature for pasteurization: A simulation study, *Renewable Energy*, Volume 163, 2021, pp. 2153-2164. <https://doi.org/10.1016/j.renene.2020.10.103>.
36. Muruganandam, D., Jayapriya, J., Suresh, M., Chitradevi, S., Puthilibai, G., and Sudhakar, M. 2020. Simple study on behavior of composites with augmentation of Silicon carbide on Al6061 aluminium alloy based on mechanical properties. *Materials Today: Proceedings*. 33, 4573–4577. [doi: 10.1016/j.matpr.2020.08.189](https://doi.org/10.1016/j.matpr.2020.08.189).
37. Singh, S.P., Geethan, K.A.V., Elilraja, D., Prabhuram, T., and Durairaj, J.I. 2019. Optimization of dry sliding wear performance of functionally graded Al6061/20% SiC metal matrix composite using Taguchi method. *Materials Today: Proceedings*. 22, 2824–2831.
[doi: 10.1016/j.matpr.2020.03.414](https://doi.org/10.1016/j.matpr.2020.03.414).
38. Rao, P.S.R., and Mohan, C.B. 2020. Study on mechanical performance of silicon nitride reinforced aluminium metal matrix composites. *Materials Today: Proceedings*. 33, 5534–5538.
[doi: 10.1016/j.matpr.2020.03.495](https://doi.org/10.1016/j.matpr.2020.03.495).
39. Rao, R. G., Ghosh, M., Ganguly, R. L., Bose, S. C.P, and Sahoo, K. L. 2020. Mechanical properties and age hardening response of Al6061 alloy based composites reinforced with fly ash. *Material Science Engineering A*. 772, 138823.
[doi: 10.1016/j.msea.2019.138823](https://doi.org/10.1016/j.msea.2019.138823).
40. Rao, C. R. P., Bhagyashekar, M. S., and Viswanath, N. 2014. Machining Behavior of Al6061-Fly Ash Composites. *Procedia Materials Science*. 5, 1593–1602.
[doi: 10.1016/j.mspro.2014.07.347](https://doi.org/10.1016/j.mspro.2014.07.347).
41. Sahoo, S., Samal, S., and Bhoi, B. 2020. Fabrication and characterization of novel Al-SiC-hBN self-lubricating hybrid composites. *Materials Today Communication*. 25, 101402.
[doi: 10.1016/j.matcom.2020.101402](https://doi.org/10.1016/j.matcom.2020.101402).
42. Senthilkumar, J., Kumar, P.S.M., and Balasubramanian, M. 2020. Effect of hot extrusion on mechanical and microstructural characteristics of stir cast AA6061/SiC/graphite hybrid composites. *Materials Today: Proceedings*. 33, 3–6.
[doi: 10.1016/j.matpr.2020.10.104](https://doi.org/10.1016/j.matpr.2020.10.104).
43. Siddappa, P.N., Shivakumar, B. P., Yogesha, K. B., Mruthunjaya, M, and Girish, D. P. 2019. The effect of TiC particulate reinforcement on dry sliding wear behaviour of Al based composites. *Materials Today: Proceedings*. 22, 2291–2299.
[doi: 10.1016/j.matpr.2020.03.350](https://doi.org/10.1016/j.matpr.2020.03.350).
44. Singh, H., and Bhowmick, H. 2020. Lubrication characteristics and wear mechanism mapping for hybrid aluminium metal matrix composite sliding under surfactant functionalized MWCNT-oil. *Tribology International*. 145, 106152.
[doi: 10.1016/j.triboint.2019.106152](https://doi.org/10.1016/j.triboint.2019.106152).
45. Yashpal, Jawalkar, C. S., Kant, S., Panwar, N., Sharma, M.D., and Pali, H. S. 2020. Effect of particle size variation of bagasse ash on mechanical properties of aluminium hybrid metal matrix composites. *Materials Today: Proceedings*. 21, 2024–2029.
[doi: 10.1016/j.matpr.2020.01.319](https://doi.org/10.1016/j.matpr.2020.01.319).
46. Ezatpour, H.R., Sajjadi, S.A., Sabzevar, M. H., and Huang, Y. 2014. Investigation of microstructure and mechanical properties of Al6061-nanocomposite fabricated by stir casting. *Materials Design*. 55, 921–928.
[doi: 10.1016/j.matdes.2013.10.060](https://doi.org/10.1016/j.matdes.2013.10.060).
47. Kalaiselvan, K., Murugan, N., and Parameswaran. 2011. Production and characterization of AA6061-B4C

- stir cast composite. *Materials Design*. 32(7) 4004–4009.
[doi: 10.1016/j.matdes.2011.03.018](https://doi.org/10.1016/j.matdes.2011.03.018).
48. Pazhouhanfar, Y., and Eghbali, B. 2018. Microstructural characterization and mechanical properties of TiB₂ reinforced Al6061 matrix composites produced using stir casting process. *Materials Science Engineering A*. 710, 172–180.
[doi: 10.1016/j.msea.2017.10.087](https://doi.org/10.1016/j.msea.2017.10.087).
49. Panwar, N., and Chauhan, A. 2018. Optimizing the effect of reinforcement, particle size and aging on impact strength for Al 6061-red mud composite using Taguchi technique. *Sadhana - Academic Proceeding in Engineering Science*. 43(7), 1–10.
[doi: 10.1007/s12046-018-0870-6](https://doi.org/10.1007/s12046-018-0870-6).
50. Mishra, A. K. and Srivastava, R. K. 2017. Wear Behaviour of Al-6061/SiC Metal Matrix Composites. *Journal of The Institution of Engineers Series C*. 98(2), 97–103.
[doi: 10.1007/s40032-016-0284-3](https://doi.org/10.1007/s40032-016-0284-3).
51. Nayana, D. A., Marachakkanavar, M., and Kantli, N. 2018. Tribological Behavior of Al6061 Alloy Reinforced with Fly Ash Particles. *Techno-Societal*. 2016, 915–923.
[doi: 10.1007/978-3-319-53556-2](https://doi.org/10.1007/978-3-319-53556-2).
52. Pandiyarajan, R., Maran, P., Marimuthu, S., and Ganesh, K. C. 2017. Mechanical and tribological behavior of the metal matrix composite AA6061/ZrO₂/C. *Journal of Mechanical Science and Technology*. 31(10), 4711–4717.
[doi: 10.1007/s12206-017-0917-3](https://doi.org/10.1007/s12206-017-0917-3).
53. Prashant, S. N., and M.N.V. A. 2012. Preparation and Evaluation of Mechanical and Wear Properties of Al6061 Reinforced with Graphite and SiC. *International Journal of Mechanical Engineering and Robotics Research*. 1(3), 106–112.
54. Umanath, K., Selvamani, S. T., Palanikumar, K. K., and Niranjana Varma, D. 2014. Metal to metal worn surface of AA6061 hybrid composites casted by stir casting method. *Procedia Engineering*. 97, 703–712.
[doi: 10.1016/j.proeng.2014.12.300](https://doi.org/10.1016/j.proeng.2014.12.300).
55. Ravi, B., Naik, B.B.B., and Prakash, J.U. 2015. Characterization of Aluminium Matrix Composites (AA6061/B4C) Fabricated by Stir Casting Technique. *Materials Today: Proceedings*. 2(4–5), 2984–2990.
[doi: 10.1016/j.matpr.2015.07.282](https://doi.org/10.1016/j.matpr.2015.07.282).
56. Raju, H., and Krupakra, P. V. 2019. Corrosion characterization of Al 6061/Red Mud MMCs in hydrochloric Acid,” *Materials Today: Proceedings*. 22, 1765–1770.
[doi: 10.1016/j.matpr.2020.03.009](https://doi.org/10.1016/j.matpr.2020.03.009).
57. Auradi, V., Rajesh, G. L. and Kori, S. A. 2014. Processing of B 4 C Particulate Reinforced 6061Aluminum Matrix Composites by Melt Stirring Involving Two-step Addition. *Procedia Materials Science*, 6, 1068–1076.
[doi: 10.1016/j.mspro.2014.07.177](https://doi.org/10.1016/j.mspro.2014.07.177).
58. Bhandare, R. G., and Sonawane, P. M. 2013. Preparation of Aluminium Matrix Composite by Using Stir Casting Method. *International Journal of Engineering Advance Technology*. 3(2), 61–65.
59. Adeosun, S. O., Akpan, E. I., Gbenedor, O. P., and Balogun, S. A. 2016. Ductility and hardness of chloride cleaned AA6011/SiCp composites. *Transactions Nonferrous Metals Society of China (English Ed.)* 26(2), 339–347.
[doi: 10.1016/S1003-6326\(16\)64124-9](https://doi.org/10.1016/S1003-6326(16)64124-9).
60. Kandpal, B. C., Kumar, J., and Singh, H. 2017. Fabrication and characterisation of Al₂O₃/aluminium alloy 6061 composites fabricated by Stir casting. *Materials Today: Proceedings*. 4(2), 2783–2792.
[doi: 10.1016/j.matpr.2017.02.157](https://doi.org/10.1016/j.matpr.2017.02.157).
61. Sonawane, P. M., and Karnik, M. G. 2017. Experimental Investigation of Optimum level of Reinforcement within 6061Al Alloy for better Tribological and Mechanical Properties. *Materials Today: Proceedings*. 4(2), 3290–3299.
[doi: 10.1016/j.matpr.2017.02.215](https://doi.org/10.1016/j.matpr.2017.02.215).
62. Suresh, S., Moorthi, N.S.V., Vettivel, S.C., Selvakumar, S., and Jinu, S.R. 2014. Effect of graphite addition on mechanical behavior of Al6061/TiB₂ hybrid composite using acoustic emission. *Materials Science Engineering A*. 612, 16–27.
[doi: 10.1016/j.msea.2014.06.024](https://doi.org/10.1016/j.msea.2014.06.024).
63. James, S.J., Venkatesan, K., Kuppan, P., and Ramanujam, R. 2014. Comparative study of composites reinforced with SiC and TiB₂. *Procedia Engineering*. 97, 1012–1017.
[doi: 10.1016/j.proeng.2014.12.378](https://doi.org/10.1016/j.proeng.2014.12.378).
64. Raviraj, M. S., Sharanprabhu, C. M., and Mohankumar, G. C. 2014. Experimental Analysis on Processing and Properties of Al-TiC Metal Matrix Composites. *Procedia Materials Science*. 5, 2032–2038.
[doi: 10.1016/j.mspro.2014.07.536](https://doi.org/10.1016/j.mspro.2014.07.536).
65. Gopalakrishnan, S., and Murugan, N. 2012. Production and wear characterisation of AA 6061 matrix

- titanium carbide particulate reinforced composite by enhanced stir casting method. *Composite Part B Engineering*. 43(2), 302–308.
[doi: 10.1016/j.compositesb.2011.08.049](https://doi.org/10.1016/j.compositesb.2011.08.049).
66. Moses, J.J., and Sekhar, S.J. 2017. Investigation on the Tensile Strength and Microhardness of AA6061/TiC Composites by Stir Casting. *Transactions Indian Institute of Metals*. 70(4). 1035–1046.
[doi: 10.1007/s12666-016-0891-y](https://doi.org/10.1007/s12666-016-0891-y).
67. Pandey, U., Purohit, R., Agarwal, P., Dhakad, S. K., and Rana, R. S. 2017. Effect of TiC particles on the mechanical properties of aluminium alloy metal matrix composites (MMCs). *Materials Today: Proceedings*. 4(4), 5452–5460.
[doi: 10.1016/j.matpr.2017.05.057](https://doi.org/10.1016/j.matpr.2017.05.057).
68. Ilandjezian, R., and Gopalakannan, S. 2017. Tensile Fracture and Compression failure Behavior of Cenosphere Reinforced AA6061 Metal Matrix Composite. *Procedia Engineering*. 173, 1239–1245.
[doi: 10.1016/j.proeng.2016.12.137](https://doi.org/10.1016/j.proeng.2016.12.137).
69. Ramesh, C. S., Keshavamurthy, R., and Madhusudhan, J. 2014. Fatigue Behavior of Ni-P Coated Si 3 N 4 Reinforced Al6061 Composites. *Procedia Materials Science*. 6, 1444–1454.
[doi: 10.1016/j.mspro.2014.07.124](https://doi.org/10.1016/j.mspro.2014.07.124).
70. Sharma, P., Paliwal, K., Garg, R. K., Sharma, S., and Khanduja, D. 2017. A study on wear behaviour of Al/6101/graphite composites. *Journal of Asian Ceramic Society*. 5(1), 42–48.
[doi: 10.1016/j.jascer.2016.12.007](https://doi.org/10.1016/j.jascer.2016.12.007).
71. Kumar, B. A., Murugan, N., and Dinaharan, I. 2014. Dry sliding wear behavior of stir cast AA6061-T6/AlNp composite. *Transactions Nonferrous Metals Society of China*. 24(9), 2785–2795.
[doi: 10.1016/S1003-6326\(14\)63410-5](https://doi.org/10.1016/S1003-6326(14)63410-5).
72. Suresh, S., Gowd, G. H., and Devakumar, M. L. S. 2020. Mechanical and wear Characteristics of Aluminium Alloy 7075 Reinforced with Nano-Aluminium Oxide/ Magnesium Particles by Stir casting Method. *Materials Today: Proceedings*. 24, 273–283.
[doi: 10.1016/j.matpr.2020.04.276](https://doi.org/10.1016/j.matpr.2020.04.276).
73. Yu. LI, Q. lin LI, D. LI, W. LIU, and SHU, G.G. 2016. Fabrication and characterization of stir casting AA6061—31%B4C composite. *Transactions Nonferrous Metals Society of China*. 26(9), 2304–2312.
[doi: 10.1016/S1003-6326\(16\)64322-4](https://doi.org/10.1016/S1003-6326(16)64322-4).
74. Bhushan, R. K., Kumar, S., and Das, S. 2010. Effect of machining parameters on surface roughness and tool wear for 7075 Al alloy SiC composite. *International Journal of Advance Manufacturing and Technology*. 50(5–8), 459–469.
[doi: 10.1007/s00170-010-2529-2](https://doi.org/10.1007/s00170-010-2529-2).
75. Bhushan, R. K., Kumar, S., and Das, S. 2013. Fabrication and characterization of 7075 Al alloy reinforced with SiC particulates. *International Journal of Advance Manufacturing and Technology*. 65(5–8), 611–624.
[doi: 10.1007/s00170-012-4200-6](https://doi.org/10.1007/s00170-012-4200-6).
76. Zakaulla, M., Khan, A. R. A., and Mukunda, P. G. 2015. Evaluation of the Taguchi Method for Wear Behavior of Al6061/Cu-SiC/Cu-Gr Hybrid Composite. *Materials Today: Proceedings*. 2(4–5), 2951–2958.
[doi: 10.1016/j.matpr.2015.07.262](https://doi.org/10.1016/j.matpr.2015.07.262).
77. N. D. Shiri, T. Bhat, S. Bhat, and G. Kumar, “Investigation of the effect of aging variables on the impact behaviour of Al 6061 alloy and its composites,” *IET Conf. Publ.*, vol. 2013, no. 648 CP, 2013.
[doi: 10.1049/cp.2013.2540](https://doi.org/10.1049/cp.2013.2540).
78. N. Panwar and A. Chauhan, “Optimizing the effect of reinforcement, particle size and aging on impact strength for Al 6061-red mud composite using Taguchi technique,” *Sadhana - Acad. Proc. Eng. Sci.*, vol. 43, no. 7, pp. 1–10, 2018.
[doi: 10.1007/s12046-018-0870-6](https://doi.org/10.1007/s12046-018-0870-6).
79. M. Abdul kader, N., Mohammed, R. and Hanoos, “The Effect of Nanoparticles Additives on Impact Strength of Metal Matrix Composites,” *Eng. Technol. J.*, vol. 35, no. 1, pp. 73–76, 2017.
80. D. Mummoothi, M. Rajkumar, and S. Ganesh Kumar, “Advancement and characterization of Al-Mg-Si alloy using reinforcing materials of Fe₂O₃ and B₄C composite produced by stir casting method,” *J. Mech. Sci. Technol.*, vol. 33, no. 7, pp. 3213–3222, 2019.
[doi: 10.1007/s12206-019-0616-3](https://doi.org/10.1007/s12206-019-0616-3).
81. B. Prakash and M. Manimaran, “Investigations on mechanical properties of Al6061-SiC nanocomposites fabricated via stir casting process,” *Mater. Today Proc.*, vol. 39, no. xxxx, pp. 22–25, 2020.
[doi: 10.1016/j.matpr.2020.05.172](https://doi.org/10.1016/j.matpr.2020.05.172).
82. D. Muruganandam, J. Jayapriya, M. Suresh, S. Chitradevi, G. Puthilibai, and M. Sudhakar, “Simple study on behavior of composites with augmentation of Silicon carbide on Al6061 aluminium alloy based on mechanical properties,” *Mater. Today Proc.*, vol. 33, no. xxxx, pp. 4573–4577, 2020.

- [doi: 10.1016/j.matpr.2020.08.189](https://doi.org/10.1016/j.matpr.2020.08.189).
83. S. Sarkar, A. Bhirangi, J. Mathew, R. Oyyaravelu, P. Kuppan, and A. S. S. Balan, "Fabrication characteristics and mechanical behavior of Rice Husk Ash-Silicon Carbide reinforced Al-6061 alloy matrix hybrid composite," *Mater. Today Proc.*, vol. 5, no. 5, pp. 12706–12718, 2018.
[doi: 10.1016/j.matpr.2018.02.254](https://doi.org/10.1016/j.matpr.2018.02.254).
84. A. K. Virkunwar, S. Ghosh, and R. Basak, "Wear characteristics optimization of Al6061-Rice husk ash metal matrix composite using Taguchi method," *Mater. Today Proc.*, vol. 19, no. xxxx, pp. 546–550, 2019.
[doi: 10.1016/j.matpr.2019.07.731](https://doi.org/10.1016/j.matpr.2019.07.731).
85. A. Chinnamahammad Bhasha and K. Balamurugan, "Studies on mechanical properties of Al6061/RHC/TiC hybrid composite," *Int. J. Light. Mater. Manuf.*, vol. 4, no. 4, pp. 405–415, 2021.
[doi: 10.1016/j.ijlmm.2021.06.003](https://doi.org/10.1016/j.ijlmm.2021.06.003).
86. H. I. Akbar, E. Surojo, D. Ariawan, A. R. Prabowo, and F. Imanullah, "Fabrication of AA6061-sea sand composite and analysis of its properties," *Heliyon*, vol. 7, no. 8, p. e07770, 2021.
[doi: 10.1016/j.heliyon.2021.e07770](https://doi.org/10.1016/j.heliyon.2021.e07770).
87. Kumar, A., Pal, K., and Mula, S. 2021. Effects of cryo-FSP on metallurgical and mechanical properties of stir cast Al7075 e SiC nanocomposites. *Journal of Alloys Compound*. 852, 156925, [doi: 10.1016/j.jallcom.2020.156925](https://doi.org/10.1016/j.jallcom.2020.156925).
88. Ramadoss, N., Pazhanivel, K., and Anbuchezhian, G. 2020. Synthesis of B 4 C and BN reinforced Al7075 hybrid composites using stir casting method. *Integrative Medicin Research*. 9(3), 6297–6304.
[doi: 10.1016/j.jmrt.2020.03.043](https://doi.org/10.1016/j.jmrt.2020.03.043).
89. Keshavamurthy, R., Jagadeesha, T., and Kumar, R. S. 2020. Investigations on mechanical behavior of hot rolled Al7075 / TiO 2 / Gr hybrid composites. *Ceramic International*.
[doi: 10.1016/j.ceramint.2020.10.236](https://doi.org/10.1016/j.ceramint.2020.10.236).
90. Gosavi, S. V., and Jaybhaye, M. D. 2020. Microstructural studies on aluminium metal matrix composite (Al7075-SiC) fabricated through stir casting process. *Materials Today: Proceedings*. [doi: 10.1016/j.matpr.2020.05.094](https://doi.org/10.1016/j.matpr.2020.05.094).
91. Raghuvaran, P., Baskaran, J., Aagash, C., Ganesh, A., and Krishna, S. G. 2020. Proceedings Evaluation of mechanical properties of Al7075-SiC composites fabricated through stir casting technique. *Materials Today: Proceedings*.
[doi: 10.1016/j.matpr.2020.09.191](https://doi.org/10.1016/j.matpr.2020.09.191).
92. Bhowmik, A., Dey, D., and Biswas, A. 2020. Tribological behaviour of Aluminium-Titanium Diboride (Al7075-TiB 2) Metal Matrix Composites prepared by stir casting process. *Materials Today: Proceedings*. 2–6.
[doi: 10.1016/j.matpr.2020.02.436](https://doi.org/10.1016/j.matpr.2020.02.436).
93. Sethi, S., Kumar, S., Choudhury, S., Shekhar, S., and Saha, B. 2020. Synthesis and characterization of AA7075 / TiB 2 aluminum matrix composite formed through stir casting method. *Materials Today: Proceedings*.
[doi: 10.1016/j.matpr.2020.02.418](https://doi.org/10.1016/j.matpr.2020.02.418).
94. Gudipudi, S., Nagamuthu, S., Subbu, K., Prakasa, S., and Chilakalapalli, R. 2020. Engineering Science and Technology , an International Journal Enhanced mechanical properties of AA6061-B 4 C composites developed by a novel ultra-sonic assisted stir casting. *Engineering Science and Technology an International Journal*.
[doi: 10.1016/j.jestch.2020.01.010](https://doi.org/10.1016/j.jestch.2020.01.010).
95. Kumar, S. A., Vignesh, J. H., and Joshua, S. P. 2020. Investigating the effect of porosity on aluminium 7075 alloy reinforced with silicon nitride (Si 3 N 4) metal matrix composites through STIR casting process. *Materials Today: Proceedings*. 3–8.
[doi: 10.1016/j.matpr.2020.07.690](https://doi.org/10.1016/j.matpr.2020.07.690).
96. Hemalatha, K., Ashwin, R., Santhanam, M., Riyaz, M. M., Sozhamannan, G. G., and Venkatachalapthy, V. S. K. 2020. Experimental study on behaviour of SiC and Graphene on AL7075 hybrid metal matrix composite. *Materials Today: Proceedings*. 0–4.
[doi: 10.1016/j.matpr.2020.05.744](https://doi.org/10.1016/j.matpr.2020.05.744).
97. Khare, R. K., Gupta, Ghosh, S. S., and Chhabra, D. 2020. Effect of carbon black on mechanical properties of Al7075 / Al 2 O 3 / B 4 C reinforced aluminum composite. *Materials Today: Proceedings*. 3–5.
[doi: 10.1016/j.matpr.2020.04.803](https://doi.org/10.1016/j.matpr.2020.04.803).
98. Kannan, A., Mohan, R., Viswanathan, R., and Sivashankar, N. 2020. Experimental Investigation on Surface Roughness, Tool Wear And Cutting Force in Turning of Hybrid (Al7075+SiC+Gr) Metal Matrix Composites. *Journal of Materials Research and Technology*.
[doi: 10.1016/j.jmrt.2020.11.074](https://doi.org/10.1016/j.jmrt.2020.11.074).
99. Rajasekaran, A., and Pugazhenthii, R. 2019. Study of mechanical properties of stir casted Al7075 / SiCp

- composites after thermomechanical treatment. *Materials Today: Proceedings*.
[doi: 10.1016/j.matpr.2019.10.131](https://doi.org/10.1016/j.matpr.2019.10.131).
100. Sahu, M.K., and Sahu, R. K. 2019. Synthesis , microstructure and hardness of Al 7075 / B4C / Fly-ash composite using stir casting method. *Materials Today: Proceedings*.
[doi: 10.1016/j.matpr.2019.09.150](https://doi.org/10.1016/j.matpr.2019.09.150).
 101. Kumar, M. R., Reddappa, H. N., Suresh, R, and Gangadharappa, M. 2018. Effect of Heat Treatment on Tensile Strength of Al7075 / Al 2 O 3 / SiCp Hybrid Composite by Stir Casting Technique. *Materials Today: Proceedings*. 5(10), 22460–22465.
[doi: 10.1016/j.matpr.2018.06.616](https://doi.org/10.1016/j.matpr.2018.06.616).
 102. Devaganesh, S., Venkatesh, N., and Kumar, P.K.D. 2020. Investigation on influence of solid lubricants over mechanical behavior of hybrid Al7075-SiC metal matrix composites. *Materials Today: Proceedings*. 27, 2864–2869.
[doi: 10.1016/j.matpr.2020.01.609](https://doi.org/10.1016/j.matpr.2020.01.609).
 103. Malhotra, P., Tyagi, R. K., Singh, N. K., and Sikarwar, B. S. 2020. Experimental investigation and effects of process parameters on EDM of Al7075/SiC composite reinforced with magnesium particles. *Materials Today: Proceedings*. 21, 1496–1501.
[doi: 10.1016/j.matpr.2019.11.069](https://doi.org/10.1016/j.matpr.2019.11.069).
 104. Balaji, V., Sateesh, N., and Hussain, M. M. 2015. Manufacture of Aluminium Metal Matrix Composite (Al7075-SiC) by Stir Casting Technique. *Materials Today: Proceedings*. 2(4–5), 3403–3408.
[doi: 10.1016/j.matpr.2015.07.315](https://doi.org/10.1016/j.matpr.2015.07.315).
 105. Bhushan RK, Kumar S, Das S. 2009. Optimisation of porosity of 7075 Al alloy 10% SiC composite produced by stir casting process through Taguchi method. *International Journal of Materials Engineering Innivation*. 1(1), 116-129.
[doi:10.1504/IJMATEI.2009.024031](https://doi.org/10.1504/IJMATEI.2009.024031).
 106. Sardar, S., Karmakar, S. K., and Das, D. 2018. Evaluation of Abrasive Wear Resistance of Al2O3/7075 Composite by Taguchi Experimental Design Technique. *Transactions of Indian Institute of Metals*. 71(8), 1847–1858, 2018.
[doi: 10.1007/s12666-018-1317-9](https://doi.org/10.1007/s12666-018-1317-9).
 107. Veeravalli, R. R., Nallu, R., and Mohiuddin, S.M.M. 2016. Mechanical and tribological properties of AA7075-TiC metal matrix composites under heat treated (T6) and cast conditions. *Journal of Materials Research Technology*. 5(4), 377–383.
[doi: 10.1016/j.jmrt.2016.03.011](https://doi.org/10.1016/j.jmrt.2016.03.011).
 108. Naik, M.N., Reddy, K.D., Ramaiah, P.V., Narayana, B.V., and Reddy, G.B. 2017. Exploration of Mechanical behaviour and Wear Behaviour of Al4C3 Reinforced Aluminium Metal Matrix Composites *Materials Today: Proceedings*. 4(2), 2989–2998.
[doi: 10.1016/j.matpr.2017.02.181](https://doi.org/10.1016/j.matpr.2017.02.181).
 109. Imran, M., Khan, A. R. A., Megeri, S., and Sadik, S. 2016. Study of hardness and tensile strength of Aluminium-7075 percentage varying reinforced with graphite and bagasse-ash composites. *Resource Technology*. 2(2), 81–88.
[doi: 10.1016/j.refit.2016.06.007](https://doi.org/10.1016/j.refit.2016.06.007).
 110. Sahoo, A. K., Pradhan, S., and Rout, A. K. 2013. Development and machinability assessment in turning Al/SiCp-metal matrix composite with multilayer coated carbide insert using Taguchi and statistical techniques. *Archeive of Civil and Mechanical Engineering*. 13(1), 27–35.
[doi: 10.1016/j.acme.2012.11.005](https://doi.org/10.1016/j.acme.2012.11.005).
 111. C. H. Gireesh, K. G. D. Prasad, and K. Ramji, “Experimental investigation on mechanical properties of an Al6061 hybrid metal matrix composite,” *J. Compos. Sci.*, vol. 2, no. 3, pp. 1–10, 2018.
[doi: 10.3390/jcs2030049](https://doi.org/10.3390/jcs2030049).
 112. A. Raturi, K. K. S. Mer, and P. Kumar Pant, “Synthesis and characterization of mechanical, tribological and micro structural behaviour of Al 7075 matrix reinforced with nano Al2O3 particles,” *Mater. Today Proc.*, vol. 4, no. 2, pp. 2645–2658, 2017.
[doi: 10.1016/j.matpr.2017.02.139](https://doi.org/10.1016/j.matpr.2017.02.139).
 113. S. Devaganesh, P. K. D. Kumar, N. Venkatesh, and R. Balaji, “Study on the mechanical and tribological performances of hybrid SiC-Al7075 metal matrix composites,” *J. Mater. Res. Technol.*, vol. 9, no. 3, pp. 3759–3766, 2020.
[doi: 10.1016/j.jmrt.2020.02.002](https://doi.org/10.1016/j.jmrt.2020.02.002).

Comparison of Primary Alcoholic Fuel Properties for MPFI SI Engines

DVVS Reddy Saragada¹, Danaiah Puli², Vinjamuri SN CH Dattu³

^{1,3} Research Scholar, Department of Mechanical Engineering, Lincoln University College, Malaysia

² Research Supervisor, Department of Mechanical Engineering, Lincoln University College, Malaysia

dvvsbreddy.s@gmail.com¹, drdanaiahpuli@gmail.com², dathuthermal@gmail.com³

Abstract

Now a day's fuels are acted as a most Significant prominent role for future generations. By using the different alternate fuels use to survive the world. In Various alternate fuels like Alcohol have a good octane number and it gives fewer emission values. In fact, the resources are used in a good manner but consumption of fuel rate is more in Light and Heavy-duty engines. Unwanted waste material from sugar mills contains large amounts of Isoamyl alcohol. This paper will give you more knowledge about the comparison of various alcoholic fuel properties in multi-point fuel injection spark-ignition engines. Earlier researchers are conducted Several experimental studies on primary alcohol petrol blends on SI engines were done and created awareness of the potential benefits. The physical and thermo-chemical properties of Primary-generation alcohols have been discussed and compared.

Keywords: Primary alcohol, , SI Engine, Combustion, Emission

Introduction: Energy research is still a significant topic. Fuel seems to be the predominant major source research work in fuels science during the last 90 years. The scope is vast, encompassing many themes of growing concern, such as environmental issues and pollution. Alternative fuels for SI engines include compressed natural gas (CNG), hydrogen (H₂), liquefied petroleum gas (LPG), and alcohol fuels (methanol and ethanol), while biodiesel, di-methyl ether (DME), and jet propellant-8 (JP-8).are examples for CI engines. In premixed charge compression ignition, As an alternative fuel for faster combustion, naphtha is introduced. [1]

Ethanol produced from sugarcane and agricultural residue provides additional money to farmers while also benefiting the environment and ensuring the safe disposal of farm stubble. As an outcome, ethanol is a viable biofuel that may be combined with gasoline to power sprayers, reducing environmental pollution.[2]

Over the globe, gasoline is one of the large-scale authorities for the enhancement and improvement of mankind's day to day exercise leads to continuous improvement. With the accelerated expansion in the global populace in the course of the previous middling years, the fuel exigencies further heightened at an alike substantial standard in mechanization and transport region supremacy to a hike in gasoline oil cost, that is precisely overwhelmed by world monetary action.[1].

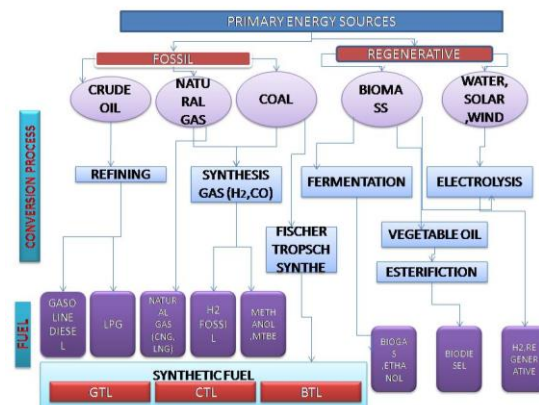


Fig.1 Industrial routes for fossil and renewable fuels [14]

Alcohols are the particular biological admixtures that endure expressed by the existence of one, two or more hydroxyl associations ($-OH$) which are obsessed to the graphite atom in alkyl associations or hydrocarbon conglomerate. **Main Types of Alcohols:** Alcohols are comprehended positioned upon the existence of hydroxyl troop accustomed. The region of this hydroxyl troop on the point of together will difference the environmental and synthetically decors of several boozes. Effectively there continue three stereotypes of alcohols restricted as elementary, secondary and triennial. Alcohols besides their upsurge in microscopic heft contribute to enhancing fewer condensation pressures, scalding points, densities, and viscosities upsurge.

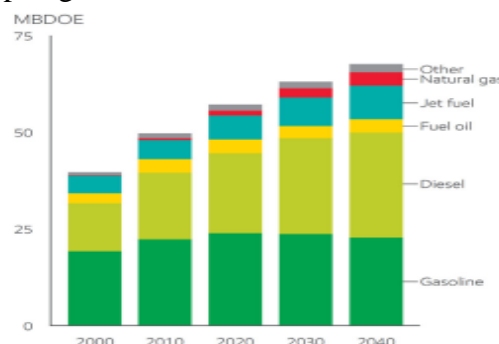


Fig.2 Global Transportation by fuel[15]

Features of Primary Alcoholic Fuels: Either low - molecular - weight alcohols as well as molecular weights alcohols can be produced using domestic energy assets. Burning in spark-ignition engines gives out high performance. Combustion of alcohol in ICE produces more ignition pressure with lower knocks. With lower and appetitive tendency specific consumption is achievable with high octane values. Negotiable release of ash content. [16]

Significance and Aspects of Alcoholic Fuels: seeking sustainable growth by increasing the use of alternative fuels produced from renewable energy sources and minimizing the concerns about limiting fossil fuel energy. Boosting engine efficiency and emissions by utilizing alternative fuels' better physical or chemical qualities over traditional fuels reducing the imbalanced use of traditional petroleum-based fossil fuels

Present Contribution: Competent bona fide defined empirical data that simplify the portrayal those secondary and tertiary alcoholic fuels backdrops have on concoction arrangement and ignition up a realistic range of engine performing circumstances. The

prime aspiration of the present effort has been to exercise on Primary alcoholic fuels contrasting primary alcohols. In the environment, encyclopedic research was embarked upon to contribute vigorously to the first season that aforesaid a thoroughly confirmed statistics is conferred for primary alcoholic fuels. It is retained a certain these dossiers subsidize to an index of ignition arrearage that is crucial for improving our intelligence of the elemental constitutional instruments of alcoholic fuels practice concealed by pragmatic spark ignition operated working surroundings.[17-23]

Alcohol paraphernalia on sanctification: Vapour latch and bite opening Each flow rate chance of an oxygenate added to typical unleaded gasoline of 87 (RON.MON)/ 2 octane going to stand (where RON seems to be the exploration octane number and MON is the motor octane number) raises the mixed octane standing in the range from 0.1 to 0.3 showed that lends of methanol with advanced alcohols increased antiknock performance to a lesser extent than methanol alone. The energy delivery system must be capable of producing a rich enough admixture to allow the use of an alcohol gasoline combination to begin. The oxygen content, and from the other hand, plays a major role since composites with higher oxygen concentration tended to have quicker honey pets than composites with lower oxygen content[17] The dropped density in each alcohol blends mode results in further, as a consequence preceding assignment in utmost gas shipping and the long run lowering the machine energy affair.[19] Alcohols had surfaced because the maximum aggressive seeker utmost of the notorious occasion energies due to the fact they may be made out of renewable means which include waste cloth every one of those alcohols has the functionality for its operation in buses because it is less expensive than the essential alcohol and has comparable chemical properties to gasoline. The gas should be absolutely wracked, comminuted, wracked and combined inclusively with the air to have a rapid-fire combustion process. Currently, an adding number of strict law enforcement at the contaminant produced with the aid of using auto machines inclusively with a parlous figure of energy has extended the desire for occasion gas with proper machine performance, green gas frugality and drop emigration adulterants.[20]

Operation of Alcohol Material Rates: To have a balanced composition and quality, as well as trustworthy machine functioning, the packages of alcohol power must adhere to the world's accessible rules.[20]

RON The addition of alcohol to gas composites increases the octane range, allowing you to improve antiknock conduct and redundant excellent timing, resulting in improved combustion strain and necklace. The greater the molecular weight for alcohol, the more volume bit with inside the composites is required to have the same volume of oxygen content material as smaller molecular weight alcohols.

HV Because the gas absorbs luke warmness from the cylinder during vaporization, the air-gas combination is compressed redundantly, boosting thermal efficacy for alcohol-gas admixture as the carbon fragment number is increased in the composites.

HB bonds It occurs between the fairly conclusive H toms and solitary pairs of O₂ atoms of new particles. HB is an energetically electronegative element that originates at intervals particles in and a hydrogen atom.

BP: HB is not the only alcohol with a high intermolecular strength. They collide and compete with van der Waals diffusion and dipole-dipole synergies. For whole alcohols, the

HB and dipole-dipole synergies are complimentary, although diffusion increases as the degree of alcohol expansion increases. The specific allures turn out nicely as the pieces stretch and accept more electrons as the proportions of the transient dipoles hammered evolve. Because of the aforementioned reason, the BP increases as the total number of C atoms in the groups increases. It precedes higher energy to overwhelm the diffusion forces, resulting in a rise in BP.

RON Simulates energy performance under decreased machine operation; octane number is a quantitative dimension in which energy is utilised in a machine while accounting for the unusual miracle when air-energy admixture is knock" or tone-kindling. Normal combustion occurs when the honey goes thru the cylinders until about the end of the combustion phase with little or no noticeable modification or speed. Bus-ignition or pre-ignition occurs when the admixture burns and glows before the honey reaches it.

Meanwhile, eruption produces machine knocking, which occurs when there is an unexpected increase in reaction rate and pressure proliferation, resulting in pressure swells. The addition of alcohol to gasoline composites raises the octane level, which improves antiknock and allows for more advanced timing, which results in advanced combustion pressure and advanced necklace.

The greater the molecular size of the ethanol, the larger the quantum of space bit in the composites required to get the same quantum of oxygen levels as low - molecular - weight alcohols. Alcohol energies have a high octane number due to the presence of oxygen content (wt) in the composites. As the OC number rises, so will the machine's knock. Furthermore, the spark-ignition machine may function at an advanced contraction rate without knocking owing to an increase in the octane number of energies, which results in a lower ignition tendency. Aside from refining the antiknock, increasing the octane number will result in more advanced timing, which will result in advanced combustion pressure and advanced necklace.

HV It is defined as the heat emitted by energy when it is totally burned and measured at constant volume or constant pressure, after which the hot gas is cooled to its initial temperature (ASTM D240-17). Heat capacity is classified as advanced heating value (HHV) or lower heating value (LHV) (LHV). The heating value of alcohol energies grows as the amount of carbon snippets added to the composites. In other words, a rise in carbon and hydrogen content correlates to an increase in the molecule of alcohol energy and a decrease in oxygen content. To address this issue, experimenters have proposed using alcohol with four or more carbon tittles to get a lower heating value comparable to gasoline.

LHV is defined as the amount of heat (kJ/kg) required to transform one unit mass of a liquid at its full boil into one unit mass of vapour with no temperature rise. When compared to gasoline, alcohol energy with improved heat of vaporisation has a higher energy conversion capacity. Alcohol energy will reduce the temperature of the air entering the machine while increasing the volumetric efficacy of the machine power affair. Also, because of the high heat of vaporization, alcohol energies are simpler to decimate during the contraction stroke. This is due to the fact that when the energy absorb heat from the cylinders during vaporization, the air-energy admixture is compressed more fluently, therefore perfecting thermal effectiveness for the alcohol-gasoline combination over

gasoline. Nonetheless, enhanced heat of vaporization of alcohol energies has drawbacks, particularly in its ability to start the machine in cold settings. The recent advancement in energy delivery methods and improved molecular weight alcohol workouts appears to be the outcome of overcoming cool launch circumstances. The advancement of idle heat of vaporization has resulted in improved machine necklace. This is explained by the fact that having advanced evaporation rate lowers the input temperature owing to alcohol energy freely vaporizing and sinking in the input manifolds.

Viscosity The viscosity of energy is an essential metric, particularly for the functioning of gasoline machines. In addition, the viscosity of energy also influences assessing machine ignition quality and volume computations which will affect machine operation. Because viscosity increased with sugar content, increased gasoline will have advanced viscosity. Nonetheless, incorporating oxygenated compounds such to alcohol energies into gasoline will raise octane standing but have no effect on existing viscosity. Because of the increase in alcohol concentration in the amalgamation admixture, the viscosity of the amalgamation energy is increased.

RVP is the relative pressure (pressure differential based on air pressure) that indicates how quickly energies dematerialise. It is also known as volatile or achromatic pressure since how quickly the energy evaporates contributes to the ozone sub-caste, which affects the girding landscape. The volatile of alcohol energies decreases as the number of carbon tittles increases. Alcohols with more than four carbon tittles have lower inclinations towards vapour cinch and cavitation problems. Energies must be adequately unpredictable to have an easy machine launch and sufficient vaporization for energy distribution between the cylinders.

Density is a dimension of resist to fluid inflow caused by the inner disunion of one component of a fluid flowing over another, and it is based on temperature and molecular weight. Advanced density can result in inferior energy separation process, which can result in poor vaporization. All of these factors can result in higher canvas dilution, worse overall combustion, and fewer migrations. Energy with a high kinematics density may result in poor separation process during energy dispersion, affecting machine deposits and wear on the energy system, requiring more energy to transfer the energy into the machine. the density of the alcohols increases as the carbon chains becomes longer. This means that advanced molecular weight alcohol has advanced density compared to the lower alcohol content.

OC The total concentration of oxygen of energy blends is measured by the amount of energy content, which includes C, H_2, N_2, O_2 . The level of oxygen of alcohol decreases as the carbon chain length increases. The oxygen content in alcohol-gasoline composites, known as oxygenates energies, improves combustion (homogeneous combustion), and reduces CO with HC emigrations.

The **FP** of energy is the lowest or smallest temperature at which the energy may be heated to the point that the vapour emits flashes when open honey is passed over it under specified conditions. Flashpoint is a metric that can predict potential fire threats during energy transfer, management, and storage.

IE: Depending on the content of the admixture The minimum ignition energy for hydrocarbons is expected to be around 0.2 MJ. The limitations of flammability are

determined by the source of ignition. The most frequent sources are sparks, which have low ignition energy that decreases as electrode distance rises, achieves its smallest value at a specific distance, and then begins to climb again. Because the electrode removes a great amount of heat from the nascent honey at short lengths, only a tiny amount of ignition energy is required. As the distance grows, the face area to volume rate falls, and the amount of ignition energy required reduces as well.

Quality of Alcohols Energies for SI Engines: Originally, it is also the volatile of energy that defines the major character to decide its felicity on the SI machine dependent on the fractional composition as it is an admixture of several hydrocarbons. Second, in order for the machine to start and warm up easily, the energy should be vaporising at.0 the ambient temperature. Thirdly is the operating range performance In general, energy containing reactive HC and chemical contaminants that have been held for an extended period of time likely to create the gum. It will cause operational issues in the case of carbon deposits on the machine and gum deposits in the manifold, reducing overall efficiency.

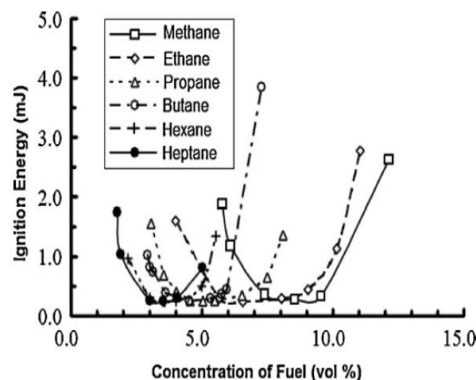


Fig 3. Minimum ignition energy [7,10]

Conditions demanded Alcohols Energies for SI Engines: The first one is the energy must be fully wracked, comminuted, wracked and fully mixed with the air to have a fast combustion process. The alternate bone is nippy during starting the machine and dependable at any ambient condition. The third bone in the face of the combustion chamber should remain free from carbon and other deposits to achieve a smooth combustion process. The fourth one is The cylinder face, the piston and the piston rings should be free from inordinate wear and erosion. The fifth bone is the combustion process; the energy must stay free from thermal stresses especially the machine due to the development of the temperature grade. The sixth bone is the no emigrations of dangerous exhaust feasts during the completion of combustion stages. Generally, energies are separated by their sources and phases. In terms of its sources, energy is divided into two which is natural and artificial.

Selection Procedure for Alcohols Energies for SI Engines: The first one is the type of outfit needed to store and supply the energy in the machine, the alternate bone is the spicy value per unit volume of the energy, and the third bone is the cost of the energy at the point of the machine. Compass The current work provides an overview of secondary and tertiary alcohols that are have been tested in SI machines. The focus is related to specialized issues, implicit machine effectiveness and emigrations, but not on energy costs, product or vacuity. Points at serving the anthology with a background of

the graces and enterprises of implicit unborn energies and machine generalities from a specialized environment. The report covers the main secondary and tertiary alcohols.

Review-System: The material is gathered substantially by searching the Scopus databases, which covers all applicable journals and publications on the field, but also from other internet sources, from our exploration and experience. To find the most applicable papers the hunt has thus been performed in two sequences, the first fastening to find the applicable alcoholic energies. Utmost of the alcoholic energies sections are written in a way to give an overview of the more well-known aspects of the energy group.

Advantages of SI Engines: Easy to control, run veritably fairly by using stoichiometric operation and a three-way catalytic motor It lends itself veritably well to either liquid or gassy energy operation, with either lean-burn or stoichiometric operation. The energy can be fluently handed to the machine through cheap low-pressure injection systems.

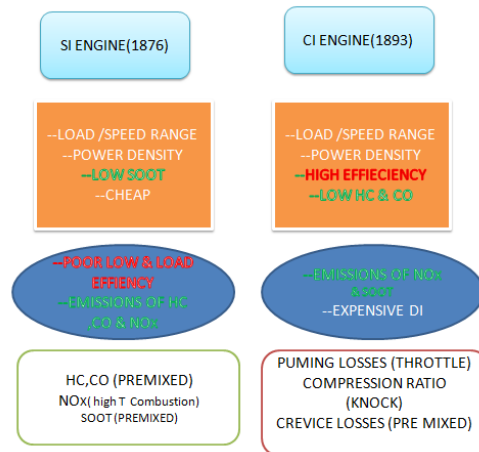


Fig 4. ICE Pros and Cons- Red efficiency, Green emissions. [17]

Comparison of alternative fuels for SI engines [3,4,5] and conventional fuels.

Item	Gasoline	Diesel	Methane	Hydrogen	LPG		Alcohol	
					Propane	Butane	Methanol	Ethanol
Formula (phase)	$C_nH_{1.87n}$	$C_nH_{1.8n}$	CH_4	H_2	C_3H_8	C_4H_{10}	CH_4O	C_2H_6O
Density (kg/m ³)	0.71–0.79	0.83–0.87	0.72	0.09	0.51	0.58	0.792	0.785
BP (°C)	27–225	-	- 161.49	-	- 41.99	- 0.5	64.7	78
Low heat value (MJ/kg)	43.97	42.49	49.89	119.96	45.98	45.49	19.89	26.89
OC (RON)	91-97	-	119	≥ 1119.89	110	102	108	108
CN	-	51.5	-	-	-	-	-	-
Stoichio metric Air Fuel(A/F)	14.59	14.44	17.33	34.33	15.58	15.39	6.37	9.2
LH of vaporisati	306	271	510	-	425	386	1169	839

on (kJ/kg)								
FS (m/s)	0.37–0.43	-	0.38	1.85	0.38	0.37	-	0.39

Properties of Fuels [6-13]

Properties	Gasoline	Isoamyl Alcohol	Isobutyl Alcohol
Chemical formula	C_8H_{18}	$C_5H_{12}O$	$C_4H_{10}O$
MW, g/mol	95.18	87.99	73.97
Density (kg/m ³)	719–776	802.3	801
Oxygen content (% weight)	0	17.89	Not Pertained
Viscosity (mm ² /s)	0.5–0.6 (at 25 °C)	3.69	Not Pertained
Stoichiometric air-fuel ratio	14.19–15.0	11.69	20.19
Boiling point (°C)	209.58	130.89	106.89
Lower heating value (MJ/kg)	43.99	34.64	33.84
Latent Heat of Vaporization (kJ/kg)	381.89–399.58	620.79	579
Research Octane Number	90–102	112	113
Motor Octane Number	83–91	85	95
Emission $1/\lambda_{max}^b$ (cm ⁻¹)	44000	22,850	22,900
Emission λ_{max} (nm)	440.09	438	437
Specific Gravity	0.67-0.75	0.799	0.802

Conclusion: Until recently, only a few research publications have disseminated alcohol energy packages in the collaborative form of knowledge, including the negative effect of alcohol energy operation and its reactions in spark-ignition machine performance and exodus. As a result, this research is focused on the physical and chemical components of alcohol energies, as well as contemporary literature data for spark-ignition engines.

This article will also go through the exercises on the packages of alcohol energy to the already accessible spark ignition equipment. The benefits and drawbacks of alcohol energy operation are also highlighted. This evaluation reveals that continuous investigation and development are still required, particularly on secondary and tertiary alcoholic energy parcels, since it will result in lower machine performance and higher emigrations.

Still, it is unclear why and how the packets of alcohol energy effect machine performance and exhaust emigrations. As a result, in this review, a full explanation of basic alcoholic energy packets and their influence on machine performance and exhaust exodus will be offered.

This article also includes a complete assessment of alcohol energies by previous experimenters. Finally, there will be a talk on vital energy rates that should be performed in order to improve machine performance and reduce exhaust emigrations. There is no one desire energy that can be coupled as an optimal substitute for fossil fuels. Each of the colourful campaigns has both great and negative features. Several emerging energies have exciting characteristics, but they need to be explored deeper and have yet to establish their utility.

New machine generalities adapt to new necessary energies more easily than classic bones. Styles of exploration and implicit exploration conditioning Exploration and development

of clean and efficient machines require advanced abecedarian understanding of energy packets. The present styles and standard tools are insufficient to provide comparable knowledge or meaningful comparisons of energy in different combustion techniques, and should thus be fleshed out and expanded further.

The initial measure should be an increased bit of drop-in energies in fossil energies for typical SI machines. It is necessary to scan appropriate and arising indispensable energies, as well as the fashionable arising machine generalities. Integration with electroenergies is a critical component. Understanding the stylish important energy campaigners necessitates the integration of numerous exploratory disciplines.

Other considerations: Exploration shows that spark ignition combustion machines may be adapted to operate effectively and sustainably with a wide range of essential fuels, albeit with certain cost and performance trade-offs. Because of this rigidity, ICEs are a necessary aspect of the transition from reactive energy reliance to sustainable systems that combine cost-effective resources, the energy grid, and mobility. Some of the alcohol energy packets that impact the machine include idle heat of vaporisation, reduced heating value, and exploration octane number.

The benefits and drawbacks of main alcoholic energies indicate that cautious selection and additional investigation are required before using a spark-ignition machine.

Currently, interest in altering the alcohol energy packets is increasing rapidly, driven by three key factors: terrain, frugality, and trustworthiness. It is limiting the dazzling impact in energy application in terms of the landscape. For greater profitability, the frugality employs waste gas aqueducts in the factory/source, comparable to end flash gas or heavy hydrocarbons. While trustworthiness enhances vacuity by avoiding complicated and costly energy treatment gear. The need to operate with varied secondary and tertiary alcoholic energies. It will be important to stretch the allowed energy parcels and have the inflexibility to employ new sources for environmental, financial, and trustworthiness reasons. Primary alcoholic energies are thought to be safe and, in most situations, are linked to significant risk reduction in terms of cancer, other health difficulties, and environmental issues, a commodity that is seldom acknowledged. Emigrations of soot, NO_x, HC, and CO vary across energies due to changes in running, whether the energy is gassy or liquid, and are typically lower than for gasoline. The very little variations observed during machine operation suggest that product and distribution will have a greater impact on the environmental performance and operating costs of the various essential energy. Eventually, further exploration in secondary and tertiary alcoholic energies could contribute to a piece of new scientific knowledge in automotive diligence, especially in energy-effective vehicles.

Nomenclature

AET	Auto Ignition Temperature	IAA	Isoamyl Alcohol
AFT	Adiabatic Flame Temperature	LEL	Lower Explosive Level
BP	Boiling Point	LHE	Latent Heat of Evaporation
C	Carbon	LHV	Latent Heat of Vaporization

c	Specific Heat	MON	Motor Octane Number
CO	Carbon monoxide	MW	Molecular Weight
CP	Critical Pressure	O ₂	Oxygen
CT	Critical Temperature	OC	Oxygen Content
CV	Calorific Value	RON	Research Octane Number
DV	Dynamic Viscosity	RVP	Relative Vapor Pressure
EC	Energy Content	SI	Spark Ignition
FP	Flash Point	SIE	Spark Ignition Engine
FS	Flame Speed	SEC	Standard Enthalpy of Combustion
H	Hydrogen	SEF	Standard Enthalpy of Formation
HB	Hydrogen Bonding	SME	Standard Molar Entropy
HC	Hydrogen Content	TA	Tertiary Alcohol
HHV	Higher Heating Value	IBA	Isobutyl Alcohol
HV	Heating Value	UEL	Upper Explosive Limit
ICE	Internal Combustion Engine	VP	Vapor Pressure
IE	Ignition Energy	Wt	Weight

References

- [1] ChoongsikBae, JaeheunKim, Alternative fuels for internal combustion engines, The Combustion Institute. Published by Elsevier, Volume 36, Issue 3, 2017, Pages 3389-3413.
- [2] Srikar G Kulkarni , Dr. M. C. Navindgi, Review Paper on Sugarcane Bioethanol as an Anticipating Biofuel for IC Engines, ISSN- 2278-0181, Pub. IJERT, Volume 10, Issue 03 (March 2021).
- [3] J.B. Heywood, Internal Combustion Engine Fundamentals, McGraw-Hill, New York, 1988.
- [4] C. Gong, B. Deng, S. Wang, Y. Su, Q. Gao, X. Liu, Energy Fuels 22 (2008) 3779–3784.
- [5] S. Mani Sarathy, P. Oßwald, N. Hansen, K. Kohse-Höinghaus, Prog. Energy Combust. Sci. 44 (2014) 40–102.
- [6] Kheiralla AF, El-Awad M, Hassan MY, Hussen MA. Effect of ethanol–gasoline blends on fuel properties characteristics of spark ignition engines. UofKEJ 2011;1(2):22–8.
- [7] Yang Y, Dec JE, Dronniou N, Simmons B. Characteristics of isopentanol as a fuel for HCCI engines. SAE Int J Fuels Lubric 2010;3(2):725–41.
- [8] Masum BM, Masjuki HH, Kalam MA, Palash SM, Habibullah M. Effect of alcoholgasoline blends optimization on fuel properties, performance and emissions of a SI engine. J Cleaner Prod 2015;86:230–7.
- [9] Masum BM, Masjuki HH, Kalam MA, Rizwanul Fattah IM, Palash MS, Abedin MJ. Effect of ethanol-gasoline blend on NOx emission in SI engine. Renew Sustain
- [10] Internet: Tupraş, “Urun Spesifikasyonu Kurşunsuz Benzin 95 Oktan”, <https://www.tupras.com.tr/>.

- [11] Sharif A. Selective additives for improvement of gasoline octane number. *Tikrit J Eng Sci* 2010;17(2):22–35.
- [12] Sarathy SM, Oswald P, Hansen N, Kohse-Hoinghaus K. Alcohol combustion chemistry. *Progr Energy Combust Sci* 2014;44:40–102.
- [13] Hotta SK, Sahoo N, Mohanty K. Comparative assessment of a spark ignition engine fueled with gasoline and raw biogas. *Renewable Energy* 2019;134:1307–19.
- [14] K. Reif, *Gasoline Engine Management: Systems and Components*, Springer Vieweg, 2015 ISBN 978-3-648-03964-6.
- [15] *The Outlook for Energy: A View to 2040*, Exxonmobil.
- [16] *Alcohol Fuels - Current Technologies and Future Prospect* chapter - *Alcohol Fuels as an Alternative Fuels - Bringing New Heights in Sustainability* Sivakumar Kasibhatta.
- [17] J.WG Turner, A.GJ.Lewis, Sam Akehurst, Chris J Brace, Sebastian Verhelst, Jeroen Vancoillie², Louis Sileghem, Felix Leach and Peter P Edwards AF for SIE Performance, Efficiency & Emission Effects At Mid To HB rates or B- Mixtures and P- Components. Part D: IMechE Proc. J.AE, 2018, Vol. 232(1) 36–56.
- [18] M Gautam, D W Martin II Combustion characteristics of higher-alcohol gasoline blends *Proceedings of the Institution of Mechanical Engineers, Part A: J.Power and Energy* 2000, 214–497.
- [19] J. Serras-Pereira, P. G. Aleiferis & D. Richardson An Analysis of the Combustion Behavior of Ethanol, Butanol, Iso-Octane, Gasoline, and Methane in a DI- SIRE Combust. *Sci. Technol.*, 2013, 185: 484–513.
- [20] Hazim Sharudin, Nik Rosli Abdullah, A.M.I. Mamat, N.H. Badrulhisam, Rizalman Mamat Application of Alcohol Fuel Properties in Spark Ignition Engine: A Review *Jurnal Kejuruteraan* 2018, SI 1(7) 37– 47.

A Retrospect on Microstructural growth and Mechanical Characteristics of Materials obtained by Friction Stir Processing

¹Dr.Ch.Srinivasa Rao, ²Dr.G.Vijay kumar

¹Professor, Dept. of Mechanical Engineering, KHIT, A.P. India.

²Professor, Dept. of Mechanical Engineering, PVPSIT, A.P. India.

ABSTRACT: Friction stir processing is a method of joining materials by surface modification. The process is based on a similar principle as friction stir welding. Metals and alloys with improved surface properties are desirable in a variety of industrial applications. The limited mechanical and tribological properties of most metals and alloys make them not suitable for all applications. Furthermore, these properties have an effect on component service life. As a result, there is an impetus for the creation of materials with improved properties. However, in Friction stir processing, the tool has a shoulder and pin and is rubbed over a single workpiece material. The changes in microstructure and in mechanical properties occur due to intensive plastic deformation. The present paper consists of a research review on the changes in microstructure during friction stir processing. It also includes the influence of the microstructure on mechanical properties.

Keywords: Microstructural evolution, mechanical properties, ferrous and nonferrous materials, friction stir processing.

1. INTRODUCTION

Friction stir welding (FSW) is a material joining technique. It is a solid-state joining process. A cylindrical tool made of high-strength material is used to apply frictional force on two faying surfaces. Heat is generated due to rotation and friction. The heat generated softens the location near the tool surface. Mechanical pressure is applied to the softened material. For a long time, FSW is being used for joining Aluminium and its alloys. Nowadays, some of the dissimilar metals and alloys are also joined by FSW. Friction stir processing (FSP) is used to produce surface composites. In FSP, a non-consumable rotating tool is plunged into a single workpiece material. The tool has a pin and a shoulder to enhance tensile strength or material toughness [1].

In FSW, the tool joins two workpiece materials, but in FSP, the tool rubbed on a single piece of material. With proper implementation of the process, the material can be mixed without changing the phase. The principle of FSP is shown in figure-1[2]. As shown, the tool rotates and plunges into the workpiece and moves in the desired direction.

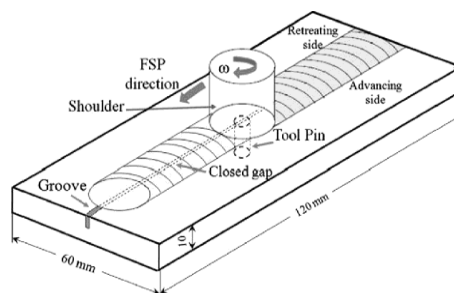


Fig.1 Principle of FSP setup [2]

FSP is an innovative technique for developing new materials with improvement in resistance to creep, wears, and fatigue. Materials developed are particularly suitable in various applications of the automotive and aerospace industries [3]. FSP involves severe plastic deformation of materials. The technique was developed based on the principle of FSW [4]. The grain refinement, homogeneity, and density of the material can be improved with FSP and thus enhances the strength and plasticity. The mechanical properties and superplasticity of alloys were improved using FSP [5]. For example, FSP enables the production of Mg alloys with the additive manufacturing process and may produce Mg-based surface composites. Aluminium surface composites with enhanced surface properties such as mechanical properties and corrosion resistance can be fabricated by FSP [6]. The reinforcement materials used in the composite materials can change their properties. The reinforcement materials can be metals, ceramics, or polymeric materials. The yield stress of FSP composites with SiO₂ nano-sized particles was improved [7].

2. MICROSTRUCTURAL EVOLUTIONS

The microstructural zones in a welded joint acquired by FSW/FSP appear in figure-2. The zone that is not influenced by heat concerning microstructure or mechanical properties is the unaffected base metal zone. It is closer to the weld zone. At the weld zone, the material undergoes a thermal cycle. The change in microstructure also occurs in this zone. Grain development and solubilization happen in this zone. The region in the weld place that makes equiaxed grains is the Nugget zone. Recrystallization of material happens because of heat and plastic distortion. In the thermomechanically-affected zone (TMAZ), the material is subjected to in-elastic deformation. The heat produced also affects the material microstructure. In TMAZ, the grains are long and no recrystallization of material occurs.



Figure-2. The microstructural zones in a friction stir welded/processed joint [8]

Friction stir process has been used to fabricate steel specimens. The microstructural studies indicate the growth of grain structure due to a complicated process involving geometrical deformation and relocation of grain boundaries [9]. The mechanical properties of FSP materials are obtained by tensile testing generally. Bending tests are also used to find the mechanical properties. Testing of Chromium alloy steels processed by FSW for estimation of mechanical properties is carried and compared with parent materials [10]. The sigma phase in stainless is used to characterize the physical and mechanical properties. FSW was also utilized to join 304 stainless steel materials and the sigma phase formation was studied. The results indicate that the formation of the sigma phase is due to the presence of delta ferrite at elevated temperatures [11]. The various zones in the microstructural studies were shown in figure-3.

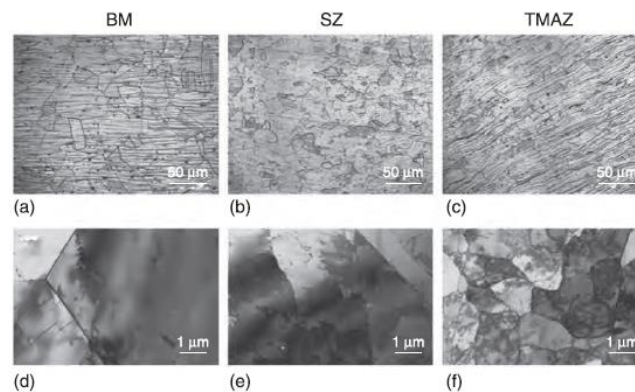


Figure-3. The zones in 304 stainless steel [11]

Tools of cylindrical and square pin profiles were fabricated. The influence of tool shape and profile on the mechanical properties of FSW copper joints was studied. It is confirmed that the deformation and heat generated are more with a square profile tool [12]. Both experiments and mathematical models were used to estimate and compare the mechanical properties of pure copper. “A mathematical model was developed to test the accuracy of experiments. The model is based on the design of experiments. The results obtained were compared. The tensile strength is more with the square and triangular profile tools [13]. FSW has been used to fabricate welded joints of brass consisting of 60% copper and 40% zinc. Various rotational and traveling speeds were used to get good quality welded joints. The microstructural studies indicate that the material hardness is more in the stir zone than the other at all the operating conditions [14]. Experiments have also conducted on microstructural studies of copper and 30%Zn brass alloy at numerous welding conditions. The results indicate that the stir zone has a very fine grain structure. Coarser grains are found in TMAZ [15]. An experimental investigation has been conducted on the FSW of Aluminium 6063-T5 and T4 alloys. A Transmission electron microscope was used to find the microstructural studies and found that the increase in hardness value in the stir zone is less at lower rotational speeds [16]. The study of grain refinement and density of particles in various regions of FSW welded joint is also of importance. Tests were conducted to explore the microstructure and mechanical properties of FSW aluminium 7050-T651 alloys [17]. Porosity is a common problem during the joining of magnesium alloys using traditional fusion welding techniques. This problem can be conveniently eliminated by using FSW. The influence of process parameters on the tensile properties of FSW magnesium alloys was investigated [18]. It is not easy to join AZ31 magnesium alloy by the conventional fusion welding process. FSW was utilized to join AZ31 magnesium alloy materials and a study on grain structure evolution was obtained with an electron backscattering system [19]. FSP has been used to produce AZ91/SiC surface composites. Nanoparticles of SiC were added to AZ91 magnesium alloy by FSP. Microstructural studies were conducted by a change in process parameters [20]. Three different samples of Ti-6Al-4V were obtained by FSP. The microstructural studies revealed that the stir zone composition and phase depend more on spindle speed and less on travel speed”[21]. Investigations on FSW Ti-6Al-4V composites were carried to study microstructure and hardness profiles in various zones. The hardness value in the Thermomechanical affected zone was found to be less. A new model has been proposed after studying the microstructure [22].

3. MECHANICAL PROPERTIES

In both FSW and FSP, the heat required for cladding is obtained by friction. The processes involve severe plastic deformation of the material. Thus, the mechanical properties alter when compared with base materials. It is essential to be familiar with the properties like hardness, static, and fracture properties of the welded materials or processed materials. Process parameters, residual stresses, and distortion will influence the mechanical properties to be achieved. Mechanical properties particularly hardness profiles across the joints are related to the microstructure. Changes in microstructure and mechanical properties are demonstrated by the hardness profiles.

FSW was used to join Al6082-T6 materials. The joint cross-section was observed to get the hardness profile. The average welding hardness of the samples was found to be lower than the base material hardness. The hardness value is less TMAZ RS [22-23]. The mechanical properties were inspected along the thickness direction of Al2019 aluminium compounds. The zone, which is closer to the welded surface, has a higher hardness when compared to middle and lower parts [24]. FSW was used to join Mg–Zn–Y–Zr alloys obtained by the rolling process of 6 mm thick to find the hardness of weld nugget. From the observation, the weld nugget hardness was found to be more than the base material [25]. The hardness was improved because of the abatement of rotating speed and fine grain size. The microstructural development and changes because of FSW/FSP not just alter the hardness profile and further affects other mechanical properties like strength and ductility.

FSP was used to join Al2024-T4 materials. The elasticity of the material was improved with increased rotational and travelling speeds [4]. Friction stir welding was performed on lap joints of Al2024-T3 to find affect due to changes in various process parameters [26]. It was accounted for from the tests that the elasticity was improved with various weld lines. An exploratory data on FSP of Aluminium, Copper, magnesium, and Titanium combinations were accounted for [27]. FSW of pure titanium initiated a crack in HAZ [28]. FSW was used to join Ti-5111 plates of thickness 12.7mm. An increase in yield strength and malleability was observed in the stir zone” [29]. From the reports, it was seen that an increase in tensile strength of an FSW joint (figure-4) at reliable traverse speed and an increase in rotational speed [30].

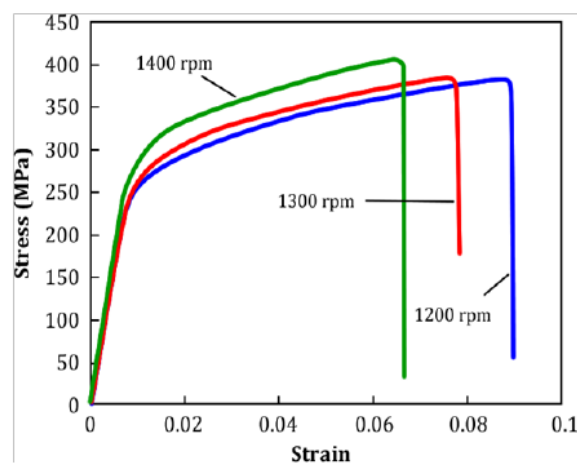


Figure-4: Stress-strain curve 7075 alloys indicating the increase in tensile strength due to increase in rotation speed [30].

Multi-pass- Friction stir process was utilized to fabricate roll bonded Al-B₄C composites. Microstructural changes, wear, and fracture behavioural studies were carried. The number of tool passes may influence the mechanical properties of materials. Improvement in homogeneity and microhardness of Al/B₄C composite material was found due to increase in number of tool passes [31]. Multi pass friction stir process was likewise used to join Mg–Al composite plates. Energy ray techniques such as Dispersive X ray analysis (EDX) can be used to study microstructure. Energy particle technique such as transmission electron microscopy (TEM) also used to study the microstructure. EDX and TEM was used to study FSW Mg/Al composite plates. The micro structural studies indicate the formation of transition zone without any effects at the boundary composite plates [32]. Processing parameters also influences mechanical properties during FSP. An increase in rotational speed and tool diameter improved the tensile properties of FSP processed AZ31B magnesium alloys [33]. Experiments were conducted to study the strain hardening capacity in various zones of FSW Aluminium alloy. The stir zone was with more strain hardening capacity than the other regions [34].

4. RESIDUAL STRESSES AND FATIGUE BEHAVIOUR:

The FSW process causes the distortion of a welded joint due to residual stresses generated. X-ray diffraction (XRD) was utilized to find the residual states in an FSW alloy 625 (UNS N06625). The results indicated that the process parameters have a distinct influence on residual stresses generated [35]. The residual stresses generated lead to the formation of the crack in the weld region. The stresses may further cause the change in the shape of the joint. The residual stress distribution in FSW AA2024-T4 aluminium alloys was investigated. It was found from the examination that the stresses are more with complex geometries than with simple butt welds [36].

The mechanical properties of the welds can be estimated by the stresses generated. An increase in ultimate tensile strength is observed by considering the compressive residual stresses [37]. The residual stresses in SZ and TMAZ contribute to the improvement of the mechanical properties of FSW joints [38]. The residual stresses also influence service life and the overall performance of FSW joints. The process parameters also influence the formation of residual stresses. The increase in traverse speed of FSW tool will increase the longitudinal stresses of FSW Al5083 [39]. The residual stresses in dissimilar FSW of 5754 aluminium alloy and C 11000 copper alloy were estimated on nine samples. It was observed from the experiments that the stresses estimated were compressive and increments with depth [40]. Fatigue characterization is also a significant factor for some. The fatigue behaviour of FSW welds is obtained by considering crack propagation.

Metal inert gas welding was used to join Al6061-T6 and Al6082-T6 alloys. FSW was also carried on the same materials. The Stress –number of cycle data is shown in figure-5(a) and figure-5(b). FSW specimens have higher fatigue life than MIG specimens [42].

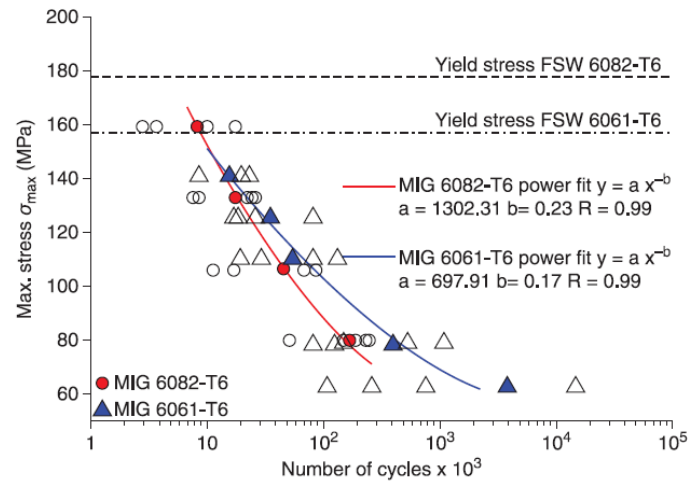


Figure-5 (a): Stress amplitude-No of cycles data (MIG welded specimens) [42]

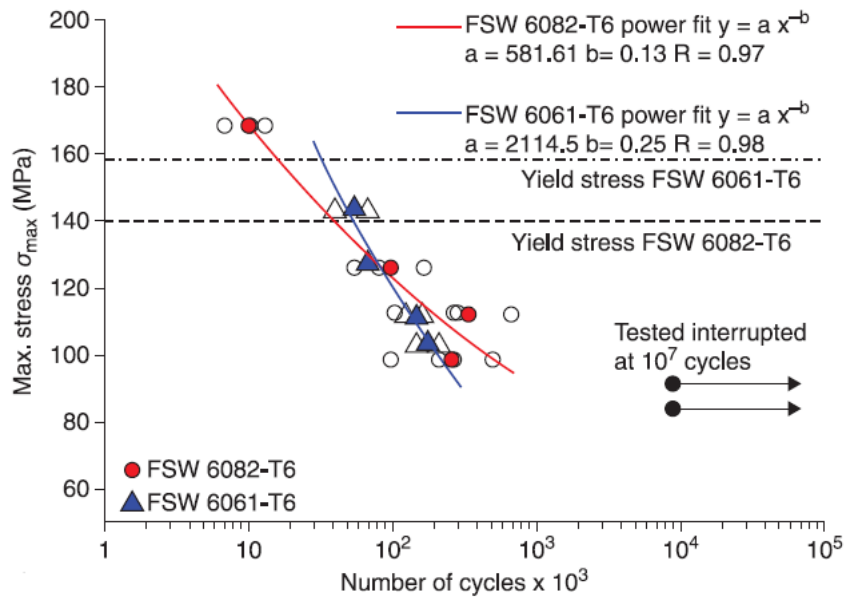


Figure-5 (b): Stress amplitude-No of cycles data (FSW specimens) [42]

5. CONCLUSIONS

Friction stir processing is best suitable for surface modification through the joining of Aluminium, copper, magnesium, titanium, and steel. The particle distribution on the surface of the materials is easy due to intensive plastic deformation. The suitability of FSW/FSP is reviewed for the development of the microstructure and mechanical properties. There is a critical improvement in properties such as grain refinement, strength, hardness, and Young's modulus of FSW/FSP materials. The influence of process parameters, residual stresses generated during FSP. The fatigue behaviour on mechanical properties is also reported. From the literature survey, it has ascertained the change in microstructure during FSW/FSP and improvement in mechanical properties when compared with other joining techniques and with base materials

REFERENCES

[1] Z.Y.Ma., Friction Stir Processing Technology: A Review., Metallurgical and Materials

Transactions A volume 39, (2008), pages 642–658

[2] Sudhakar.M., Srinivasa Rao.CH., and MeeraSaheb. K, Production of Surface Composites by Friction Stir Processing - A Review, *Materials Today: Proceedings* 5(2018), 929–935.

[3] R.S Mishra., Z.YMa.,ICharit., Friction stir processing: a novel technique for fabrication of surface composite, *Materials Science and Engineering: A*, Volume 341, Issues 1–2, (2003), Pages 307-310

[4] R.S. Mishra, and Z.Y. Ma, Friction stir welding and processing, *Materials Science and Engineering:R: Reports*, Issues 1-2, 50 (2005) 1–78

[5] Wen Wang et al, Friction Stir Processing of Magnesium Alloys: A Review, *Acta Metallurgica Sinica (English Letters)* (2020) 33:43–57

[6] V. P. Mahesh & Amit Arora, Effect of Tool Shoulder Diameter on the Surface Hardness of Aluminum-Molybdenum Surface Composites Developed by Single and Double Groove Friction Stir Processing, *Metallurgical and Materials Transactions A* volume 50, pages 5373–5383(2019)

[7] Lee, C.J.; Huang, J.C.; Hsieh, P.J.). "Mg-based nano-composites fabricated by friction stir processing". *Scripta Materialia*. (2006), 54 (7): 1415–1420.

[8] Farrokhi, H., Heidarzadeh, A. and Saeid, T, 'Friction stir welding of copper under different welding parameters and media ', *Science and Technology of Welding and Joining*, (2013) 18 (8): 697 – 702.

[9] Mironov, S., Sato, Y.S. and Kokawa, H. (2008), ' Microstructural evolution during friction stir processing of pure iron ', *Acta Materialia*, 56 (11): 2602 – 14.

[10] Thomas, W.M., Threadgill, P.L. and Nicholas, E.D., 'Feasibility of friction stir welding steel ', *Science and Technology of Welding and Joining*, (1999), 4 (6): 365 – 72.

[11] Park, S.H.C., Sato, Y.S., Kokawa, H., Okamoto, K., Hirano, S. and Inagaki, M., 'Rapid formation of the sigma phase in 304 stainless steel during friction stir welding ', *Scripta Materialia*, (2003), 49 (12): 1175 – 80.

[12] Khodaverdizadeh, H., Heidarzadeh, A. and Saeid, T., 'Effect of tool pin profile on microstructure and mechanical properties of friction stir welded pure copper joints ', *Materials and Design*, (2013), 45: 265 – 70.

[13] Heidarzadeh, A., Saeid, T., Khodaverdizadeh, H., Mahmoudi, A. and Nazari, E ' Establishing a mathematical model to predict the tensile strength of friction stir welded pure copper joints', *Metallurgical and Materials Transaction B*, (2013), 44 (1): 175 – 183

[14]. Park, H.S., Kimura, T., Murakami, T., Nagano, Y., Nakata, K. and Ushio, M. 'Microstructures and mechanical properties of friction stir welds of 60% Cu–40% Zn copper alloy ', *Materials Science and Engineering A*, (2004), 371 (1 – 2): 160 – 9.

[15] SarvghadMoghaddam, M., Parvizi, R., Haddad-Sabzevar, M. and Davoodi, A., 'Microstructural and mechanical properties of friction stir welded Cu-30Zn brass alloy at various feed speeds: Influence of stir bands ', *Materials and Design*, (2011), 32 (5): 2749 – 55.

[16] Sato, Y.S., Urata, M. and Wa, H. 'Parameters controlling microstructure and hardness during friction stir welding of precipitation-hardenable aluminum alloy 6063 ', (2002), *Metallurgical and Materials Transaction A*, 33A (3): 625 – 35

[17] Su, J.Q., Nelson, T.W., Mishra, R. and Mahoney, M., 'Microstructural investigation of

- friction stir welded 7050-T651 aluminium ', *ActaMaterialia*, (2003), 51 (3): 713 – 29.
- [18] Padmanaban, G. and Balasubramanian, V. 'An experimental investigation on friction stir welding of AZ31B magnesium alloy ', *International Journal of Advanced Manufacturing Technology*, (2010), 49 (1 – 4): 111 – 21.
- [19] Sudden, U.F.H.R., Mironov, S., Sato, Y.S., Kokawa, H. and Lee, C.W. ' Grain structure evolution during friction stir welding of AZ31 magnesium alloy ', *ActaMaterialia*, (2009), 57 (18): 5406 – 18
- [20] Asadi, P., Besharati-Givi, M.K. and Faraji, G., ' Producing ultrafine-grained AZ91 from as-cast AZ91 by FSP ', *Materials and Manufacturing Processes*, (2010), 25 (11): 1219 – 26.
- [21] John c. Lippold and Jason j. Livingston, microstructure evolution during friction stir processing and hot torsion simulation of Ti-6Al-4V, *metallurgical and materials transactions a*, volume 44a, 2013, 3815-3825
- [22] L.H.WuD.WangB.L.XiaoZ.Y.Ma, 'Microstructural evolution of the thermomechanically affected zone in a Ti-6Al-4V friction stir welded joint', *Scripta Materialia Volumes 78–79*, May 2014, Pages 17-20
- [23] Moreira, P.M.G.P., et al., Mechanical and metallurgical characterization of friction stir welding joints of AA6061-T6 with AA6082-T6 ', *Materials & Design*, (2009), 30(1): 180 – 7
- [24] Xu, W. et al. (2013), 'Influence of welding parameters and tool pin profile on microstructure and mechanical properties along with the thickness in a friction stir welded aluminum alloy', *Materials & Design*, 47 (0): 599 – 606.
- [25] Xie, G.M. et al. (2011), ' Effect of rotation rate on microstructures and mechanical properties of FSW Mg- Zn-Y-Zr alloy joints ', *Journal of Materials Science & Technology*, 27 (12): 1157 – 64.
- [26] Papadopoulos, M. et al. (2013), 'Mechanical behavior of AA 2024 friction stir overlap welds', *International Journal of Structural Integrity*, 4 (1): 8
- [27] Anna P. Zykova, 'A Review of Friction Stir Processing of Structural Metallic Materials: Process, Properties, and Methods', *Metals* 2020, 10(6), 772.
- [28] Lee, W.-B. et al. (2005), 'Microstructural investigation of friction stir welded pure titanium', *Materials Letters*, 59 (26): 3315 – 18.
- [29] 6. Nimer, S., Wolk, J. and Zupan, M. (2013), 'Local property characterization of friction stir welded Ti-5111: Transverse orientation measurements', *ActaMaterialia*, 61 (8): 3050 – 9.
- [30] SdBayazid et al., 'A review on friction stir welding, parameters, microstructure, mechanical properties, post-weld heat treatment and defects', *Material Science & Engineering International Journal*. 2018;2(4):116–126.
- [31] Moslem Paidar et al, 'Influence of multi-pass FSP on the microstructure, mechanical properties and tribological characterization of Al/B₄C composite fabricated by accumulative roll bonding (ARB)', *Surface and Coatings Technology*, Volume 361, 2019, 159-169
- [32] Zhimin Ding *et al* 'Microstructure of Mg solid solution layer during multi-pass FSP of Mg/Al Composite Plates' *Vacuum*, Volume 172, 2020, 109078, 1-6
- [33] S. Ramesh babu, et al., *Microstructural Changes and Mechanical Properties of Friction Stir Processed Extruded AZ31B Alloy*, *Procedia Engineering*, Volume 38, 2012, 2956-2966
- [34] Murshid Imam et al., Microstructural Characteristics and Mechanical Properties of Friction Stir Welded Thick 5083 Aluminum Alloy, *Metallurgical and Materials Transactions A*, volume 48, 208–229(2017)

- [35] Guilherme Vieira Braga Lemos et al., Residual stress characterization in friction stirwelds of alloy 625, journal of materials research technology, 2019, 8(3), 2528-2537
- [36] Fratini, L., Pasta, S. Residual stresses in friction stir welded parts of complex geometry. International Journal of Advanced Manufacturing Technology, 59, 547–557 (2012)
- [37] Jalal Fathi et al., 'Friction stir welding of aluminum 6061-T6 in presence of water cooling: Analyzing mechanical properties and residual stress distribution', International Journal of Lightweight Materials and Manufacture 2 (2019), 107-15
- [38] Y.S. Lim, S.H. Kim, K.J. Lee, Effect of residual stress on the mechanical properties of FSW joints with SUS409L, Advances in Materials Science and Engineering, (2018).
- [39] Peel, M. et al. (2003), 'Microstructure, mechanical properties and residual stresses as a function of welding speed in aluminium AA5083 friction stir welds', ActaMaterialia, 51(16): 4791 – 801.
- [40] ET Akinlabi, I Dinaharan and S Akinlabi, 'Characterization of residual stresses in dissimilar friction stir welded aluminum and copper', Indian journal of engineering and material sciences, v 24, 2017, 207-214.
- [41] Moreira, P.M.G.P., de Figueiredo, M.A.V. and de Castro, P.M.S.T. (2007), ' Fatigue behavior of FSW and MIG weldments for two aluminium alloys ', Theoretical and Applied Fracture Mechanics, 48 (2): 169 – 177
- [42] AbbasiGharacheh, M. et al. 'The influence of the ratio of "rotational speed/traverse speed" (ω /v) on mechanical properties of AZ31 friction stir welds ', International Journal of Machine Tools and Manufacture, (2006), 46 (15): 1983 – 7.

CERAMIC MATERIAL TOOLS – A Review

K. I. Vishnu Vandana¹, M. P. Krishna Sai², K. Navya Sri³

1-Assistant professor, Department of Mechanical Engineering, PVPSIT, Vijayawada.
2,3 – UG Students, Department of Mechanical Engineering, PVPSIT, Vijayawada.

ABSTRACT

Due to the improved intrinsic properties of ceramic materials, the usage of ceramic material tools for metal cutting is quickly growing. The paper reviews application different ceramic materials in modern manufacturing world mainly as a tool material. Researchers also compared the ceramic tools with commercially available tools and reported satisfactory results with ceramic tools. The present paper also reviewed the nature of the workpiece and the machine tool, among other parameters affecting the use of ceramic tools.

INTRODUCTION

To improve, stay and grow healthy in industrial sectors one should always follow the present trends on the production of materials. Hence ceramic cutting tools are the best technologies to utilize and get quick and quality outputs. The mechanical properties specially stiffness of result materials is being evolve and amplify. All customary types of machining procedure are similar to turning and milling and drilling based on stiffness of the cutting tools substance cut. As a result, the growth of cutting tools is critical for improving mechanical properties, particularly in high-speed, long-duration machining. Additionally, cutting tools material should be perfect to sustain during utmost cutting situations such as very rigid temperature, and friction between the cutting tool finishing and work piece surface.

MECHANICAL PROPERTIES:

- * At a higher temperature, stiffness is increased.
- * To minimize plastic distortion at the cutting edge, the material has a high deformation resistance.
- * Stiffness is important for accuracy when moving forwards.
- * To withstand a large mechanical stress, strong fatigue resistance is required.
- * Crack resistance is high.

THERMAL PROPERTIES:

- * To move the temperature away from the cutting edge, high thermal conductivity is used.
- * Extremely resistant to thermal stress.
- * Stable chemical composition.

TRIBOLOGICAL PROPERTIES:

- * The wear defiance.
- * Enough lubricity to prevent icing on the cutting surface.

Ceramic cutting tool materials, for particular, are developed for machining cast irons and super alloys, as well as enhanced surface finishing of difficult-to-cut materials.

The important points:

High power and energy are used when cutting material with a harsh tool, particularly for mild

machining.

Display a high sensitivity to collapsing and abrasive.

Capability of the cutting speed is high.

Because ceramics are drawn back due to less thermal conductivity, cutting tools have low toughness and resistance to mechanical and thermal shock in the early days of ceramics.

Later, with better speed machining, those defects became a bit more pronounced, and in order to minimize cycle time, a restricted average to depth of cut was used.

As illustrated below, ceramic cutting tools can be divided into four categories:

Ceramics composed with Al_2O_3 .

Ceramics based on Si_3N_4 .

Ceramics made with sialon.

Aluminum oxide (Al_2O_3) and silicon nitride (Si_3N_4) are the two main groups. The combination of flexible rigidity and increased toughness considerably increases resistance to abrasive and sticky ear. When compared to oxide ceramics, the bottom thermal elongation and upper thermal conductivity of composites boost thermal shock resistance and thermal shock cycling capacities.

Over the last two decades, significant progress has been made in improving the durability and stiffness of ceramic materials. Fracture-surface bridging, particle dispersion of distinct phases in a matrix, fiber reinforced composites, macroscopic crack deflection, and phase change driven toughening as indicated by zirconia are just a few of the promising ideas. Cutting tools made of Silicon nitride Si_3N_4 form ceramics, which are more advanced than Al_2O_3 type ceramics, were utilized for cutting in the 1980s.

when comparing numerous advantages and outcomes the flexural strength of silicon nitride ceramic cutting tools, for example, can range from 700 to 1100 MPa. Silicon nitride ceramic cutting tools are resistant to crack formation and have efficient or super thermal shock resistance, fracture toughness, and consistent cutting performance. silicon nitride is a kind of silicon nitride that is Si_3N_4 is divided into many types: reaction-bonded silicon nitride (Si_3N_4 RB), hot pressed silicon nitride (Si_3N_4 HIP), sintered reaction bonded Si_3N_4 , sintered Si_3N_4 , and $SiAlON$, all of which are grey in color. Si_3N_4 RB and HIP are Si_3N_4 alloys containing yttrium oxide, Al_2O_3 , and TiC , respectively. Several strategies are used to improve the cutting tool material's characteristics. Cryogenics is one of the procedures available.

Cryogenics is a frequently used approach for enhancing mechanical and physical characteristics of materials by decreasing the tool to a temperature of roughly $\hat{1}96^{\circ}C$ at a consistent pace, stabilizing it at that temperature for a period duration, around 24 hours, and then heating back to room temperature. Cooling slowly to a sub - zero temperature such as $\hat{1}45^{\circ}C$, $\hat{1}96^{\circ}C$, soaking for a set duration from 4 to 48 hours, heating leisurely to cellar temperature, tempering are the procedures to be completed.

The hardness parameter had a direct impact on the selection and manufacture of cutting tools; it has an impact on cutting conditions such as cutting speed, feed, and depth of cut, as explained in this study. Ceramics are indeed a type of material that has the ability to be used as cutting tools. Ceramics are extremely hard or strong, may increase hardness at higher temperatures, and have a low reactivity when compared to steel. As a result, ceramics may be used at any cutting speed without distortion or wear processes limiting tool life.

In further advanced ceramic materials contains a high-end technology that has a large broad base of current and potential application and a increasing file of material structures. So, the ground level and strong content of ceramic cutting tools are elaborated with in papers.

LITERATURE SURVEY

D H JACK et.al. (1986) [1] In short that ceramic cutting tools are strong and they keep their hardness at hot temperatures and function poorly as metals. They also said that ceramic tools may be utilised at high cutting speeds without distortion or disintegration, which affects the tool's life. Ceramics as a toolbox has the disadvantage of lack of durability and resilience to mechanical and thermal shocks. They're approaching the end of their market share index, which is less than 4%. As the number of mechanical instruments capable of harnessing the benefits of ceramic grows and the development of building materials increases, that number will definitely rise. However, due to the intrinsic qualities of the materials, they will never be able to completely replace carbide cemented as a cutting tool, but they complement it well.

G.Brandt et.al. (1987) [2] Described part of the area and structure of metal plants using optic & image and volume analysis. They found that the structure of the protective layers depends not only on the structure of the steel plants but also on the cutting tools and cutting conditions and concluded that the effect was probably due to the reaction between CaO (and SiO₂) and Al₂O₃ construction. Low soluble components of low durability soften the tool and accelerate aging. As a result, the procedures used to enhance the wear of cement carbide tools may differ from those used to improve the wear of ceramic cutting tools.

J. High Technology et.al.(1987)[3] evaluated the choice of tool materials depending on the operating environment of the machine and the system, as well as the machine tool utilised in the process, is prone to a variety of environmental consequences. After a significant duration of gradual growth, ceramics is now widely employed as a tool in metallurgical processes, and the goal of this research is to examine the fundamental reasons for this development.

J.Vigneau et.al. (1988)[4] Performed flexible tests and established relationships between mathematical distributions of the cutting time until the tool failed. During mechanical testing and bending tests, it has been established, the potential for significant microstructural defects in the specified volume of clay materials.

S.Lo Casto et.al. (1992)[5]Mechanical tests under continuous cutting circumstances, ceramic cutting tools are used. The test is carried out with AISI 1040 steel with a cutter speed of 5 to 11 metres per second. On both the crater and flank, the ageing process was studied. The wear resistance of zirconia alumina-toughened submicron particle size has been shown. Tic, TiN, and ZrO₂ * inclusions in alumina demonstrated somewhat lower ageing resistance than those listed above. Chemical instability appeared to be the cause of the failure of silicon carbide feathers alumina, silicon nitride, and tungsten carbide inserts, and the researchers found that of all the tools evaluated, contamination was the most relevant factor at high speed. Finally, due to the well-known duplication of its compounding phase, the silicon nitride insert had the most significant adverse effects.

Xingzhong Zhao et.al. (1996) [6] researched Austenitic stainless steel using Si₃N₄ ceramic as a tool. The ageing of the ceramic tool is mostly produced by adherence between the rubbing surfaces, according to experimental data, and wear rises with load and speed. When oils are used to lubricate something, it's called lubrication, coefficient such of collision of smooth

pears and the coating of ceramic coating is reduced. To diagnose ageing, researchers used electron microscopy scans, electron probe microanalysis, and X-ray dissection investigations. They also discovered that ceramic ageing in Si₃N₄ ceramic / stainless steel sliding contacts is mostly caused by the adhesion peeling process. Stainless steel transfers to the ceramic surface, and then the actions are chopped and pressed repeatedly until they are stripped down to the ceramic scraping surface.

Senthil Kumar et.al. (2003) [7] Studied a ceramic-based alumina cutting tool and was informed that it is one of the most attractive in the manufacture of steel, carbide tools are used to increase its durability. In this study, two types of ceramic cutting tools were used: Ti [C, N] alumina ceramic cutting tool combined with strong zirconia alumina ceramic cutting tool. Performance such of solid measurements of tool wear and tear have been used to analyse steel, cutting strength and finishing of the working surface. These ceramic-based alumina tools for cutting tools produce a good finish for solid metal performance concluding that in the usage of steel, the performance of ceramic cutting tools has been determined to be satisfactory. Surface polish is good with the Ti [C, N] alumina ceramic cutting tool.

K.U. Leuven et.al. (2006) [8] reviewed for the requirements of the equipment for cutting ceramics, taking into account industry tendency to greater dry cutting, as well as the necessity for advanced geometric tools The focus will be on materials and holes, with a special focus on the manufacturing of steel-based alloys. Results regarding the vertical couple test clearly show that the chemical stability of the stages in the couple's interaction test can be directly related to the worn behaviour and the actual cutting performance of the cutting tool material, under those mechanical conditions where chemical wear is a sign. The main method of wearing tools, that is, especially under dry and high-speed conditions

Altin et.al. (2006) [9] examined the as incinerators of Inconel 718 nickel-based super alloy equipment were tested experimentally, the effects of cutting speed on wearables and tool life were investigated. The majority of the time, the flank and notch are worn in a round form (RNGN). When using SNGN tools at low cutting speeds, little flank wear is evident, however when using RNGN tools at high cutting speeds, it is visible. It was determined that, based on the test findings, the maximum cutting speed is 250 m/min, and that cutting tool life is significantly affected above this speed. When compared to round type installations with slower cutting speeds, square type installations performed better.

Qiu like et.al. (2007) [10] investigate whether Ceramics cutting tools may be used to cut metal and preserve stiffness, strength, abrasion resistance, and a long working life even at high cutting speeds. Unusual earth additions can improve the mechanical qualities of cutting tools, such as durability, hardness, abrasion resistance, and fatigue resistance. They also came to the conclusion that the ceramics cutting tool is an essential area for usage in current architectural ceramics. Good hardness, high resistance to abrasion, and great machine utilization under extreme temps are all benefits.

Li Xikum et.al. (2007) [11] Si₃ N₄ included in, Si₃N₄- Tic composite, Si₃N₄- TiC- Co composite materials, Si₃ N₄-WC-Zr Oz composite materials, TiCN composite materials, and some important components were researched on improvement in production, supplementation, and methods on ceramic tools. In addition, improvements in organic compound manufacturing and gradients complexity of coated ceramics have been addressed. Applications had been devised on the fly. And it was found that CC tools had greater

hardness and resistance properties than standard high-speed steel and tough alloy cutting tools.

B.Q.Liu et.al.(2009)[12] To solve the problem of splitting the moustache and making fine cutting tools, With a technique of decreasing carbo thermally at a temp of 1250–1550 C, in-situ growing technology is employed to directly insert the TiC_xN_{1-x} molecules into the Al_2O_3 matrix. TiO_2 , carbon, nickel, and sodium chloride make up the components. For testing, several molar concentrations of TiO_2 : C were utilised, ranging from 1: 3, 1: 4, 1: 5, and 1: 7 TiO_2 : C. Only a few handlebar moustaches can be generated at a reaction temperature of 1550 C when the molar ratio is 1: 3. In certain molar measurements, a substantial quantity of moustache can be seen throughout the composite temperature, leading to the conclusion that most TiC_xN_{1-x} moustaches have a diameter of 1-3 μm and a powder line-aspect ratio of 10-30. The stoichiometric mass of TiO_2 to C 1: 4 and a caused a decrease temperature of 1250 C are ideal for TiC_xN_{1-x} beard growth.

Deng jianxin et.al. (2012) [13] High heat tri biological test in unlubricated circumstances was used to investigate the friction and wear behaviour of Al_2O_3/TiC Ceramics tool materials that were assessed in ambient air at a temperature of about 800 °C. The wear rates and friction coefficients are calculated. They discovered that the friction coefficient of Al_2O_3/TiC varies based on the test temperature, and that it also reduces as the temperature rises. Its major abrasive wear mechanism uses Al_2O_3/TiC ceramics at temperatures less than 400 °C.

Jonpeng song et.al. (2012) [14] The compounds were examined using a scanning electron microscopy (SEM), X-ray diffraction (XRD), and energy - dispersive x spectrometry (EDS) (EDS). TiB_2 and TiC were among the matrix's components. Between both the additives and the matrix, there are no complicated chemical interactions. Fine WC granules and comparable matrix grains made up the microstructure. Matrix character growth was prevented and the mechanical characteristics of the $TiB_2 - TiC$ combinations were enhanced when the suitable WC content was added. Between both the additives and the matrix, there are no complicated chemical interactions. Fine WC granules and comparable matrix grains made up the microstructure. Matrix letter development was prevented and the mechanical characteristics of the $TiB_2 - TiC$ composites were enhanced when the correct WC content was added.

Asit Behera et.al. (2013) [15] With the use of a pin just on disc machine, the wear behavior of three composite specimens created from constituting elements such as alumina oxide, titanium dioxide, and copper were described. The three specimen pellets are created using the powder metallurgy technique, which involves growing steadily the heating rate from 1000 to 7000 degrees Celsius at a pace of 300 degrees Celsius per minute.

Dow Whitney et.al. (2014) [16] The chapter is a form of ceramics product, a cutting tools tool, which is frequently referred to in the metals trade as "inserting." It is the most significant component of the overall cutting machine tool, despite its modest size (nearly limitless in comparison to the lathe size of a high-speed machine tool). This chapter discusses the many types of cutting tools and how to utilize them. But it's more than that; it's all about production. These sections were written with a specific sort of individual in mind, namely, someone who enjoys doing things. Let us not forget the ideals that have led to America's wealth; let me repeat the following reality: productive efficiency is critical for American economic progress.

Awadhesh Pal et.al. (2014) [17] Carried experimental investigations testing the performance of AISI 4340 solid steel for solid phase using mixed TiC aluminum alloy tools, hard rotation (55 HRC) and mild rotations (35 and 45 HRC) were achieved. Based on test findings, mathematical models that may forecast machine performance, such as microcontroller interface temperature, cutting strength, and surface stiffness, are established. Using the ANOVA technique, the influence of the harshness of the operating piece and cutting conditions, such as cutting speed, cutting depth, and feed, on different reactions was examined. Radial pressure is 15-20% more than solid force and around 102-112 percent greater than axial force, according to research. With increased feed value, facial rigidity has been seen to rise considerably.

Rainer Telle (2015) [18] compared among the structures of solid materials and concluded that, with the exception of Alumina, zirconium, silicon nitride, and silicon are the most suited materials for particular cutting and grinding processes, as opposed to diamonds and cubic boron nitride. They also discovered that new issues in the realm of materials have arisen as a result of recent advances, charaitemization and emphasized that the specificity of the quantity of small structures should be reconsidered in order to integrate grain boundary structures with the small structural defects. Analysis and evaluation methods should be developed that allow for faster obtaining data that allows for accurate predictions for vast sections of the structure. Further discussions about current solutions to such issues may be found in the steel industry's quality control systems, but pottery demands the highest level of surface refining of such operations.

W.K.Lee et.al. (2015) [19] Proposed about the insertion of workpiece profile signature to look for fractures in cutting tools. Dslr camera is used to capture workpiece profile pictures. Edge profiles are using a fixed intermediary approach, images were retrieved to sub-pixel precision. We also conclude that the occurrence of aging of ceramic-based alumina by cutting and fracturing was detected in the signature of the working piece profile using examination of the spectrum. Despite prior research that employed a transcript to get more data, the technique based on the notion of a narrow pixel edge region allows for faster and more precise extracting data.

Long li et.al. (2017) [20] Ceramic cutting edges have gotten increased attention as a result of their exceptional craftsmanship, according to the author. This research compares and contrasts the properties of two kinds of ceramic cutting tools: alumina and silicon nitride. We describe the existing circumstances for the production and the use of these two kinds of ceramic tools, and we outline the primary path for ceramic cutting tool development in the future, concluding that ceramics cutting edges are the most potential cutting material in the 20th century. Ceramic cutting tools boost production efficiency, reduce transaction cost, and make green processing more practical due to their advantages of high heating, excellent stability, chemical stability, strong oxidizing resistance, temperature resistance, and corrosion resistance.

A.A.Vereschaka et.al. (2017) [21] Developed a dampening mechanism that allows ceramic tools to be more reliable by reducing the high strain that happens during cutting. Using a C45-based hydraulic device, which seems less stiff than a mechanical product, results in a decrease and stabilization of high pressure in the machine region when cutting ceramic and carbide tools. It has been demonstrated that minimizing the possibilities of failure by

mitigating extreme pressures and vibrating processes caused by cutting with a ceramic tool and cutting heavy steel reinforcement is an excellent technique to increase the dependability of the ceramic tool.

Jiaao Wang et.al. (2017) [22] investigated that to study the impact of sliding speed and load bearing capacity on the coefficients of anti-aging, the tribological characteristics of ATG when slipping on a metal possessing GCr15 were investigated. The cutting efficiency of ATG equipment for the 40Cr steel machinery was also evaluated and compared to commercial tools. In addition, the tools' capacity to endure cracking and depth of cut enhanced with the inclusion of graphene platelets. The ATG ceramics tools put in the microwave had a maximum length that was 125 percent longer than high - temperature ceramic tools and 174 percent longer than cement carbide tools.

T Norfauzi et.al. (2019) [23] Studied about development of a cutting tool for with the introduction of chromic, zirconia hardened alumina (ZTA) is created. The powders of Aluminium (Al_2O_3), Zirconia (ZrO_2), and Chromia (Cr_2O_3) were treated in a ball mill, assembled in a Cold Isostatic Press (CIP), and submerged in water at a specific temperature of 1400C for 9 hours. The creation of ceramic materials including Al_2O_3 - ZrO_2 combined with Cr_2O_3 was completed, along with the selection of appropriate PEG bonding and CIP compression. Modern machines are mechanically tested using AISI 1045 to ensure that the cutting parameters and wear procedures are correct.

Daniel Finkeldei et.al. (2019) [24] Resistant to the aerospace, energy, and nuclear sectors, according to the statement. However, the machine is difficult to operate due to the high temperature compared with low thermally conductivity and high temperature. As a result, the quick climbing tools' wear is measured. Previous research has attempted to heat up a professional piece in the area to minimise material power and tool ageing. Nickel-based alloys, such as Inconel 718, are recognised for their appealing high-performance materials low machine weight, according to the study. The life of a tools is shortened while cutting such materials because of the excellent tensile pressure and strain, especially near the conclusion of the grinding operation. Low-cost removal materials are commonly used to monitor the condition of the equipment and the integrity of the workplace as a viable solution.

Da-wang Tan et.al. (2020) [25] Investigated that Silicon nitride (Si_3N_4) cutting-edge ceramic cutting tool has been successfully achieved through phase and microstructure control. Tool strength with 49.7% and 4.9 percent, - Si_3N_4 has a pressure of 20.1GPa and 17.5GPa, respectively. The Hardness values of tools ranges from 17.5 to 20.1GPa. The life lifetime of cutting tools Si_3N_4 rose from 1200 m to 2400 m in continual metal cutting, while the - Si_3N_4 concentration grew from 4.9 wt. percent to 49.7 wt. percent. The dressing techniques comprised abrasive coat, adhesion coating, and chemical coating, according to the results of the SEM examination.

Senol sirin et.al. (2021) [26] Studied about the nickel alloy X-750 it is a critical field working material. Which has higher previous mechanical and thermal structures and high-end attributes make it tough to use, especially when utilising carbide tool materials. As a result, ceramics cutting tools (CCTs) having superior endurance, heat and resistance to abrasion, and chemical bonding resistance are needed and materials are a good choice in the use of such materials and conclude that in the present case milling is used to create the nickel alloy X-

750. Tool that uses the Sialon Ceramic tool under several stable mechanical properties, namely, dry, MQL and hand mixed with Nano fluid-MQL at different performance parameters.

CONCLUSION

Major areas of research that have been presented in the previous sections inform that the ceramic materials as cutting tools have wide range of applications and abilities. Ceramic cutting tools increase manufacturing productivity while simultaneously lowering processing costs. Ceramic tool material are excellent for elevated machining and are also used extensively in the dry cutting of hardened steels.

REFERENCES:

- [1] P 0 Box 109, Torrington Avenue, Coventry, UK DH.Jack Sandvik Hard Materials Ltd experimental and theoretical investigation on Ceramic Cutting Tool Materials pp 267-273.1986.
- [2] The creation of protective layers during machining with ceramic cutting tools was studied by G. BRANDT and M. MIKUS. Pages. 99–112 in 1987.
- [3] Greensburg, Pennsylvania 15601, USA. Kennametal Inc., PO Box 369, Greensburg, Pennsylvania 15601, USA. Have looked into Ceramics Cutting Tools -A Review pp 113-127.1987.
- [4] Submitted by R. Geslot; S.N.E.C.M.A./France - J. Vigneau, P. Bordel; S.N.E.C.M.A./France. Worked for the Reliability of Ceramic Cutting Tools. pp 101-104.1988.
- [5] Wear mechanisms of ceramic tools were explored by S. Lo Caste, E. Lo Valvo and V. F. Ruisi, E. Lucchini and S. Maschio. pp 227-235.1992.
- [6] The Tribological features of Si₃N₄ ceramic sliding over stainless steel were studied by Xingzhong Zhao, Jiajun Liu U, Baoliang Zhu, Hezhuo Miao, and Zhenbi Luo. 1996.
- [7] Using alumina-based ceramic cutting tools, A. Senthil Kumar, A. Raja Durai, and T. Sornakumar examined the machinability of hardened steel. 2003, pp. 109-117.
- [8] K.U.Leuven, Worked on the fabrication, wear and performance of Ceramics cutting tools. pp 1776-1785.2006.
- [9] When cutting Inconel 718 using ceramics tools, A. Altin, M. Nalbant, and A. Taskesen explored the effects of cut and feed rate on tool life and tool life. 2007; pp. 2518-2522.
- [10] Study on Wear resistance Mechanisms of Ceramics Cutting Tools was conducted by Qiu Like, Li Xikun, Qiu Guanming, Ma Weimin, Sun Yanbin, and Yu Huadong. pp 309-316.2007.
- [11] Composition, Characteristics, and Development of Advanced Ceramic Cutting Tools were discussed by Li Xikun, Liu Jing, Qiu Like Cui Tong, Qiu Guanming, and Sun Yanbin. pp 287-295, 2007.
- [12] B.Q. Liu, C.Z. Huang, M.L. Gu, H.L. Liu, B.Q. Liu, C.Z. Huang, C.Z. Huang, C.Z. Huang, C.Z. Huang, C.Z. Huang. In situ growth of TiC_xN_{1-x} whisker in Al₂O₃ matrices for ceramic materials was worked on. pp 613-615.2009.
- [13] Deng Jianxin, Zhang Hui, Wu Ze, Lian Yunsong, Xing Youqiang, Li Shipeng, Unlubricated friction and wear behaviour of Al₂O₃/TiC ceramics cutting tool materials from

high temperature tribological testing. pp 17-26.2012.

[14] Microstructure and mechanical characteristics of TiB₂-TiC-WC composites ceramic tool materials were explored by Jinpeng Song, Chuanzhen Huang, Bin Zou, Hanlian Liu, and Jun Wang. pp 67-74.2012.

[15] Using a pin-on-disc wear machine, Asit Behera¹, S.C. Chaine, and Ajit Behera examined the tribological properties of Al₂O₃/TiO₂/Cu composites. pp 16672-16674.2013.

[16] Dow Whitney, a retired professor from the University of Florida's Department of Materials Science and Engineering in Gainesville, Florida, explored Ceramic Cutting Tools. pp 492-502.2014.

[17] Machinability Assessment by Experimental Research during Harder and Soft Turning of Reinforced Steel was worked on by Awadhesh Pala, S.K. Choudhury, and Satish chinchankar. pp 80-91.2014.

[18] The Rainer Telle Institut für Gesteinshuttenkunde der, RWTH Aachen, Aachen, Germany investigated Ceramic Properties. pp 1-49.2015.

[19] Recognition of breakage in cutting tools from work profile signatures using image processing and rapid Fourier transform, W.K. Leea, M.M. Ratnama, Z.A. Ahmadb. Pp 1-12.2015.

[20] Long Li and Yunfang Li, from the standpoint of mechanical processing, reported to develop and trend of cutting tools. pp 1-5.2017.

[21] A.A.Vereschaka, A.D. Batakob, A. A. Krapostin, N.N. Sitnikov, and G.V. Oganyan investigated the use of a damping system and micro multi-layered composite coatings to improve the dependability of ceramic cutting tools. pp 563-568.2017.

[22] Jiaao Wang, Yu Chenga, Yong Zhanga, Zengbin Yina, Xiao Hua, and Qin Yuana examined the friction and wear behaviour of microwave sintered Al₂O₃/TiC/GPLs ceramic sliding on bearing steel, as well as their cutting performance in hardened steel dry turning. pp 14827-14835.2017.

[23] Manufacturing and machining efficiency of ceramic cutting tools based on Al₂O₃-ZrO₂-Cr₂O₃ compositions were investigated by T Norfauzi, AB Hadzley, UAA Azlanb, AA Afuzaa, MM Faiz, and MF Naima. pp 1-10.2019.

[24] End machining of Inconel 718 utilizing hard Si₃N₄ ceramic tooling was explored by Daniel Finkeldei, Marcus Sexauer, and Friedrich Bleicher. pp 1131-1135.2019

[25] Da-Wang Tan, Lin-Lin Zhu#, Wan-Xin Wei, Jun-Jie Yu, Yu-Zhang Zhou, Wei-Ming Guo#, Hua-Tay Lin worked on modifying phase composition and microstructure to improve the performance of Si₃N₄ ceramic cutting tools. pp 1-36.2020

[26] Senol Sirin, Murat Sarkaya, Agr Vakkas Yldrm, Turgay Kvak investigated the machinability the nickel alloy X-750 using a SiAlON ceramic cutter under dry, MQL, and hBN mix nanofluid-MQL conditions. Pp 1-19.2021.

Application of Artificial Neural Networks and Genetic Algorithm for Optimization of Process Parameters in Pocket Milling of AA7075

M. Rajyalakshmi^{1,2*} Dr. M. Venkateswara Rao³

¹, Acharya Nagarjuna University, Andhra Pradesh, *j.rajyalakshmi@gmail.com

² Department of Mechanical Engineering, PVP Siddhartha Institute of Technology,
Vijayawada, Andhra Pradesh

³ Professor, Department of Mechanical Engineering, Bapatla Engineering College, Bapatla,
Andhra Pradesh

*j.rajyalakshmi@gmail.com, #9440387264

ABSTRACT: Mould preparation is the important phase in the plastic industry for the injection moulding process. The surface roughness of the mould affects the surface finish of the final plastic product. Quality product with better production rate is required to meet the competition in the present market. To achieve this objective, manufacturers try to select the best combination of parameters. Multi-objective optimization is one such technique to obtain the optimal process parameters that give better quality with a good production rate. The current paper describes the application of Multi-Objective Genetic Algorithms (MOGA) on the Artificial Neural Network (ANN) model for pocket milling on AA7075. Through the application of ANN with MOGA minimum surface roughness (SR) is achieved with better Material Removal Rate (MRR). From the confirmation experiments, it is evident that Follow Periphery tool path gives a better Surface finish with higher MRR and the percentage error observed is 1.9553 and 1.8282 respectively.

Key Words: Aluminium, ANN, Optimization, Pocket Milling, RSM, Tool Trajectory

1. INTRODUCTION

Pocket milling is the process used in mould preparation in the plastic industry. Plastic product is accepted when the surface quality of the product is fine. Surface quality is dependent on the surface roughness of the mould used for injection moulding. To generate the mould pockets different tool trajectories are used, which are broadly classified as linear and non-linear tool paths [1]. Selection of tool path along with optimal process parameters leads to efficient performance in mould preparation with minimum surface roughness[2]. Though several machining parameters influence the machining conditions, Spindle speed, table feed, Depth of cut influence the surface integrity of the workpiece[3]. The path followed by the tool while generating the pocket profiles affects the surface roughness [4]. In addition to these parameters, proper selection of stepover and tool path strategy selected to generate pockets also influences the surface roughness[5].

Many researchers tried to optimize the process parameters for better surface quality and MRR. With the application of Response surface methodology (RSM) Alauddin et. al.,[6] developed a model to predict surface roughness. From the study, they have identified Feed as the dominating factor for surface roughness.

Routara et al.,[7] studied the influence of tool trajectories on surface roughness by modelling with RSM. They have identified that the selection of a proper tool path affects the surface

roughness. Michel Bouard, et al.[8] developed a toolpath computation method with a Uniform Cubic B-spline curve. A constraint-based optimization algorithm is applied to the model to generate the pocket with a minimum. Rajyalakshmi and Suresh babu [9] applied response surface methodology to find the optimal combination of machining parameters to minimize surface roughness in Al7075 alloy. Several researchers applied modern and Evolutionary algorithms to optimize machining parameters to get minimum surface roughness[10]–[17].By the application of ANN on experimental values, Zubaidi et al.[18]identified that Modeling with ANN gives better results compared to traditional algorithms. On the experimental data obtained with three types of tools, Zain et al [19]used the ANN model to predict surface roughness. By changing the combinations of hidden layers they have optimized the machining parameters to get minimum surface roughness. Ghosh et al.,[20] modelled surface roughness with ANN and RSM to optimize the machining parameters. They have also applied the Particle Swarm Optimization (PSO) Technique on regression equations obtained with RSM. They have identified a good agreement between the experimental and predicted values of SR through confirmation experiments. Venkatesh and Suresh Kumar [21] modelled and optimized the cutting conditions to get minimum surface roughness using ANN and simulated annealing(SA). Comparing the predicted values from RSM with that of experimental, they have identified that ANN is well suited for modelling and optimization of the parameters.

Multiple Response optimization is one of the emerging techniques in the field of manufacturing to select optimized parameters to reduce machining cost and machining time. Gök et al.,[22]studied the effect of tool path on acceleration in addition to the machining variables through experimentation and identified that tool path affects the surface roughness and cutting forces. Through MOGA Gjelij et al.,[23]optimized the machining parameters in end applied multi-objective GA (MOGA) to optimize the cutting parameters. Their experimental studies revealed that values of parameters obtained through MOGA were within the limits of confirmation test results. Yanis et al.,[24] applied RSM and ANN to optimize the machining parameters inside milling with eco-friendly coolant. From the experimental results, they have concluded that ANN model prediction is in good agreement with the confirmation test results. Usha and Rao[25] used multi-response optimization using GA to optimize the machining parameters in turning. From the experimental studies, they have identified that MOGA gives better results for the responses that are to be optimized.

From the above studies, it was observed that most of the studies were on single response optimization. Very little work was reported on Pocket milling with stepover as one of the influencing factors. The influence of tool trajectories on the responses can also be considered for the study. ANN is proved to be one of the efficient tools for optimizing the process parameters. ANN coupled with GA can be effectively used for multi-response optimization. Hence, In the present work, it is planned to optimize the process parameters with the tool trajectories, FollowPeriphery (FP)and Zigzag (ZZ), by applying ANN and MOGA on the experimental data while generating pockets.

2. MATERIAL AND METHODOLOGY

2.1Material:

AA7075 is an Aluminium alloy with Zinc and magnesium as primary constituents. Due to its advantages like fatigue strength, corrosion resistance etc., it is commonly used in marine, aircraft building, automotive and plastic industries. The composition of the selected material is given in Table 3. AA7075 with a specimen size of 80mm x70mm with a depth of 10mm is used for the current study.

Table 1: Chemical composition of Al7075

Element	Al	Zn	Mg	Cu	Si	Others
% Composition by wt.	89.264	5.745	2.623	1.623	0.215	Remaining

2.2 Experimental Method:

Design of Experiments (DOE) is a statistical process to identify the number of experimental runs with low cost for larger and more realistic design problems. Response Surface Methodology (RSM) is one such method to reduce the number of experimental runs to get more data based on the number of factors and levels. In RSM Central Composite Design (CCD) and Box-Behnken (BB) design are two available models for deciding the number of experimental runs. It was identified that Box -Behnken design is more economical when the experimentation has three factors and three levels.

Box-Behnken model gives reliable results and independent quadratic equations to estimate coefficients[26]. However, they don't show runs from a factorial experiment. In the BB model factors have 3 levels and experimental runs at extreme levels of the factors that are either lower or higher levels are not included. The combinations of these parameters are at the midpoints of the process space and the centre. Each factor must have three levels to generate the design combinations. The designs have limited capability for orthogonal blocking compared to the central composite designs.

The experimental data is subjected to ANN modelling. Second-order regression equations are obtained using the modelled data. Multi-objective Genetic algorithms are applied to these regression equations using the MAT lab optimization toolbox. The flow chart shown in figure 1 indicates the procedure followed for multi-objective optimization. ANOVA is also applied to ANN results to know the most influencing factor for the responses in both the tool paths.

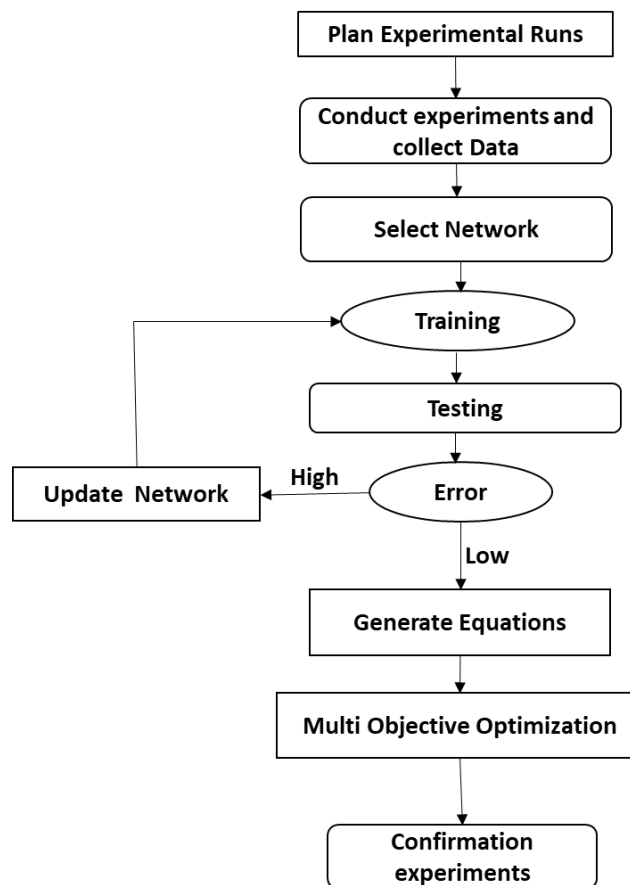


Figure1. Flow chart of the present work Procedural Map

3. Simulation and Experimental procedure

3.1 Simulation:

The pocket profile is modelled and simulated with Nx software. Selected tool path strategies were applied to generate the pocket in simulation as shown in Figure 2. For each tool trajectory and the combination of parameters, NC programs were generated.

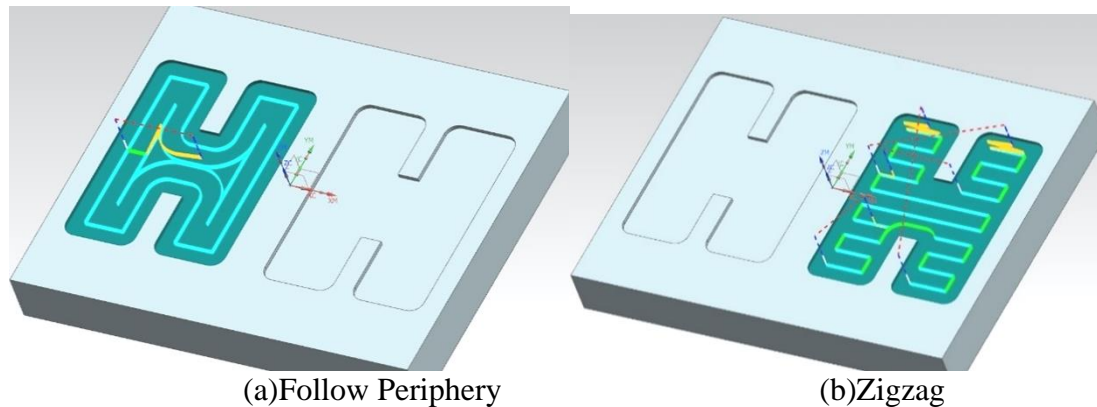


Figure 2: Tool trajectory for Pocketing

4.2 Experimental factors:

For the current study, Spindle Speed (S) (RPM), Feed (F) (mm/min) and step-over (SO) (%) were selected. Three levels are defined by L1, L2 and L3 for each factor as shown in table 2. Levels of the parameters are identified based on the production data book and sample experiments. Surface Roughness (SR) and Material Removal Rate (MRR) are considered as quality parameters. Controllable factor levels and codes are shown in the following table 2.

Table 2: Assignment of Levels to Factors

Input Factors	Units	L1	L2	L3	Output Response
S	RPM	3000	4000	5000	SR(μm) MRR (g/s)
F	mm/min	500	1000	1500	
SO	%	20	40	60	
Level Code		-1	0	1	

As Box-Behnken design of RSM gives economical runs for three factors with three levels, the number of experiments with run order in a coded manner is generated with that DOE using Design Expert as shown in Table 3.

Table 3: Order of Experimental Run

Run Order	Std. Order	Speed	Feed	SO
1	8	1	0	1
2	7	-1	0	1
3	5	-1	0	-1
4	2	1	-1	0
5	9	0	-1	-1
6	3	-1	1	0
7	1	-1	-1	0
8	13	0	0	0
9	6	1	0	-1
10	11	0	-1	1
11	10	0	1	-1

12	12	0	1	1
13	15	0	0	0
14	4	1	1	0
15	14	0	0	0

4.3 Experimental set-up:

Pocket milling operations were carried out on a Vertical Machining Center (AMC MCV-350 model) with a Fanuc series controller. A tungsten carbide coated tool with four flutes and six mm diameter is used to generate pockets on the given specimen. The experiments were conducted as per the run order generated by the Design Expert 11.0 software for Response Surface Methodology. Mitutoyo Surftest SJ-210 is used to measure surface roughness. The sample cut off length is set to 2.5mm. An average of five sample lengths is considered as a mean surface roughness (Ra). The weights of the workpiece before machining and after machining were measured using a precision balance with 0.01gm least count. Material Removal Rate (MRR) is calculated using equation 1:

$$MRR = \frac{W_i - W_f}{t} \text{ g/sec} \text{-----(1)}$$

Where, W_i, W_f are the weights of the workpiece before and after machining. 't' is the machining time taken to complete the given profile.

5. RESULTS AND DISCUSSION:

Experimentation was done as stated in the former discussion. After completion of each of the experiments, the surface roughness is measured and tabulated. The workpiece is weighed before and after machining. The absolute difference between the weights is calculated and divided by machining time, noted at the time of the corresponding experiment, to calculate MRR. The same procedure is followed for the two tool paths. The experimental values of both the responses for the two selected tool paths are shown in table 4.

Table 4: Experimental SR and MRR values for two tool Trajectories

Run	FP		ZZ	
	SR	MRR	SR	MRR
1	1.266	0.04175	1.251	0.05221
2	1.088	0.07615	1.032	0.08279
3	1.528	0.0998	0.9383	0.09843
4	1.155	0.05566	0.95	0.06327
5	1.112	0.23524	1.137	0.1354
6	1.425	0.10667	1.522	0.11467
7	0.934	0.06238	1.229	0.06936
8	0.792	0.15563	1.361	0.08651
9	1.421	0.10688	1.506	0.11467
10	0.79	0.03984	0.834	0.05039
11	1.384	0.10936	1.5	0.11881
12	1.322	0.22818	0.98	0.09635
13	1.276	0.02434	0.91	0.04435
14	0.938	0.0998	1.033	0.044225
15	1.103	0.0835	0.767	0.05584

5.1 Modeling with ANN:

Nowadays ANN is gaining more attention in the field of modelling and optimization due to its efficiency in improving the results. ANN model contains artificial neurons connected from the input node to the output node with several hidden layers. The output is obtained as a nonlinear function of inputs, by assigning weights to each node and edge. The weights associated with neurons can be modified regarding training data sets. After completion of training, the model generates the output for the unknown inputs. ANN models can also be used for specific applications having multiple factors. The feed-forward and feedback networks are commonly used in ANN architecture [27]. Feedforward neural networks are those in which signal moves only in one way i.e., input to output. In the case of Feedback, network signals can travel in both directions and forms cycles in acyclic graphs.

The experimental data obtained from the FP tool trajectory is normalized to get an efficient network model as the responses are with conflicting objectives. The trial and error method is used to select the best-suited model in ANN. Minimum Mean Square Error (MSE) is one of the indications of a good model in ANN. By applying the Levenberg-Marquardt algorithm to train the data, a better ANN model is achieved with the given data set. Three inputs are given to the network while two outputs are obtained after training. A sample ANN model developed with 6 neurons in the hidden layer is shown in figure 4.

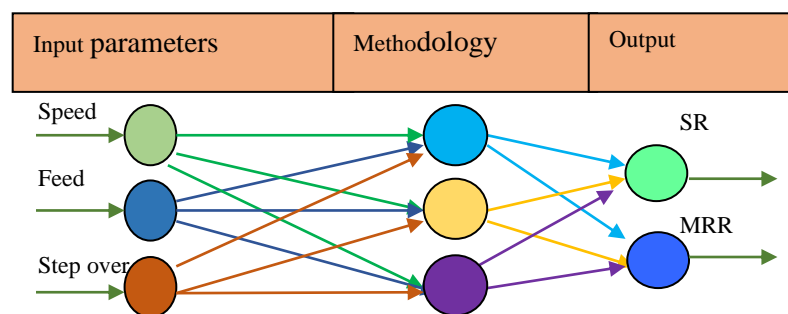


Figure 3: ANN model with 3 input and 2 output

The number of neurons required in the hidden layer for proper training of the network is decided depending on the MSE. Trial and error training is done with 5, 6 and 7 neurons in the hidden layer. From the performance graphs shown in figure 5, it is evident that model 6 neurons in the hidden layer have low Mean square error. The Mean Square Error (MSE) value for 5, 6 and 7 neurons is also given as 0.050997, 0.00027661 and 0.0073642 respectively. Hence the model with 6 neurons in the hidden layer is selected for training the data set.

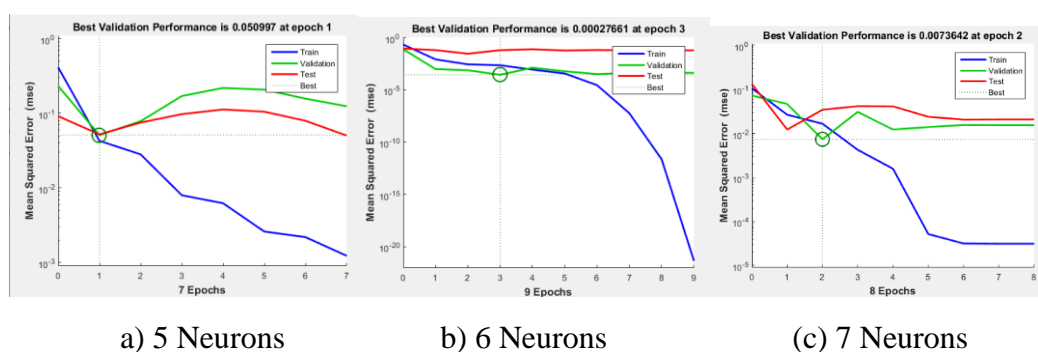
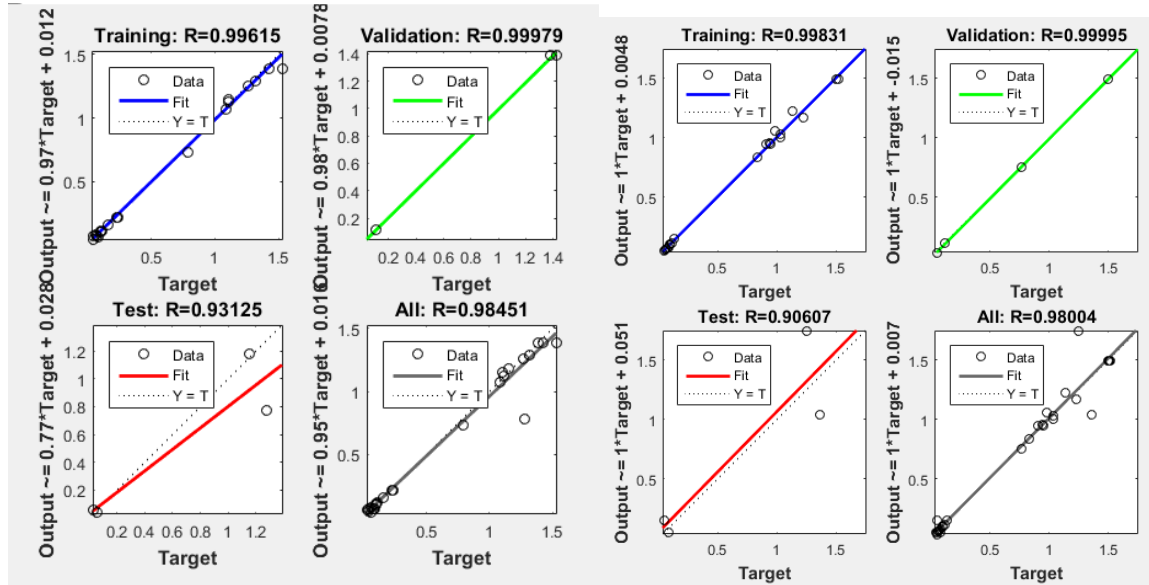


Figure 5: Performance graphs of ANN model with 5, 6, and 7 neurons in the hidden layer.

Experimental data given to the ANN tool is classified as 80% training, 10% Testing and 10% Validation. With higher training data, the model can be efficiently tested and validated [28].

Figure 6 shows the overall R-value of the 6 neurons for FP and ZZ tool trajectories with 80% training data.



(a) FP Tool Trajectory

(b) ZZ Tool Trajectory

Figure6: Overall R values with 10% validation for FP and ZZ tool trajectories.

From Figure 6, It is evident that the overall R-value for 10% validation and testing data is higher (0.98451) when compared to 15% and 20% validation and testing data. This may be due to the availability of more training data (80%) from the data set for proper training of the model. Hence, The ANN model with 6 neurons in the hidden layer with 80% training, 10% validation and 10% testing data set is considered optimal.

ANN modelling is also applied for the experimental data obtained from the zigzag tool path strategy and the ANN results obtained for the two responses in both tool trajectories is shown in table6

Table 6: Experimental Vs prediction through ANN for SR and MRR for two tool paths

Run	ANN Model				Error Percentage			
	FP		ZZ		FP		ZZ	
	SR	MRR	SR	MRR	SR	MRR	SR	MRR
1	1.28371	0.04216	1.24919	0.05281	x	0.982	0.1447	1.1492
2	1.06005	0.07438	1.03166	0.07931	2.5689	2.3244	0.0329	4.2034
3	1.53173	0.10414	0.95837	0.09352	0.2441	4.3487	2.139	4.9883
4	1.19945	0.05703	0.94802	0.06186	3.8485	2.4614	0.2084	2.2285
5	1.13173	0.22674	1.12221	0.13020	1.7743	3.6133	1.3008	3.8405
6	1.41734	0.10757	1.49343	0.11324	0.5375	0.8437	1.8771	1.2471
7	0.93474	0.06469	1.16857	0.06943	0.0792	3.7031	4.917	0.1009
8	0.81537	0.16156	1.30419	0.08487	2.9508	3.8103	4.1741	1.8957
9	1.41734	0.10757	1.49343	0.11324	0.2576	0.6456	0.8347	1.2471
10	0.81566	0.03945	0.83280	0.05151	3.2481	0.9789	0.1439	2.2227
11	1.41734	0.10757	1.49343	0.11324	2.409	1.6368	0.438	4.6882

12	1.36166	0.22053	1.00621	0.10108	3	3.3526	2.6745	4.9092
13	1.21328	0.02461	0.94558	0.04626	4.9154	1.1093	3.9099	4.3067
14	0.97652	0.09976	1.00299	0.04519	4.1066	0.0401	2.9051	2.182
15	1.10604	0.08397	0.75546	0.05338	0.2756	0.5629	1.5046	4.4054
Average Percentage Error					2.10763	2.0275	1.81365	2.90766

An empirical relation is generated with the obtained results, for both the responses with design expert 12. From the ANOVA results of ANN models, it is identified that Speed is the influencing factor for SR and Feed is the influencing factor for MRR in both the tool paths.

5.2 Multi Objective Optimization:

From The previous studies, it is observed that Genetic Algorithms (GA) is one of the best optimization techniques suitable for multi-objective optimization[29]. The principle of GA is based on the survival of the fittest through natural selection. The solutions that satisfy a specific criterion for the objective function is carried to the next generation. otherwise, the solution is rejected. This can be achieved through the genetic operators called ‘Reproduction’, Cross over’ and ‘Mutation’. The initial population is selected from the population and it is subjected to the genetic operators after calculating the fitness function. Several generations are evaluated through the genetic operators and fitness function converging towards the optimal solution. The solution search is terminated when the solution set doesn’t get any improvement in the value. Multi-objective optimization using GA is applied through the MATLAB toolbox. The Genetic operators selected for multi-objective optimization for both the tool paths are shown in table 7.

Table 7: GA parameter settings

GA Parameter	Set Value
Population Size	100
Cross over probability	0.8
Mutation probability	0.1
Number of Generations	200

5.3 Optimization with ANN Model:

Second-order response equations generated from the predicted values of the ANN model are used for multi-objective optimization as stated below.

For Follow periphery tool path:

$$\text{Minimize } f_1 = 1.42 + 0.146S - 0.0324F - 0.013SO - 0.1316SF + 0.1481SSO + 0.1348FSO - 0.0608S^2 - 0.1157F^2 - 0.2708SO^2$$

Minimize $f_2 = -$

$$(0.1076 + 0.0133S + 0.02643F + 0.0567SO + 0.00547SF + 0.01714SSO + 0.03613FSO - 0.00965S^2 - 0.03902F^2 - 0.03719SO^2)$$

For Zigzag tool path:

$$\text{Minimize } f_1 = 1.493 + 0.00896S - 0.00798F + 0.1085SO - 0.1285SF - 0.1436SSO + 0.0586FSO - 0.18256S^2 - 0.2304F^2 - 0.2865SO^2$$

$$\text{Minimize } f_2 = -(0.11324 + 0.0091S + 0.0173F + 0.0144SO + 0.00438SF - 0.00243SSO + 0.023841FSO - 0.02013S^2 - 0.0276F^2 - 0.01344SO^2)$$

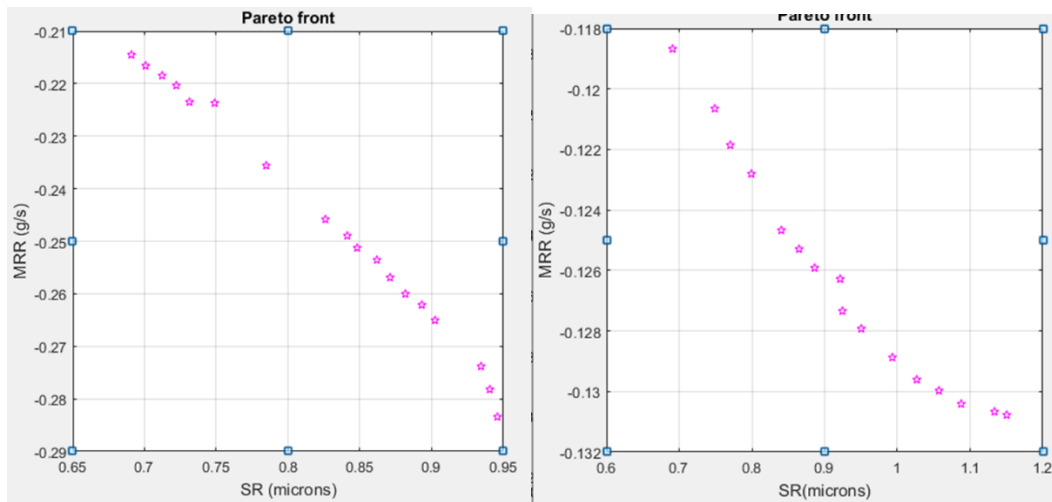
Where f1, f2 are the surface roughness and MRR respectively. Lower and upper boundaries of the parameters are considered as [-1,1] for the three input parameters Speed, Feed and Stepper

The range of parameters is similar to the regression model. The Pareto results obtained for the ANN model is as shown in table 8.

Table 8: Pareto Results of SR and MRR values for two tool Trajectories

Run	Follow periphery		Zigzag	
	SR	MRR	SR	MRR
1	0.74861	0.22375	0.69055	0.11868
2	0.94562	0.28338	1.14975	0.13079
3	0.94036	0.27816	1.14975	0.13079
4	0.71194	0.21843	1.13357	0.13068
5	0.84839	0.25134	0.76982	0.12185
6	0.86182	0.25353	0.94968	0.12793
7	0.90198	0.26505	0.69055	0.11868
8	0.82603	0.24579	0.99353	0.12886
9	0.69057	0.21457	0.79946	0.12281
10	0.72181	0.22039	1.08767	0.13042
11	0.84135	0.24901	1.05747	0.12999
12	0.88175	0.26011	0.84012	0.12466
13	0.70058	0.21666	0.92068	0.12629
14	0.73159	0.22357	0.92446	0.12733
15	0.89296	0.26214	0.86460	0.12528

The Pareto results obtained from MOGA are shown in figure 7. for both the tool paths.



(a) Follow periphery (b) Zigzag
Figure 7: Pareto results for ANN model Equations

The coded values are decoded, and confirmation experiments are conducted for randomly selected Pareto results. The confirmation test results are shown in Table 9.

Table 9: Experimental Vs prediction through ANN for SR and MRR for two tool paths

Run	Pareto Values				Confirmation Test Results				% Error			
	Follow periphery		Zigzag		Follow periphery		Zigzag		Follow periphery		Zigzag	
	SR	MRR	SR	MRR	SR	MRR	SR	MRR	SR	MRR	SR	MRR
1	0.7486 1	0.22375	0.94968	0.12792	0.72037	0.22974	0.97204	0.12297	3.7723	2.6797	2.3537	3.8687
2	0.7119 4	0.21843	0.99353	0.12886	0.72972	0.22064	0.97297	0.12296	2.4974	1.0129	2.0694	4.5731
3	0.7218 1	0.22039	0.92068	0.12629	0.72910	0.22539	0.95709	0.12254	1.0101	2.2723	3.9543	2.9688
4	0.7315 9	0.22357	0.92446	0.12733	0.72763	0.22055	0.95727	0.12206	0.5413	1.3478	3.5496	4.1452
									1.9553	1.8282	2.9817	3.8889

The percentage error observed is as shown in figure 8.

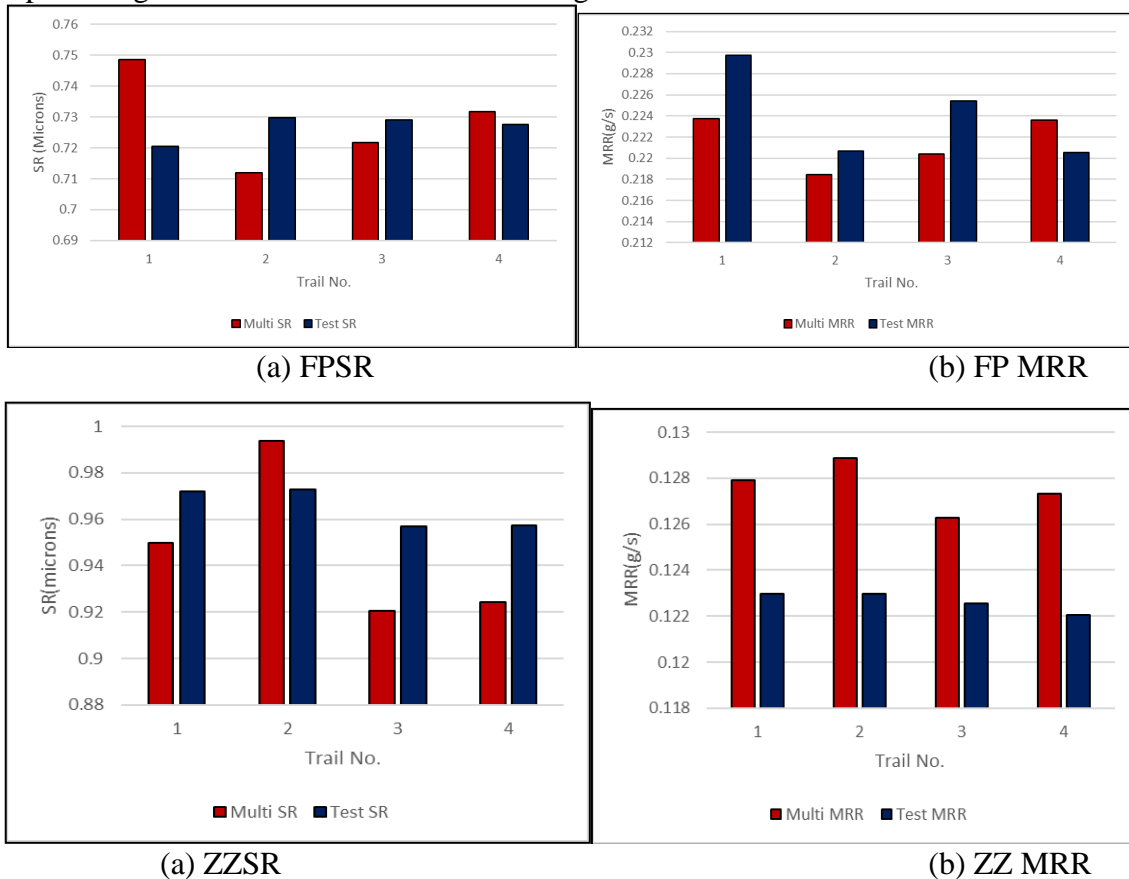


Figure 8: Comparison of Confirmation test and optimum predicted values for ANN Model with Multi-objective GA

From the confirmation test results, it is observed that the average percentage error for SR and MRR is 1.9553% and 1.8282% respectively for the following periphery and that of Zigzag tool trajectory is 2.9817% and 3.8889% respectively.

Conclusions

In the current work, Response Surface Methodology combined with ANN and multi-objective optimization is applied in pocket milling of AA7075 using two tool path strategies to find the best combination of parameters and the tool path. From the studies, the following observations are made:

1. Though speed for SR and feed for MRR are observed as influencing factors from ANOVA for individual responses, Step over is identified as the most influencing factor for both the responses when considered multi-objective optimization.

2. The R^2 values of the generated models are given as 0.9597, 0.9641, 0.874, 0.9437 indicates the effective relationship between the input and output parameters in the ANN model.

3. Multi-response optimization values achieved through GA for SR and MRR for both the tool path strategies are validated with confirmation experiments.

4. The average error observed for Follow periphery SR and MRR for the ANN model and confirmation experiments shows that the predicted values are in good agreement with the confirmation results when compared with that of ZZ values.

5. From the analysis, it is observed that better surface roughness and material removal rate are observed in follow periphery, Hence, FP tool trajectory is suggested for AA7075 material to reduce the production cost.

The multi-objective GA combined with ANN gives a global solution for the given problem. To reduce the production time thus reduce the production cost, optimization of process parameters gives good results along with the good quality of production.

References:

- [1] T. R. Kramer, "Pocket Milling with Tool Engagement Detection," *J. Manuf. Syst.*, vol. 11, no. 2, pp. 112–123, 1992.
- [2] P. G. Benardos and G. C. Vosniakos, "Predicting surface roughness in machining: A review," *Int. J. Mach. Tools Manuf.*, vol. 43, no. 8, pp. 833–844, 2003.
- [3] N. Agarwal, "Surface Roughness Modeling with Machining Parameters (Speed , Feed & Depth of Cut) in CNC Milling," *Mech. Eng.*, vol. 2, no. 1, pp. 55–61, 2012.
- [4] C. K. Toh, "A study of the effects of cutter path strategies and orientations in milling," *J. Mater. Process. Technol.*, vol. 152, no. 3, pp. 346–356, 2004.
- [5] C. Gologlu and N. Sakarya, "The effects of cutter path strategies on surface roughness of pocket milling of 1.2738 steel based on Taguchi method," *J. Mater. Process. Technol.*, vol. 206, no. 1–3, pp. 7–15, 2008.
- [6] M. Alauddin, M. A. El Baradie, and M. S. J. Hashmi, "Computer-aided analysis of a surface-roughness model for end milling," *J. Mater. Process. Technol.*, vol. 55, no. 2, pp. 123–127, Nov. 1995.
- [7] B. C. Routara, A. Bandyopadhyay, and P. Sahoo, "Roughness modeling and optimization in CNC end milling using response surface method: Effect of workpiece material variation," *Int. J. Adv. Manuf. Technol.*, vol. 40, no. 11–12, pp. 1166–1180, 2009.
- [8] M. Bouard, V. Pateloup, and P. Armand, "Pocketing toolpath computation using an optimization method," *CAD Comput. Aided Des.*, vol. 43, no. 9, pp. 1099–1109, 2011.
- [9] P. S. B. Rajyalakshmi, M. "OPTIMIZATION OF PROCESS PARAMETERS FOR POCKET MILLING OF AL7075 USING RESPONSE SURFACE METHODOLOGY," *Int. J. Mech. Prod. Eng. Res. Dev. IJMPERD*), vol. 9, no. 4, pp. 649–658, 2019.
- [10] T. P. Mahesh and R. Rajesh, "Optimal Selection of Process Parameters in CNC End Milling of Al 7075-T6 Aluminium Alloy Using a Taguchi-fuzzy Approach," *Procedia Mater. Sci.*, vol. 5, pp. 2493–2502, 2014.
- [11] S. Rawangwong, J. Chatthong, W. Boonchouytan, and R. Burapa, "An investigation of optimum cutting conditions in face milling aluminum semi solid 2024 using carbide tool," *Energy Procedia*, vol. 34, pp. 854–862, 2013.
- [12] U. Mohammed Iqbal, V. S. Senthil Kumar, and S. Gopalakannan, "Application of Response Surface Methodology in optimizing the process parameters of Twist Extrusion process for AA6061-T6 aluminum alloy," *Meas. J. Int. Meas. Confed.*, vol. 94, pp. 126–138, 2016.

- [13] F. Dweiri, M. Al-Jarrah, and H. Al-Wedyan, “Fuzzy surface roughness modeling of CNC down milling of Almic-79,” *J. Mater. Process. Technol.*, vol. 133, no. 3, pp. 266–275, 2003.
- [14] H. Perez, E. Diez, J. Perez, and A. Vizan, “Analysis of machining strategies for peripheral milling,” *Procedia Eng.*, vol. 63, pp. 573–581, 2013.
- [15] M. S. Sukumar, P. Venkata Ramaiah, and A. Nagarjuna, “Optimization and prediction of parameters in face milling of Al-6061 using taguchi and ANN approach,” *Procedia Eng.*, vol. 97, pp. 365–371, 2014.
- [16] M. D. Selvam, G. Karuppusami, and A. K. S. Dawood, “Optimization of Machining Parameters for Face Milling Operation in a Vertical Cnc Milling Machine Using Genetic Algorithm,” *An Int. J. (ESTIJ)*, vol. 2, no. 4, pp. 2250–3498, 2012.
- [17] O. Çolak, C. Kurbanoglu, and M. C. Kayacan, “Milling surface roughness prediction using evolutionary programming methods,” *Mater. Des.*, vol. 28, no. 2, pp. 657–666, 2007.
- [18] S. Al-zubaidi, J. A. Ghani, C. Hassan, and C. Haron, “Application of ANN in Milling Process : A Review,” *Model. Simul. Eng.*, vol. 2011, 2011.
- [19] A. Mohd, H. Haron, and S. Sharif, “Expert Systems with Applications Prediction of surface roughness in the end milling machining using Artificial Neural Network,” *Expert Syst. Appl.*, vol. 37, no. 2, pp. 1755–1768, 2010.
- [20] G. Ghosh, P. Mandal, and S. C. Mondal, “Modeling and optimization of surface roughness in keyway milling using ANN , genetic algorithm , and particle swarm optimization,” *Int. J. Adv. Manuf. Technol.*, 2017.
- [21] V. Mundada and S. Kumar Reddy Narala, “Optimization of Milling Operations Using Artificial Neural Networks (ANN) and Simulated Annealing Algorithm (SAA),” *Mater. Today Proc.*, vol. 5, no. 2, pp. 4971–4985, 2018.
- [22] A. Gök, K. Gök, M. B. Bilgin, and M. A. Alkan, “Effects of cutting parameters and tool-path strategies on tool acceleration in ball-end milling,” *Mater. Tehnol.*, vol. 51, no. 6, pp. 957–965, 2017.
- [23] A. Gjelaj, B. Berisha, and F. Smaili, “Optimization of turning process and cutting force using multiobjective genetic algorithm,” *Univers. J. Mech. Eng.*, vol. 7, no. 2, pp. 64–70, 2019.
- [24] A. S. M. M Yanis, S. Shari, I. Yani1, A. Arifin, and B. Khona’ah, “Application of RSM and ANN in Predicting Surface Roughness for Side Milling Process under Environmentally Friendly Cutting Fluid Application of RSM and ANN in Predicting Surface Roughness for Side Milling Process under Environmentally Friendly Cutting Flu,” 2019.
- [25] M. Usha and G. S. Rao, “Optimization of Multiple Objectives by Genetic Algorithm for Turning of AISI 1040 Steel Using Al 2 O 3 Nano Fluid with MQL,” *Tribol. Ind.*, vol. 42, no. 1, pp. 70–80, 2020.
- [26] S. L. C. Ferreira *et al.*, “Box-Behnken design: An alternative for the optimization of analytical methods,” *Anal. Chim. Acta*, vol. 597, no. 2, pp. 179–186, 2007.
- [27] N. E. Karkalos, N. I. Galanis, and A. P. Markopoulos, “Surface roughness prediction for the milling of Ti-6Al-4V ELI alloy with the use of statistical and soft computing techniques,” *Meas. J. Int. Meas. Confed.*, vol. 90, pp. 25–35, 2016.
- [28] U. Mukkamala and S. R. Gunji, “Mathematical Modelling of Engineering Problems Comparison of Regression Model with Multi-layer Perceptron Model While Optimising Cutting Force Using Genetic Algorithm,” vol. 7, no. 2, pp. 265–272, 2020.
- [29] N. Hatem, Y. Yusof, A. Kadir, and M. A. Mohammed, “A Review of Tool Path Optimization in CNC Machines : Methods and Its Applications Based on Artificial Intelligence,” vol. 29, no. 4, pp. 3368–3380, 2020.

Miniature liquid cooled Heat sink

K Sathish¹, P. Gopala Krishnaiah ^{*2}, G Jaswanth³

^{1,2,3} Department of Mechanical Engineering, PVP Siddhartha Institute of Technology
Kanuru, Vijayawada AP India,
[*gopalakrishnaiah@pvpsiddhartha.ac.in](mailto:gopalakrishnaiah@pvpsiddhartha.ac.in)

Abstract: This paper continues recent research of the authors, considering the control synthesis in the presence Today, both military and civilian applications require miniaturized optical systems in order to give an imagery function to vehicles with small payload capacity. After the development of megapixels focal plane arrays (FPA) with micro-sized pixels, this miniaturization will become feasible with the integration of optical functions in the detector area. In the field of cooled infrared imaging systems, the detector area is the Detector – Dewar-Cooler Assembly (DDCA).It is a case study taken on the problems araised on an electronic component named as Detector cooler assembly, which used in defence applications like BEL ., As the temperature of the cooler used in the Detector Cooler Assembly is raised by the extensive usage and while cooling whole assembly,more amount of heat is rejected.This rejected heat obsorbed by the surface of the cooler and it becomes hot.

Key Words: cooled infrared imaging systems, payload capacity, uncertain parameters, Detector Cooler Assembly, Barbalat’s Lemma, Detector Dewar Cooler Assembly.

1. INTRODUCTION

The present paper is known to gain some experience from the different topic that will help a lot to make a relation between the theoretical & practical knowledge. It adds valuable experience like knowing real life problems and many mechanical instruments, handling a variety of situations, simultaneously, organizing and analyzing data, budgets or improving teamwork, writing, and speaking ability. To get a sound knowledge about different aspects of work, This paper covers the whole which have done successfully about the Liquid cooled miniature heat sink.

2. HEATSINK DESIGN AND SELECTION

A heat sink is a passive heat exchanger that transfers the heat generated by an electronic or a mechanical device to a fluid medium, often air or a liquid coolant, where it is dissipated away from the device, thereby allowing regulation of the device's temperature. In computers, heat sinks are used to cool CPUs, GPUs, and some chipsets and RAM modules. Heat sinks are used with high-power semiconductor devices such as power transistors and optoelectronics such as lasers and light-emitting diodes (LEDs), where the heat dissipation ability of the component itself is insufficient to moderate its temperature.

A heat sink is designed to maximize its surface area in contact with the cooling medium surrounding it, such as the air. Air velocity, choice of material, protrusion design and surface treatment are factors that affect the performance of a heat sink. Heat sink

attachment methods and thermal interface materials also affect the die temperature of the integrated circuit. Thermal adhesive or thermal paste improve the heat sink's performance by filling air gaps between the heat sink and the heat spreader on the device. A heat sink is usually made out of aluminium or copper.

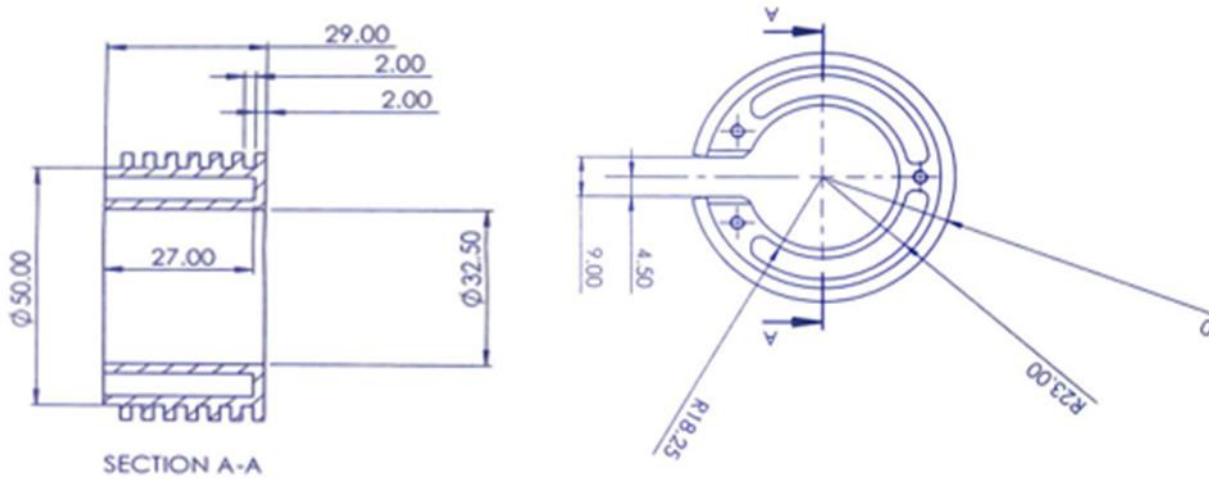
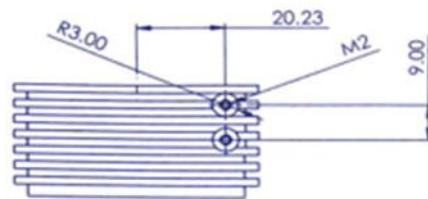
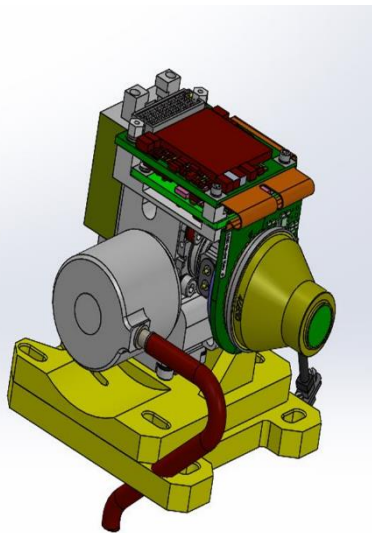


Fig 1a. Detector Cooler Part Assembly



PI	-	ORIGINAL	KS.J	HCS	BWR				
VER	ECO NO.	REL. DATE	CHANGE	DO	ENGR	APVD	NEXT ASSY. NUMBER	ITEM	QTY
MATERIAL		FINISH		PROJECTION		ALL DIMENSIONS ARE IN MM UNLESS OTHERWISE SPECIFIED			LAB/OFFICE
AL ALLOY 6061-T6		REFER NOTES							MAC
DRAWN	CHECKED	ENGINEER	SCALE	TITLE					
N GANESH	KIRAN SAJJ	N GANESH	NTS	NAME					
DT 22.06.2021	DT 22.06.2021	DT 22.06.2021	SOL. TYPE	NUMBER		SHEET NO.		VER.	
			MP	PART NO		000		P1	
						NO OF SH		SIZE	
						001		A3	

Fig.1b Detector Cooler 3D Assembly

Fig 2a Heat sink part assembly

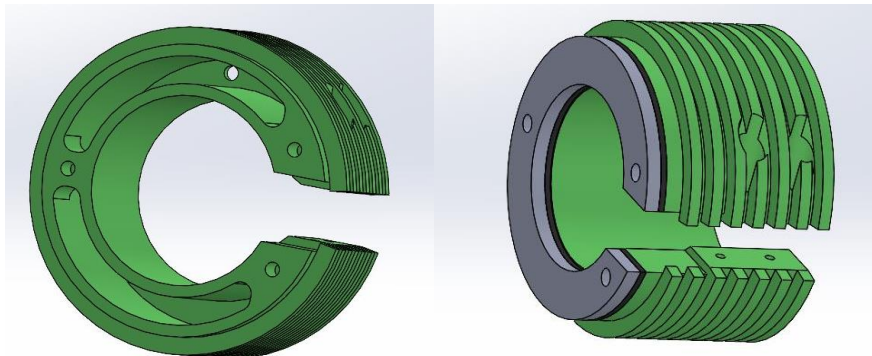


Fig 2b Heat sink 3D assembly

Given $R_1 = 16.25\text{mm} = 0.01625\text{m}$ $R_2 = 18.25\text{mm} = 0.01825\text{m}$
 $R_3 = 23\text{mm} = 0.023\text{m}$ $R_4 = 25\text{mm} = 0.025\text{m}$

3. ANALYSIS ON HEAT SINK

3.1 APPLYING STEADY STATE CONDUCTION

CASE1 : Assuming that the material is aluminium alloy with thermal conductivity, $k=175$ w/mk.
And coolant is Ethylene glycol with thermal conductivity $k=0.2489$ w/mk.

$$Q = \frac{(\Delta T)_{\text{overall}}}{R_{\text{equivalent}}} = \frac{T_1 - T_{\infty}}{R_1 + R_2 + R_3 + R_4}$$

$$R_1 = \frac{1}{2\pi Lk} \times \ln\left(\frac{R_2}{R_1}\right)$$

$$= \frac{1}{2\pi \times 0.029 \times 175} \times \ln\left(\frac{0.01825}{0.01625}\right)$$

$$= 3.64 \times 10^{-3} \text{ k/w}$$

$$R_2 = \frac{1}{2\pi} \left[\frac{0.7}{L \times k} \ln\left(\frac{R_3}{R_2}\right) + \frac{0.3}{Lk} \ln\left(\frac{R_3}{R_2}\right) \right]$$

$$= \frac{1}{2\pi} \left[\frac{0.7}{0.027 \times 0.2489} + \frac{0.3}{0.029 \times 175} \right] \ln\left(\frac{0.023}{0.01825}\right)$$

$$= 3.837 \text{ k/w}$$

$$R_3 = \frac{1}{2\pi Lk} \times \ln\left(\frac{R_4}{R_3}\right)$$

$$= \frac{1}{2\pi \times 0.029 \times 175} \times \ln\left(\frac{0.025}{0.023}\right)$$

$$= 2.614 \times 10^{-3} \text{ k/w}$$

$$R_4 = \frac{1}{2\pi L h_0 R_4}$$

[Assuming heat transfer coefficient of air, $h_0 = 10$ w/m²k]

$$R_4 = \frac{1}{2\pi \times 0.029 \times 10 \times 0.025}$$

$$= 21.95 \text{ k/w}$$

$$\text{Heat flow, } Q = \frac{T_1 - T_{\infty}}{R_1 + R_2 + R_3 + R_4}$$

$$= \frac{80 - 30}{3.64 \times 10^{-3} + 3.837 + 2.614 \times 10^{-3} + 21.95}$$

$$= 1.9385 \text{ w}$$

$$= \frac{T_1 - T_2}{R_1} \gg T_2 = 79.992^\circ\text{C}$$

$$= \frac{T_2 - T_3}{R_2} \gg T_3 = 72.554^\circ\text{C}$$

$$= \frac{T_3 - T_4}{R_3} \gg T_4 = 72.54^\circ\text{C}$$

$$= \frac{T_4 - T_{\infty}}{R_4} \gg T_{\infty} = 29.99^\circ\text{C}$$

[If we take heat transfer coefficient of air as 20 w/m²k]

$$\text{Then, } R_4 = \frac{1}{2\pi \times 0.029 \times 20 \times 0.025} \\ = 10.976 \text{ k/w}$$

$$\text{And, Heat flow, } Q = \frac{80-30}{3.64 \times 10^{-3} + 3.837 + 2.614 \times 10^{-3} + 10.976} \\ = 3.374 \text{ w}$$

$$Q = \frac{T_1 - T_2}{R_1} \gg T_2 = 79.987^\circ\text{C}$$

$$Q = \frac{T_2 - T_3}{R_2} \gg T_3 = 67.04^\circ\text{C}$$

$$Q = \frac{T_3 - T_4}{R_3} \gg T_4 = 67.03^\circ\text{C}$$

$$Q = \frac{T_4 - T_\infty}{R_4} \gg T_\infty = 29.99^\circ\text{C}$$

CASE-2: Assuming that the material of heat sink is copper with thermal conductivity, $k=386$ w/mk.

$$R_1 = \frac{1}{2\pi Lk} \times \ln\left(\frac{R_2}{R_1}\right) \\ = \frac{1}{2\pi \times 0.029 \times 386} \times \ln\left(\frac{0.01825}{0.01625}\right) \\ = 1.65 \times 10^{-3} \text{ k/w}$$

$$R_2 = \frac{1}{2\pi} \left[\frac{0.7}{Lk} \ln\left(\frac{R_3}{R_2}\right) + \frac{0.3}{Lk} \ln\left(\frac{R_3}{R_2}\right) \right] \\ = \frac{1}{2\pi} \left[\frac{0.7}{0.027 \times 0.2489} + \frac{0.3}{0.029 \times 386} \right] \ln\left(\frac{0.023}{0.01825}\right) \\ = 3.835 \text{ k/w}$$

$$R_3 = \frac{1}{2\pi Lk} \times \ln\left(\frac{R_4}{R_3}\right) \\ = \frac{1}{2\pi \times 0.029 \times 386} \times \ln\left(\frac{0.025}{0.023}\right) \\ = 2.614 \times 10^{-3} \text{ k/w}$$

$$R_4 = \frac{1}{2\pi L h_0 R_4}$$

[Assuming heat transfer coefficient of air, $h_0=10$ w/m²k]

$$R_4 = \frac{1}{2\pi \times 0.029 \times 10 \times 0.025} \\ = 21.95 \text{ k/w}$$

$$\text{Heat flow, } Q = \frac{T_1 - T_\infty}{R_1 + R_2 + R_3 + R_4} \\ = \frac{80-30}{3.64 \times 10^{-3} + 3.837 + 2.614 \times 10^{-3} + 21.95} \\ = 1.94 \text{ w}$$

$$= \frac{T_1 - T_2}{R_1} \gg T_2 = 79.996^\circ\text{C}$$

$$= \frac{T_2 - T_3}{R_2} \gg T_3 = 72.556^\circ\text{C}$$

$$= \frac{T_3 - T_4}{R_3} \gg T_4 = 72.553^\circ\text{C}$$

$$= \frac{T_4 - T_\infty}{R_4} \gg T_\infty = 29.99^\circ\text{C}$$

[If we take heat transfer coefficient of air as 20 w/m²k]

$$\text{Then, } R_4 = \frac{1}{2\pi \times 0.029 \times 20 \times 0.025} = 10.976 \text{ k/w}$$

And , Heat flow, $Q = \frac{80-30}{1.65 \times 10^{-3} + 3.835 + 1.85 \times 10^{-3} + 10.976}$
 $= 3.375 \text{ w}$

$= \frac{T_1 - T_2}{R_1} \gg T_2 = 79.994^\circ\text{C}$

$= \frac{T_2 - T_3}{R_2} \gg T_3 = 67.03^\circ\text{C}$

$= \frac{T_3 - T_4}{R_3} \gg T_4 = 67.01^\circ\text{C}$

$= \frac{T_4 - T_\infty}{R_4} \gg T_\infty = 29.996^\circ\text{C}$

From case-1 and case-2 ,we concluded that aluminium alloy is best than the copper.

And if heat transfer coefficient of air is increased is then the rate of heat flow is increased and vice versa.

CASE-3: Heat Transfer Through A Heat Sink Without Coolant.I.E.,Fully Aluminium Alloy Heat Sink.

(Fig.3.2)

We know that: $Q = \frac{(\Delta T)_{\text{overall}}}{R_{\text{equivalent}}}$
 $= \frac{T_1 - T_\infty}{R_1 + R_2}$
 $= \frac{80-30}{\frac{1}{2\pi \times 0.029} \left[\frac{1}{175} \ln\left(\frac{0.025}{0.01625}\right) + \frac{1}{10 \times 0.025} \right]}$

[Assuming heat transfer coefficient of air, $h_0 = 10 \text{ w/m}^2\text{k}$]

$Q = 2.27 \text{ w}$

[If we take heat

transfer coefficient of air as $20 \text{ w/m}^2\text{k}$]

$Q = 4.54 \text{ w}$

3.2 Applying Transient Conduction :

If we apply transient conduction on this heat sink,

Taking thermal conductivity, $k = 175 \text{ w/mk}$

Heat transfer coefficient of air, $h = 10 \text{ w/m}^2\text{k}$

Biot number, $Bi = \frac{hL}{k}$

$\therefore L = \frac{V}{A} = \frac{\frac{\pi}{4}(0.05^2 - 0.0325^2) \times 0.029}{\pi \times 0.05 \times 0.029}$

$L = 0.0072 \text{ m}$

$\therefore Bi = \frac{10 \times 0.0072}{175} = 4.119 \times 10^{-4}$

Since $Bi < 0.1$, we apply lumped parameter system.

From data book, $C = 875 \text{ j/kg k}$

$\rho = 2770 \text{ kg/m}^3$

$A_s = \pi DL = 4.53 \times 10^{-5} \text{ m}^2$

$V = \frac{\pi}{4}(D^2 - d^2) \times L = 3.78 \times 10^{-5} \text{ m}^3$

Initial temperature, $T_o = 70^\circ\text{C}$

Surrounding temperature, $T_{\infty} = 30^{\circ}\text{C}$

Heat transfer coefficient, $h = 10 \text{ w/m}^2\text{k}$

w.k.t:

$$\frac{T - T_{\infty}}{T_0 - T_{\infty}} = e^{\left[-\frac{hA_s}{CV\rho} \times \tau\right]}$$

For time, $\tau = 60 \text{ min}$

$$\frac{T - 30}{70 - 30} = e^{\left[-\frac{10 \times 4.53 \times 10^{-3}}{875 \times 3.78 \times 10^{-5} \times 2770} \times 60 \times 60\right]}$$

$$T = 35.09^{\circ}\text{C}$$

Total heat flow upto 60 min:

$$\begin{aligned} q_{60} &= \rho CV(T - T_0) \\ &= 2770 \times 875 \times 3.28 \times 10^{-5} (35.09 - 30) \\ &= -2975.31 \text{ j/hr} \end{aligned}$$

For time, $\tau = 30 \text{ min}$

$$\frac{T - 30}{70 - 30} = e^{\left[-\frac{10 \times 4.53 \times 10^{-3}}{875 \times 3.78 \times 10^{-5} \times 2770} \times 30 \times 60\right]}$$

$$T = 44.27^{\circ}\text{C}$$

Total heat flow upto 30 min:

$$\begin{aligned} q_{30} &= \rho CV(T - T_0) \\ &= 2770 \times 875 \times 3.28 \times 10^{-5} (44.27 - 30) \\ &= -2045.5 \text{ j/30min} \end{aligned}$$

3.3 Heat Transfer Through Circumferential Fins :

For finding heat transfer coefficient, h :

$$\text{Take, } T_w = 60^{\circ}\text{C}$$

$$T_{\infty} = 30^{\circ}\text{C}$$

$$\text{Then, film temperature, } T_f = \frac{T_w + T_{\infty}}{2} = \frac{60 + 30}{2} = 45^{\circ}\text{C}$$

Then, we take the properties of air at 45°C from data book

$$\rho = 1.1105 \frac{\text{kg}}{\text{m}^3}$$

$$\vartheta = 17.455 \times 10^{-6} \text{ m}^2/\text{sec}$$

$$P_r = 0.6985$$

$$K = 0.02791 \text{ w/mk}$$

$$\rightarrow \beta = \frac{1}{T_{f \text{ in k}}} = \frac{1}{45 + 273} = 3.14 \times 10^{-3} \text{ k}^{-1}$$

$$\begin{aligned} \rightarrow \text{Grashoff's number, } Gr &= \frac{g \cdot \beta \cdot D^3 \cdot \Delta T}{\vartheta^2} \\ &= \frac{9.81 \times 3.144 \times 10^{-3} \times 0.05^3 \times 30}{(17.455 \times 10^{-6})^2} \\ &= 379614.77 \end{aligned}$$

$$\therefore GrPr = 2651560.9196$$

Since $GrPr < 10^7$ flow is laminar

And

$$\text{Nu} = \left\{ 0.60 + 0.387 \left[\frac{\text{Gr Pr}}{\left\{ 1 + \left(\frac{0.539}{\text{Pr}} \right)^{0.5625} \right\}^{0.96}} \right] \right\}^{0.167}^2$$

$$= 14.48$$

$$\text{Nu} = \frac{hD}{k} \quad [\text{for cylinders}]$$

$$h = \frac{\text{Nu} \times k}{D} = \frac{14.48 \times 0.02791}{0.05}$$

$$h = 8.08 \text{ w/m}^2\text{k}$$

circumferential rectangular fins :

$$Q = \eta A_s h (T_w - T_\infty)$$

$$L_c = L + \frac{t}{2} = 0.004 \text{ m}$$

$$r_{2c} = r_1 + L_c = 0.029 \text{ m}$$

$$A_m = 2\pi (r_{2c}^2 - r_1^2)$$

$$= 1.357 \times 10^{-3} \text{ m}^2$$

$$m = \sqrt{\frac{2h}{kA}} = \sqrt{\frac{2 \times 8.08}{175 \times 0.002}} = 6.76$$

$$\eta = \frac{\tanh \left[mL \sqrt{\frac{\left(1 + \frac{r_2}{r_1}\right)}{2}} \right]}{mL \sqrt{\frac{\left(1 + \frac{r_2}{r_1}\right)}{2}}}$$

$$= 0.9998 = 99.98\%$$

$$Q = 0.9998 \times 1.357 \times 10^{-3} \times 8 \times 30$$

$$= 0.325 \text{ w (for only one fin)}$$

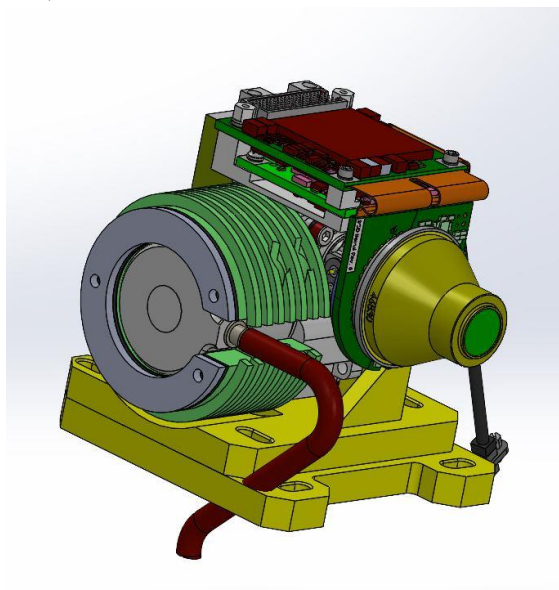


Fig. 3 Final Assembly

4. CONCLUSIONS

To conclude from our calculations the heat flow through the heat sink with coolant is less effective when compared to the heat sink completely made up of aluminium. } the heat transfer through fins is good. And also concluded from our observations, if we circulate the coolant in the heat sink it works more effective i.e., it transfers more rate of heat transfer.

REFERENCES

- [1] Dede, E. M. (2012). Optimization and design of a multipass branching microchannel heat sink for electronics cooling. *Journal of Electronic Packaging*, 134(4).
- [2] Silvério, V., Cardoso, S., Gaspar, J., Freitas, P. P., & Moreira, A. L. N. (2015). Design, fabrication and test of an integrated multi-microchannel heat sink for electronics cooling. *Sensors and Actuators A: Physical*, 235, 14-27.
- [3] Arshad, A., Jabbal, M., Sardari, P. T., Bashir, M. A., Faraji, H., & Yan, Y. (2020). Transient simulation of finned heat sinks embedded with PCM for electronics cooling. *Thermal Science and Engineering Progress*, 18, 100520.
- [4] Saenen, T., & Baelmans, M. (2012). Numerical model of a two-phase microchannel heat sink electronics cooling system. *International journal of thermal sciences*, 59, 214-223.
- [5] Bhattacharya, A., & Mahajan, R. L. (2002). Finned metal foam heat sinks for electronics cooling in forced convection. *J. Electron. Packag.*, 124(3), 155-163.
- [6] PastUkhov, V. G., Maidanik, Y. F., Vershinin, C. V., & Korukov, M. A. (2003). Miniature loop heat pipes for electronics cooling. *Applied Thermal Engineering*, 23(9), 1125-1135.
- [7] Jaworski, M. (2012). Thermal performance of heat spreader for electronics cooling with incorporated phase change material. *Applied Thermal Engineering*, 35, 212-219.
- [8] Bahiraei, M., & Heshmatian, S. (2018). Electronics cooling with nanofluids: a critical review. *Energy Conversion and Management*, 172, 438-456.
- [9] Singh, R., Akbarzadeh, A., Mochizuki, M., Nguyen, T., & Nguyen, T. (2009). Thermal characterization of copper microchannel heat sink for power electronics cooling. *Journal of thermophysics and heat transfer*, 23(2), 371-380.
- [10] de Oliveira, P. A., & Barbosa, J. R. (2017). Performance assessment of single and multiple jet impingement configurations in a refrigeration-based compact heat sink for electronics cooling. *Journal of Electronic Packaging*, 139(3), 031005. February 22, 2022

Comparative Analysis of Elliptical and Square Unit Cell for The Prediction of Effective Thermal Conductivity

Kamala Priya B¹, Sravani V², Dilip Kumar K³

¹Department of Mechanical Engineering, Assistant Professor, LakireddyBalireddy College of Engineering, Mylavaram, Andhra Pradesh, India.

^{a)}Kamala.jkp@gmail.com

²Department of Mechanical Engineering, Assistant Professor, Prasad V Potluri Siddhartha Institute Of Technology, Kanuru, Vijayawada , Andhra Pradesh, India.

^{b)}sravanivemuri@pvpsit.ac.in

³Department of Mechanical Engineering, Professor, LakireddyBalireddy College of Engineering, Mylavaram, Andhra Pradesh, India.

dilip_011@yahoo.co.in

Abstract. The main work concentrates on the determination of Effective Thermal conductivities of Unidirectional Fibre-reinforced composites using the Finite Element Method. By considering the Elliptical and Square Fibre mechanical models of a Representative Volume Element (RVE), the Thermal Conductivities of each component (Fibre, Matrix) of the composite is evaluated through the influence of fibre type and arrangement on effective thermal conductivities in the transverse (K₂) and through-thickness thickness (K₃) directions. The Elliptical and Square Models with and without deboned of Thermal Conductivities of Fibre-Reinforced Composites using Finite Element Method applied to Representative Volume Element are determined. The results declared that the Effective Thermal Conductivities of Composites can be enhanced with Voids in a Matrix and random arrangement of Fibres in a Matrix.

Keywords: Thermal Conductivity, Fibre reinforced composites, Heat transfer, Finite Element Method

1. INTRODUCTION

Due to their high specific strength and stiffness, composite materials are commonly used in structural applications. The qualities of the fibre and matrix materials, as well as their proportions in the composite, determine the heat conductivity of a fibre-reinforced composite. From the review of literature, it is observed that various analytical and numerical methods have been adopted to predict the thermal conductivity of the composites. M.R.Sanjay et al [1] have been exploring the mechanical properties and characteristics of natural glass-fibre-reinforced polymer composites. A.Shirisha et al[2] examined the mechanical properties of hybrid composite materials, such as polyester matrix composites reinforced with glass fibres. Springer and Tsai [3] proposed a numerical method for predicting Transverse Thermal Conductivity based on the Shear Loading analogy. By using the 3D Finite Element Method, G. Sambasivarao et al [4] predicted the effective transverse thermal conductivity for square and hexagonal unit cell models for different ranges of volume fractions and the models can extend for imperfections such as

voids in the matrix, cracks in fibres as well as matrix and fibre-matrix debonding. Tsai [5] determined the Transverse Thermal Conductivities for a square array of unit cells considering two circular filaments. Islam and Pramila [6] investigated Thermal Conductivity along the Transverse direction for Ideal FRP Composites, Composites with Interfacial Thermal Barrier Resistance and Composites with cracks. Xiaomin Deng [7] were examined the fracture mechanics basis and consequences of interfacial fracture mechanics theories for the investigation of debonding and delamination in composite materials. In a combination of matrix cracking with an interfacial perfect debonding T.J.Lu and J.W.Hutchinson[8] computed the overall longitudinal thermal conductivity of unidirectional fibre reinforced composites and discussed heat transmission mechanisms across cracks and deboned interfaces. Given taking into account Square and Hexagonal arrays, Yaun Lu [9] computed the transverse thermal conductivity by Boundary Collection Method for both Square and Circular cylinders.

In this paper, the comparison of Effective Thermal Conductivities, K_2 and K_3 of Unidirectional Fibre Reinforced composites of Elliptical and Square models with and without deboned for staggered arrangements are discussed on insertion of third phase material between the composites

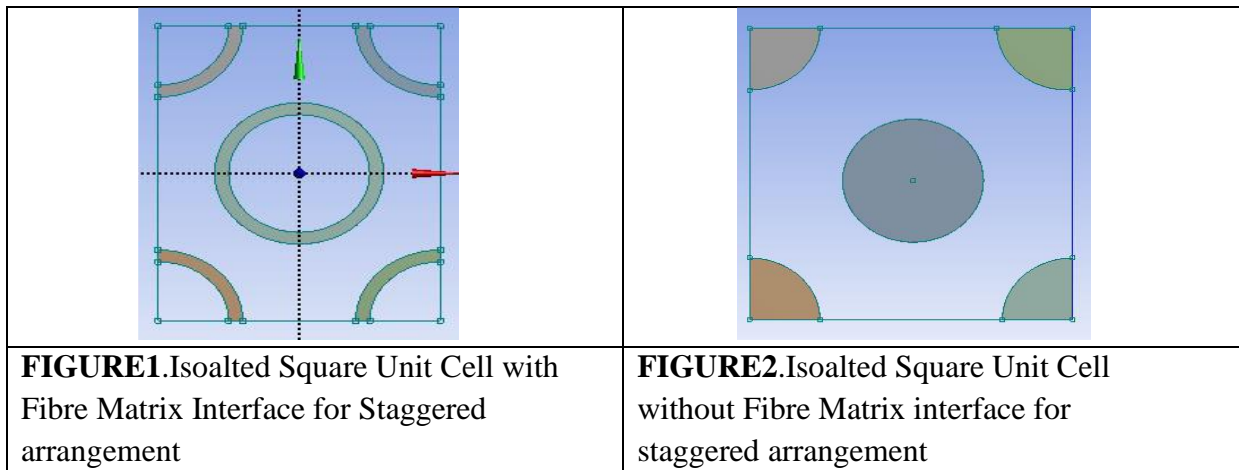
2. PROBLEM STATEMENT

The concentration of the work is to compare the Effective Thermal Conductivities, K_2 and K_3 of Unidirectional Fiber-Reinforced composites on insertion of thin third phase material between the matrix and the fibre.

Methodology

The present analysis of the Elliptical and Square model with a staggered arrangement of fibers with and without debonding is proved for Fiber volume fractions ranging from 0.1 to 0.6 with appropriate Thermal boundary conditions positioned in the direction of heat flow.

A composite periodic Fibres, it is commonly and satisfactory to draw outcome for the whole structure by taking into account only unit cell so-called a representative volume element (R.V.E) which is as shown in Fig. 1,2,3, and 4 are used for the analysis.



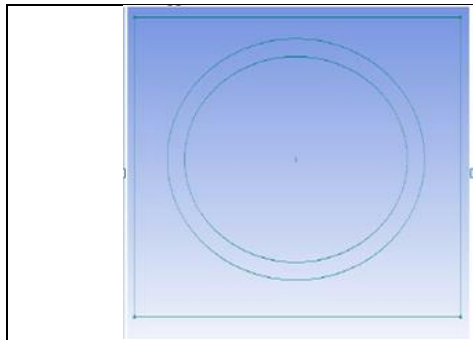


FIGURE 3. Isolated Elliptical Unit Cell with Fibre Matrix interface for staggered arrangement

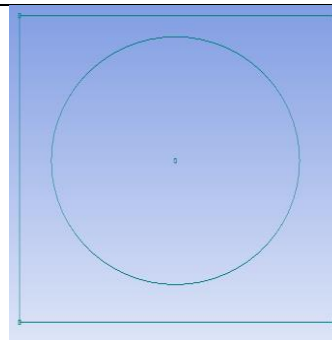


FIGURE 4. Isolated Elliptical Unit Cell without Fibre Matrix interface for staggered arrangement

3. GEOMETRY

The cross-sectional area of fibre relative to the total cross-sectional area of unit cell is a measure of volume of fibre relative to the total volume of the composite which is called fibre volume fraction (V_f).

$$V_f = \frac{\pi/4 * r^2}{a^2}$$

Where, r is radius of fibre, a is edge length of square unit cell, V_f volume fraction of fibre.

3.1 Finite Element Models

A one fourth portion of Unit cells of Elliptical and Square are designed using Ansys as shown in figure and the representative volume element for the whole structure of those models are designed as shown in figure 5,6,7 and 8 is selected for the analysis.

The Heat flow attained from the ANSYS is substituted in Equation $q = -K dt/dx$ and Thermal Conductivity in the respective direction is calculated in W/m-k. Correspondingly the Volume fraction of Fibre is constantly varied from 0.1 to 0.6 by changing the parameter 'r' which is the radius of Fibre.

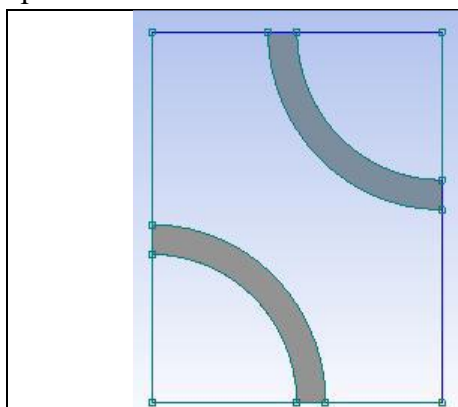


FIGURE 5. One fourth portion of Square Unit Cell with Fibre Matrix interface for staggered arrangement

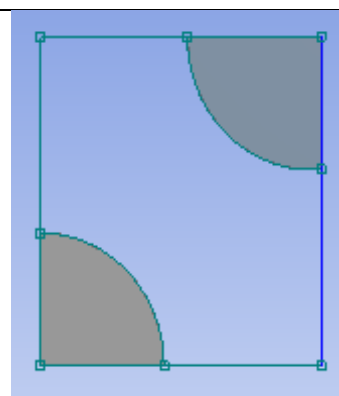


FIGURE 6. One fourth portion of Square Unit Cell without Fibre Matrix interface for staggered arrangement

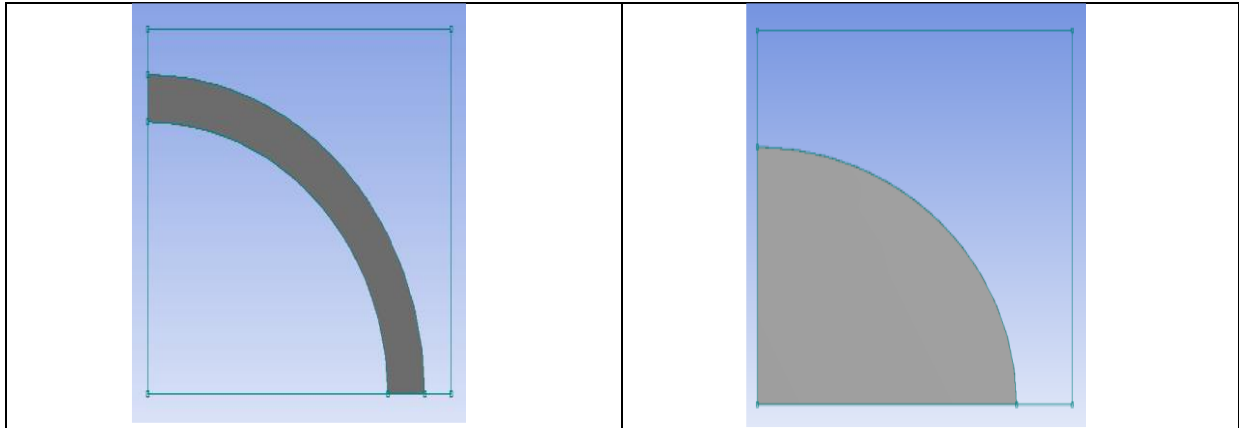


FIGURE 7. One fourth portion of Elliptical Unit Cell with Fibre Matrix interface for staggered arrangement

FIGURE 8. One fourth portion of Elliptical Unit Cell without Fibre Matrix interface for staggered arrangement

3.2 Temperature boundary conditions for one-fourth model are as follows:

For prediction of K_2 :

$$T(0,y) = T_1 ; T(a,y) = T_2$$

For prediction of K_3 :

$$T(x,0) = T_1 ; T(x,a) = T_2$$

All other faces are subjected to adiabatic boundary conditions.

3.3 Material Properties

Fibre Conductivity

In the analysis, thermal conductivity values are normal to be in the range of 5 to 100. The materials in this normal range are Carbon and Glass fibres.

Matrix Conductivity

Polymer is advised for the present analysis. The effective thermal conductivity of Fibre Matrix interface with and without deboned are reviewed with the estimated matrix thermal conductivity value.

4. ANALYSIS OF RESULTS

The following figures 9,10,11,12,13,14,15 & 16 shows the analytical results of Elliptical and Square unit cell for staggered fibres in transverse and through thickness directions respectively.

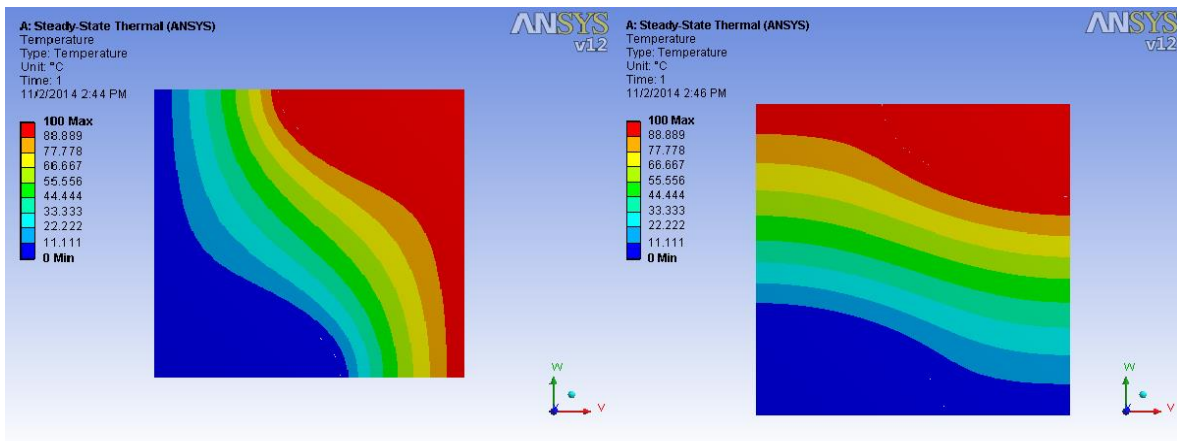


FIGURE 9 ANSYS Plot shows the temperature variation in Elliptical Unit Cell with Fiber Matrix Interface for Staggered Fibers in Transverse Direction

FIGURE 10 ANSYS Plot shows the temperature in Elliptical Unit Cell with Fiber Matrix for Staggered Fibers through thickness Direction

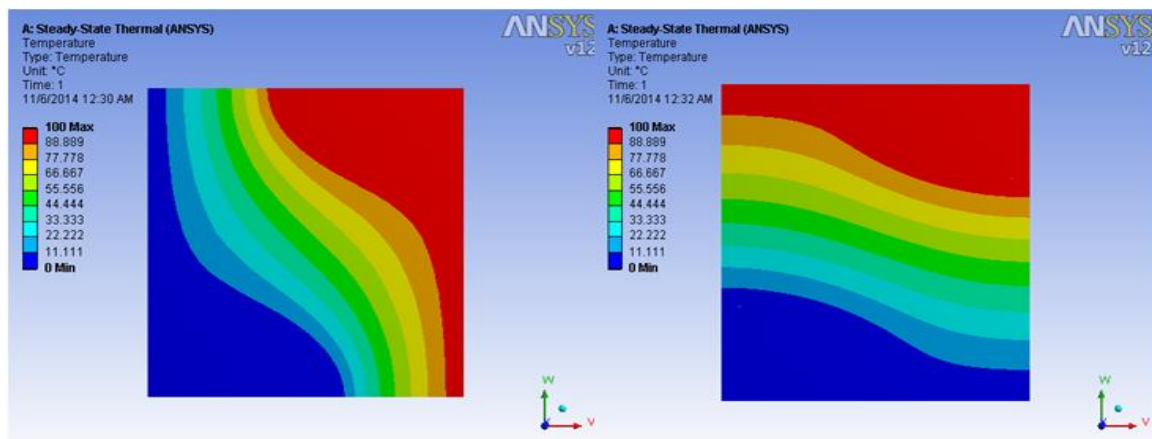


FIGURE 11 Ansys plot shows the Temperature variation In elliptical unit cell for staggered fibers in transverse direction

FIGURE 12 Ansys plot shows the Temperature variation in elliptical unit cell for staggered fibres through thickness Direction

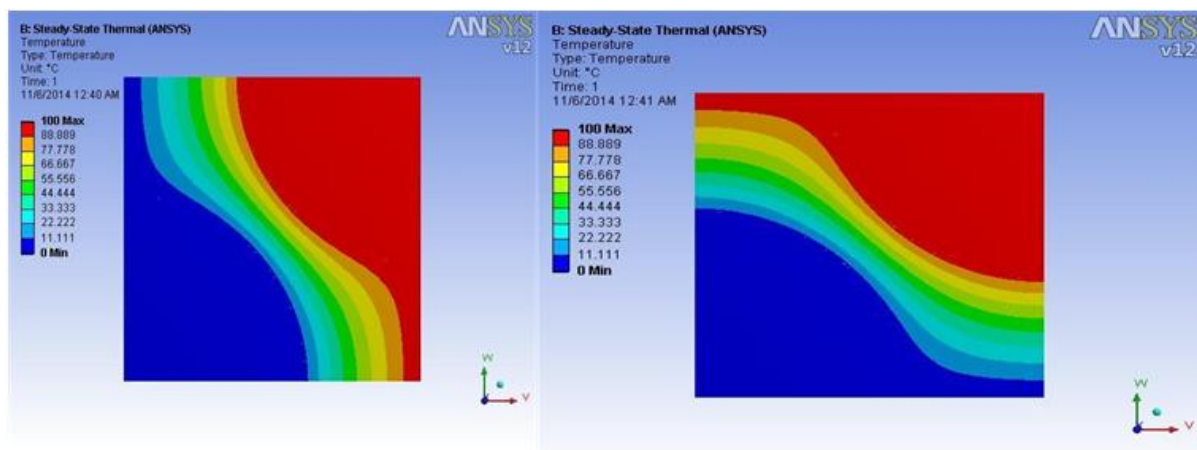


FIGURE 13 Ansys Plot shows the temperature Variation in square unit cell with fibre matrix Interface for staggered fibres in transverse direction

FIGURE 14 Ansys plot shows the temperature variation in square unit cell with fibre matrix interface for staggered fibres through thickness direction

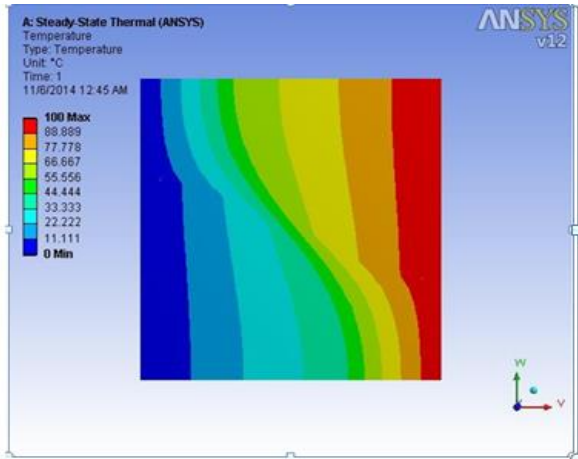


FIGURE 15 Ansys plot shows the temperature variation in Square unit cell for staggered Fibres in transverse direction

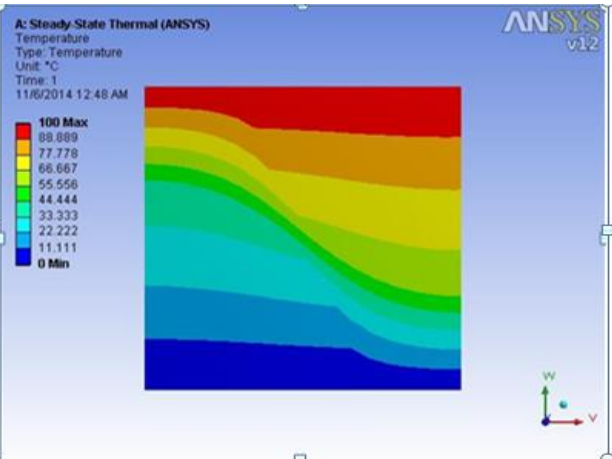
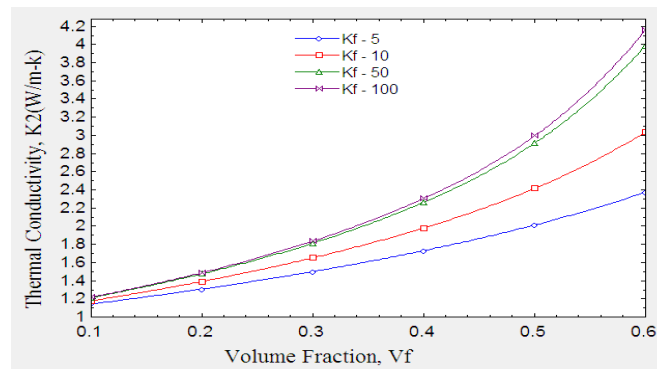


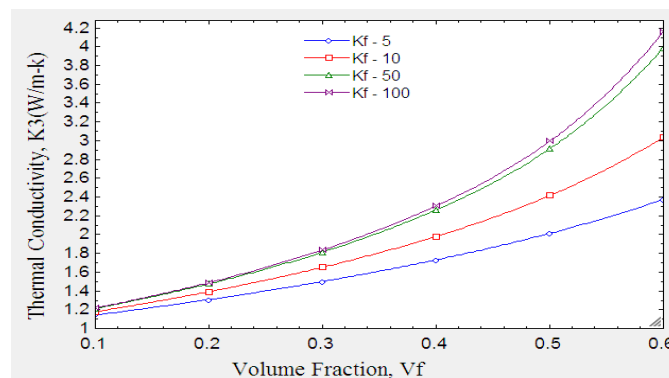
FIGURE 16 Ansys plot shows the temperature variation in Square unit cell for staggered Fibres through thickness direction

4.1 Staggered square unit cell

Here, for both Transverse (K_2) and through Thickness (K_3) directions, a similar variation in Thermal Conductivity is observed with increase in volume fraction up to 20%. A wide divergence of Thermal Conductivity values are identified from 20% to 60%. Closer Transverse Thermal Conductivity values are observed for Fiber Conductivities 50W/m-k, 100W/m-k.



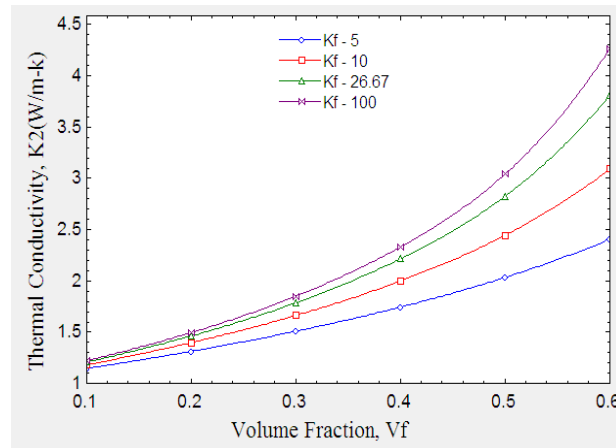
GRAPH 1. Thermal Conductivity K_2 (W/m-k) Vs Volume Fraction V_f plot for Staggered Square Unit Cell.



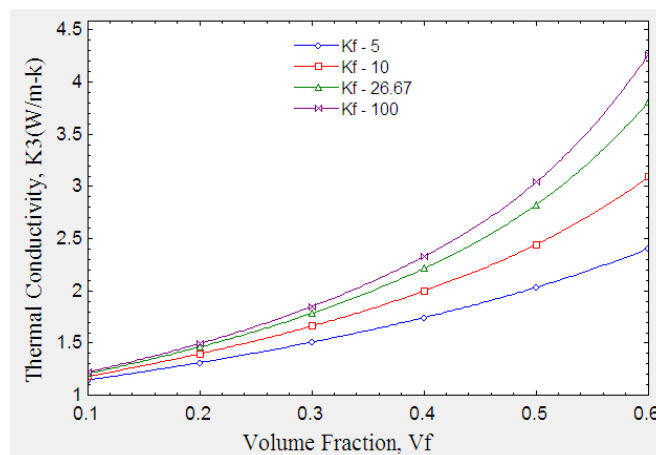
GRAPH 2. Thermal Conductivity K_3 (W/m-k) Vs Volume Fraction V_f plot for Staggered Square Unit Cell

4.2 Staggered Square Unit Cell With Fiber Matrix Deboned

In both Transverse (K_2) and Thickness (K_3) directions, a similar variation in Thermal Conductivity is observed with an increase in volume fraction up to 0.2. A wide divergence of Thermal Conductivity values is identified from 0.2 to 0.6.



GRAPH 3. Thermal Conductivity K_2 (W/m-k) Vs Volume Fraction V_f plot for Staggered Square Unit Cell

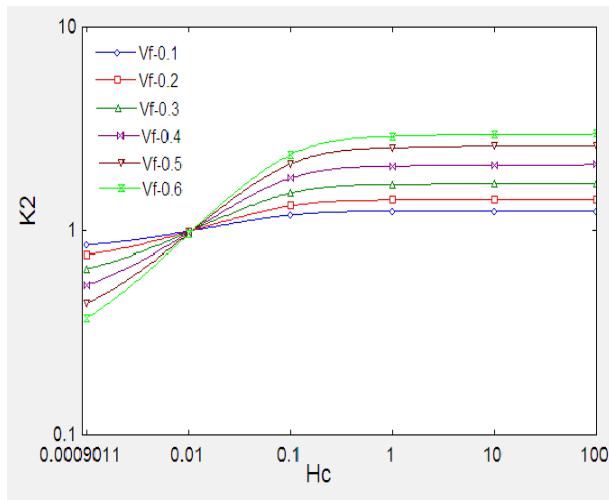


GRAPH 4. Thermal Conductivity K_3 (W/m-k) Vs Volume Fraction V_f plot for Staggered Square Unit Cell.

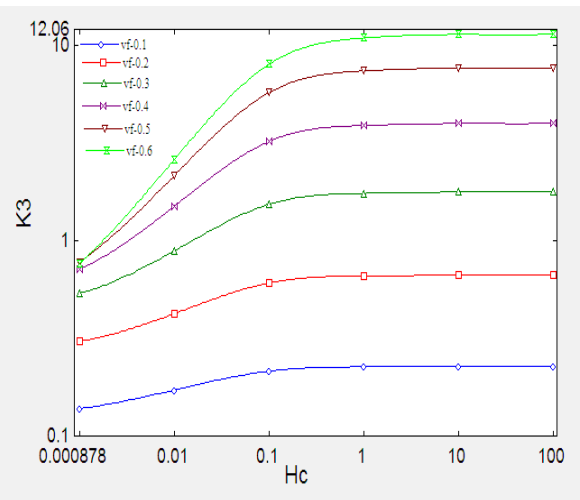
4.3 Elliptical Unit Cell with Fiber Matrix Interface for Staggered Fibers through Transverse and Thickness Thermal Conductivities

Staggered Elliptical Unit Cell with Fibre Matrix Interface Staggered Elliptical Unit Cell with Fibre Matrix Interface From graph 5, it is observed that with an increase in thermal conductance, the Effective Thermal Conductivity (K_2) value is observed to be similar at 0.01 W/m²k for all the volume fractions considered and third phase conductivities decreases below this value due to negligible Fiber Matrix Interface. Transverse effective conductivity which is estimated is the combination of conductivity of matrix and third phase conductivities which causes K_2 value lower than matrix value and the effect is seen greater at higher fiber volume fractions. Third phase conductivity (K_c) is taken from 0.001 to 100 W/m-k for the analysis, which covers nearly the gap to highest conductivity materials. It is evident from graph 6, the Thermal Conductance values ranging

from 1W/m²k to the maximum conductance value, negligible or no variation is observed for 100% deboning. This is obvious as the V_f increases, the area resisting, heat flow also increases.



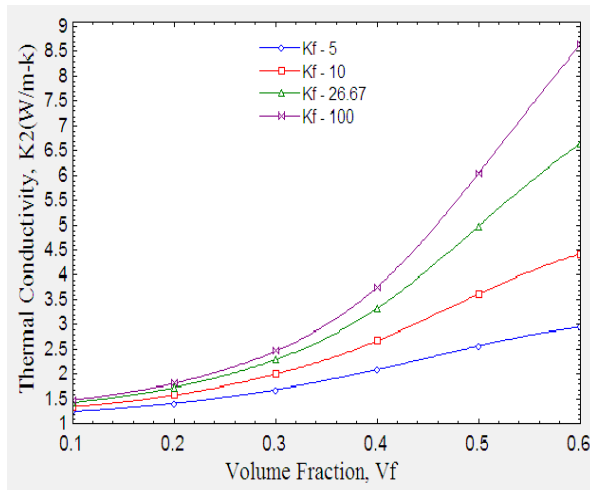
GRAPH 5 Thermal Conductivity K_2 (W/m-k) Vs Thermal Conductance K_c (W/m²k) plot for $K_f=5$ to 100



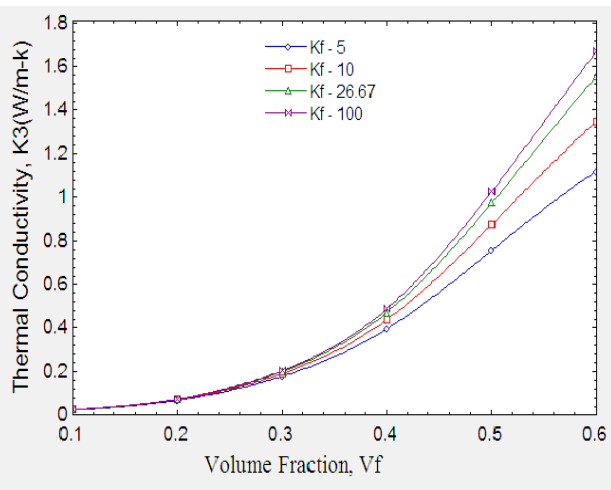
GRAPH 6 Thermal Conductivity K_3 (W/m-k) Vs Thermal Conductance K_c (W/m²k) plot for $K_f=5$ to 100

4.4 Elliptical unit cell model for staggered pattern of fibers through transverse and thickness thermal conductivities

Graph7 shows that similar variation in Thermal Conductivity is observed with an increase in volume fraction up to 0.2. A wide divergence of Thermal Conductivity values is identified from 0.2 to 0.6. Graph8 shows that a similar variation in Thermal Conductivity is observed with an increase in volume fraction up to 0.3. A wide divergence of Thermal Conductivity values is identified from 0.3 to 0.6.



GRAPH7. Thermal Conductivity K_2 (W/m-k) Vs Thermal Conductance K_c (W/m²k) plot for $K_f=5$ to 100 Staggered Elliptical Unit Cell



GRAPH8. Thermal Conductivity K_3 (W/m-k) Vs Thermal Conductance K_c (W/m²k) plot for $K_f=5$ to 100 Staggered Elliptical Unit Cell

Conclusions

- In the Transverse direction of the elliptical unit cell with fibre matrix interface for staggered fibres, it is observed that with an increase in thermal conductance, the Effective Thermal Conductivity (K_2) value is observed to be a similar value for all

the volume fractions considered and third phase conductivities decreases below this value due to negligible Fiber Matrix Interface and through Thickness direction, Third phase conductivity (K_c) is taken from 0.001 to 100 W/m-k for the analysis which covers nearly gap to highest conductivity materials and neither negligible nor variation is observed for 100% bonding.

- In a square unit cell with fibre matrix interface for staggered fibres, both Transverse (K_2) and through Thickness (K_3) directions, a similar variation in Thermal Conductivity is observed with an increase in volume fraction up to 20%. A wide divergence of Thermal Conductivity values is identified from 20% to 60%. Closer Transverse Thermal Conductivity values are observed for Fiber Conductivities 50W/m-k, 100W/m-k.
- Similar variation of thermal conductivity is observed for elliptical and square models in transverse and through-thickness directions with an increase in volume fraction up to 20%.
- A wide divergence of thermal conductivity values are observed in both elliptical and square models from 20% to 60% and from 20% to 30% respectively.

References

1. M.R.Sanjay, G.R.Arputha and B.Yogesha., *Materials Today : Proceedings* vol 2, Issue 4-5, (2015), pp. 2959-2967.
2. A.Shirisha, B. Sri Ramji., *ijammc*.(2015).03.08 Vol 5 Issue 1, pp.53-56
3. Springer, G. S. and T Sai S. W., *Thermal Conductivities of Unidirectional Materials*, *Journal of Composite Materials*, vol. 1, (1967), pp. 166.
4. G. Sambasiva Rao¹, T. Subramanyam² and V. Balakrishna Murthy., *3D finite element models for the prediction of effective transverse thermal conductivity of Unidirectional fiber reinforced composite*, *International Journal of Applied Engineering Research*, ISSN 0973-4562 Volume 3, Number 1 (2008), pp. 99–108 Tsai
5. Islam, R. Md. And Pramila, A., *Thermal Conductivity of Fiber reinforced Composites by the FEM*, *Journal of Composite Materials*, vol. 33, (1999), pp. 1699-1715.
6. Xiaomin, D., *Mechanics of debonding and delamination in composites: asymptotic studies*, *Composites Engineering*, vol. 5, (1995), pp. 1299- 1315.
7. Lu, T. and Hutchinson, J., *Effect of matrix cracking on the overall thermal conductivity of Fiber reinforced composites*, *Philosophical Transactions of Royal Society (London A*, 351, 1995), pp. 595- 61
8. Yaun Lu-shih, (1995), *The Effective Thermal Conductivities of Composites with 2D arrays of circular and square cylinders*, *Journal of Composite Materials*, 29, pp. 483-505.

Effect of Engine Performance on Nozzle Variation for a Bio Fueled DI Diesel Engine

J. Surendra¹, Dr. Ravi Kadiyala²

¹Assistant Professor, Department of Mechanical Engineering, Prasad V Potluri Siddhartha Institute of Technology, Kanuru, Krishna District, Andhra Pradesh, India. Email: jasti.surendra@gmail.com

²Principal, Dhanekula Institute of Engineering & Technology, Ganguru, Krishna District, Andhra Pradesh, India. Email: kadiyalaravi_72@gmail.com

Abstract: As of late plant oils are considered as substitute fills for diesel because of ecological and financial reasons. All the properties of plant oils are nearer to diesel except viscosity and volatility which effects on engine performance because of poor atomization of fuel in combustion chamber. Precise control over atomization is necessary to improve the engine performance. The present work aims at the performance evaluation of bio fueled diesel engine by the variation of spray hole diameter and number of holes. Three variants of nozzle which include 0.28X3 (0.28mm diameter and 3 holes), 0.26X4, 0.25X5 holes are used for the evaluation of efficiencies at different loads.

Introduction

Vegetable oils are efficient among the alternatives to the fossil fuel. Many researchers have reported that vegetable oils can be directly used in diesel engine without any engine modification. But direct use of vegetable oils in diesel engines creates problems like choking and gum formation due to high viscosity of vegetable oils. Hence the biofuels are produced by transesterification of bio vegetable oils which reduces the viscosity. Further research and development are necessary to improve the performance of bio fueled diesel engines. All the properties of biofuel are closer to diesel except viscosity which affects the atomization process of fuel there by entire combustion process. The atomization process may be improved by varying the nozzle design.

In the present work, palm oil is converted into palm methyl ester by transesterification process. Palm methyl ester (Bio Diesel) properties are tested in comparison with diesel oil, further performance characteristics were experimentally investigated on single cylinder D.I Diesel engine fueled with diesel initially and then by bio diesel at 3 loading by varying the nozzle hole diameter and number of holes. Three variants of nozzle which include 0.28X3 (0.28mm diameter and 3 holes), 0.26X4, 0.25X5 holes are used for the evaluation of efficiencies at different loads.

Preparation of Palm Methyl Esters and its properties

The viscosity of vegetable oils can be reduced by Transesterification process. Transesterification is the process of converting a complex ester (tri glyceride) into a mixture of simple esters by treating with alcohol in presence of alkali (Catalyst). Transesterification of triglycerides gives a mixture of glycerol and esters. Vegetable oils mainly comprises of 90 to 98% of try glycerides and small amounts of mono-glycerides,

di-glycerides, and free fatty acids. In the transesterification process, try glycerides of vegetable oils react with alcohol in presence of catalyst and transforms into a mixture of esters and glycerol. The esters thus produced are used as biodiesel. The base catalysts promote the faster reaction process in transesterification process of vegetable oils along with an advantage of less corrosive property than compared to acid catalysts. So, KOH is used as catalyst for transesterification process. Initially palm methyl Esters are prepared with 100ml of palm oil for identifying the required quantities of alcohol and catalyst for high yield and then the bio diesel is produced with established proportions

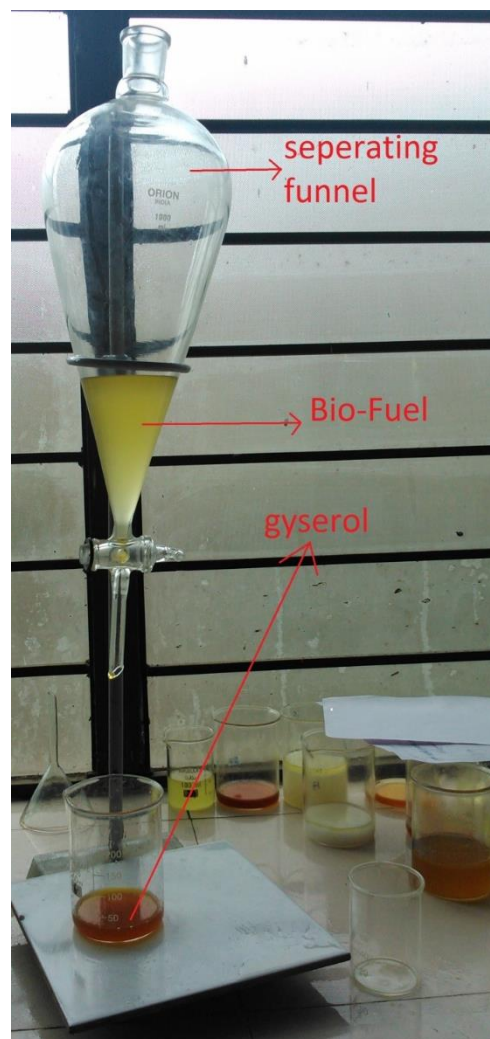
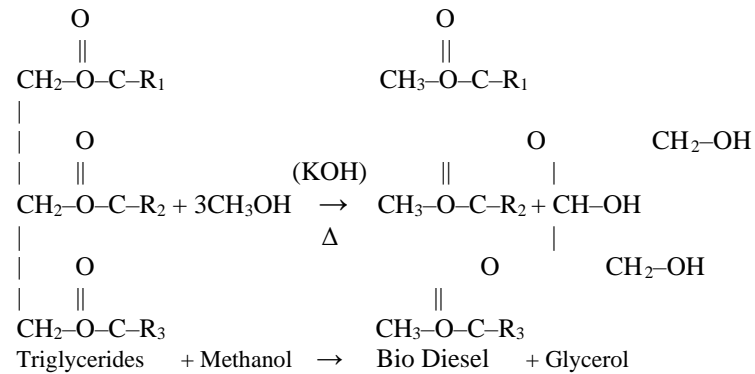


Figure1: Experimental setup for preparing bio diesel

Experimentation

The experimentation for evaluating the performance characteristics of biofuel compared to diesel is carried out at IC Engines laboratory on single cylinder DI Diesel engine loaded with rope brake diameter. The specifications of the engine are listed in table 1. The experimentation is done with engine operated with three different nozzles which include 0.28X3 (0.28mm diameter and 3 holes), 0.26X4, 0.25X5 holes at 3 different load conditions. When the engine is initially run on diesel fuel, and then on biodiesel fuel, the observations were made and then the performance characteristics are evaluated for all the running conditions and compared.

Table 1: Specifications of the Test Engine

Model	
Type	Four Stroke, Direct Ignition
Number of cylinders	1
Bore	80mm
Stroke	110mm
Total Cylinder volume	553cm ³
Injector operating Pressure	200bar
Number of nozzle holes	3
Nozzle hole diameter	0.28mm

Table 2: Performance characteristics with Biofuel

Load	No. of Holes	Hole Diameter (mm)	BSFC (Kg/Kw-hr)	IP (KW)	B.Th. Efficiency	I. Th. Efficiency	Mechanical Efficiency	Vol. Efficiency
Part	3	0.28	0.92	1.31	9.76	20.97	46.58	43.51
Half	3	0.28	0.7	1.75	12.86	21.42	60.06	44.54
Full	3	0.28	0.65	2.09	13.79	20.74	66.58	44.27
Part	4	0.26	0.99	1.2	9.19	18.26	50.32	43.57
Half	4	0.26	0.79	1.58	11.46	18.44	62.14	43.6
Full	4	0.26	0.75	1.89	12.05	17.6	68.33	42.73
Part	5	0.25	1.04	1.48	8.7	21.09	41.26	42.72
Half	5	0.25	0.78	1.92	11.65	21.22	54.91	42.98
Full	5	0.25	0.69	2.26	13.01	21.12	61.56	43.23

Table 3: Performance characteristics with Diesel

Load	No. of Holes	Hole Diameter (mm)	BSFC (Kg/Kw-hr)	IP (KW)	B.Th. Efficiency	I. Th. Efficiency	Mechanical Efficiency	Vol. Efficiency
Part	3	0.28	0.85	1.28	9.82	20.6	47.65	43.58
Half	3	0.28	0.66	1.72	12.74	20.86	61.04	42.5

Full	3	0.28	0.62	2.09	13.66	20.11	67.94	42.78
Part	4	0.26	0.95	1.03	8.81	15.12	58.25	42.21
Half	4	0.26	0.79	1.42	10.62	15.24	69.71	41.21
Full	4	0.26	0.73	1.75	11.51	15.26	75.42	41.35
Part	5	0.25	0.97	1.22	8.66	17.64	49.18	40.76
Half	5	0.25	0.79	1.59	10.68	17.54	61	41.46
Full	5	0.25	0.72	1.9	11.55	17.3	61.84	41.72

Results and Discussions

Brake specific fuel consumption:

BSFC of engine when operated by biofuel and diesel at various loads (3 loads) with three different types of nozzles is shown in figure 1.

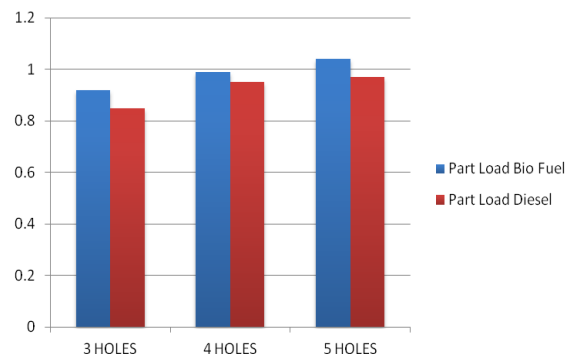


Figure 1(a):BSFC at Part Load

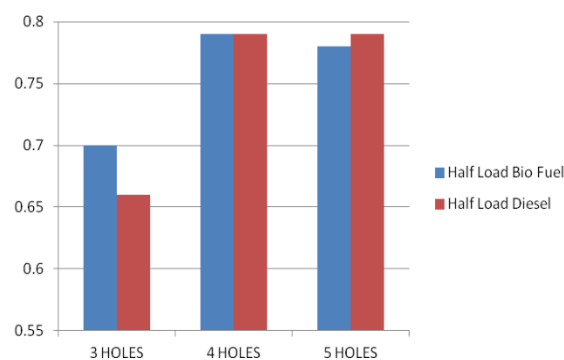


Figure 1(b): BSFC at Half Load

It was observed that almost in all the cases BSFC is slightly more with the use of Bio fuel than that of the diesel fuel or almost the same.

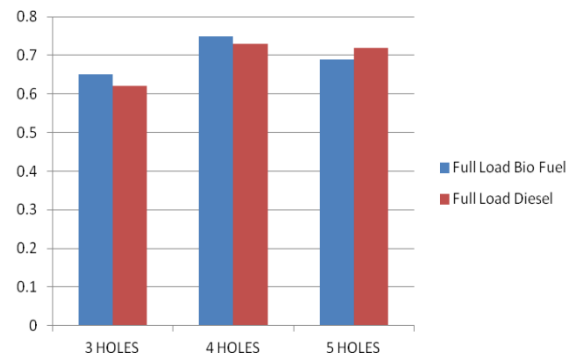


Figure1(c): BSFC at Full Load

Indicated power:

Indicated power of engine when operated by biofuel and diesel at various loads (3 loads) with three different types of nozzles is shown in figure 2

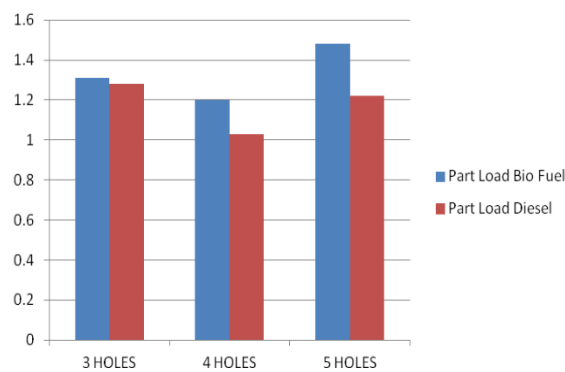


Figure 2(a): Indicated Power at Part Load

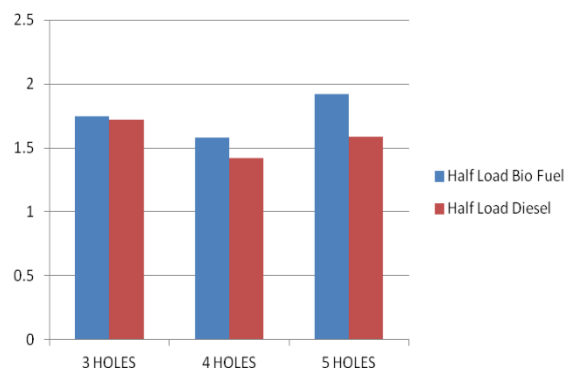


Figure 2(b): Indicated Power at Half Load

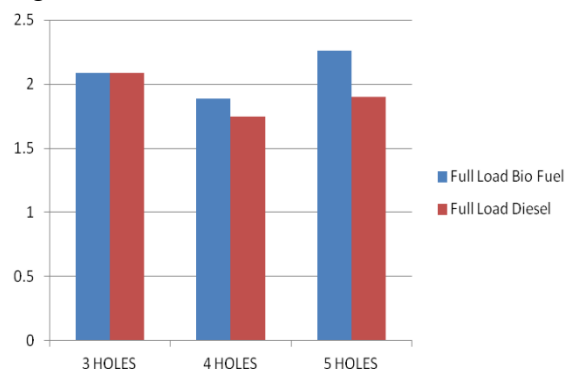


Figure 2(c): Indicated Power at Full Load

Comparison is made with pairs of pillar diagrams at each configuration with bio fuel and diesel. It was observed that the increase in indicated power is more with 5 hole injector.

Hence we can say that the increase in indicated power is due to the improved combustion phenomena inside the cylinder which could be due to improved atomization of bio fuel.

Brake thermal efficiency:

Brake thermal efficiency of engine when operated by biofuel and diesel at various loads (3 loads) with three different types of nozzles is shown in figure 3

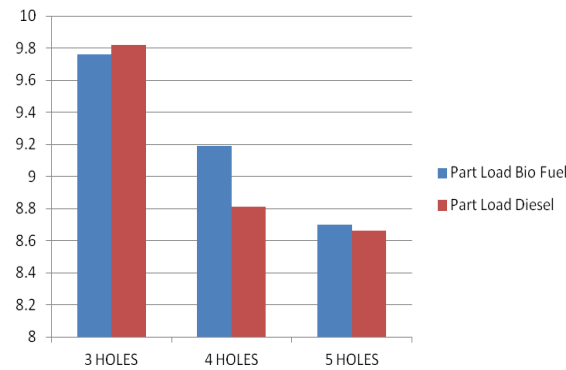


Figure 3(a): Brake Thermal Efficiency at Part Load

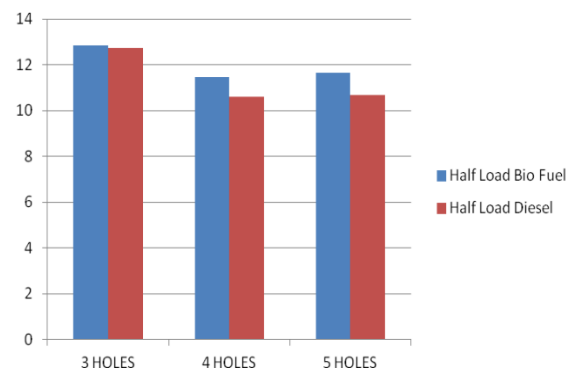


Figure 3(b): Brake Thermal Efficiency at Half Load

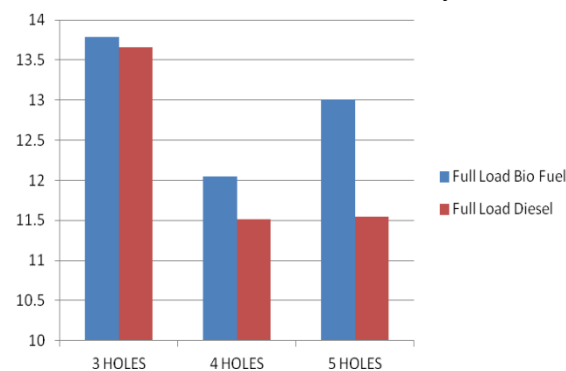


Figure 3(c): Brake Thermal Efficiency at Full Load

Above graphs reveals that the Brake Thermal efficiency is more with bio fuel than that of diesel counter part in almost all the cases.

Indicated Thermal Efficiency:

Indicated thermal efficiency of engine when operated by biofuel and diesel at various loads (3 loads) with three different types of nozzles is shown in figure 4

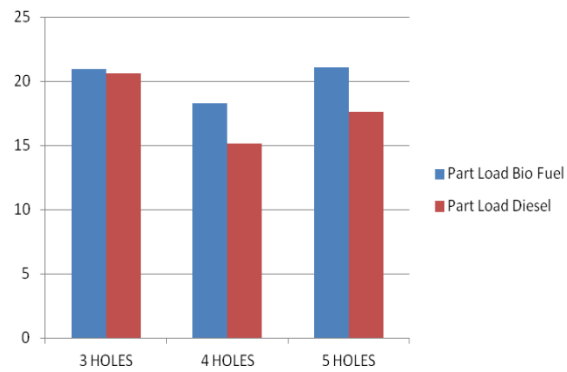


Figure 4(a): Indicated Thermal Efficiency at Part Load

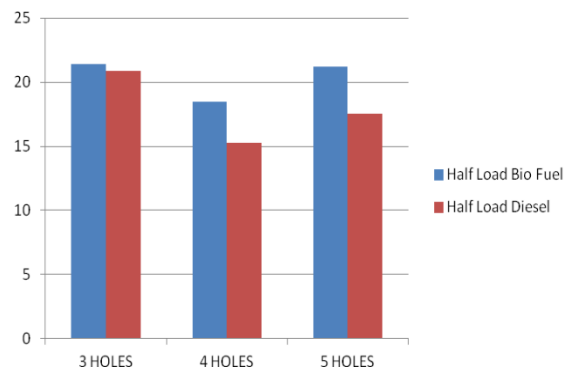


Figure 4(b): Indicated Thermal Efficiency at Half Load

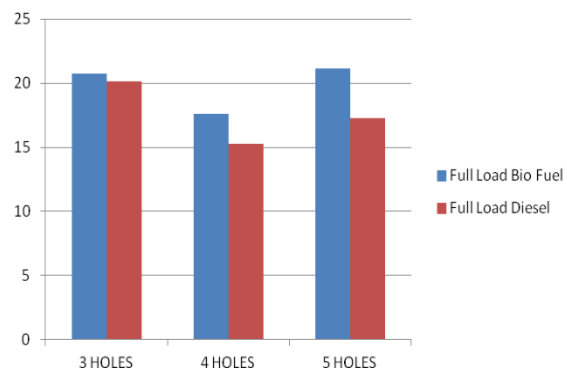


Figure 4(c): Indicated Thermal Efficiency at Full Load

Above graphs reveals that the Indicated Thermal efficiency is more with bio fuel than that of diesel counter part in almost all the cases.

Mechanical efficiency

Mechanical efficiency of engine when operated by biofuel and diesel at various loads (3 loads) with three different types of nozzles is shown in figure 5

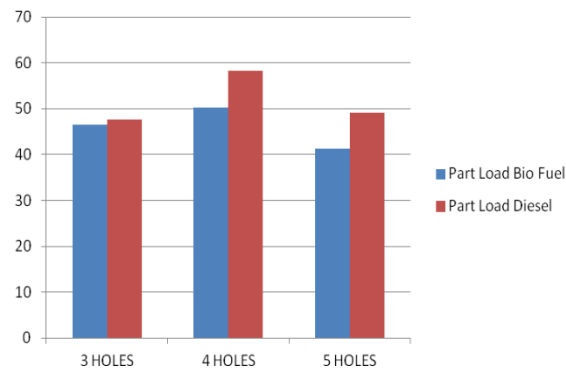


Figure 5(a): Mechanical Efficiency at Part Load

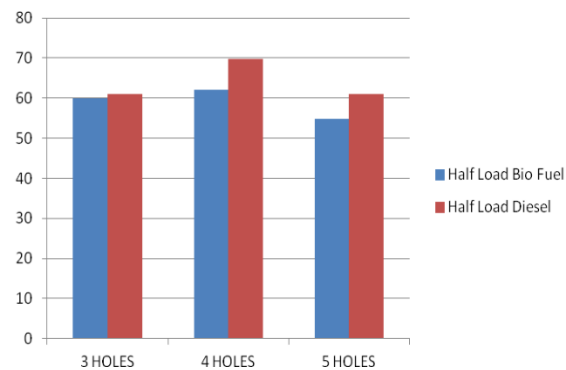


Figure 5(b): Mechanical Efficiency at Half Load

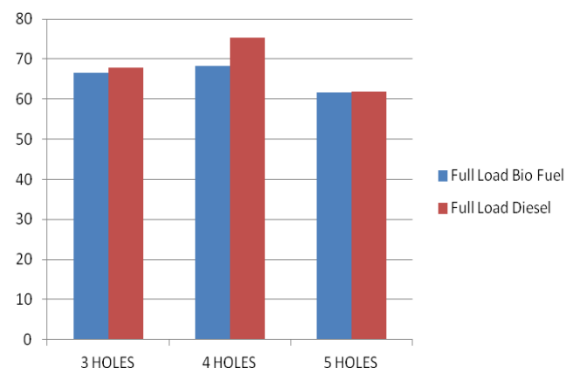


Figure 5(c): Mechanical Efficiency at Full Load

Above graphs reveals that the Mechanical Efficiency is more with bio fuel than that of diesel counterpart in almost all the cases.

Conclusions

1. Specific fuel consumption is observed to be little higher with the increase in number of holes on the injector.
2. Increase of indicated power with biofuel is more to that of diesel counterpart in all the cases which might be due to the improved combustion phenomena because of improved atomization of fuel due to multiple holes on the nozzle.
3. Indicated thermal efficiency, brake thermal efficiency and mechanical efficiency were observed to be higher in case of biofuel than that its diesel counterpart. And no sacrifice in efficiency is observed in all the cases of nozzles.
4. Four-hole nozzles shall be comfortably used with biofuel with little sacrifice in SFC and almost similar efficiencies as that of the conventional nozzles.

REFERENCES

- [1] Ravi Kadiyala, B. V. Appa Rao, S. Chandra Prasad, Ch. Satyanarayana, and I. N. Nirnjan kumar “Some comparative performance studies on DI diesel engine with pungam methyl ester and diesel oil,” proceedings of 19th national conference of I.C Engines and Combustion, Annamalai university, Chidambaram. Dec 21-23, 2005, pp. 47-54.
- [2] Cenk Sayin, Metin Gumus, Mustafa Canakci “Influence of injector hole number on the performance and emissions of a DI diesel engine fueled with biodiesel-diesel fuel blends”, Applied thermal engineering 61, 2013, pp 12-128
- [3] V.I.E. Ajiwe1, V.O. Ajibola and C.M.A.O. Martins “Biodiesel fuels from palm oil, palm oil methylester and ester-diesel blends” Bull. Chem. Soc. Ethiop. 2003, 17(1), 19-26
- [4] Tate RE, Watts KC, Allen CAW, Wilkie KI. “The densities of three biodiesel fuels at temperatures up to 300 °C.” Fuel 2006; 85:1004–9.
- [5] Tate RE, Watts KC, Allen CAW, Wilkie KI. “The viscosities of three biodiesel fuels at temperatures up to 300 °C.” Fuel 2006; 85:1010–5.
- [6] Lee CS, Park SW, Kwon SI. “An experimental study on the atomization and combustion characteristics of biodiesel-blended fuels.” Energy Fuels 2005; 19:2201–8.
- [7] Chen PC, Wang WC, Roberts WL, Fang T. “Spray and atomization of diesel fuel and its alternative from a single – hole injector using a common rail fuel injection system.” Fuel 2013; 103:850–61.
- [8] Gao Y, Deng J, Li C. “Experimental study of the spray characteristics of biodiesel on inedible oil.” Biotechnology Adv 2009; 27:616–24.
- [9] Jose M. Desantes, Raul Payri, Antonio Garcia, and Julien Manin “Experimental Study of Biodiesel Blends’ Effects on Diesel Injection Processes.” Energy & Fuels 2009, 23, 3227–3235

Experimental Investigation of a Wing with Serrations at its Trailing Edge using Naca 0012 Airfoil

T J Prasanna Kumar, B Teja, A Rohith Kumar, B HarshaVardhan, A Anil Sai

Dept of Mechanical Engineering, PVP Siddhartha Institute of Technology, AP, India-520007.

Corresponding author Email: tjpk.mech@gmail.com

ABSTRACT

A wing is a type of fin that produces lift, while moving through air or some other fluid. As such, wings have streamlined cross-sections that are subjected to aerodynamic forces and act as airfoils. A wing's aerodynamic efficiency is expressed as its lift-to-drag ratio. The lift that a wing generates at a given speed and angle of attack can be one to two orders of magnitude greater than the total drag on the wing. A high lift-to-drag ratio requires a significantly smaller thrust to propel the wings through the air at sufficient lift.

Aircraft wings may feature some of the following:

- A rounded leading edge cross-section
- A sharp trailing edge cross-section
- Leading-edge devices such as slats, slots, or extensions
- Trailing-edge devices such as flaps or flaperons (combination of flaps and ailerons)
- Winglets to keep wing tip vortices from increasing drag and decreasing lift

Dihedral, or a positive wing angle to the horizontal, increases spiral stability around the roll axis, whereas anhedral, or a negative wing angle to the horizontal, decreases spiral stability. The potential applications of serrated wing are:- Aerospace applications, Hydraulic machines, and Turbine and compressor blades. Typically, aerodynamic and hydrodynamic surfaces have sharp or moderately blunt trailing edges from which the wake is developed. The strength, distribution, direction of wake, turbulence separation, vorticity, and the location of the wake where it is originated are sources of increase in drag and reduction in lift, both of which are highly undesirable.

The present work related to the field of aerodynamics and, more specifically, to a Wing for reducing drag and increasing lift on aerodynamic or on hydrodynamic surfaces with sharp and even serrations at the trailing edge of the wing. An airfoil model will be fabricated using NACA series airfoil coordinates and further investigation on aerodynamic characteristics will be done. Experimental results may be validated using low speed subsonic wind tunnel.

The flow behaviour is further characterized both experimentally and computationally in terms of aerodynamic characteristics such as Lift Drag and side forces. Respective Lift, Drag, and side forces Vs Angle of attack plots may be plotted.

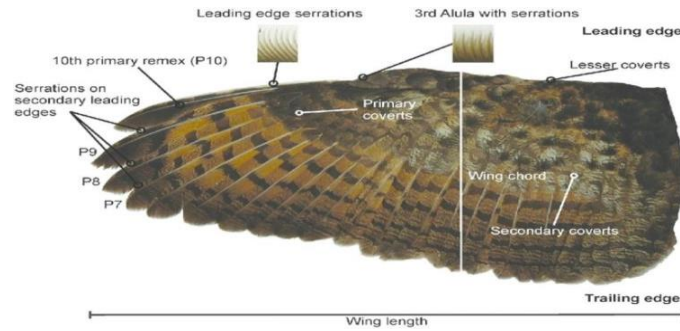
1. INTRODUCTION

In recent centuries the word's meaning has extended to include lift producing appendages of insects, bats, pterosaurs, boomerangs, some sail boats and aircraft, or the inverted Airfoil on a

race car that generates a downward force to increase traction.

In nature wings have evolved in dinosaurs, birds, mammals, fish, reptiles and plants as means of locomotion. Various species of penguins and other flighted or flightless water birds such as auks, cormorants, guillemots, shear waters, eider and scoter ducks and diving petrels are avid swimmers, and use their wings to propel through water.

1.1 WING OF A BIRD:



1.2 Airfoil of a wing

An Airfoil is the shape of a wing, blade (of a propeller, rotor, or turbine), or sail (as seen in cross-section). An Airfoil- shaped body moved through a fluid produces an aerodynamic force. The component of this force perpendicular to the direction of motion is called lift. The component parallel to the direction of motion is called drag. Subsonic flight Airfoils have a characteristic shape with a rounded leading edge, followed by a sharp trailing edge, often with a symmetric curvature of upper and lower surfaces. Foils of similar function designed with water as the working fluid are called hydrofoils.

Most foil shapes require a positive angle of attack to generate lift, but cambered Airfoils can generate lift at zero angle of attack. This "turning" of the air in the vicinity of the Airfoil creates curved stream lines, resulting in lower pressure on one side and higher pressure on the other. This pressure difference is accompanied by a velocity difference, via Bernoulli's principle, so the resulting flow field about the Airfoil has a higher average velocity on the upper surface than on the lower surface.

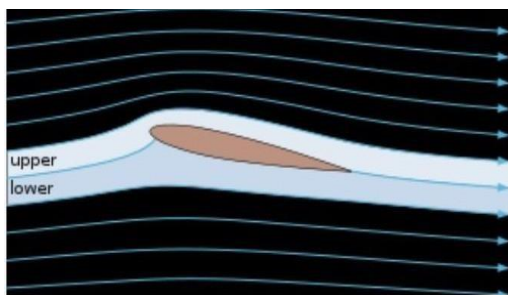


Fig1.1 Streamlines around a NACA 0012 Airfoil

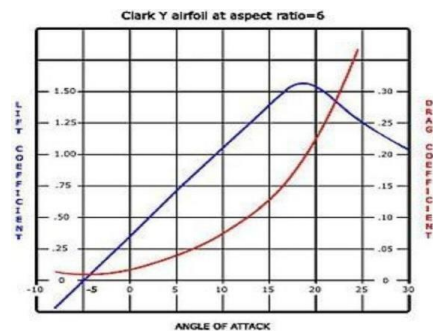


Fig1.2 Lift and Drag curves at moderate angle of attack typical Airfoil

A fixed-wing aircraft's wings, horizontal, and vertical stabilizers are built with Airfoil-shaped cross sections, as are helicopter rotor blades. Airfoils are also found in propellers, fans, compressors and turbines. Sails are also Airfoils, and the underwater surfaces of sailboats, such as the center board and keel, are similar in cross-section and operate on the same principles as Airfoils.

Swimming and flying creatures and even many plants and sessile organisms employ Airfoils/hydrofoils: common examples being bird wings, the bodies of fish, and the shape of sand dollars. An Airfoil-shaped wing can create down force on an automobile or other motor vehicle, improving traction. Any object with an angle of attack in a moving fluid, such as a flat plate, a building, or the deck of a bridge, will generate an aerodynamic force (called lift) perpendicular to the flow. Airfoils are more efficient lifting shapes, able to generate more lift (upto a point), and to generate lift with less drag.

A lift and drag curve obtained in wind tunnel testing is shown on the right. The curve represents an Airfoil with a positive camber so some lift is produced at zero angle of attack. With increased angle of attack, lift increases in a roughly linear relation, called the slope of the lift curve. At about 18 degrees this Airfoil stalls, and lift falls off quickly beyond that. The drop in lift can be explained by the action of the upper-surface boundary layer, which separates and greatly thickens over the upper surface at and past the stall angle.

Airfoil design is a major facet of aerodynamics. Various Airfoils serve different flight regimes. A symmetric Airfoil can generate lift at zero angle of attack, while a cambered Airfoil may better suit frequent inverted flight as in an aerobatic airplane. In the region of the ailerons and near a wingtip, a symmetric Airfoil can be used to increase the range of angles of attack to avoid spin-stall. Thus, a large range of angles can be used without boundary layer separation. Subsonic Airfoils have a round leading edge, which is naturally insensitive to the angle of attack.

A laminar flow wing has a maximum thickness in the middle camber line. Analyzing the Navier-Stokes equations in the linear regimes shows that a negative pressure gradient along the flow has the same effect as reducing the speed. So, with the maximum camber in the middle, maintaining a laminar flow over a larger percentage of the wing at a higher cruising speed is possible. However, some surface contamination will disrupt the laminar flow, making it turbulent.

1.3 Airfoil terminology

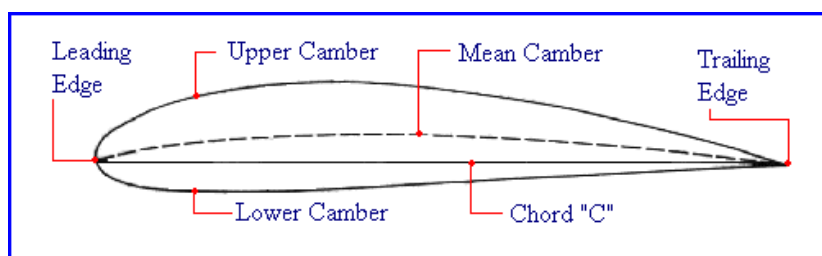


Fig: 1.3 Airfoil Nomenclature

The various terms related to Airfoils are defined below:

The suction surface (a.k.a. upper surface) is generally associated with higher velocity and lower static pressure. The pressure surface (a.k.a. lower surface) has a comparatively higher static pressure than the suction surface. The pressure gradient between these two surfaces contributes to the lift force generated for a given Airfoil.

The geometry of the Airfoil is described with a variety of terms:

- The leading edge is the point at the front of the Airfoil that has maximum curvature (minimum radius).
- The trailing edge is defined similarly as the point of minimum curvature at the rear of the Airfoil.
- The chord line is the straight line connecting leading and trailing edges.
- The chord length, or simply **chord**, is the length of the chord line. That is the **reference dimension** of the Airfoil section.
- The mean camber line or mean line is the locus of point's midway between the upper and lower surfaces. Its shape depends on the thickness distribution along the chord; the thickness of an Airfoil varies along the chord.

It may be measured in either of two ways:

Thickness measured perpendicular to the camber line. This is sometimes described as the "American convention". Thickness measured perpendicular to the chord line. This is sometimes described as the "British convention". Some important parameters to describe an Airfoil's shape are its camber and its thickness. For example, an Airfoil of the NACA 4-digit series such as the NACA 2415 (to be read as 2–4–15) describes an Airfoil with a camber of 0.02 chord located at 0.40 chord, with 0.15 chord of maximum thickness.

1.4 Aerodynamic forces on wing

The aerodynamic force is the force exerted on a body by the air (or some other gas) in which the body is immersed, and is due to the relative motion between the body and the gas. The aerodynamic force arises from two causes:

The normal force due to the pressure on the surface of the body

The shear force due to the viscosity of the gas, also known as skin friction

Pressure acts locally, normal to the surface, and shear force acts locally, parallel to the surface. The net aerodynamic force over the body is due to the pressure and shear forces integrated over the total exposed area of the body.

1.4.1 Lift (force)

Lift is the force that directly opposes the weight of an airplane and holds the airplane in the air. Lift is generated by every part of the airplane, but most of the lift on a normal airliner is generated by the wings. Lift is a mechanical aerodynamic force produced by the motion of the airplane through the air. Because lift is a force, it is a vector quantity, having both a magnitude and a direction associated with it. Lift acts through the center of pressure of the object and is directed perpendicular to the flow direction.

1.4.2 CO-EFFICIENT OF LIFT (C_L)

$$C_L = \left(\frac{L}{\frac{1}{2}\rho V_\infty^2 S} \right) \quad \text{Eq-1}$$

Where,

L, ρ , **V**, **S**, C_L are Lift, Density of free stream, Velocity of free stream, Area of finite wing, and coefficient of lift respectively.

1.4.3 Drag (force)

Drag is the aerodynamic force that opposes an aircraft's motion through the air. Drag is generated by every part of the airplane. Drag is a force and is therefore a vector quantity having both a magnitude and a direction. Drag acts in a direction that is opposite to the

motion of the aircraft. Lift acts perpendicular to the motion. There are many factors that affect the magnitude of the drag. Many of the factors also affect lift but there are some factors that are unique to aircraft drag.

1.4.4 CO-EFFICIENT OF DRAG (C_D)

$$C_D = \left(\frac{D}{\frac{1}{2}\rho V_\infty^2 S} \right) \quad \text{Eq-2}$$

Where

D , ρ , V , S , C_D are lift, density of free stream, velocity of free stream, area of finite wing, and coefficient of drag respectively.

1.5 Types of drag

1.5.1 Pressure drag

Pressure drag arises because of the shape of the object. The general size and shape of the body are the most important factors in form drag; bodies with a larger presented cross-section will have a higher drag than thinner bodies; sleek ("streamlined") objects have lower form drag.

1.5.2 Skin friction drag

Skin friction drag arises from the friction of the fluid against the "skin" of the object that is moving through it. Skin friction arises from the interaction between the fluid and the skin of the body, and is directly related to the wetted surface, the area of the surface of the body that is in contact with the fluid.

Various techniques are used to study the actual airflow around the geometry and compare it with theoretical results, which must also take into account the Reynolds number and Mach number for the regime of operation.

2. Experimentation on Wind tunnel



Figure 2.1 Low Speed Subsonic Wind tunnel Setup

2.1 Forces and Moments Measurements

With the model mounted on a force balance, one can measure lift, drag, lateral forces, yaw, roll, and pitching moments over a range of angle of attack. This allows one to produce common curves such as lift coefficient versus angle of attack (shown).

2.2 Experimentation of Wing with NACA 0012 airfoil without serrations at trailing edge



Figure 2.2 Finite wing designed and fabricated using NACA 0012 airfoil coordinates
The NACA airfoils are airfoil shapes for aircraft wings developed by the National Advisory Committee for Aeronautics (NACA). The shape of the NACA airfoils is described using a series of digits following the word "NACA". The parameters in the numerical code can be entered into equations to precisely generate the cross-section of the airfoil and calculate its properties.

For example, the NACA 2412 airfoil has a maximum camber of 2% located 40% (0.4 chords) from the leading edge with a maximum thickness of 12% of the chord.

The aerodynamic of Airfoils has been studied by Kutta (1902) on thin Airfoils and Joukowski (1905) on Airfoils with thickness. These Airfoils were obtained from a circular cylinder by conformal mapping. The theory of Joukowski for 2-D flow, so for an infinite wing, marks the beginning of the modern aerodynamic. At the same time, appeared the works of pioneers of the aviation, the Wright brothers, who based their study on the analysis of the stability of the plane made by Lanchester in 1894. They had a good understanding of wing and Airfoil behavior well beyond that of other experimenters at that time. During twenty years, the theories of Joukowski and Prandtl have been the starting points of many theoretical and experimental works, and permit us in this context to describe the aerodynamic properties of the elliptical wing and of arbitrary plan form. This elliptical wing leads to an also elliptical distribution for the local circulation and to the famous minimum induce drag.

3 ANALYSIS OF WING WITHOUT SERRATIONS

Design and fabricate of NACA 0012 airfoil. Performed an experiment to find out the Aerodynamics forces over modeled finite wing such as Lift and Drag forces. Perform an experiment on wing with without serrations to find out the Aerodynamic characteristics such as Lift force, Drag forces. Then performed calculations on the observations and converted them to Non-Dimensional form. Finally plotted graphs and compared the results.

3.1 Observations from Wind tunnel testing:

Aerodynamic parameters obtained from the wind tunnel experiment were tabulated for various angles of attack for both the normal wing section as well as for the serrated wing. The important parameters which receive the prime importance amongst all are the coefficient of lift, and coefficient of drag.

Table 3.1 Lift forces obtained at different Angle of attack, α

S.No	Angle of Attack, α in Degrees	Lift Force, L
1	0	0
2	2	11.76
3	4	18.816
4	6	26.264
5	8	34.104
6	10	39.984
7	12	45.472
8	15	43.512

Table 3.2 Drag forces obtained at different Angle of attack, α

S.No	Angle of Attack, α in Degrees	Drag Force, D
1	0	0
2	2	0.392
3	4	0.392
4	6	0.784
5	8	1.96
6	10	2.744
7	12	3.528
8	15	5.88

Table 3.3 Coefficient of Lift obtained at different Angle of attack, α

S.No	Angle of Attack, α in Degrees	Coefficient of Lift, C_L
1	0	0
2	2	0.3
3	4	0.48
4	6	0.67
5	8	0.87
6	10	1.02
7	12	1.16
8	15	1.11

Table: 3.4 Coefficient of Drag, obtained at different Angle of attack, α

S.No	Angle of Attack, α in Degrees	Coefficient of Drag, C_D
1	0	0
2	2	0.392
3	4	0.392
4	6	0.784
5	8	1.96
6	10	2.744
7	12	3.528
8	15	5.88

3.2 ANALYSIS OF SERRATED WING (NACA 0012) IN WIND TUNNEL

The use of passive flow control methods for enhancing aerodynamic characteristics has been the subject of much research. Inspired by “Tubercles” found on hump back whales which have been shown to increase the lift coefficient in the post stall region, thus increasing maneuverability of the whale. These modifications were found to increase the maximum lift coefficient compared to an unmodified wing section at a constant chord Reynolds number, however the now exposed bluntness also increased the drag coefficient. In a recent study, Gruber et al experimentally studied the Airfoil noise reduction by using trailing edge modifications such as slotted, saw-tooth and random profiles. It was shown that by modifying the trailing edge the scattering efficiency and hence the noise produced by the Airfoil has been substantially reduced. Similarly it has been shown by Xiao Liu that the trailing-and leading edge serrations can also significantly change the aerodynamic performance of the Airfoil.



Fig: 2.4 Schematic of a serrated wing

This work had shown the efficiency of wing with serrations at its trailing edge. Overall comparative study with the experimental results obtained from wind tunnel testing's as well as with the modified wing section is also presented. Design and Fabricated a finite wing with NACA 0012 airfoil configuration. Performed an experiment to find out the Aerodynamic forces such as Lift, Drag. Cutting a V shaped serrations for the same wing section with an angle of 30° in between the adjacent serrations at the trailing edge of the wing section. Again performed same experiment on the serrated wing to find the Aerodynamic forces such as Lift, Drag. Performed calculations on the observations and converted them to Non-dimensional form. Finally plotted the graphs and compared the results.

3.3 Observations from Wind tunnel testing:

Aerodynamic parameters obtained from the wind tunnel experiment were tabulated for various angles of attack for both the normal wing section as well as for the serrated wing. The important parameters which receive the prime importance amongst all are the coefficient of lift, and coefficient of drag.

Table-3.5 Lift force (L) Versus Angle of Attack (α)

S.No	Angle of Attack, α in Degrees	Lift Force, L
1	0	0
2	2	11.6424
3	4	17.9928
4	6	25.0488
5	8	31.3992
6	10	37.7496
7	12	41.9832
8	15	40.572

Table-3.6 Drag force (D) Versus Angle of Attack (α)

S.No	Angle of Attack, α in Degrees	Drag Force, D
1	0	0
2	2	0
3	4	0.3528
4	6	0.7056
5	8	1.4112
6	10	2.1168
7	12	2.8224
8	15	4.2336

Table-3.7 Lift Coefficient versus Angle of Attack

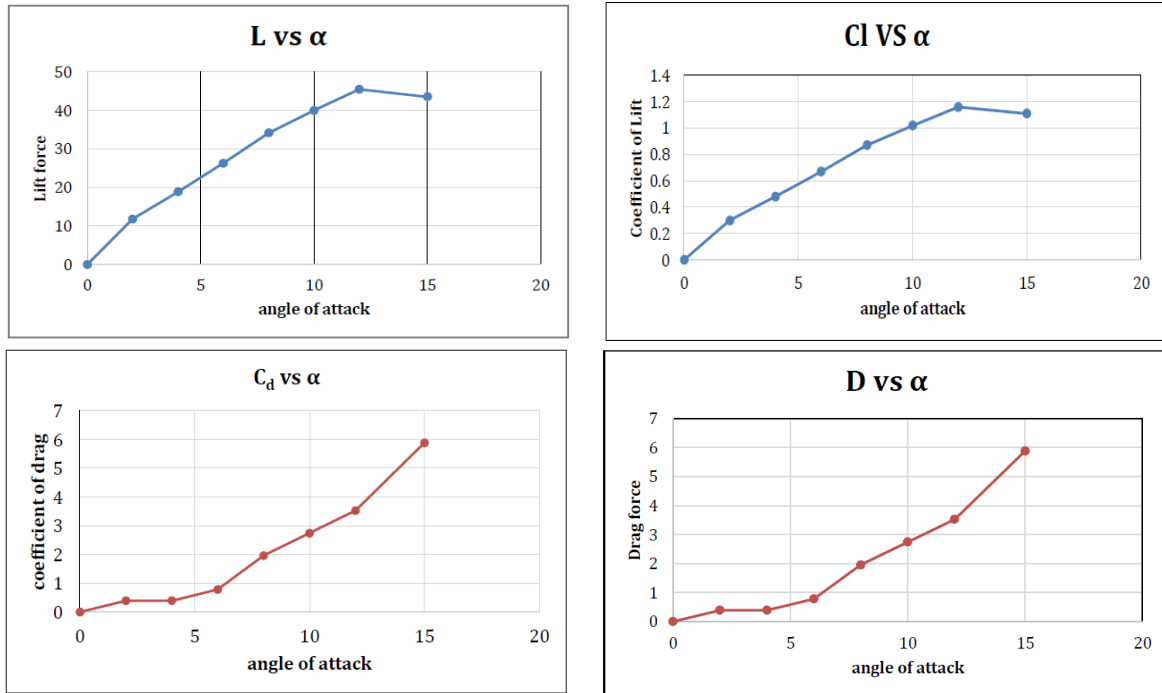
S.No	Angle of Attack, α in Degrees	Coefficient of Lift, C_L
1	0	0
2	2	0.33
3	4	0.51
4	6	0.71
5	8	0.89
6	10	1.07
7	12	1.19
8	15	1.15

Table-3.8 Coefficient of Drag Versus Angle of Attack

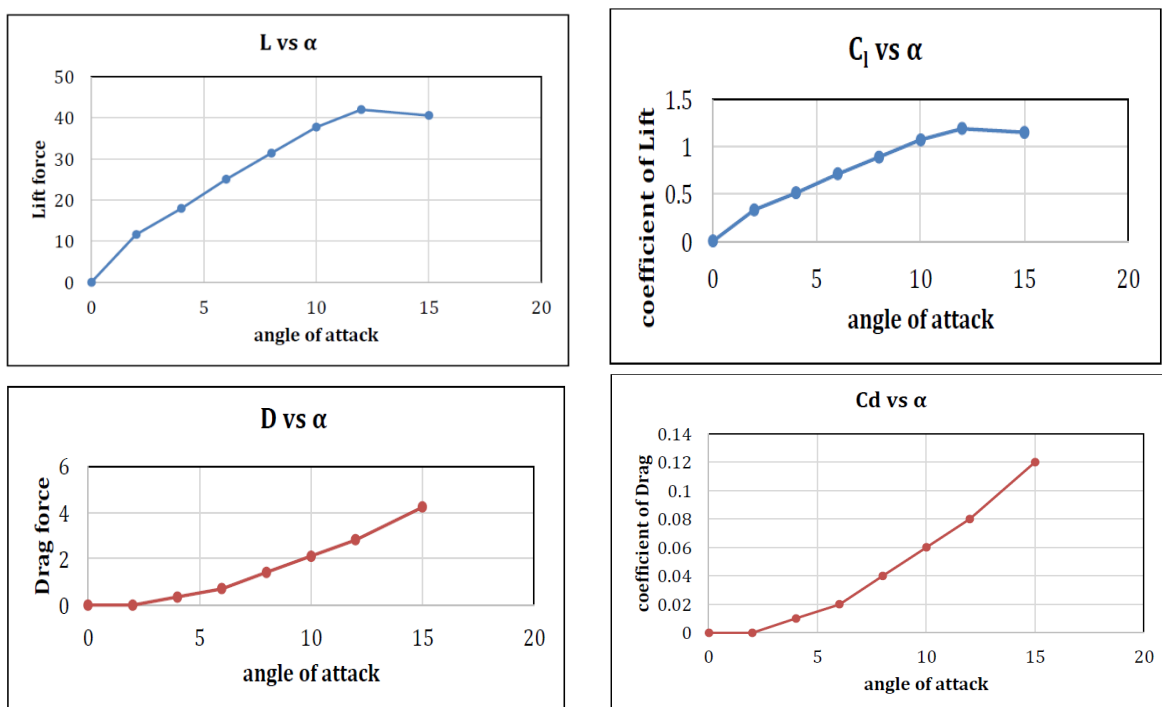
S.No	Angle of Attack, α in Degrees	Coefficient of Drag, C_D
1	0	0
2	2	0
3	4	0.01
4	6	0.02
5	8	0.04
6	10	0.06
7	12	0.08
8	15	0.12

4. RESULTS AND DISCUSSIONS

4.1 Coefficient of Lift & Coefficient of drag curves w.r.t different Angle of Attack plotted for both serrated and plain finite wing models

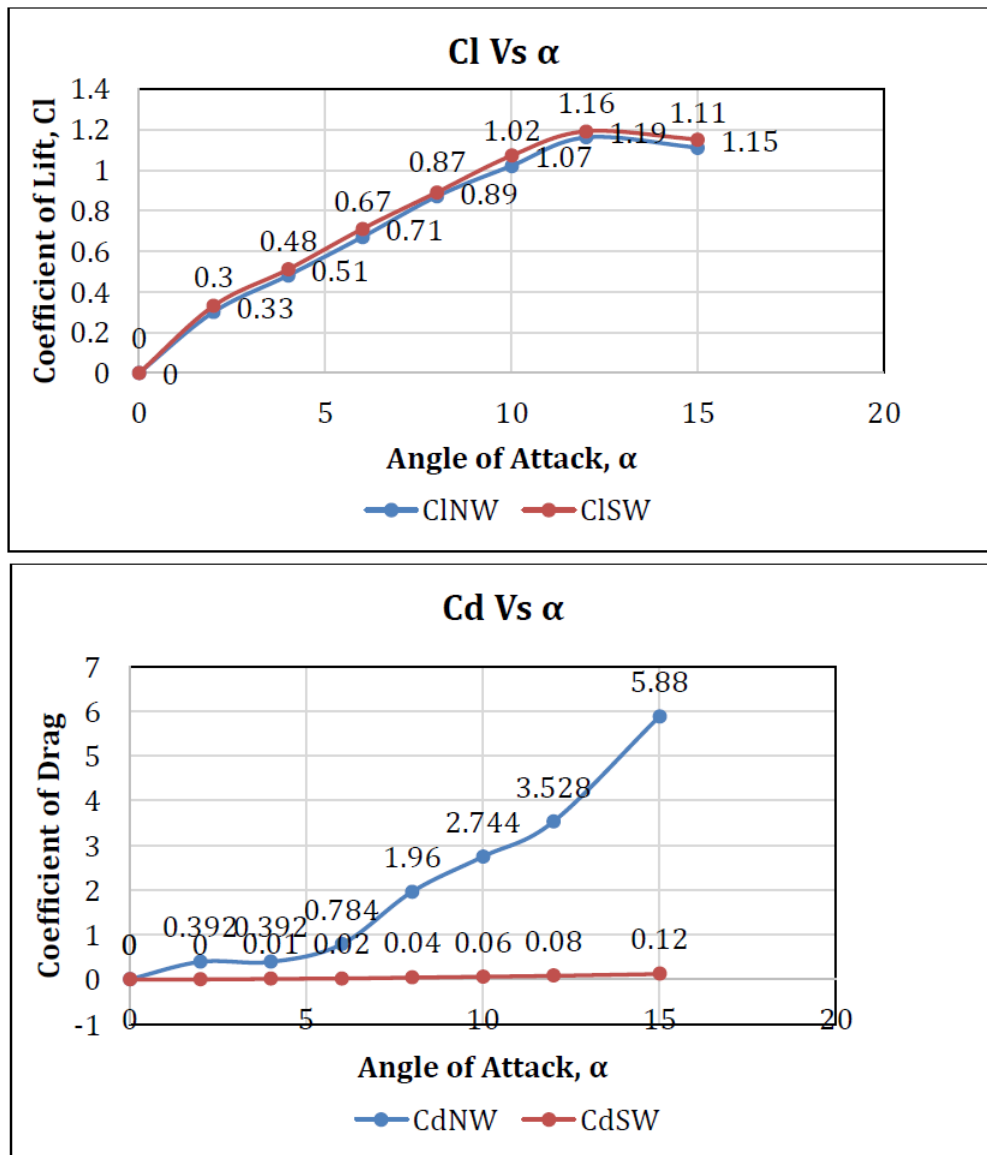


From the above plots, the $C_l, C_d, V_s \alpha$ curves are for finite wing without serrations which are close to theoretical curves of NACA 0012



From the above plots, the $C_l, C_d, V_s \alpha$ curves are for finite wing with serrations, it is observed that slight increase in Coefficient of lift, where as there is drag reduction at typical angle of attack.

4.2 Comparative Plots between finite Wing model with Serrations and Without Serrations



5. CONCLUSIONS

The results of saw tooth serrations have shown that for wind speed of 40m/s considered in this study, the lift coefficient of the NACA 0012 base wing section increases up to 7% compared to then on - serrated NACA 0012 base wing section over the angle of attack (α) range of 0° to 15°. For the same range of angles of attack, the coefficient of drag of the NACA 0012 base wing section with saw tooth serrations showed decrement of 14.28% compared to the NACA 0012 base wing section without these serrations. The results also show that the critical angle of attack (α) of the NACA 0012 base wing section with saw tooth serrations has an increase in its value compared to the wing section without these serrations.

6. REFERENCES

- [1] John D. Anderson, Fundamentals of Aerodynamics, Tata McGraw Hill publications 2nd edition
- [2] E. Lo Houghton and PW Carpenter, Aerodynamics for Engineering Students, 5th edition, Butterworth-Heinerman
- [3] Daniel P Raymer, Aircraft Design: A Conceptual Approach, 5th edition, AIAA Education Series
- [4] E. N. Jacobs, K. E. Ward, & R. M. Pinkerton, “The Characteristics of 78 Related Airfoil Sections from Tests in the Variable-Density Wind Tunnel”, 1933, NACA report number 460
- [5] Eastman N. Jacobs and Albert Sherman, “Airfoil Section Characteristics as Affected By variations of the Reynold’s number” NACA report number 586
- [6] Darrol Stinton, the Design of the Aeroplane. BSP Professional Books (October 1985)
- [7] M. Gruber, P. F. Joseph, and T. P. Chong, Experimental investigation of airfoil self noise and turbulent wake reduction by the use of trailing edge serrations, in 16th AIAA/CEAS Aeroacoustics Conference (31st AIAA Aeroacoustics Conference), 2010.
- [8] H. C. Seetharam, E. J. Rodgers, and J. W. H. Wentz, “Experimental Studies of Flow Separation of the NACA 2412 Airfoil at Low Speeds,” 2019.
- [9] S. Kandwal, Dr. S. Singh Computational Fluid Dynamics Study of Fluid Flow and Aerodynamic Forces on an Airfoil IJERT, Vol. 1 Issue 7, September – 2012.
- [10] H. Abbot, A von Doenhoff., “Theory of Wing Sections, Including summary of airfoil data”, Dover publications Inc. New York.

A Study on effect of stacking sequence in SLJ with laminated FRP composite

M. Radhadevi^{1*}, Dr. G. Vijay Kumar²

¹ Asst. Professor, Dept. of Mechanical Engineering, PVP Siddhartha Institute of Technology, Andhra Pradesh, India.

² Professor, Dept. of Mechanical Engineering, PVP Siddhartha Institute of Technology, Andhra Pradesh, India.

*Corresponding author e-mail id: devi.radham@gmail.com

Abstract:

In the present research work, effect of stacking sequence in the Single Lap Joint (SLJ) made up of laminated FRP composite is studied to investigate the interlaminar normal and shear stresses. 3D finite element model is prepared and carried out the Geometrical non-linear analysis by varying the stacking sequence of laminate composite. The interlaminar stresses (normal and Shear stresses) are greatly influenced w.r.t. stacking sequence. At various stacking sequences ranging from 0° to 90° is analyzed and found the interlaminar stress values at the interfaces of adhered and adhesive of lap joint. The results from the analysis will be useful for efficient design of Single lap joint.

Keywords: SLJ, Interlaminar Stresses, Non-linear analysis, stacking sequence.

INTRODUCTION

S.k. Panigrahi and B. Pradhan [1] analyzed the propagation of damage in the adhesively bonded single lap joint. Vijeta et al. [2] studied the interlaminar stresses in the SLJ made of laminate FRP composite through non-linear finite element analysis. Murat Demir Aydin [3] carried out the non - linear analysis of SLJ to evaluate stress distribution on adherends (AS4/3501-6) and adhesive (FM73) layer. M. Khodja et al. [4] developed fem analysis and observed the importance of studying peel and shear stresses in the overlap region of the SLJ. R.R. Das et al. [5] analyzed the tubular joints made of Boron / Epoxy FRP composites to investigate the adhesion failure. S. Kumar and S. Tampi [6] developed 2D analytical model & FEM model for SLJ to predict the stresses under mechanical & thermal loading conditions made of similar/dissimilar adherends. Sk. Panigrahi [7] studied the Single Lap Joint which consists of pre-embedded delaminated FRP adherends to evaluate the interlaminar stresses and SERR values. K. Senthil et al. [8] developed FEM model to investigate the effect of debond shape, size and debond growth on structural behavior of SLJ. F. Kadioglu [9] investigated the behavior of SLJ under buckling loading conditions with increase in adherends thickness. F. Kadioglu [10] studied the behavior of SLJ made of AL6061 and AL7075 adherend materials by varying the overlap length and adherends thickness.

The main objective of present work is to investigate the effect of stacking sequence in SLJ to evaluate interlaminar stresses at the interfaces of adherends and adhesive.

PROBLEM MODELLING AND METHODOLOGY

The present research problem deals with 3D geometrical nonlinear analysis of SLJ made of laminated FRP composite by varying the stacking sequence of the lap joint to evaluate the interlaminar stresses. The Model is prepared using ANSYS software. The model dimensions of SLJ are shown in Fig. 1 (dimensions of the adherends are taken as: length =100 mm, width = 25mm and thickness=0.5mm. Overlap length of the joint = 12.5 mm and thickness of adhesive = 0.1mm). Theory of elasticity method is used in solving the problem. Finite element mesh is generated using ‘SOLID 45’ – 3D brick element using three-dimensional stress-strain relations. The element size in the bonded region (Fig. 2) is 0.25mm x 0.25mm x 0.125mm for the adherends and 0.25mm x 0.25mm x 0.05mm for adhesive layer.

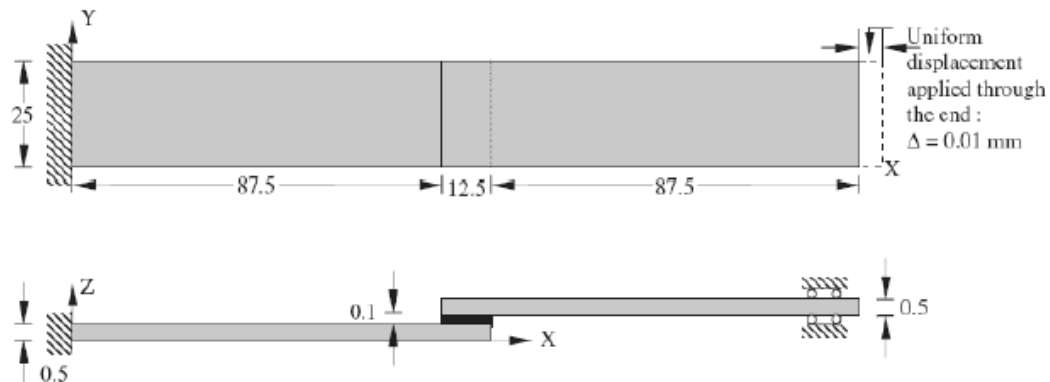


Fig. 1- Details of Single lap joint [1].

In the present work, the finite element model is validated and later this model is extended for geometric nonlinear analysis of SLJ made of angle-ply FRP adherends bonded with epoxy resin adhesive subjected to uniform longitudinal loading. 10MPa of uniform longitudinal load in 5 steps is used for linear and geometric non-linear analysis. One side of the joint is fixed and the other side is constricted to have only longitudinal displacement. In this work, the effect of stacking sequence in the single lap joint is analyzed through investigation of Inter-laminar normal stress (σ_{zz}), and Inter-laminar shear stresses (τ_{zx} , in longitudinal and τ_{yz} in transverse plane) at the interfaces of adherends and adhesive, and at the central plane of adhesive. The following laminate stacking sequences are considered for the present research work.

UD1 -	0°/0°/0°/0°,	APS 30 -	30°/-30°/-30°/30°,
UD2 -	90°/90°/90°/90°,	APAS 30 -	30°/-30°/30°/-30°,
CPS1 -	0°/90°/90°/0°,	APS 45 -	45°/-45°/-45°/45°,
CPS2 -	90°/0°/0°/90°,	AP AS 45 -	45°/-45°/45°/-45°,
CP AS 1 -	0°/90°/0°/90°,	APS 60 -	60°/-60°/-60°/60° and
CP AS 1 -	90°/0°/90°/0°,	APS 60 -	60°/-60°/60°/-60° .

The Mechanical properties from the reference [1] are as below.

i) FRP (adherend) T300/934 Graphite/epoxy

$E_x = 127.5$ GPa; $E_y = 9.0$ GPa; $E_z = 9.0$ GPa; $\nu_{xy} = \nu_{xz} = 0.28$; $\nu_{yz} = 0.41$,
 $G_{xy} = G_{xz} = 4.8$ GPa; $G_{yz} = 2.55$ GPa

ii) Adhesive (Epoxy)

Young's modulus (E) = 2.8 GPa; Poisson's ration (ν) = 0.4

RESULTS AND DISCUSSION

Validation:

Fig 2 shows the finite element mesh at the bonded region of SLJ. Validation of finite element model is done through comparison of stresses at interfaces of single lap joint with the results of reference [1] for linear analysis performed for axial strain loading and reference [2] for linear and geometric non-linear analysis performed for Longitudinal uniform pressure loading. Table 1 represents the comparison of maximum Inter-laminar stress values at Top Interface and Bottom interface. Close agreement between the reference and present values is found.

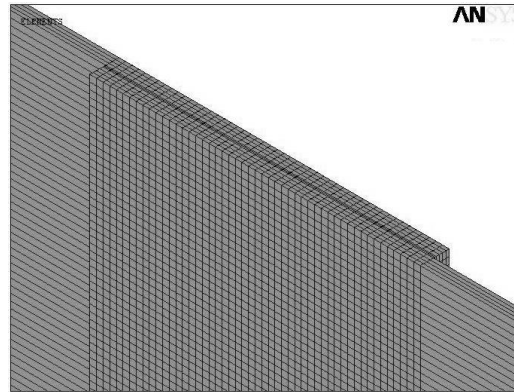


Fig. 2 - Bonded region of SLJ.

Table 1: Validation of FEM model

Location	Normal stress σ_{zz} (Mpa)				Shear stress τ_{zx} (Mpa)			
	Linear		Non-linear		Linear		Non-linear	
	Ref [1]	Present	Ref [2]	Present	Ref [1]	Present	Ref [2]	Present
Top Interface	0.40	0.41	1.24	1.25	0.39	0.40	1.16	1.18
Bottom Interface	0.39	0.39	1.25	1.27	0.38	0.39	1.15	1.17

Variation of the maximum stresses:

In the analysis of results, the non-linear analysis results are taken in to the consideration believing that the non-linear analysis is realistic.

Fig. 3 shows the linear variation of out of plane normal stress, σ_{zz} w.r.t fiber angle θ at different loads at top interface of adherends and adhesive. The normal stress, σ_{zz} observed to be maximum at Angle-ply Symmetric 60° ($60^\circ/-60^\circ/-60^\circ/60^\circ$) and minimum at Cross-ply Symmetric-1 ($0^\circ/90^\circ/90^\circ/0^\circ$). Fig. 4 shows the non-linear variation of out of plane normal stress, σ_{zz} w.r.t fiber angle θ at different loads at top interface of adherends and adhesive. The normal stress, σ_{zz} observed to be maximum at Angle-ply Symmetric 45° ($45^\circ/-45^\circ/-45^\circ/45^\circ$) and minimum at Cross-ply Anti Symmetric-1 ($0^\circ/90^\circ/0^\circ/90^\circ$).

Fig. 5 shows the linear variation of shear stress, τ_{zx} w.r.t fiber angle θ at different loads at top interface of adherends and adhesive. The shear stress, τ_{zx} observed to be maximum at Angle-ply Symmetric 60° ($60^\circ/-60^\circ/-60^\circ/60^\circ$) and minimum at Cross-ply Symmetric-1 ($0^\circ/90^\circ/90^\circ/0^\circ$). Fig. 6 shows the non-linear variation of shear stress, τ_{zx} w.r.t fiber angle θ at different loads at top interface of adherends and adhesive. The shear stress, τ_{zx} observed to be maximum at Angle-ply Symmetric 30° ($30^\circ/-30^\circ/-30^\circ/30^\circ$) and minimum at

Cross-ply Symmetric-1 ($0^\circ/90^\circ/90^\circ/0^\circ$).

Fig. 7 shows the linear variation of shear stress, τ_{yz} w.r.t fiber angle θ at different loads at top interface of adherends and adhesive. The shear stress, τ_{yz} observed to be maximum at Angle-ply Symmetric 60° ($60^\circ/-60^\circ/-60^\circ/60^\circ$) and minimum at Uni-Directional-1 ($0^\circ/0^\circ/0^\circ/0^\circ$). Fig. 8 shows the non-linear variation of shear stress, τ_{yz} w.r.t fiber angle θ at different loads at top interface of adherends and adhesive. The shear stress, τ_{yz} observed to be maximum at Angle-ply Symmetric 60° ($60^\circ/-60^\circ/-60^\circ/60^\circ$) and minimum at Cross-ply Symmetric-2 ($90^\circ/0^\circ/0^\circ/90^\circ$).

Fig. 9 shows the linear variation of out of plane normal stress, σ_{zz} w.r.t fiber angle θ at different loads at Bottom interface of adherends and adhesive. The normal stress, σ_{zz} observed to be maximum at Angle-ply Symmetric 60° ($60^\circ/-60^\circ/-60^\circ/60^\circ$) and minimum at Cross-ply Symmetric-1 ($0^\circ/90^\circ/90^\circ/0^\circ$). Fig. 10 shows the non-linear variation of out of plane normal stress, σ_{zz} w.r.t fiber angle θ at different loads at Bottom interface of adherends and adhesive. The normal stress, σ_{zz} observed to be maximum at Angle-ply Symmetric 45° ($45^\circ/-45^\circ/-45^\circ/45^\circ$) and minimum at Cross-ply Anti Symmetric-2 ($90^\circ/0^\circ/90^\circ/0^\circ$).

Fig. 11 shows the linear variation of shear stress, τ_{zx} w.r.t fiber angle θ at different loads at Bottom interface of adherends and adhesive. The shear stress, τ_{zx} observed to be maximum at Angle-ply Symmetric 60° ($60^\circ/-60^\circ/-60^\circ/60^\circ$) and minimum at Cross-ply Symmetric-1 ($0^\circ/90^\circ/90^\circ/0^\circ$). Fig. 12 shows the non-linear variation of shear stress, τ_{zx} w.r.t fiber angle θ at different loads at Bottom interface of adherends and adhesive. The shear stress, τ_{zx} observed to be maximum at Angle-ply Symmetric 30° ($30^\circ/-30^\circ/-30^\circ/30^\circ$) and minimum at Cross-ply Symmetric-1 ($0^\circ/90^\circ/90^\circ/0^\circ$).

Fig. 13 shows the linear variation of shear stress, τ_{yz} w.r.t fiber angle θ at different loads at Bottom interface of adherends and adhesive. The shear stress, τ_{yz} observed to be maximum at Angle-ply Symmetric 60° ($60^\circ/-60^\circ/-60^\circ/60^\circ$) and minimum at Uni-Directional-1 ($0^\circ/0^\circ/0^\circ/0^\circ$). Fig. 14 shows the non-linear variation of shear stress, τ_{yz} w.r.t fiber angle θ at different loads at top interface of adherends and adhesive. The shear stress, τ_{yz} observed to be maximum at Angle-ply Symmetric 60° ($60^\circ/-60^\circ/-60^\circ/60^\circ$) and minimum at Cross-ply Symmetric-2 ($90^\circ/0^\circ/0^\circ/90^\circ$).

Fig. 15 shows the linear variation of out of plane normal stress, σ_{zz} w.r.t fiber angle θ at different loads at Mid surface of adhesive. The normal stress, σ_{zz} observed to be maximum at Angle-ply Symmetric 60° ($60^\circ/-60^\circ/-60^\circ/60^\circ$) and minimum at Uni-Directional-1 ($0^\circ/0^\circ/0^\circ/0^\circ$). Fig. 16 shows the non-linear variation of out of plane normal stress, σ_{zz} w.r.t fiber angle θ at different loads at Mid surface of adhesive. The normal stress, σ_{zz} observed to be maximum at Angle-ply Symmetric 45° ($45^\circ/-45^\circ/-45^\circ/45^\circ$) and minimum at Uni-Directional-1 ($0^\circ/0^\circ/0^\circ/0^\circ$).

Fig. 17 shows the linear variation of shear stress, τ_{zx} w.r.t fiber angle θ at different loads at Mid surface of adhesive. The shear stress, τ_{zx} observed to be maximum at Angle-ply Symmetric 60° ($60^\circ/-60^\circ/-60^\circ/60^\circ$) and minimum at Uni-Directional-1 ($0^\circ/0^\circ/0^\circ/0^\circ$). Fig. 18 shows the non-linear variation of shear stress, τ_{zx} w.r.t fiber angle θ at different loads at Mid surface of adhesive. The shear stress, τ_{zx} observed to be maximum at Angle-ply Symmetric 60° ($60^\circ/-60^\circ/-60^\circ/60^\circ$) and minimum at Uni-Directional-1 ($0^\circ/0^\circ/0^\circ/0^\circ$).

Fig. 19 shows the linear variation of shear stress, τ_{yz} w.r.t fiber angle θ at different loads at Mid surface of adhesive. The shear stress, τ_{yz} observed to be maximum at Angle-ply Symmetric 45° ($45^\circ/-45^\circ/-45^\circ/45^\circ$) and minimum at Cross-Ply Symmetric-1 ($0^\circ/90^\circ/90^\circ/0^\circ$).

Fig. 20 shows the non-linear variation of shear stress, τ_{yz} w.r.t fiber angle θ at different loads at Mid surface of adhesive. The shear stress, τ_{yz} observed to be maximum at Angle-ply Symmetric 45° ($45^\circ/-45^\circ/-45^\circ/45^\circ$) and minimum at Cross-ply Symmetric-1 ($0^\circ/90^\circ/90^\circ/0^\circ$).

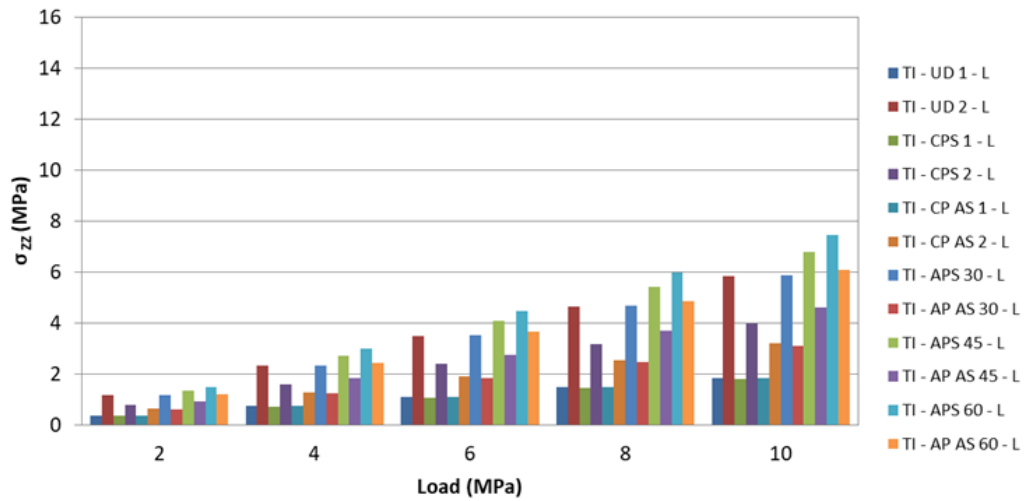


Fig. 3- Linear variation of σ_{zz} at Top Interface

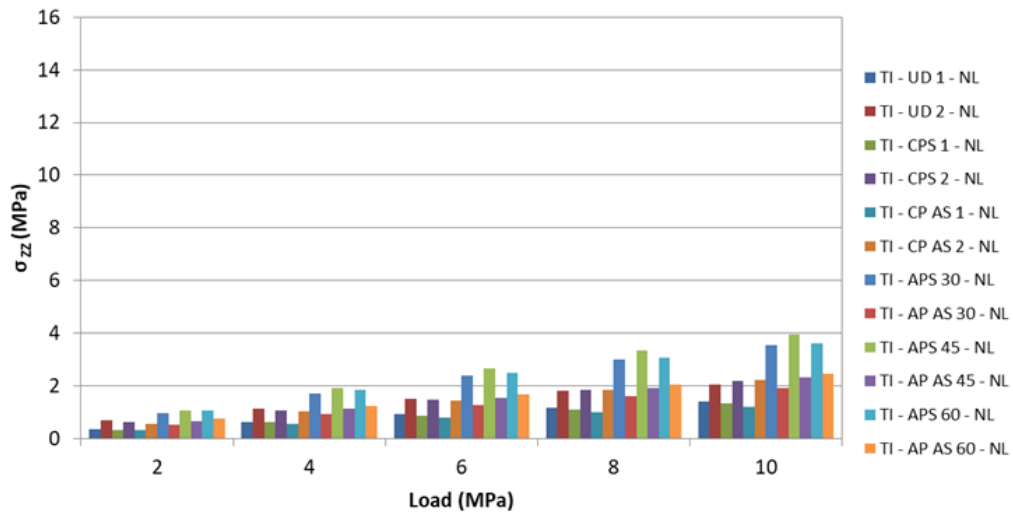


Fig. 4- Non-linear variation of σ_{zz} at Top Interface

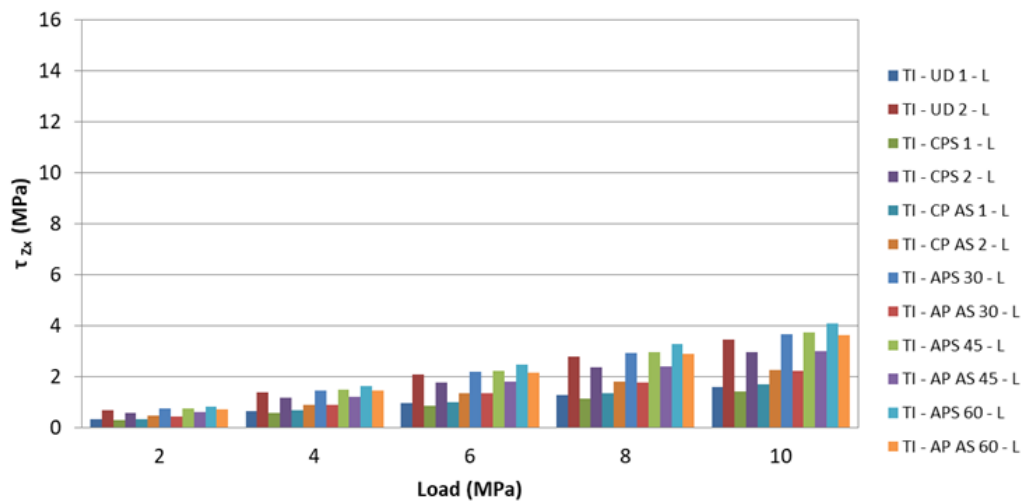


Fig. 5- Linear variation of τ_{zx} at Top Interface

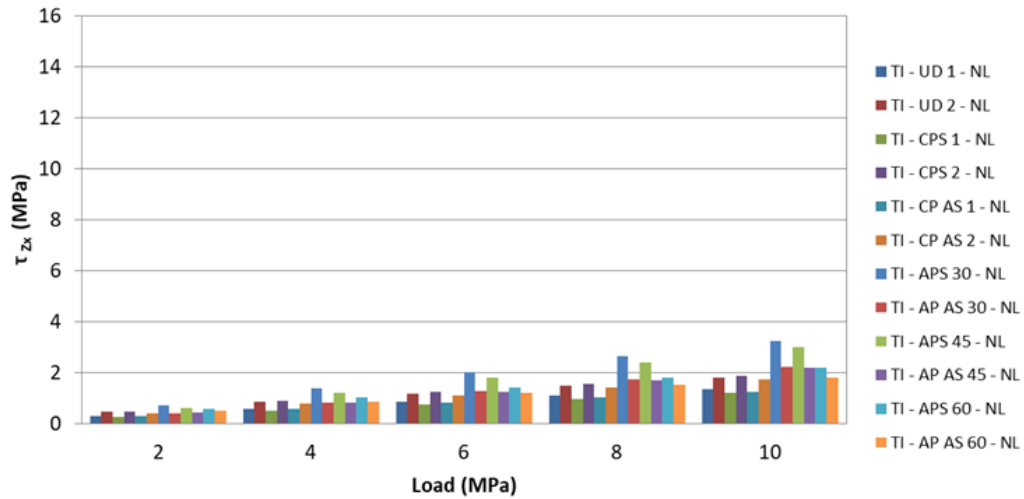


Fig. 6- Non-linear variation of τ_{zx} at Top Interface

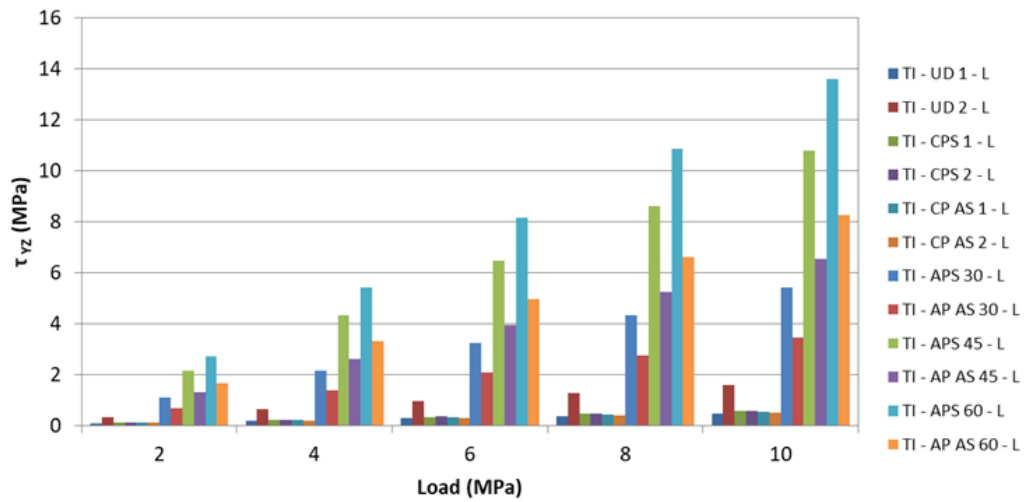


Fig. 7- Linear variation of τ_{yz} at Top Interface

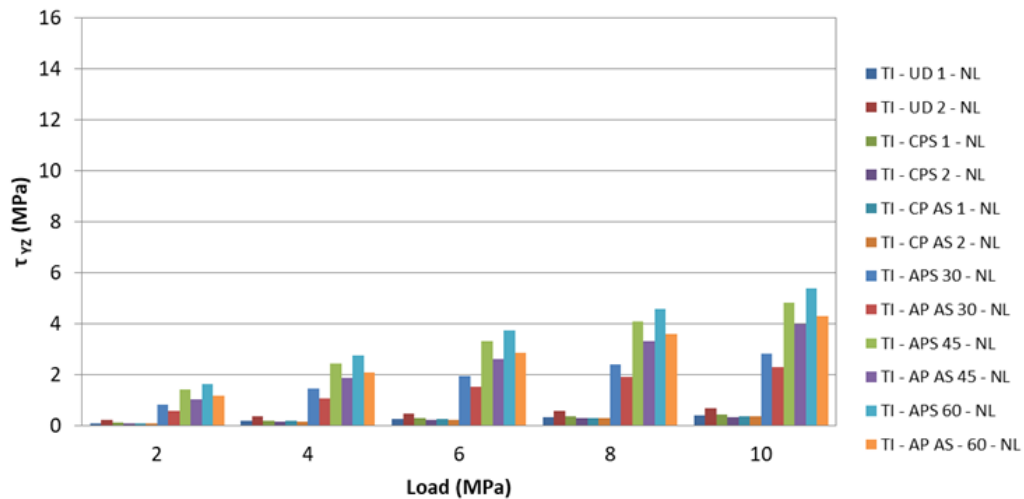


Fig. 8- Non-linear variation of τ_{yz} at Top Interface

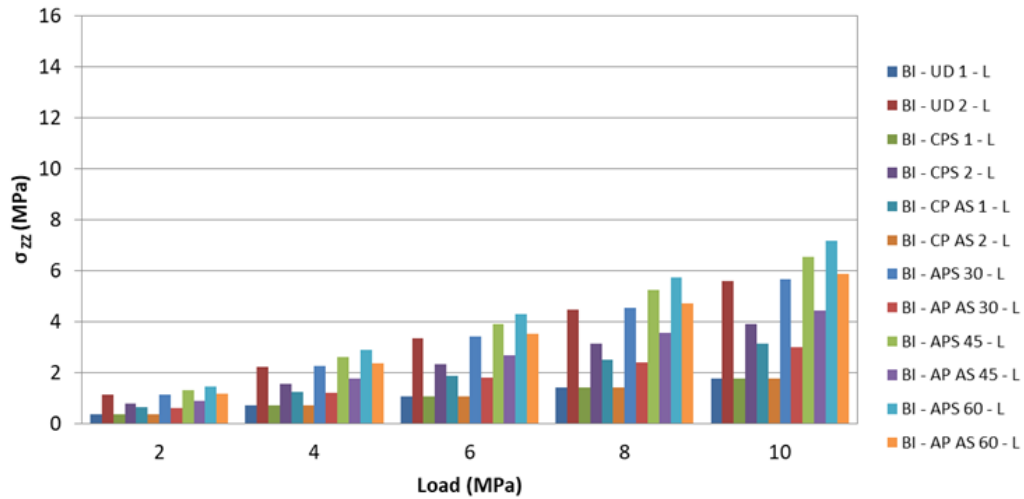


Fig. 9- Linear variation of σ_{zz} at Bottom Interface

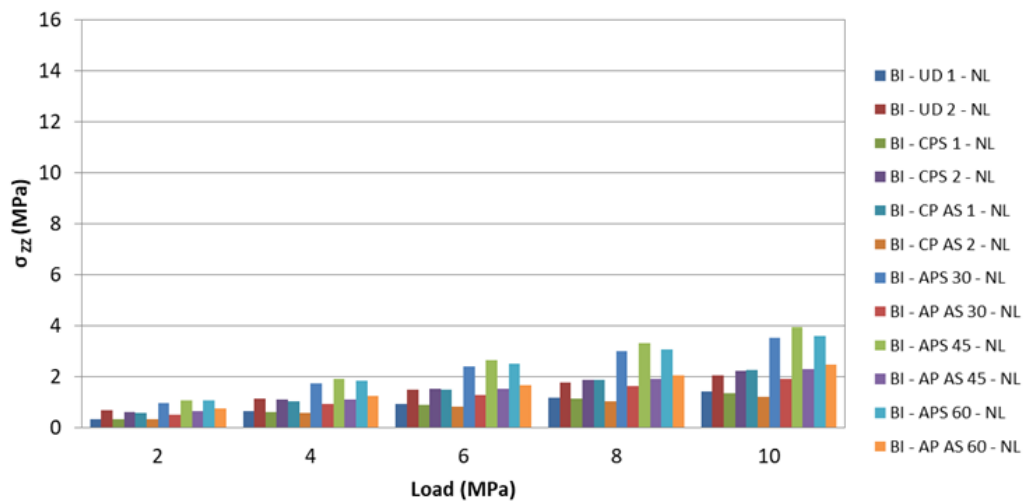


Fig. 10- Non-linear variation of σ_{zz} at Bottom Interface

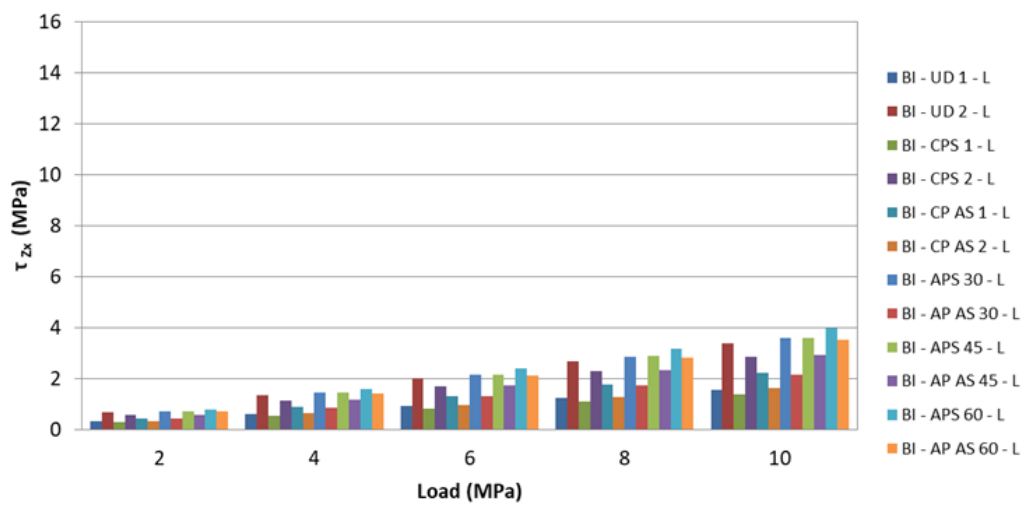


Fig. 11- Linear variation of τ_{zx} at Bottom Interface

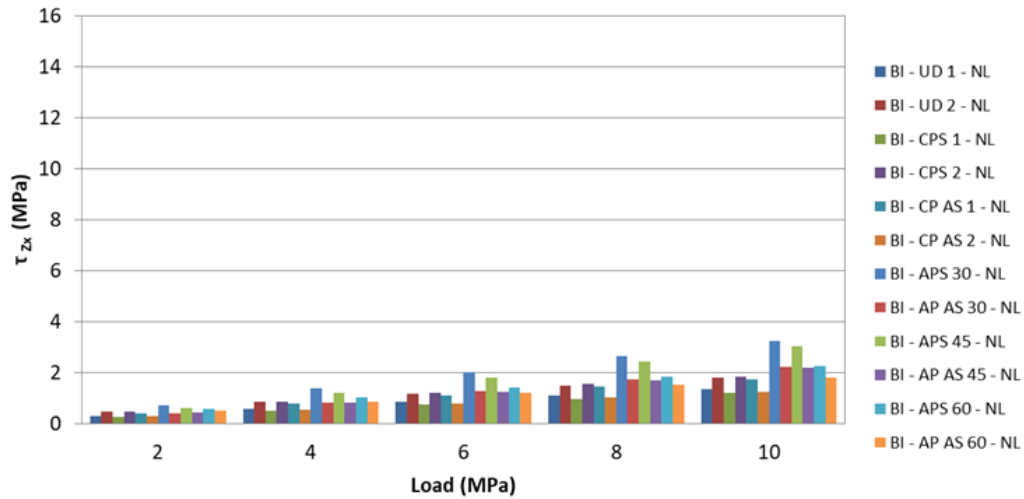


Fig. 12- Non-linear variation of τ_{zx} at Bottom Interface

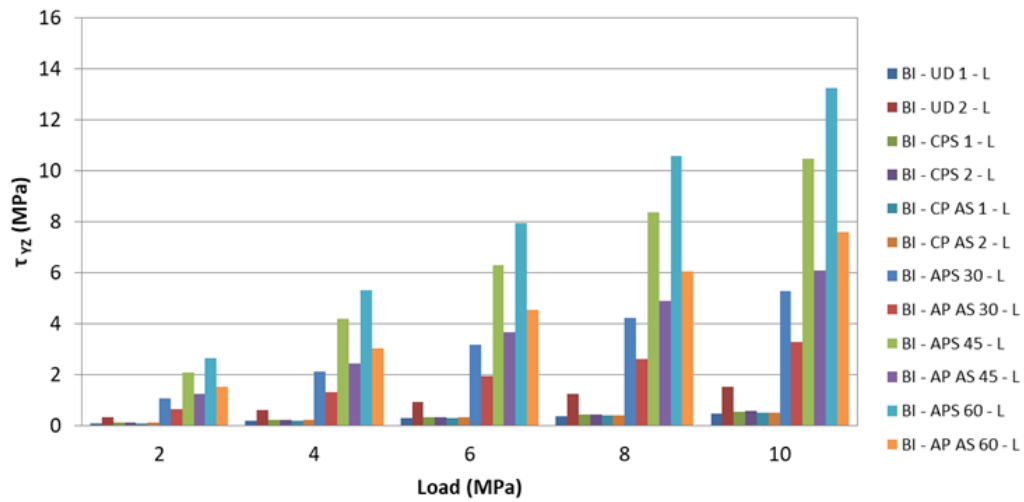


Fig. 13- Linear variation of τ_{yz} at Bottom Interface

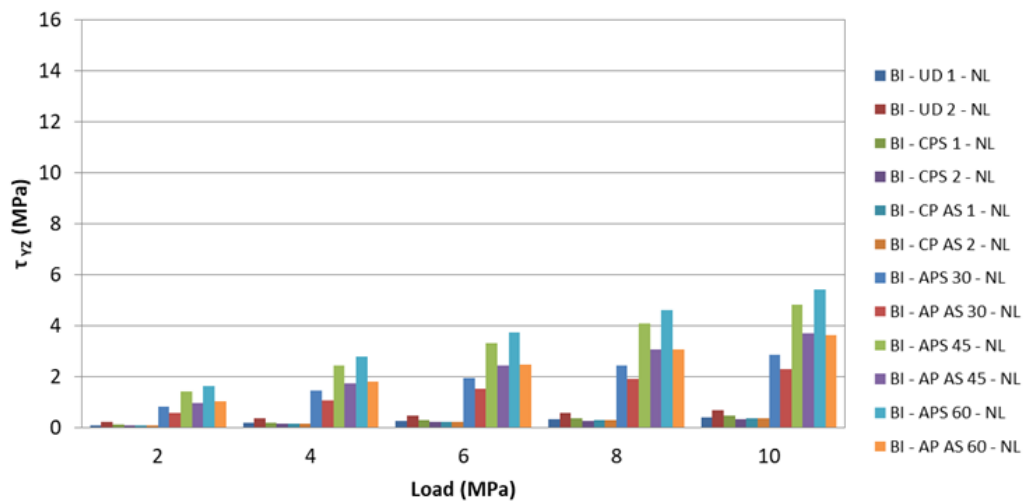


Fig. 14- Non-linear variation of τ_{yz} at Bottom Interface

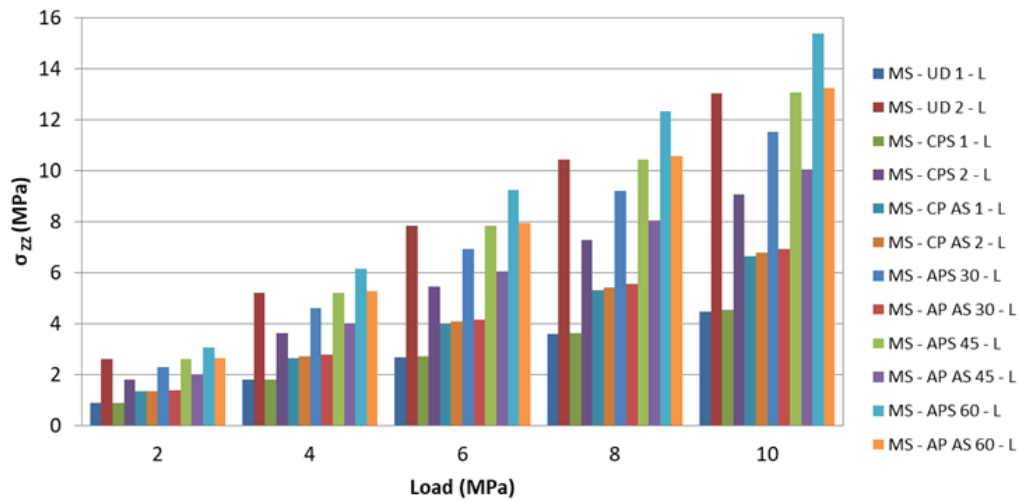


Fig. 15- Linear variation of σ_{zz} at Mid surface of adhesive

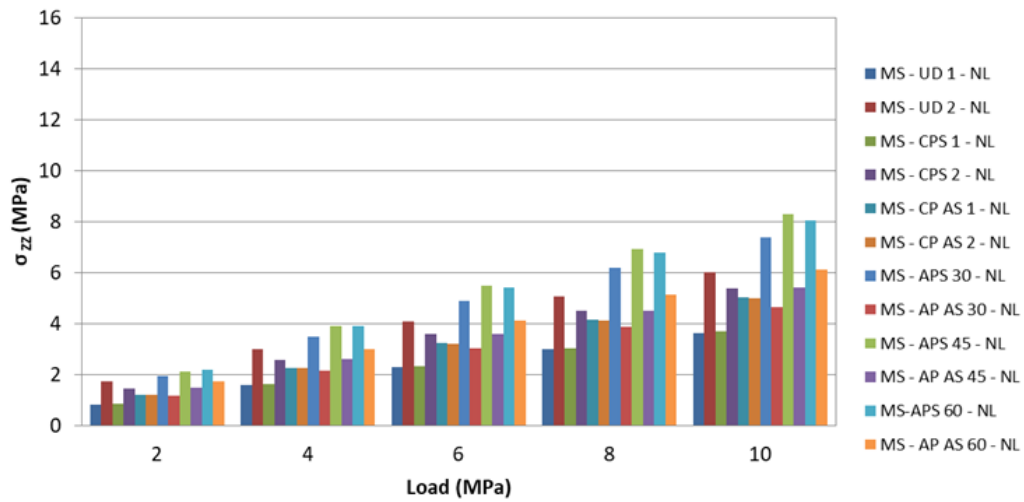


Fig. 16- Non-linear variation of σ_{zz} at Mid surface of adhesive

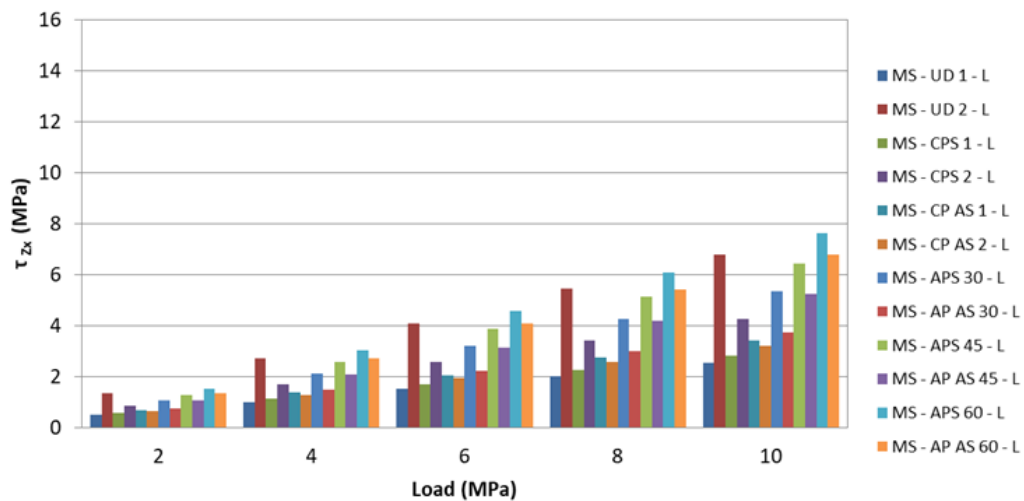


Fig. 17- Linear variation of τ_{zx} at Mid surface of adhesive

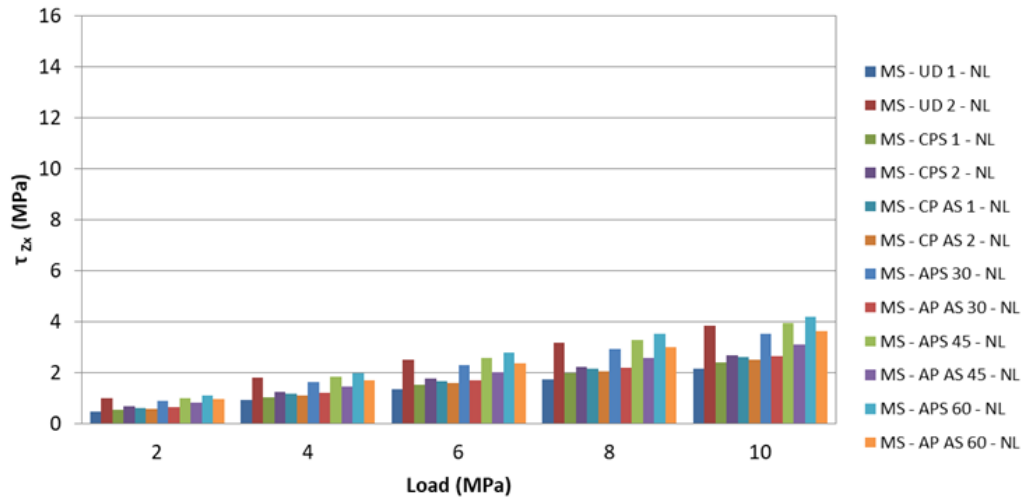


Fig. 18- Non-linear variation of τ_{zx} at Mid surface of adhesive

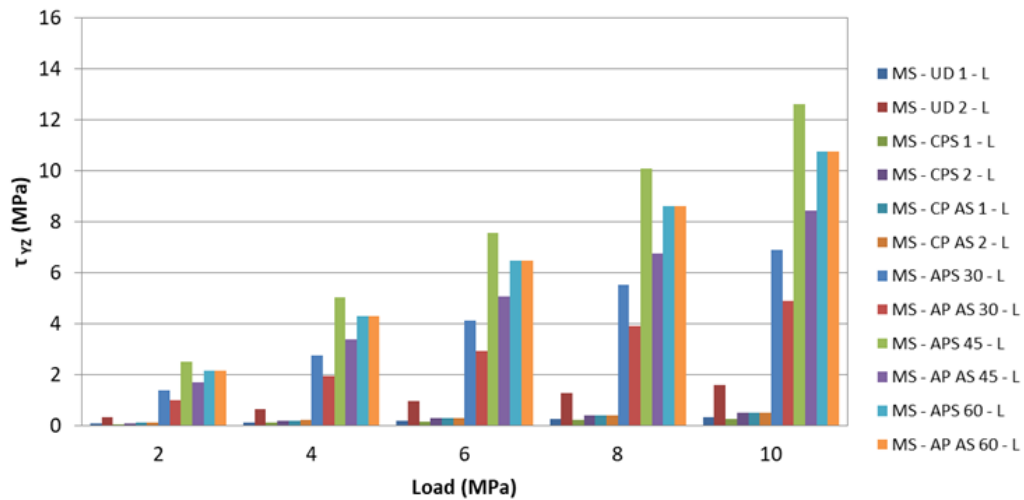


Fig.19- Linear variation of τ_{yz} at Mid surface of adhesive

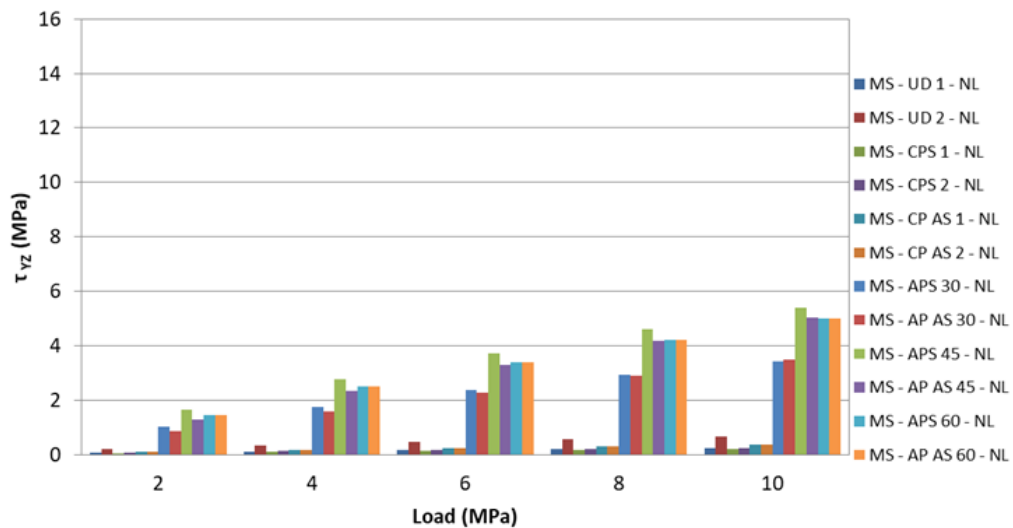


Fig. 20- Non-linear variation of τ_{yz} at Mid surface of adhesive

CONCLUSIONS

The 3D Finite element model is prepared and performed the geometric non-linear analysis by changing the stacking sequence to evaluate the interlaminar stresses at the bonded region of SLJ. The interlaminar stresses (normal and Shear stresses) are greatly influenced w.r.t. stacking sequence. The reason is due to variation of inter-layer mismatch from one case to other. The results from the analysis will be useful for efficient design of single lap joint. The following conclusions are drawn from the analysis:

- The Normal stress (σ_{zz}) observed to be maximum at Angle-ply Symmetric 45° (45°/-45°/-45°/45°) at top interface, bottom interface and mid surface of adhesive.
- The shear stress (τ_{zx}) observed to be maximum at Angle-ply Symmetric 30° (30°/-30°/-30°/30°) at top interface and bottom interface. The shear stress (τ_{zx}) observed to be maximum at Angle-ply Symmetric 60° (60°/-60°/-60°/60°) at mid surface of adhesive.
- The shear stress (τ_{yz}) observed to be maximum at Angle-ply Symmetric 60° (60°/-60°/-60°/60°) at top interface and bottom interface. The shear stress (τ_{yz}) observed to be maximum at Angle-ply Symmetric 45° (45°/-45°/-45°/45°) at mid surface of adhesive.

REFERENCES

- [1] S. K. Panigrahi, and B. Pradhan, “Three dimensional Failure analysis and Damage Propagation Behavior of Adhesively Bonded Single Lap Joints in Laminated FRP Composites”, *Journal of Reinforced plastics and Composites*, 2007, 26(2), 183-201.
- [2] N. Vijeta ,V. Bala Krishna Murthy, G. Ranga Janardhana and V.V. Sridhara Raju, “Non-Linear Analysis of adhesively Bonded Single Lap Joint in Laminated FRP Composites”, *International Journal of Applied Engineering Research*, 2010, 5(15), 2557–2564.
- [3] M. D. Aydin, “3-D nonlinear stress analysis on adhesively bonded single lap composite joints with different ply stacking sequences,” *Journal of Adhesion*, 2008, 84, 15–36.
- [4] M. Khodja, A. Ahmed, F. Hamida, G. Corderley, and S. Govender, “Stress Evaluation of Adhesively Bonded Lap Joints with Aluminum 2024-T3 Adherents Using FEA,” *Material Research Proceedings*, 2018, 4, 23–28
- [5] R. R. Das and B. Pradhan, “Adhesion failure analyses of bonded tubular single lap joints in laminated fibre reinforced plastic composites,” *International Journal of Adhesion and Adhesives*, 2010, 30(6), 425–438.
- [6] S. Kumar and S. Tampi, “Modeling of single-lap composite adhesive joints under mechanical and thermal loads,” *International Journal of Adhesion Science and Technology*, 2016, 30(7), 759–783.
- [7] S. K. Panigrahi, “Structural design of single lap joints with delaminated FRP composite adherends,” *Composites: Part B*, 2013, 51, 112–120.
- [8] K. Senthil, A. Arockiarajan, and R. Palaninathan, “Numerical study on the onset of initiation of debond growth in adhesively bonded composite joints,” *International Journal of Adhesion and Adhesives*, 2018, 84, 202–219.
- [9] F. KADIOGLU, “Mechanical behaviour of adhesively single lap joint under buckling conditions,” *Chinese Journal of Aeronautics*, 2021, 34(2), 154–164.
- [10] F. Kadioglu, M. Demiral, and M. El Zaroug, “Effects of overlap length on the strength of bolted, bonded and hybrid single lap joints with different adherend materials and thicknesses,” *Journal of Adhesion Science and Technology*, 2019, 33(20), 2191–2206.

Comprehensive review on thermo physical characteristics of nano-based coolants

Md.Abbas¹, K. Dileep¹, K.Bala Subrahmanyam¹, Vidya.Ch²

¹ UG student, Mechanical Engineering Department, P.V.P. Siddhartha Institute of Technology, Vijayawada, A.P.

² Assistant Professor, Mechanical Engineering Department, P.V.P. Siddhartha Institute of Technology, Vijayawada, A.P.

Abstract: Industrial revolution demands for upgrading the performance of each sub component of energy harvesting application. One such vital application is automotive industry. In automotive systems researchers always attempts to focus equally on energy input aspects of the system as if the out put parameters. Since last two decades many research teams have put efforts to increase the heat transfer capacity of engine cooling system while keeping the pumping power minimum. As part that journey researches have revealed that the thermodynamic characteristics of the coolant play a key role in achieving the objective. The present comprehensive review attempts to recap the progress of various nano fluids in enhancing the thermodynamic properties.

Introduction:

Nano fluids are basically a two-phase mixture with dispersion of tiny solid particles [1]. Due to the dispersion of very minute size nano particles the fluid suspension undergoes very chaotic movements which leads to enhancement of flow properties[2]. Nano fluids are finding diverse number of applications because of their thermodynamics properties. One usual application is utilization as cooling media in heavy duty transport systems. Rapid development was recorded in the progress of nano fluids as heat exchange media. That inspired us to consolidate various investigations which took place in the recent years to apply nano fluids in heat exchangers.

Literature review:

Ravikanth S. Vajjha et al [3] have conducted experiments to study thermal conductivity of Al₂O₃ and CuO based nano fluids with water as base fluid. Their research reported that the thermal conductivity of the nano suspensions follows upward trend by increasing the particle concentration. Based on the experimentation results the team have proposed an empirical correlation following a model which is a combination of static component of maxwell theory with account of chaotic Brownian motion of the dispersed nano particles.

$$k_{nf} = \frac{kp + 2kbf - 2(kbf - kp)\phi}{kp + 2kbf + (kbf - kp)\phi} kbf + 5 \times 10^4 \beta \phi \rho_{bf} C_{pbf} \sqrt{\frac{kT}{\rho p d p}} f(T, \phi)$$

S.Ravi babu et al [4] studied the thermo physical properties of Al₂O₃ based nano fluid with water as well as water and ethylene glycol mixture as base fluid for varying concentrations ranging between 0 to 1.6% on weight basis. Based on sensitivity analysis it was noticed that

thermal conductivity is more prone to high volume fractions of nano particles in comparison to lower concentration. Their investigation reported that the dynamic viscosity of nano samples enhanced by around 12% with pure water as base fluid while lying between 11 to 13% for water ethylene glycol blends. Their investigation concluded that the density variation of ethylene glycol blend nano fluids was comparatively lower than water based nano fluids which would be contributing for the reduction of pumping power.

Their research reports that the maximum augmentation occurs in the thermal conductivity is 11.37% at 1.6 vol% for (water + EG) based Al₂O₃ nano fluids. It is also observed that, dynamic viscosity by 10.36% by 1.6 vol%, for (water + EG)/Al₂O₃ nano fluids compared to water + EG blend. the viscosity of water + EG based, alumina nano fluid for various nano particle loading, from 0.2 to 1.6 Vol% and at different temperatures, from 30 °C to 70 °C. It is observed that, the viscosity is increased with the addition of alumina nano particles, and the viscosity improvement is increased with the increase in nano particle loading. The maximum enhancement is observed at 10.36%, for water + EG based alumina nano fluid. The viscosity correlation is developed, based on the parameters like Volume fraction, Temperature, Volume fraction * Volume fraction as

$$\mu_{nf} = \mu_{bf}(0.994 + 0.00457\phi + 0.0145\phi^2 - 0.0000001T)$$

I.M. Mahbulul et al [5] studied the influence of particle size towards the variation of viscosity for Al₂O₃ and ZnO based nano fluids. The study considered a volume fraction of nano particles ranging between 2.5% to 15% with a step size of 2.5% while varying the particle diameter from 20nm to 100nm. According to DLVO theory the research team have concluded that the interparticle spacing along with the period of free movement of particles with out aggregation are the pivotal factors to understand the variation of viscosity of nano fluids.

$$k_m = \frac{k_{pe} + 2k_f + 2(k_{pe} - k_f)\phi m}{k_{pe} + 2k_l - (k_{pe} - k_f)\phi m} k_f$$

S.M.Peyghambarzadeh [7] have conducted experiment to compare the heat transfer performance of pure water and pure EG with the binary mixtures. And some amount of Al₂O₃ is added to the base fluids and determined how the heat transfer performance is effected by experimentally. The liquid flow rate changes range between 2-6l per minute. In the best conditions, the heat transfer enhancement of about 40% compared to the base fluids has been recorded. Finally they concluded that the heat transfer behaviour of the nano fluids highly depended on the particle concentration and flow conditions and lightly dependent on the temperature. Their result indicates that the nano fluids have great potential for heat transfer enhancement and are highly suited to apply in particular heat transfer processes. The heat transfer coefficient and corresponding Nusselt number can be derived as follows

$$Nu = \frac{h \cdot d}{k} = \frac{mC_p(T_{in} - T_{out})}{A(T_b - T_w)}$$

N.P.Sigisthana et al [8] have studied Continued advances in the automotive industry require the need for more efficient engines. A high-performance engine should have better fuel efficiency such as its high performance. I vehicle performance is improved as engine size and power increase. However, radiator size increases with engine power. The addition of Fin has been one of ways to increase radiator cooling speed. This approach leads to better air

development convective heat transfer as it provides a large area for heat transfer. Development of heat transfer for many industrial applications by adding liquid nano particles have been an important topic for the past 10 years. This article included the element of collision and the forced convection heat transfer of the dispersed nano particle water as a basic fluid made in a car radiator by testing and numbering. The test set includes a vehicle radiator, and effects on the development of heat transfer under operating conditions are analyzed. Numerical results indicate nano fluid concentration, operating temperature, particle size and the shape, as well as the properties of the nano particle dispersed in the basic liquid, are important influence on coefficient of heat transfer.

The study of heat transfer using Al_2O_3 using low fraction nano fluids in turbulent flow with constant temperature . CFD modeling of the nano fluid flow adopting the single phase approach. Volume fraction of 1% is found an effective heat transfer enhancement in nano fluids.

Volume concentration of a nano particles is set between the range of 0 to 1 vol% and at different temperature, range from 10 °C to 50 °C in order to verify the influence of volume concentration on viscosity, specific heat, density and thermal conductivity of nano fluid. The result verified that viscosity, density and thermal conductivity of a nano fluid increases proportionally with the increment in volume concentrations. Heat transfer coefficient can be evaluated by applying the Equation 6 which is as below

$$h = EXP \frac{mCp(T_{in}-T_{out})}{As(T_b-T_s)}$$

Xiang-Qi Wang [9] have investigated thermal properties and applications of nano fluids by theoretical and numerical, research on flexible heat transfer using solid nanometer particles with a base size the flu has started over the past decade. Recent research on nano fluids, as such suspensions are common called, shows that synthetic nano particles significantly change the transport and transfer properties of heat suspension features. This first part of the review summarizes recent research on theory as well research into the numbers of various thermal structures and the use of nano fluids.

N.T.Ravi Kumar et al [10] carried out experimental investigation on double pipe heat exchanger with return bend using Fe_2O_3 nano fluid. Their investigation reported a Nusselt number enhancement of 14.7% with 0.06vol% of nano particle concentration at $Re=30000$. The same research group has extended their work further with longitudinal strip inserts and concluded an enhanced in Nusselt number value by 41.29% for the Reynolds number value of 28,954.[11] Peclet number exhibits prominent influence on heat transfer coefficient of a shell and tube heat exchanger when operated with Al_2O_3 and TiO_2 nano fluids for a volume concentration of 0.5 and 0.3% respectively. [12] Experimental investigation registered an enhanced heat transfer performance of a plate heat exchanger loaded with MWCNTs. However, an undesirable effect of augmented friction factor and pressure drop was also noticed.[13]Utilization of TiO_2 nano fluid imparted increased heat transfer rates to a concentric tube heat exchanger.[14] Majan Goodarzi et al have put an effort to augment the performance of double pipe heat exchanger by dispersing nitrogen doped graphene nano sheets in terms of thermal conductivity, specific heat as well as convective heat transfer rates. Their study reported enhanced thermal characteristics followed by a little penalty in pumping power.

Conclusions:

Depleting fossil energy reserves as well as alarming environmental changes leading to a call for efficient energy conversions along with conservations. To achieve these primary goals nano fluids have drawn attention because of their contribution in the field of heat exchange applications. In order to commercialize the idea on large scale in industrial applications, critical focus is demanded on the following aspects.

- 1) Scientific evaluation of physical as well as chemical stability of these fluids in both quiescent as well as turbulent conditions, since that property decides the success in thermal management studies.
- 2) A reliable and easily accessible database of thermal, chemical and physical characteristics of different possible nano fluids.
- 3) A root level understanding regarding the interaction of tiny particles as well as between the nano particles to flow conduit walls and the details regarding development of thermal boundary layers also needed to be analysed with the aid of experimental investigations along with simulations in order to understand the mechanism underlying heat transfer enhancement.
- 4) Influence of additives or surfactants on the chemical properties and chemical stability of the nano fluids needs to be addressed carefully.

REFERENCES

- [1] Stephen U. S. Choi, Nano fluids: From Vision to Reality Through Research, *J. Heat Transfer*. Mar 2009, 131(3): 033106 , <https://doi.org/10.1115/1.3056479>.
- [2] Sarit Kumar Das, Stephen U. S. Choi & Hrishikesh E. Patel (2006) Heat Transfer in Nano fluids—A Review, *Heat Transfer Engineering*, 27:10, 3-19, DOI: 10.1080/01457630600904593
- [3] Ravikanth S Vajjha, Debendra K Das, Praveen K Namburu, Numerical study of fluid dynamic and heat transfer performance of Al₂O₃ and CuO nano fluids in the flat tubes of a radiator, *International journal of heat and fluid flow*, 31 (2010) 613-621.
- [4] Ravi babu S, Sambasiva rao G, Thermal conductivity and viscosity of water and ethylene glycol blend based alumina nano fluids – an experimental study, *International Journal of Mechanical and Production*, Vol. 7, Issue 5, Oct 2017, 183-190.
- [5] Fundamentals of Heat Exchanger Design, Ramesh K.Shah and Dusan P.Sekulic.
- [6] Gaganpreet, Sunita Srivastava, Effect of aggregation on thermal conductivity and viscosity of nano fluids, *Applied nano science*, (2012) 2:325-331.
- [7] S.M.Peyghambarzadeh, S.H.Hashemabadi, S.M.Hoeisini, M.Seifi Jamnani, Experimental study of heat transfer enhancement using water/ethylene glycol based nano fluids as a new coolant for car radiators, *International communications in het and mass transfer*, 38, (2011) 1283-1290.
- [8] N.P.Sigithasan, Design and development of automobile radiator aided with nano particles as cooling fluid.
- [9] Xiang-Qi Wang and Arun S. Mujumdar, A review on nano fluids - part i: theoretical and numerical investigations, *Brazilian journal of chemical engineering*, Vol. 25, No. 04, pp. 613 - 630, October - December, 2008

- [10] N.T. Ravi Kumar, P. Bhramara, Birhanu Mulat Addis, L. Syam Sundar, Manoj K. Singh, Antonio C.M. Sousa, Heat transfer, friction factor and effectiveness analysis of Fe₃O₄/water nano fluid flow in a double pipe heat exchanger with return bend, *International Communications in Heat and Mass Transfer* 81 (2017) 155–163
- [11] N.T. Ravi Kumar, P. Bhramara, L. Syam Sundar, Manoj K. Singh, Antonio C.M. Sousa, Heat transfer, friction factor and effectiveness of Fe₃O₄ nano fluid flow in an inner tube of double pipe U-bend heat exchanger with and without longitudinal strip inserts, *Experimental Thermal and Fluid Science* 85 (2017) 331–343
- [12] B. Farajollahi, S.Gh. Etemad, M. Hojjat, Heat transfer of nano fluids in a shell and tube heat exchanger, *International Journal of Heat and Mass Transfer* 53 (2010) 12–17
- [13] M.M. Sarafraz, F. Hormozi, Heat transfer, pressure drop and fouling studies of multi-walled carbon nanotube nano-fluids inside a plate heat exchanger, *Experimental Thermal and Fluid Science* 72 (2016) 1–11
- [14] Jaafar Albadr, Satinder Tayal, Mushtaq Alasadi, Heat transfer through heat exchanger using Al₂O₃ nano fluid at different concentrations, *Case Studies in Thermal Engineering* 1 (2013) 38–44